Nature or Nurture? Collisionless Evolution of Galactic Disc-Halo Systems

by

Jacob S. Bauer

A thesis submitted to the
Department of Physics, Engineering Physics & Astronomy
in conformity with the requirements for
the degree of Doctor of Philosophy

Queen's University
Kingston, Ontario, Canada
September 2019

To Mom and Dad. Thank you for supporting me when I have been hard to support.

– Your Loving Son

Abstract

In this thesis, we develop and apply a novel algorithm to understand the evolution of stellar disks in ΛCDM cosmological halos. Three main scientific areas are addressed: the effects of evolving stellar disks on their host halos, understanding bar formation in cosmological settings, and the formation of vertical disc structure in response to the host halo.

First, we find that the presence of central concentrations of baryons in dark matter halos enhances adiabatic contraction causes an overall modest reduction in substructure. Additionally, the detailed evolution of stellar disks is important for the inner halo density distribution. However, properties of the halo such as the subhalo mass function are broadly unaffected by the evolution of a realistic stellar disk.

Next, we find that stellar bars invariably form in Milky Way-like galaxies. The strength of these bars is less dependent on properties like the dynamical temperature of the disk in a cosmological setting. Instead, the disk thickness plays a leading role in determining the overall bar strength. Our disks undergo notable buckling events, yielding present-day pseudobulge-disc-halo systems. We show that these are qualitatively similar to the observed Milky Way.

Finally, we show that a wide variety of vertical structure forms when stellar disks are embedded in cosmological halos. We further show that through a variety of mechanisms, similar vertical structure is excited. By examining twelve simulations of disks in cosmological halos, we show that the Sgr dSph need not be as massive as $10^{11}\,M_{\odot}$ to be consistent with observed vertical structure in the Milky Way. In fact, the recent buckling of the Milky Way's bar and its present interaction with the LMC are more likely culprits for some of the observed structure in the Milky Way's thin disk.

Statement of Originality

The research presented in this thesis was completed under the supervision of Prof. Lawrence M. Widrow at Queen's University. All of the work presented here was done by the author (Jacob S. Bauer) except where explicitly stated otherwise.

Chapter 3 contains a reproduction of a paper published in Monthly Notices of the Royal Astronomical Society as: Jacob S. Bauer, Lawrence M. Widrow, and Denis Erkal. Disc-halo interactions in ΛCDM. *Monthly Notices of the Royal Astronomical Society*, 476:198-209, 2018. For this paper, I ran all of the simulations. The writing is mine with direct input from Lawrence M. Widrow and Denis Erkal. I performed all of the calculations. The analysis was handled primarily by me under the direction of Lawrence M. Widrow, with substantial input from Denis Erkal.

Chapter 4 contains a reproduction of a paper published in Monthly Notices of the Royal Astronomical Society as: Jacob S. Bauer and Lawrence M. Widrow. Can stellar discs in a cosmological setting avoid forming strong bars?. *Monthly Notices of the Royal Astronomical Society*, 476:523-537, 2019. For this paper, I ran all of the simulations. The writing is mine with direct input from Lawrence M. Widrow. I performed all of the calculations, except the one in §2.3 which was performed by Lawrence M. Widrow. Figures 2-4 were also the work of Lawrence M. Widrow. The analysis was handled primarily by me under the direction of Lawrence M. Widrow.

Chapter 5 contains a draft of a paper submitted to Monthly Notices of the Royal Astronomical Society. Its current manuscript ID is MN-19-3241-MJ. For this work, I performed all of the simulations and writing. The analysis was handled primarily by me under the direction of Lawrence M. Widrow.

Acknowledgments

As I reach the end of this chapter of my life, I know that I did not reach this milestone unassisted. Here, I recognize those who have helped me in this accomplishment.

I want to acknowledge, first and foremost, the amazing supervision I received from Larry Widrow. His careful, unyielding approach to scientific research has not only shown me how to be a better scientist, but a more conscientious communicator. I am immensely grateful for the opportunity to work with him, and for the years of guidance that will serve me well for the rest of my life.

In addition to Larry, I want to acknowledge my other mentors, Heidi Newberg and Denis Erkal. Through my work with each of them, I learned how to evaluate myself more honestly, both professionally and personally. I am grateful that through my work with my mentors, I learned to be simultaneously self-critical and able to forgive myself for mistakes. Without Heidi's and Denis' guidance, I would not have been able to finish this work.

To all of the other faculty members and Department staff, I am tremendously grateful for your contributions to me personally, and to the program as a whole. I am proud of my friends and colleagues at Queen's, and it is through your hard work that this positive academic environment exists. I wish you all the best.

I am grateful for the years of friendship with my fellow astronomy graduate students. In their own ways, they have all kept me mostly sane for 4 years. I would not have been able to persevere without their support. Although they did not succeed in turning me into a Canadian, they did manage to make me grow a beard. I look forward to many more years of friendship.

I want to acknowledge my wonderful family for their support. Mom and Dad have been my biggest supporters through the ups and downs, and this thesis is as much their accomplishment as it is mine.

I am grateful to Rachel Peckman, Chris Weir, and Taylor Weir for our lasting friendships. In high school, Chris showed me that I was capable of pursuing science. Our adventures in Tech Club (RIP), our shenanigans at RPI (RIP), and subsequent friendship (not RIP) made me strive to be a better technologist and person.

Lastly, I want to acknowledge my partner, Alexis Hill. I can't wait to see what adventures life hold for us in Austin. I wouldn't want to be on this roller coaster called life with anyone else.

Contents

List of Tables

List of Figures

List of Abreviations

Abbreviation	Expansion
AGAMA	Action-based Galaxy Modelling Architecture
DF	Distribution Function
F(L)RW	Friedmann (Lemaître) Robertson Walker
GMC	Giant Molecular Cloud
LAMOST	Large Sky Area Multi-Object Fiber Spectroscopic Telescope
LMC	Large Magellanic Cloud
M31	Messier object 31 (Andromeda)
M33	Messier object 33
NFW	Navarro-Frenk-White
RAVE	Radial Velocity Experiment
SDSS	Sloan Digital Sky Survey
Sgr dSph	Sagittarius Dwarf Spheroidal [Galaxy]
Sgr	[The] Sagittarius [Stream]
SMC	Small Magellanic Cloud

List of Symbols

Symbol/Unit	Meaning
Gyr	Gigayear; 10^9 years
kg	Kilogram; standard SI unit of mass
kpc	Kiloparsec; 10^3 parsecs
m	meter; standard SI unit of length
$M_\odot$	Solar mass; approximately 2×10^{30} kilograms
Mpc	Megaparsec; 10^6 parsecs
Myr	Megayear; 10^6 years
$O(f)$	Big O notation; on the order of f
pc	parsec; approximately 3.1×10^{16} meters
s	second; standard SI unit of time
yr	year; approximately 3.2×10^7 seconds

Chapter 1

Introduction

1.1 Perturbations to People

Imagine you are standing on the corner of a busy Manhattan street. Every minute that passes shows the liveliness of a dynamic system, built up over many years. On an average block, there are approximately 28,154 people in the surrounding square kilometer, and a total of 1.7 million people on the island (U.S. Census Bureau, 2010). In contrast, a mere 300 years ago, the population was more disperse, and numbered in the thousands (Wikipedia, 2018). Collections of thousands of people, initially spread out, came together to form a massive, dynamic ecosystem that represents an epicentre of modern human innovation and industry. Manhattan is not unique; cities across the world did not appear overnight, but were constructed hierarchically. It is in a similar fashion that modern astrophysics believes our Milky Way, and all massive galaxies formed with stars and gas as their building blocks.

We believe that the Universe began with a period of rapid inflation, and that in the process of this inflation, pockets of the Universe emerged more dense than other regions. This is revealed to us through observations of the cosmic microwave background (CMB). The CMB is a portrait of the Universe when it was last opaque; before electrons, neutrons, and protons combined to form the first atoms. It shows temperature fluctuations, like small population overdensities, that would eventually become cosmic cities. While many physicists marvel at the physics that happens in these first moments of time, there is another story of how cosmic villages come together to form cities. This is the story of how tiny perturbations evolve to the structures astronomers see today.

When we look at the CMB, we are seeing the temperature distribution of matter through the radiation of baryonic matter, the matter that interacts with light. There is strong observational evidence to suggest that a large fraction of the matter present at this epoch is not interacting with light. This evidence is found in the power spectrum of the CMB, a function that describes the distribution of scales of the perturbations in the CMB (Eisenstein et al., 1999).

This dark matter appears to be present in the current epoch. Evidence of dark matter in modern-day galaxy clusters was first observed by Zwicky (1933), who inferred that the mass of the Coma Cluster needed to be approximately ten times higher than observed to explain the motions of the constituent galaxies. A convincing case for dark matter in individual galaxies was presented by Rubin et al. (1980), who show that the rotational speeds of stars in the disks of galaxies were too high to be explained by observed mass.

Based on enormous observational evidence, the dark matter component of the Universe appears to be substantial. If the results from the Planck satellite are taken as truth, then dark matter comprises around 84% of all matter in the Universe (Planck Collaboration et al., 2018). Dark matter influences the evolution of galaxies not only because it is not subject to radiation-based interactions, but also because it is most of what there is. Dark matter is the glue that holds galaxies together.

Although dark matter makes up 84% of the matter, matter only makes up 31.5% of the present day Universe's total energy density. The remainder contains a modest contribution from radiation, but the bulk is comprised of unaccounted dark energy (Kolb and Turner, 1990; Dodelson, 2003; Binney and Tremaine, 2008). Dark energy, whatever it is, is responsible for the accelerating expansion of the Universe, something we first learned from observations of Type 1a supernova (Riess et al., 1998; Perlmutter et al., 1999). Modern cosmology is a struggle between the competing forces of dark matter and dark energy, and both have implications for the local dynamics in the Universe.

To understand how dark matter is interacting with galaxies, we need to pin down its dynamics. This depends on what dark matter actually is. Some candidates, such as neutrinos, are relativistic particles that constitute hot dark matter. Warm and cold dark matter candidates become progressively non-relativistic, and there are many candidate particles for these models. An interesting and currently active proposal is that massive WIMPs, which were relativistic and coupled to baryons at early times, but cooled as the Universe expanded.

A model of the Universe one might consider is one comprised of cold dark matter and dark energy, described on large scales by a single parameter, Λ. This paradigm is called ΛCDM and is the prevailing model in the astronomy community. The model has been enormously successful in explaining observations, including the CMB power spectrum. While there remain open problems with ΛCDM, it appears to predict many properties on Galactic and extragalactic scales correctly (Kolb and Turner, 1990; Dodelson, 2003; Binney and Tremaine, 2008). Proposals to modify ΛCDM tend to present only slight variations on the model, such as allowing for self interacting dark matter (SIDM).

Taking ΛCDM as the ground truth, we can begin to understand how galaxies evolved from tiny villages. Dark matter, which does not interact through any force but gravity, retains a perturbed structure after inflation. The density perturbations collapse, forming potential wells of dark matter (Taylor, 2011). The exact manner in which this happens is *linear*, meaning that the amplitude of the perturbations increases proportionally with the expansion of the Universe, as measured by the scale

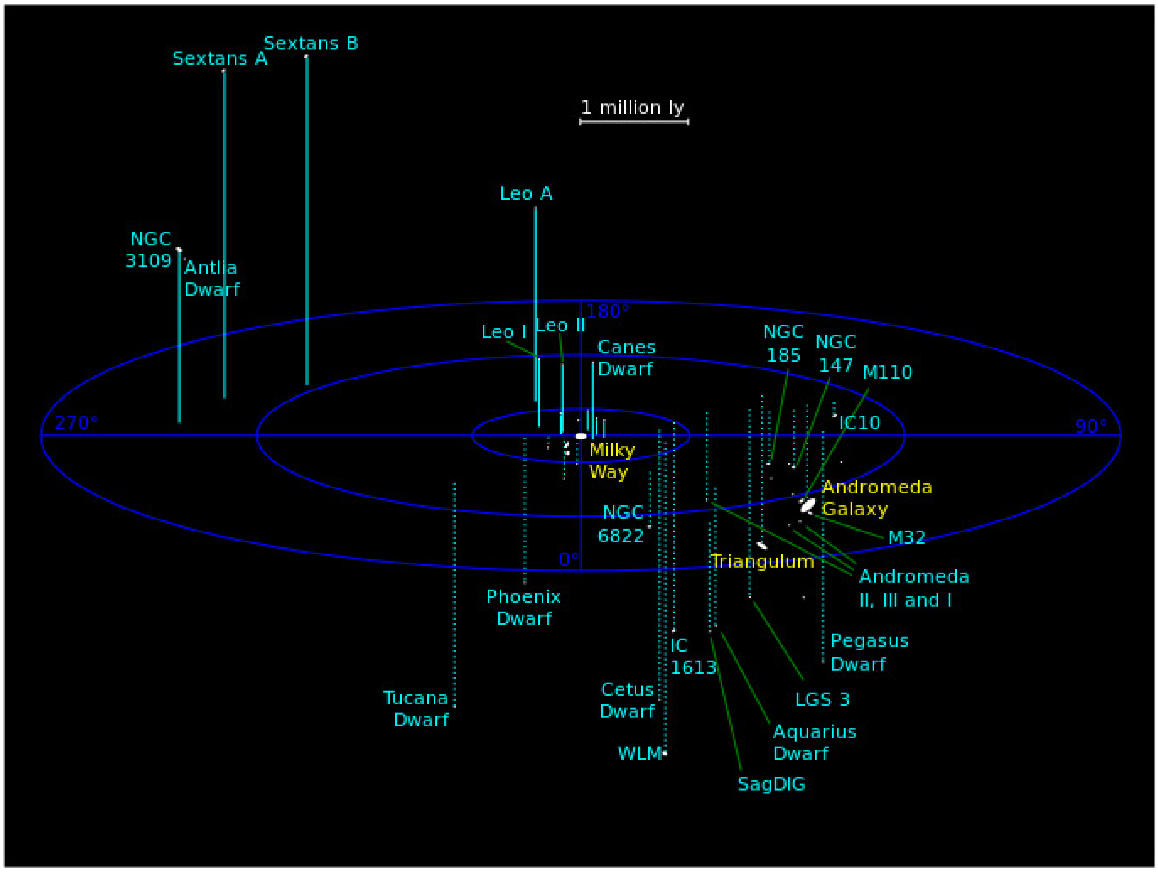

Figure 1.1: A map of the Local Group obtained from Powell (2017), and reproduced under the Creative Commons Attribution-Share Alike 2.5 Generic license.

factor.

The baryons, interacting through baryon acoustic oscillations (BAO), are delayed in falling into the potential wells made by the dark matter. As the baryons fall into the centers of the potential wells over time, the cores of the dark matter distributions, comprised of spheroidal structures called haloes, contract. After infall into a dark matter halo, the baryons cool to the point where stars are able to form. This is how the first galaxies formed.

Over time, galaxies begin to shift away from the linear mapping between perturbation and galaxy. Their forces on each other start to matter locally, and galaxies begin to merge hierarchically. Collections of galaxies form, sometimes massive clusters of 10^{15} solar masses. Other times, groups with a couple massive galaxies become host to many smaller galaxies called subhaloes. Other galaxies belong to no group or cluster, and exist in the expansive void between clusters. Dark energy continues to pull the Universe apart, while locally galaxies are kept together by dark matter. Merging of galaxies continues on local scales as larger galaxies become larger, bringing us to today.

We live in a spiral galaxy of approximately 10^{12} solar masses (dark matter + baryons), in a group with another galaxy, M31 (Andromeda), which has a roughly similar mass. Our Local Group (Fig. 1.1), as it is called, is comprised of many smaller galaxies. In our Milky Way's halo, for instance, a merger is beginning between the Milky Way and the Large and Small Magellanic Clouds (LMC/SMC), shown in the third quadrant of the inner circle around the Milky Way in Fig. 1.1. The SMC/LMC systems total approximately 10-20% of the Milky Way's mass in total (Erkal et al., 2018). Most of our subhaloes are not nearly this massive, although they number in the hundreds. The picture painted of the Local Group is that of M31 and the Milky Way devouring smaller galaxies. Of course, this will have a substantial impact on the evolution of the stars in the Milky Way, and is the crux of this thesis. By studying the Milky Way's local environment, we can hope to understand the interactions dark matter has on baryons, and perhaps infer something about how dark matter is distributed in our Galaxy.

1.2 Understanding ΛCDM with Galaxy Simulations

Many of the hardest questions in Galactic astrophysics stem from the fact that dark matter is not directly observable. As an example, what is the underlying smooth distribution of dark mass? How many dark matter subhaloes should the Milky Way have? What is the effect on large scales if we choose something other than ΛCDM? While these questions are not easily answerable by direct observation, we can complement indirect observations with a solid theoretical understanding to reach confident answers.

Simulations link theory and observations, allowing the theory to be tested. When a simulation is performed, theoretical input is considered. This includes a model of cosmology, or a model of the galaxy, the nature of dark matter, etc. All of this knowledge is reduced to a fluid system which may be solved through numerical techniques on a computer. The output of the simulation can then be compared to observations to test the underlying theory's validity.

Over the last four decades, many tools have been developed to study the structure of the present day Universe. These tools have become increasingly sophisticated as computation power and algorithms research advance. One tool is an *ab initio* cosmological simulation, which simulates the entire formation history of the Universe from some informed initial density field. This initial density field is derived from the primordial power spectrum and early-Universe baryon physics, and a sample can be drawn and evolved with periodic boundary conditions (Hahn and Abel, 2013). If done correctly, this creates a representative sample of many structures in a ΛCDM Universe. Haloes evolving in these simulations feel the full effect of the completely simulated cosmological environment. Such simulations stand in contrast to isolated galaxy simulations, which seek to explain the detailed dynamics arising from generic effects in individual galaxies. These simulations start with a prescription for what an equilibrium galaxy looks like, and study the evolution of galaxies initialized from these prescriptions. While missing some critical cosmological physics, these simulations may be run at very high resolution.

This thesis studies dynamics on a Galactic scale. Through simulations of galaxies, we can understand how dark matter influences their evolution. ΛCDM has been tested in this way for decades, and we detail some global results in what follows. In particular, we focus on where simulations of galaxies have shown discrepancies in cosmological theory.

We broadly commented on the hierarchical formation of galaxies. Over time, galaxies that merge with other galaxies should become well-mixed in the host halo. That is, there should be an underlying smooth distribution of mass in which all of the subhaloes reside. A key prediction of ΛCDM is that this smooth distribution should have a universal density profile in the limit that dark matter dominates the Universe (Navarro et al., 1997). Furthermore, the dark matter should have a density distribution somewhat resembling a squashed football, a spheroid flattened on two axes, in general. There are, in fact, the special cases of being either perfectly spherical, prolate, or oblate. Whether or not this picture holds observationally in real galaxies is an open problem. The density profile proposed by Navarro et al. (1997) is cuspy at the center, whereas some observations are more consistent with a flatter central density (de Blok, 2010). Astronomers have dubbed this the Core-Cusp Problem.

Besides the Core-Cusp Problem in the inner parts of dark matter haloes, one thing that is clear is that ΛCDM haloes should have many subhaloes. As the general theory for the formation of galaxies goes, these subhaloes were at one point independent perturbations that have since merged into the Milky Way's halo, and should have their own stellar and gas content. This means that we expect many massive subhaloes to be directly observable. Another triumph of simulations is putting an actual number on how many subhaloes we expect from ΛCDM. Surprisingly, far fewer subhaloes are actually observed (Moore et al., 1999; Klypin et al., 1999; Springel et al., 2008). This discrepancy has since been dubbed the Missing Satellite Problem, and is an open problem for ΛCDM and astronomy.

The Core-Cusp Problem and Missing Satellite Problem have received a lot of attention in the literature because of the potential problems they pose for theoretical cosmology. It is clear that to accurately recover the global properties of substructure on large scales, dark matter must be cold. Warm and hot dark matter models[1] simply do not yield substructure populations consistent with observations (Libeskind et al., 2013, for example). SIDM and fuzzy models, where the dark matter can interact on small scales, have been proposed as slight modifications to the ΛCDM paradigm, with some success (Hui et al., 2017, for example).

Despite the presence of alternate theories of cosmology, a large concerted effort has been made to understand discrepancies as a byproduct of baryonic physics. Adequate explanation of halo and substructure response to stellar and gas content would mean that alternate cosmologies are not necessary to explain the Core-Cusp Problem and Missing Satellite Problem. Initially, *ab initio* simulations included only dark matter, but have evolved over the last three decades to consider very sophisticated subgrid models of gas physics and star formation (Lucy, 1977; Cen and Ostriker, 1992; Katz

[1]Hot dark matter is comprised of matter moving at or near the speed of light (e.g. neutrinos), and warm dark matter is somewhere in between cold and hot dark matter.

et al., 1996; Springel and Hernquist, 2003; Stinson et al., 2006). These simulations can be used to realize the galaxy formation predicted by current theories. State of the art unigrid (single resolution) cosmological simulations struggle to compete with the resolution attainable by isolated galaxy simulations (Vogelsberger et al., 2014; Schaye et al., 2015), but they can still be used to make broad statements about consistency with ΛCDM. Broadly speaking, it is not clear at this stage whether or not apparent issues with ΛCDM can be resolved through these models, but they present a promising approach as computing power is sure to increase.

All of the preceding is to say that simulations are an enormously valuable tool in understanding the broad predictions of cosmology on a Galactic scale. We have used them to uncover apparent inconsistencies in ΛCDM, and have a promising means within the paradigm to move forward in resolving these inconsistencies. All of the preceding discussion has focused on the complexity of the halo environment. Ultimately, we are looking for simulations to make observable predictions, and specifically signatures outside the Galactic halo that theory is correct.

1.3 Dynamical Processes in a Chaotic Milky Way

Since dark matter is not directly probable, we must use indirect methods to infer information about the halo. For this, we need to know something about the distribution of mass in the Galaxy.

1.3.1 Distribution of Mass in the Milky Way

In addition to the dark matter halo, our Galaxy is composed of baryons in the form of a central spheroidal bulge, a thin gas disc, a thin stellar disc, and a more diffuse thick stellar disc. The thin stellar disc is where the majority of our work is focused. We see a wide variety of structure in the stellar discs of other galaxies, as well as our own Milky Way. For example, the center of our galaxy is believed to contain a stellar bar, a bar-like component of the thin disc (Binney and Tremaine, 2008). There are also non-planar features in stellar discs, such as warps (Binney and Tremaine, 2008). How these features come into being is a main focus of this thesis.[2]

There is also a stellar component of the halo, which contains remnants of old mergers and star clusters known as globular clusters. This section is organized by talking about tidal disruption of subhaloes in the Galactic halo, the dynamics of the central part of the Galaxy, and vertical structure in the Galactic disc. How the cosmological environment effects these observables is the bulk of this thesis, and we motivate here why these aspects are the subject of focus.

1.3.2 Stellar Streams from Mergers

In the hierarchical formation of galaxies, smaller galaxies merge with larger galaxies and become a part of the larger galaxy's halo. As subhaloes become more a part of the host system, they experience tidal forces that stretch and squeeze their mass content. Dark matter and stellar material is stripped from these merging galaxies over time to form streams of tidal debris. In the long run, this debris will equlibrate with the

[2]For an in-depth discussion of the features arising in stellar discs, Sellwood (2013) presents a fantastic review.

stellar halo. It should be noted that the same effects apply to globular clusters too.

Baryonic debris left behind can detected. The first stream for which this accomplished was the debris of the Sagittarius Dwarf Spheroidal galaxy (Sgr dSph), a dSph galaxy discovered by Ibata et al. (1994). The corresponding stream was later detected by Newberg et al. (2002) and Majewski et al. (2003).

These discoveries of debris associated with a merging dwarf galaxy kickstarted an onslaught of literature based on the detection of streams, and their potential uses in probing the Galactic potential. The general idea is that so long as streams approximately trace orbits in the halo, the correct Milky Way potential, dark matter and all, is the unique potential that reproduces these orbits.

More streams have been discovered since then, and a few notable ones are the Orphan Stream (Grillmair, 2006; Belokurov et al., 2007; Newberg et al., 2010), remarkable for its apparent lack of progenitor, TriAnd, A13, and the Monoceros Ring. This is by no means a complete accounting of known stellar streams. Something on the order of nearly a hundred known to exist in the Milky Way alone (Sanders and Binney, 2013; Ibata et al., 2019). While streams alone have been useful in getting some broad constraints on the Galactic potential and geometry of the halo, complications arise from the fact that streams do not follow orbits exactly (Sanders and Binney, 2013) and the fact that the Milky Way potential is predicted from theory to be time dependent.

The orbits of streams are not the only way to learn about the Milky Way's dark matter halo. It is worth mentioning that there is the possibility of using the fine structure of stellar streams to learn more about the subhalo population in the halo. Gaps form when subhaloes pass through tidal streams, and this is one direction that is being explored for leveraging stellar stream data (e.g. Erkal et al. (2016)).

1.3.3 Response of the Galactic Disc to the Cosmological Environment

We might also attempt to infer properties of the subhalo population through their effect on the Galactic disc. It is believed that the affect of the Milky Way's substructure population can be observed as wave-like behaviour in the thin disc's vertical structure (Widrow et al., 2012; Carlin et al., 2013; Williams et al., 2013; Xu et al., 2015; Carrillo et al., 2018). These waves can manifest as small corrugations in the Galactic disc, as global bending and breathing motions, or even as large warps in the Milky Way's gas (Chakrabarti et al., 2016) and stellar discs. It is worth noting that these observations are being confirmed in DR2 of the Gaia mission (Gaia Collaboration et al., 2018; Bennett and Bovy, 2019, for example).

The Milky Way's massive subhaloes are most likely inducing non-planar density patterns in the disc, and we would like to understand the nature of these patterns through simulation. Unfortunately, we need the high resolution of isolated galaxy simulations to study these effects, and the realism of an *ab initio* Galactic halo. This has motivated a long history of attempts to bridge the gap between *ab initio* cosmological simulations and those of isolated galaxies. A particularly simple class of simulations involves the interaction of a disc with a single satellite galaxy or dark matter subhalo. For example Kazantzidis et al. (2008) perform simulations in which a thin Milky Way-like disc is subjected to a series of encounters with a satellite. The masses and orbital parameters of the satellites are motivated by substructure found in a halo appropriate to a Milky Way-like galaxy from a cosmological simulation.

Their simulation demonstrated that satellite encounters lead to general disc heating as well as distinctive disc features such as bars, spiral structure, flares, and rings. Purcell et al. (2011) model the response of the Milky Way to the gravitational effects of the Sgr dSph by simulating disc-dwarf encounter for different choices of the Sgr progenitor's mass. Their conclusion is that Sgr may have triggered the development the spiral structure seen today in the Milky Way. This approach has gained considerable traction in the last couple years, with authors using single-satellite encounters to explain the existence of low-latitude streams and other vertical structure in the Milky Way's disc (Widrow et al., 2014; de la Vega et al., 2015; D'Onghia et al., 2016; Laporte et al., 2016, 2018, for example). One particularly interesting feature arising from these works is that stars may occasionally be kicked out of the galactic disc to form kicked-up disc populations (Johnston et al., 2017; Laporte et al., 2019). Such populations may explain low-latitude Milky Way structures, and possibly kinematic data of M31 (Dorman et al., 2013).

Of course, the disc of the Milky Way lives within a population of satellite galaxies and, quite possibly, pure dark matter subhaloes, and single-satellite encounters do not describe the complexity of the cosmological environment (Klypin et al., 1999; Moore et al., 1999; Springel et al., 2008). With this in mind Font et al. (2001) simulated the evolution of an isolated disc-bulge-halo model where the halo was populated by several hundred subhaloes. They concluded that that substructure played only a minor role in heating the disc, a result that would seem in conflict with those of the Kazantzidis et al. (2008) that would come later. Numerical simulations by Gauthier et al. (2006); Dubinski et al. (2008) sheds some light on this discrepancy. In these simulations, 10% of the the halo mass in an isolated disc-bulge-halo system is replaced by subhaloes with a mass distribution motivated by the cosmological studies of Gao et al. (2004). In the Gauthier et al. (2006) simulation, little disc heating occurs during the first 5 Gyr, at which point satellite interactions provoke the formation of a strong bar, which in turn leads to significant heating. Not surprisingly, when the experiment is repeated with different initial conditions for the satellites the timing of bar formation can vary. These experiments also suggest that a large fraction of the mass initially in subhaloes is tidally stripped leaving behind a complex system of tidal debris.

The aforementioned simulations, although more realistic than single-satellite encounters, have three main problems. First, they don't allow for halo triaxiality. Secondly, the disc is initialized at its present-day mass whereas real stellar discs form over several Gyr. Finally, the subhalo populations are inserted into the halo by hand. While the mass and spatial distributions of the subhaloes are motivated by cosmological simulations, they may not capture important properties of realistic haloes. This has historically been solved by modifying a traditional *ab initio* simulation. The zoom-in technique (a Monte Carlo adaptive mesh) is used to study the evolution of a disc in a single halo at high resolution. This is accomplished by resampling the initial conditions at a sequence of higher resolutions after identifying an area of interest. With sufficiently realistic feedback, impressively realistic results can be obtained. For instance, Gómez et al. (2017) presented a study of vertical structure in such simulations. In these simulations, the authors were able to look at several Milky Way-like galaxies in a variety of environments at resolutions that rival isolated galaxy simulations. These realistic studies have opened the door to a wide variety of questions pertaining to the Milky Way's interaction with the cosmological environment.

1.4 Disc Insertion Techniques for Cosmology

While highly realistic, the *ab initio* zoom-in approach still suffers from the inability to fine-tune galaxy dynamics in the same halo to perform a truly systematic study. In an effort to address these particular shortcomings, several groups have attempted to grow a stellar disc in a cosmological halo.

The general idea for growing a disc is to divide a zoom-in simulation into three phases. During the first, a cosmological simulation of a region of interest is run, and a halo is identified for study. A rigid disc potential is then slowly grown in this halo, allowing the halo particles to respond adiabatically to its time-varying potential. Finally, the rigid disc is replaced by live particles and the final phase of the simulation proceeds with live disc and halo particles. DeBuhr et al. (2012) use this scheme to introduce stellar discs into dark matter haloes from the Aquarius Project (Springel et al., 2008). They add a rigid disc potential at redshift $z = 1.3$ with a mass parameter for the disc that grows linearly with the scale factor until $z = 1$ when it reaches its final value. The disc potential is initially centered on the potential minimum of the halo and oriented so that its symmetry axis points along either the minor or major axis of the halo. During the rigid disc phase, the centre of the potential moves due to its interaction with the halo (Newton's 3rd law) so that linear momentum is conserved. However, the orientation of the disc is held fixed and therefore angular momentum isn't. To initialize the live disc, DeBuhr et al. (2012) approximate the halo potential as a flattened logarithmic potential and then determine the disc distribution function by solving the Jeans equations in axisymmetry.

A number of refinements to this scheme were introduced by Yurin and Springel (2015). In particular, they use the GALIC code to initialize the live disc Yurin and

Springel (2014). This code aims to find a stationary solution to the collisionless Boltzmann equation by adjusting the initial particle velocities so as to minimize a certain merit function. In Yurin and Springel (2015) the initial disc distribution function was assumed to depend on two integrals of motion, the energy E and angular momentum L_z. Consistency then required that they use an axisymmetrized approximation to the halo potential.

Bauer et al. (2018) improved on the scheme even further by increasing the realism of the growth phase by modelling the disc as a rigid body. The results they found were qualitatively similar to DeBuhr et al. (2012) and Yurin and Springel (2015) in terms of disc dynamics. The live phase was also improved by using the GalactICS code which actually samples a three-integral DF. This thesis is largely constructed based on this tool.

1.5 Organization and Findings of this Thesis

By applying our disc insertion tool, we address three key scientific questions. The first is how growing a disc in a cosmological halo affects the halo itself. Here, we attempt to understand how the way we grow the disc affects halo properties. The second is how bars form in cosmological environments. Previous studies using disc insertion techniques found that stellar discs all form very large bars. Large central bulges were found in Yurin and Springel (2015) to have an ameliorating affect. We explore the reasons why their disc-halo systems formed large bars, and show how we can form bars similar to the Milky Way's without including a large central bulge. The last topic we consider is how vertical structure is excited in the Milky Way. We explore the combined effect of mechanisms in the cosmological environment, and comment on how significant factors like substructure, tides, and bar buckling are for the Milky Way.

The common theme between these topics as follows. When studied in isolated galaxy simulations, stellar discs display evolution according to their "nature". We learn about what properties intrinsic to the disc change its evolution. In a fully cosmological environment, external factors will change the natural evolution of the stellar system. We refer to this aspect as "nurture". Real stellar systems evolve as a combination of the two, and we seek to understand how each plays a role in realistic environments.

As such, the thesis is organized in the following manner. In Chapter 2, we reduce the necessary theoretical background to understand this work to a succinct summary. Following this, in Chapter 3, we explore the first peer-reviewed paper on which this thesis is based. It outlines the disc insertion scheme and comments on how the dynamic nature of the Milky Way's stellar disc should affect its inner halo. Chapter 4 presents the second published paper which focuses on the question of how stable disks are against forming bars in a cosmological setting. A final paper is presented in Chapter 5, where we look at how disks form vertical structure in a cosmological setting. We conclude with summaries and ideas for future work in Chapter 6.

Bibliography

Bauer, J. S., Widrow, L. M., and Erkal, D. (2018). Disc-halo interactions in ΛCDM. *MNRAS*, 476:198–209.

Belokurov, V., Evans, N. W., Irwin, M. J., Lynden-Bell, D., Yanny, B., Vidrih, S., Gilmore, G., Seabroke, G., Zucker, D. B., Wilkinson, M. I., Hewett, P. C., Bramich, D. M., Fellhauer, M., Newberg, H. J., Wyse, R. F. G., Beers, T. C., Bell, E. F., Barentine, J. C., Brinkmann, J., Cole, N., Pan, K., and York, D. G. (2007). An Orphan in the "Field of Streams". *ApJ*, 658(1):337–344.

Bennett, M. and Bovy, J. (2019). Vertical waves in the solar neighbourhood in Gaia DR2. *MNRAS*, 482:1417–1425.

Binney, J. and Tremaine, S. (2008). *Galactic Dynamics: Second Edition*. Princeton University Press.

Carlin, J. L., DeLaunay, J., Newberg, H. J., Deng, L., Gole, D., Grabowski, K., Jin, G., Liu, C., Liu, X., Luo, A.-L., Yuan, H., Zhang, H., Zhao, G., and Zhao, Y. (2013). Substructure in Bulk Velocities of Milky Way Disk Stars. *ApJ*, 777:L5.

Carrillo, I., Minchev, I., Kordopatis, G., Steinmetz, M., Binney, J., Anders, F., Bienaymé, O., Bland-Hawthorn, J., Famaey, B., Freeman, K. C., Gilmore, G., Gibson,

B. K., Grebel, E. K., Helmi, A., Just, A., Kunder, A., McMillan, P., Monari, G., Munari, U., Navarro, J., Parker, Q. A., Reid, W., Seabroke, G., Sharma, S., Siebert, A., Watson, F., Wojno, J., Wyse, R. F. G., and Zwitter, T. (2018). Is the Milky Way still breathing? RAVE-Gaia streaming motions. *MNRAS*, 475:2679–2696.

Cen, R. and Ostriker, J. P. (1992). Galaxy formation and physical bias. *ApJ*, 399:L113–L116.

Chakrabarti, S., Angeloni, R., Freeman, K., Sargent, B., Simon, J. D., Konorski, P., Gieren, W., Sesar, B., Lipnicky, A., Blitz, L., Basri, G., Marengo, M., Vacca, W., Guhathakurta, P., Quillen, A., and Chang, P. (2016). Galactoseismology: Discovery of a cluster of receding, variable halo stars. *ArXiv e-prints*.

de Blok, W. J. G. (2010). The Core-Cusp Problem. *Advances in Astronomy*, 2010:789293.

de la Vega, A., Quillen, A. C., Carlin, J. L., Chakrabarti, S., and D'Onghia, E. (2015). Phase wrapping of epicyclic perturbations in the Wobbly Galaxy. *MNRAS*, 454:933–945.

DeBuhr, J., Ma, C.-P., and White, S. D. M. (2012). Stellar discs in Aquarius dark matter haloes. *MNRAS*, 426:983–999.

Dodelson, S. (2003). *Modern cosmology*.

D'Onghia, E., Madau, P., Vera-Ciro, C., Quillen, A., and Hernquist, L. (2016). Excitation of Coupled Stellar Motions in the Galactic Disk by Orbiting Satellites. *ApJ*, 823:4.

Dorman, C. E., Widrow, L. M., Guhathakurta, P., Seth, A. C., Foreman-Mackey, D., Bell, E. F., Dalcanton, J. J., Gilbert, K. M., Skillman, E. D., and Williams, B. F. (2013). A New Approach to Detailed Structural Decomposition from the SPLASH and PHAT Surveys: Kicked-up Disk Stars in the Andromeda Galaxy? *ApJ*, 779:103.

Dubinski, J., Gauthier, J.-R., Widrow, L., and Nickerson, S. (2008). Spiral and Bar Instabilities Provoked by Dark Matter Satellites. In Funes, J. G. and Corsini, E. M., editors, *Formation and Evolution of Galaxy Disks*, volume 396 of *Astronomical Society of the Pacific Conference Series*, page 321.

Eisenstein, D. J., Hu, W., and Tegmark, M. (1999). Cosmic Complementarity: Joint Parameter Estimation from Cosmic Microwave Background Experiments and Redshift Surveys. *ApJ*, 518:2–23.

Erkal, D., Belokurov, V., Bovy, J., and Sand ers, J. L. (2016). The number and size of subhalo-induced gaps in stellar streams. *MNRAS*, 463(1):102–119.

Erkal, D., Belokurov, V., Laporte, C. F. P., Koposov, S. E., Li, T. S., Grillmair, C. J., Kallivayalil, N., Price-Whelan, A. M., Evans, N. W., Hawkins, K., Hendel, D., Mateu, C., Navarro, J. F., del Pino, A., Slater, C. T., and Sohn, S. T. (2018). The total mass of the Large Magellanic Cloud from its perturbation on the Orphan stream. *arXiv e-prints*.

Font, A. S., Navarro, J. F., Stadel, J., and Quinn, T. (2001). Halo Substructure and Disk Heating in a Λ Cold Dark Matter Universe. *ApJ*, 563:L1–L4.

Gaia Collaboration, Katz, D., Antoja, T., Romero-Gómez, M., Drimmel, R., Reylé, C., Seabroke, G. M., Soubiran, C., Babusiaux, C., Di Matteo, P., and et al. (2018). Gaia Data Release 2. Mapping the Milky Way disc kinematics. *A&A*, 616:A11.

Gao, L., White, S. D. M., Jenkins, A., Stoehr, F., and Springel, V. (2004). The subhalo populations of ΛCDM dark haloes. *MNRAS*, 355:819–834.

Gauthier, J.-R., Dubinski, J., and Widrow, L. M. (2006). Substructure around M31: Evolution and Effects. *ApJ*, 653:1180–1193.

Gómez, F. A., White, S. D. M., Grand, R. J. J., Marinacci, F., Springel, V., and Pakmor, R. (2017). Warps and waves in the stellar discs of the Auriga cosmological simulations. *MNRAS*, 465:3446–3460.

Grillmair, C. J. (2006). Substructure in Tidal Streams: Tributaries in the Anticenter Stream. *ApJ*, 651(1):L29–L32.

Hahn, O. and Abel, T. (2013). MUSIC: MUlti-Scale Initial Conditions. Astrophysics Source Code Library.

Hui, L., Ostriker, J. P., Tremaine, S., and Witten, E. (2017). Ultralight scalars as cosmological dark matter. *Phys. Rev. D*, 95(4):043541.

Ibata, R. A., Gilmore, G., and Irwin, M. J. (1994). A dwarf satellite galaxy in Sagittarius. *Nature*, 370:194–196.

Ibata, R. A., Malhan, K., and Martin, N. F. (2019). The Streams of the Gaping Abyss: A Population of Entangled Stellar Streams Surrounding the Inner Galaxy. *ApJ*, 872:152.

Johnston, K. V., Price-Whelan, A. M., Bergemann, M., Laporte, C., Li, T. S., Sheffield, A. A., Majewski, S. R., Beaton, R. S., Sesar, B., and Sharma, S. (2017). Disk Heating, Galactoseismology, and the Formation of Stellar Halos. *Galaxies*, 5:44.

Katz, N., Weinberg, D. H., and Hernquist, L. (1996). Cosmological Simulations with TreeSPH. *ApJS*, 105:19.

Kazantzidis, S., Bullock, J. S., Zentner, A. R., Kravtsov, A. V., and Moustakas, L. A. (2008). Cold Dark Matter Substructure and Galactic Disks. I. Morphological Signatures of Hierarchical Satellite Accretion. *ApJ*, 688:254–276.

Klypin, A., Kravtsov, A. V., Valenzuela, O., and Prada, F. (1999). Where Are the Missing Galactic Satellites? *ApJ*, 522:82–92.

Kolb, E. W. and Turner, M. S. (1990). *The early universe.*

Laporte, C. F. P., Gómez, F. A., Besla, G., Johnston, K. V., and Garavito-Camargo, N. (2016). Response of the Milky Way's disc to the Large Magellanic Cloud in a first infall scenario. *ArXiv e-prints*.

Laporte, C. F. P., Gómez, F. A., Besla, G., Johnston, K. V., and Garavito-Camargo, N. (2018). Response of the Milky Way's disc to the Large Magellanic Cloud in a first infall scenario. *MNRAS*, 473:1218–1230.

Laporte, C. F. P., Johnston, K. V., and Tzanidakis, A. (2019). Stellar disc streams as probes of the Galactic potential and satellite impacts. *MNRAS*, 483:1427–1436.

Libeskind, N. I., Di Cintio, A., Knebe, A., Yepes, G., Gottlöber, S., Steinmetz, M., Hoffman, Y., and Martinez-Vaquero, L. A. (2013). Cold versus Warm Dark Matter Simulations of a Galaxy Group. *Publ. Astron. Soc. Australia*, 30:e039.

Lucy, L. B. (1977). A numerical approach to the testing of the fission hypothesis. *AJ*, 82:1013–1024.

Majewski, S. R., Skrutskie, M. F., Weinberg, M. D., and Ostheimer, J. C. (2003). A Two Micron All Sky Survey View of the Sagittarius Dwarf Galaxy. I. Morphology of the Sagittarius Core and Tidal Arms. *ApJ*, 599(2):1082–1115.

Moore, B., Ghigna, S., Governato, F., Lake, G., Quinn, T., Stadel, J., and Tozzi, P. (1999). Dark Matter Substructure within Galactic Halos. *ApJ*, 524:L19–L22.

Navarro, J. F., Frenk, C. S., and White, S. D. M. (1997). A Universal Density Profile from Hierarchical Clustering. *ApJ*, 490:493–508.

Newberg, H. J., Willett, B. A., Yanny, B., and Xu, Y. (2010). The Orbit of the Orphan Stream. *ApJ*, 711(1):32–49.

Newberg, H. J., Yanny, B., Rockosi, C., Grebel, E. K., Rix, H.-W., Brinkmann, J., Csabai, I., Hennessy, G., Hindsley, R. B., Ibata, R., Ivezić, Z., Lamb, D., Nash, E. T., Odenkirchen, M., Rave, H. A., Schneider, D. P., Smith, J. A., Stolte, A., and York, D. G. (2002). The Ghost of Sagittarius and Lumps in the Halo of the Milky Way. *ApJ*, 569(1):245–274.

Perlmutter, S., Aldering, G., Goldhaber, G., Knop, R. A., Nugent, P., Castro, P. G., Deustua, S., Fabbro, S., Goobar, A., Groom, D. E., Hook, I. M., Kim, A. G., Kim, M. Y., Lee, J. C., Nunes, N. J., Pain, R., Pennypacker, C. R., Quimby, R., Lidman, C., Ellis, R. S., Irwin, M., McMahon, R. G., Ruiz-Lapuente, P., Walton, N., Schaefer, B., Boyle, B. J., Filippenko, A. V., Matheson, T., Fruchter, A. S., Panagia, N., Newberg, H. J. M., Couch, W. J., and Project, T. S. C. (1999). Measurements of Ω and Λ from 42 High-Redshift Supernovae. *ApJ*, 517:565–586.

Planck Collaboration, Aghanim, N., Akrami, Y., Ashdown, M., Aumont, J., Baccigalupi, C., Ballardini, M., Banday, A. J., Barreiro, R. B., Bartolo, N., Basak, S., Battye, R., Benabed, K., Bernard, J.-P., Bersanelli, M., Bielewicz, P., Bock, J. J., Bond, J. R., Borrill, J., Bouchet, F. R., Boulanger, F., Bucher, M., Burigana, C., Butler, R. C., Calabrese, E., Cardoso, J.-F., Carron, J., Challinor, A., Chiang, H. C., Chluba, J., Colombo, L. P. L., Combet, C., Contreras, D., Crill, B. P., Cuttaia, F., de Bernardis, P., de Zotti, G., Delabrouille, J., Delouis, J.-M., Di Valentino, E., Diego, J. M., Doré, O., Douspis, M., Ducout, A., Dupac, X., Dusini, S., Efstathiou, G., Elsner, F., Enßlin, T. A., Eriksen, H. K., Fantaye, Y., Farhang, M., Fergusson, J., Fernandez-Cobos, R., Finelli, F., Forastieri, F., Frailis, M., Franceschi, E., Frolov, A., Galeotta, S., Galli, S., Ganga, K., Génova-Santos, R. T., Gerbino, M., Ghosh, T., González-Nuevo, J., Górski, K. M., Gratton, S., Gruppuso, A., Gudmundsson, J. E., Hamann, J., Handley, W., Herranz, D., Hivon, E., Huang, Z., Jaffe, A. H., Jones, W. C., Karakci, A., Keihänen, E., Keskitalo, R., Kiiveri, K., Kim, J., Kisner, T. S., Knox, L., Krachmalnicoff, N., Kunz, M., Kurki-Suonio, H., Lagache, G., Lamarre, J.-M., Lasenby, A., Lattanzi, M., Lawrence, C. R., Le Jeune, M., Lemos, P., Lesgourgues, J., Levrier, F., Lewis, A., Liguori, M., Lilje, P. B., Lilley, M., Lindholm, V., López-Caniego, M., Lubin, P. M., Ma, Y.-Z., Macías-Pérez, J. F., Maggio, G., Maino, D., Mandolesi, N., Mangilli, A., Marcos-Caballero, A., Maris, M., Martin, P. G., Martinelli, M., Martínez-González, E., Matarrese, S., Mauri, N., McEwen, J. D., Meinhold, P. R., Melchiorri, A., Mennella, A., Migliaccio, M., Millea, M., Mitra, S., Miville-Deschênes, M.-A., Molinari, D., Montier, L., Morgante, G., Moss, A., Natoli, P., Nørgaard-Nielsen, H. U., Pagano, L., Paoletti, D., Partridge, B., Patanchon, G., Peiris, H. V., Perrotta, F., Pettorino, V., Piacentini, F., Polastri, L., Polenta, G., Puget, J.-L., Rachen, J. P., Reinecke, M., Remazeilles, M., Renzi, A., Rocha, G., Rosset, C., Roudier, G., Rubiño-Martín, J. A., Ruiz-Granados, B., Salvati, L., Sandri, M., Savelainen, M., Scott, D., Shellard, E. P. S., Sirignano, C., Sirri, G., Spencer, L. D., Sunyaev, R., Suur-Uski, A.-S., Tauber, J. A., Tavagnacco, D., Tenti, M., Toffolatti, L., Tomasi, M., Trombetti, T., Valenziano, L., Valiviita, J., Van Tent, B., Vibert, L., Vielva, P., Villa, F., Vittorio, N., Wandelt, B. D., Wehus, I. K., White, M., White, S. D. M., Zacchei, A., and Zonca, A. (2018). Planck 2018 results. VI. Cosmological parameters. *arXiv e-prints*.

Powell, R. (2017). An Atlas of the Universe. Image obtained from `https://en.wikipedia.org/wiki/File:Local_Group.svg`.

Purcell, C. W., Bullock, J. S., Tollerud, E. J., Rocha, M., and Chakrabarti, S. (2011). The Sagittarius impact as an architect of spirality and outer rings in the Milky Way. *Nature*, 477:301–303.

Riess, A. G., Filippenko, A. V., Challis, P., Clocchiatti, A., Diercks, A., Garnavich, P. M., Gilliland, R. L., Hogan, C. J., Jha, S., Kirshner, R. P., Leibundgut, B., Phillips, M. M., Reiss, D., Schmidt, B. P., Schommer, R. A., Smith, R. C., Spyromilio, J., Stubbs, C., Suntzeff, N. B., and Tonry, J. (1998). Observational Evidence from Supernovae for an Accelerating Universe and a Cosmological Constant.

AJ, 116:1009–1038.

Rubin, V. C., Ford, Jr., W. K., and Thonnard, N. (1980). Rotational properties of 21 SC galaxies with a large range of luminosities and radii, from NGC 4605 /R = 4kpc/ to UGC 2885 /R = 122 kpc/. *ApJ*, 238:471–487.

Sanders, J. L. and Binney, J. (2013). Stream-orbit misalignment - I. The dangers of orbit-fitting. *MNRAS*, 433(3):1813–1825.

Schaye, J., Crain, R. A., Bower, R. G., Furlong, M., Schaller, M., Theuns, T., Dalla Vecchia, C., Frenk, C. S., McCarthy, I. G., Helly, J. C., Jenkins, A., Rosas-Guevara, Y. M., White, S. D. M., Baes, M., Booth, C. M., Camps, P., Navarro, J. F., Qu, Y., Rahmati, A., Sawala, T., Thomas, P. A., and Trayford, J. (2015). The EAGLE project: simulating the evolution and assembly of galaxies and their environments. *MNRAS*, 446:521–554.

Sellwood, J. A. (2013). *Dynamics of Disks and Warps*, page 923.

Springel, V. and Hernquist, L. (2003). Cosmological smoothed particle hydrodynamics simulations: a hybrid multiphase model for star formation. *MNRAS*, 339:289–311.

Springel, V., Wang, J., Vogelsberger, M., Ludlow, A., Jenkins, A., Helmi, A., Navarro, J. F., Frenk, C. S., and White, S. D. M. (2008). The Aquarius Project: the subhaloes of galactic haloes. *MNRAS*, 391:1685–1711.

Stinson, G., Seth, A., Katz, N., Wadsley, J., Governato, F., and Quinn, T. (2006). Star formation and feedback in smoothed particle hydrodynamic simulations - I. Isolated galaxies. *MNRAS*, 373:1074–1090.

Taylor, J. E. (2011). Dark Matter Halos from the Inside Out. *Advances in Astronomy*, 2011:604898.

U.S. Census Bureau (2010). 2010 Census Gazetteer Files: New York County Subdivisions.

Vogelsberger, M., Genel, S., Springel, V., Torrey, P., Sijacki, D., Xu, D., Snyder, G., Nelson, D., and Hernquist, L. (2014). Introducing the Illustris Project: simulating the coevolution of dark and visible matter in the Universe. *MNRAS*, 444:1518–1547.

Widrow, L. M., Barber, J., Chequers, M. H., and Cheng, E. (2014). Bending and breathing modes of the Galactic disc. *MNRAS*, 440:1971–1981.

Widrow, L. M., Gardner, S., Yanny, B., Dodelson, S., and Chen, H.-Y. (2012). Galactoseismology: Discovery of Vertical Waves in the Galactic Disk. *ApJ*, 750:L41.

Wikipedia (2018). History of New York City.

Williams, M. E. K., Steinmetz, M., Binney, J., Siebert, A., Enke, H., Famaey, B., Minchev, I., de Jong, R. S., Boeche, C., Freeman, K. C., Bienaymé, O., Bland-Hawthorn, J., Gibson, B. K., Gilmore, G. F., Grebel, E. K., Helmi, A., Kordopatis, G., Munari, U., Navarro, J. F., Parker, Q. A., Reid, W., Seabroke, G. M., Sharma, S., Siviero, A., Watson, F. G., Wyse, R. F. G., and Zwitter, T. (2013). The wobbly Galaxy: kinematics north and south with RAVE red-clump giants. *MNRAS*, 436:101–121.

Xu, Y., Newberg, H. J., Carlin, J. L., Liu, C., Deng, L., Li, J., Schönrich, R., and Yanny, B. (2015). Rings and Radial Waves in the Disk of the Milky Way. *ApJ*, 801:105.

Yurin, D. and Springel, V. (2014). GALIC: Galaxy initial conditions construction. Astrophysics Source Code Library.

Yurin, D. and Springel, V. (2015). The stability of stellar discs in Milky Way-sized dark matter haloes. *MNRAS*, 452:2367–2387.

Zwicky, F. (1933). Die Rotverschiebung von extragalaktischen Nebeln. *Helvetica Physica Acta*, 6:110–127.

Chapter 2

A Dynamical Recipe for Cosmological Discs

This chapter provides an overview of the background theory needed to understand subsequent chapters. In Chapter 1, we discussed simulations of galaxies being critical to having a theoretical understanding of cosmology and galaxy formation. The word "simulation" was used without fully contextualizing its significance and meaning. We provide that context in §2.1, where we describe what is actually being done when a simulation is run. In §2.2, we talk about how to apply this theory to study the evolution of equilibrium galaxies. We talk about the implications of cosmology in detail in §2.3, and explain how this specifies an extended view of the discussion in §2.1. This includes how we identify cosmic substructure and the techniques we use for analyzing the time-evolution of disc-derived quantities.

2.1 Physical Motivation of Modelling

The goal of this section is to convey to the reader what we mean by a simulation of a galactic system.

2.1.1 Thermodynamics of Self-Gravitating Systems

The baryonic mass of the Milky Way is largely concentrated in its stars. To first order, the dynamical behavior of the Milky Way is determined by stellar material and dark matter (Binney and Merrifield, 1998). While the evolution of gas is governed by the Euler equations with an equation of state, modelling in galactic dynamics requires that we understand how stars and dark matter behave.

We begin by suggesting a model of a galaxy composed only of a very large number of stars and dark matter, where all stars have the same mass. We call the probability of a star being a specific position, $\mathbf{r}$, and velocity $\mathbf{v}$, at a time, t, the distribution function (DF), $f(\mathbf{r}, \mathbf{v}, t)$. The stars and dark matter sit in a combined gravitational potential, $\Phi(\mathbf{r})$, in some near-equilibrium state. To fully describe this model, we need to understand how an ensemble of self-gravitating particles gives rise to an equilibrium distribution of stars and dark matter.

Unlike gas, which can exchange thermodynamic energy with itself through a variety of mechanisms, stars and dark matter interact only through gravity. Gravity is a long range force. In fact, the majority of the contribution to the forces on stars in galaxies comes from far outside their immediate neighborhoods (that is to say gravitational energy in non-extensive) (Binney and Tremaine, 2008).

This has a number of interesting implications. Classical equilibrium statistical mechanics tries to understand distributions of particles as ensembles with a given thermodynamic potential. Some commonly used ensembles are the microcanonical ensemble, where $f_0(\mathbf{r}, \mathbf{v})$, the equilibrium state, is determined by holding energy fixed in a closed system, and the canonical ensemble which finds f_0 holding the temperature of the system fixed (Sethna, 2006). These ensembles break down when non-extensive forces are involved (in the latter case, specifically because self-gravitating systems have no maximum entropy) (Padmanabhan, 1990; Lynden-Bell, 1999; Binney and Tremaine, 2008). Another peculiarity of self-gravitating systems is that they have a negative heat capacity (Lynden-Bell, 1999).

The implication is that self-gravitating systems of stars, which have no means to dissipate internal energy, can never be in thermodynamic equilibrium. A system which starts in dynamical equilibrium evolves to a state of higher entropy when perturbed, which is physically characterized as having a dense core and extended envelope of mass (Binney and Tremaine, 2008). Since a thermodynamic resolution of galactic dynamics is unattainable, a dynamical theory of galaxy evolution must be developed[1].

2.1.2 The Collisionless Boltzmann Equation

To provide a time-dependent dynamical prescription for our model of stars and dark matter particles, we will make a number of assumptions that hold for the entire thesis. These are:

- Galaxies are collisionless systems; one does not have to worry about energy exchanged in close encounters because close encounters of individual stars and dark matter particles seldom happen.
- All stars and dark matter particles are identical.
- Phase space probability is conserved.
- Phase space probability is incompressible.

We want to turn the assumptions listed above into a solvable equation for $f(\mathbf{r}, \mathbf{v}, t)$. This is done by recognizing that for $\mathbf{w} = (\mathbf{p}, \mathbf{q})$ (Binney and Tremaine, 2008),

$$\frac{\partial f}{\partial t} + \frac{\partial}{\partial \mathbf{w}} \cdot (f\dot{\mathbf{w}}) = 0 \tag{2.1}$$

is the continuity equation in 6D phase space that expresses conserved phase space probability. Here, $\mathbf{p}$ and $\mathbf{q}$ are any set of canonical coordinates. In general, this may

[1]For more information on the thermodynamics of self-gravitating systems, Chapter 4.10 of Binney and Tremaine (2008) and Chapter 7.3 of Binney and Tremaine (2008) provide excellent summaries.

be rewritten in what is commonly called the Collisionless Boltzmann equation (CBE),

$$\frac{\partial f}{\partial t} + \dot{\mathbf{q}} \cdot \frac{\partial f}{\partial q} + \dot{\mathbf{p}} \cdot \frac{\partial f}{\partial p} = 0. \tag{2.2}$$

The CBE is more commonly expressed in Cartesian coordinates as,

$$\frac{\partial f}{\partial t} + \mathbf{v} \cdot \frac{\partial f}{\partial \mathbf{x}} - \frac{\partial \Phi}{\partial \mathbf{x}} \cdot \frac{\partial f}{\partial \mathbf{v}} = 0, \tag{2.3}$$

where Φ is our total gravitational potential from stars and dark matter. The result is a quasilinear partial differential equation (PDE) for $f(\mathbf{r}, \mathbf{v}, t)$. The CBE is nothing more than an advection equation in phase space that expresses our view that particles are not self interacting, that they are identical, and that the phase space fluid is conserved and incompressible. In addition to the CBE which describes the evolution of the phase fluid, we have the Poisson equation, an elliptic equation describing the evolution of the potential (Binney and Tremaine, 2008),

$$\nabla^2 \Phi(\mathbf{r}, t) = 4\pi G \rho(\mathbf{r}, t) \tag{2.4}$$

where G is Newton's gravitational constant, ρ is the mass density and,

$$\nu(\mathbf{r}, t) = \int_{\mathcal{D}} f(\mathbf{r}, \mathbf{v}, t) \mathrm{d}^3\mathbf{v}, \tag{2.5}$$

where ν is the number density and $\mathcal{D}$ is the phase space. Note that the mass density and number density differ by a factor of the system mass. We are left with a 6D space + 1D time solution domain on which to compute $f(\mathbf{r}, \mathbf{v}, t)$ as well as two PDEs and an integral.

2.1.3 Monte Carlo Solution of the Collisionless Boltzmann Equation

In terms of actually solving the CBE, we run into a number of technical challenges in applying traditional finite difference and finite volume schemes for advection equations. These techniques require that some mesh be constructed, and the flows between the cells in the mesh are calculated dependent on the type of equation being solved and the current states of the cells[2]. The spatial domain is 6D, meaning a uniform mesh resolution scales in memory consumption as $O(N^6)$, where N is the number of cells on an axis. For a sanity check, a modest $N = 2^5$ element grid would take up $2^{30} \times 2^4$ bytes $\sim$ 17 GB. We obviously need more than 32 cells on an axis to represent the fine DF structure we want to study, and we are already at the limit of a single compute node to apply a finite difference scheme.

This is where Monte Carlo methods shine. The fundamental principle on which they operate is that I can evaluate the integral of any function, $f(\mathbf{x})$, over a domain $\mathcal{D}$, as (Press et al., 1992),

$$\int_{\mathcal{D}} f(\mathbf{x}) d^n\mathbf{x} = \frac{V(\mathcal{D})}{|X_s|} \sum_{\mathbf{x}_i \in X_s(\mathcal{D})} f(\mathbf{x}_i) \tag{2.6}$$

where X_s is a uniform random sample of points on $\mathcal{D}$, $V(\mathcal{D})$ is the volume of the domain, n is the dimensionality of $\mathbf{x}$, and $|X_s|$ is the cardinality, or number of points in the sample. The benefit of Monte Carlo integration is that although our result is not deterministic, the error in the integral is reduced as $1/\sqrt{N}$ *regardless of the*

[2]Chapter 19 of Press et al. (1992) discusses numerical methods for PDEs, although you could find detailed discussion of finite difference and finite volume methods in most numerical methods texts.

integral's dimension!

The point of introducing this powerful concept is simply in recognition of the fact that we need to integrate over phase space to solve Eq. (2.3). As we stated, computing these integrals on a mesh is intractable, so we represent $f(\mathbf{r}, \mathbf{v}, t)$ in another way:

$$f(\mathbf{r}, \mathbf{v}, t) \approx \sum_i m_i \delta^3(\mathbf{r} - \mathbf{r}_i)\delta^3(\mathbf{v} - \mathbf{v}_i) \tag{2.7}$$

where δ^3 is the 3D Dirac delta function, and we take the DF to be normalized to $M = \sum_i m_i$ instead of 1. We call this the N-body realization of the DF. As an extension of this idea, to find $f(\mathbf{r}, \mathbf{v}, t)$ at some point in the future, it is sufficient to find the state of our *approximation*[3] at some time in the future. This requires a more detailed exploration of how we step through time with N-body realizations.

2.1.4 Time Integration in N-Body Simulations

We have shown how to map solving the CBE, the master equation for our system of stars and dark matter, to the evolution of a finite sample of particles. The system of equations we need to solve now is,

$$\begin{aligned} \dot{\mathbf{r}}_i(t) &= \mathbf{v}_i(t) && (2.8) \\ \dot{\mathbf{v}}_i(t) &= -\left.\frac{\partial \Phi}{\partial \mathbf{r}}\right|_{\mathbf{r}=\mathbf{r}_i} . && (2.9) \end{aligned}$$

where $\dot{\mathbf{r}}_i$ and $\dot{\mathbf{v}}_i$ are the first time derivatives of $\mathbf{r}_i$ and $\mathbf{v}_i$, respectively. Our integro-differential equation system is now approximated as $6\,N$, where N is the number

[3]The author believes that this is one of the most beautiful results ever to be applied in studying the dynamics of galaxies.

of particles sampled to represent the stars and dark matter, ordinary differential equations (ODEs). These may be solved by any ODE system solver. There are two competing objectives when deciding on the best way to handle time stepping numerically; the first is that we want to maximize the accuracy of our integration scheme and the second is that we want to minimize the number of evaluations of $-\nabla\Phi$, the force. The latter consideration is a severe constraint because naively, the complexity of evaluating each pairwise force is $O(N^2)$. Although, as we will see, approximations reduce this complexity to $O(N \log N)$. We note that finding the forces amounts to solving (2.4).

Nonetheless, the force calculation will be the most time consuming aspect of the integration, and we want to minimize the number of evaluations we need. This rules out some commonly used schemes in the Runge-Kutta class of integrators, since they would require four or five calculations of the force on millions of particles (Press et al., 1992). The open question is how to construct a low-order integration scheme that preserves the Hamiltonian[4].

Define the following drift and kick operators for a forward timestep of Δt as (Quinn et al., 1997),

$$D_t(\Delta t) : \begin{cases} \mathbf{r}_i & \longrightarrow \mathbf{r}_i + \mathbf{v}_i \Delta t \\ \mathbf{v}_i & \longrightarrow \mathbf{v}_i \end{cases}, \tag{2.10}$$

[4]In a collisionless system, the Hamiltonian should be conserved (Binney and Tremaine, 2008).

and,

$$K_t(\Delta t) : \begin{cases} \mathbf{r}_i & \longrightarrow \mathbf{r}_i \\ \\ \mathbf{v}_i & \longrightarrow \mathbf{v}_i - \nabla\Phi(\mathbf{r}_i)\Delta t \end{cases} . \tag{2.11}$$

If the Hamiltonian is separable as $\mathcal{H} = T(v) + V(r)$ for T, the kinetic energy, and V, the potential energy, and we are in a Cartesian coordinate system, combinations of these operators approximately preserve the Hamiltonian. This is a property of a class of integrators known as symplectic integrators, whose derivation starts with an assumption of Hamiltonian mechanics. We use the second order Leapfrog scheme implemented in Gadget-3, based on the code in Springel (2005). It is specified as,

$$U(\Delta T) = K\left(\frac{\Delta t}{2}\right) D\left(\Delta t\right) K\left(\frac{\Delta t}{2}\right). \tag{2.12}$$

This integration scheme is reasonably accurate with only two force evaluations. It is also symplectic, meaning that the Hamiltonian of the system will not drift. Chapter 3 of Binney and Tremaine (2008) has an excellent comparison of numerical integrators, including the Leapfrog scheme given here.

The final remaining complication for the time stepping portion of solving the CBE is determining the timesteps themselves. Accelerations and velocities in astrophysical systems vary by orders of magnitude, and the timestep needs to be small compared to the timescales defined by the relevant accelerations. Because some particles experience accelerations on a different magnitude than others, we need an adaptive timestep.

The way that this is commonly implemented, including in Springel (2005), is to have a base timestep, Δt_{base}, for all particles that gets bisected at each level of temporal refinement. That is to say, particles at level 4 are updated four more times than particles at level 2. Suppose the highest level of refinement is k. The simulation proceeds in $\Delta t_{base}/2^k$ intervals, with particles at $k-1$ being updated at half of the timesteps, dividing the number of updates by two up to the coarsest level of temporal refinement. Where multiple levels need updates, particles at the lower levels are updated first.

The level of temporal refinement assigned to a given particle is determined primarily by the acceleration it experiences. That is, for GADGET-3 (Springel, 2005),

$$\Delta t_i = \min\left(\Delta t_{base}, \left(\frac{2\eta\epsilon}{|\nabla\Phi(\mathbf{r}_i)|}\right)^{1/2}\right). \tag{2.13}$$

Here, η is a free accuracy parameter and ϵ is the gravitational softening. The gravitational softening is used to prevent numerical overflow when particles rarely have close encounters. It arises from having the acceleration induced from a particle at position $\mathbf{r}_i$ be,

$$\mathbf{a}_i(\mathbf{r}) = -\frac{Gm_i}{(|\mathbf{r}-\mathbf{r}_i|^2+\epsilon^2)^{3/2}}(\mathbf{r}-\mathbf{r}_i) \tag{2.14}$$

Larger choices of ϵ reduce large errors accumulating due to large forces, but also make the force calculation less accurate.

2.1.5 Efficient Force Calculation

The Leapfrog scheme requires us to compute the force two times. Naively, we would compute a sum over Eq. (2.14) for each of the $N(N-1)/2$ unique pairs of positions in $O(N^2)$ time to compute the forces on all particles. This is also intractable, or rather is the limiting factor on how large of a simulation we can run. Methods were developed early on in the history of running N-body simulations to cope with this by approximating the potential.

The first method worth noting for this thesis is the particle mesh technique (Hénon, 1970; Frenk et al., 1983; Klypin and Shandarin, 1983). This technique considers the calculation of forces on a 3D mesh by reducing the calculation to a Fast Fourier Transform (FFT) (Press et al., 1992). One of the crowning achievements of scientific computing in the 20th century was the rediscovery of an algorithm by J. W. Cooley and John Tukey, originally discovered by Gauss, to compute the Discrete Fourier Transform (DFT) in $O(N \log N)$ complexity[5](Cooley and Tukey, 1965). Particle mesh's cloud-in-cell (CIC) algorithm was a part of a flurry of algorithms that subsequently exploited the FFT. It has a difficult time accounting for forces from particles separated by small scales on the mesh, though (Springel, 2005).

Compensating for some of the shortcomings of the particle mesh approach, Barnes and Hut (1986) introduced a new algorithm for approximating forces in $O(N \log N)$ complexity. Their algorithm took a divide an conquer approach by subdividing the simulation space into octants recursively until each particle was in its own cell. Forces would be computed pairwise for particles close together, but for distant particles, the mass distribution would be approximated as a multipole. To compute the forces, one simply does a depth-first-search (DFS) of the particle tree, going deeper if,

$$\frac{l}{d} \geq \theta \tag{2.15}$$

[5]What Gauss was doing with recursive DFT algorithms is beyond the author, but in the author's humble opinion, it is expected from the greatest mathematician to ever live.

where l is the side length of the node whose force is being computed, d is the distance from this node to the current node in the DFS, and θ is a threshold called the opening angle. In the simplest case, a cell not meeting this condition would be approximated as a point mass with the position at the center of mass of all particles deeper in its subtree. Higher order multipole expansions are typically used (4 and 8 are common choices).

In addition, the somewhat simplistic opening angle scheme is expounded upon by some codes to include a "relative opening criterion". The main idea is to use the last acceleration of the particle to determine whether or not a cell needs to be opened. Gadget-3 uses the criterion,

$$\frac{GM}{d^2}\left(\frac{l}{d}\right)^2 \geq \alpha|\mathbf{a}_{i,t-1}| \tag{2.16}$$

where M is the mass in the current DFS subtree, $|\mathbf{a}_{i,t-1}|$ is the magnitude of the acceleration of the current particle at the last time step, and α is a relative opening criterion, a free parameter. Conceptually, this means that if the point mass acceleration in the current subtree is greater than a specified fraction of this particle's acceleration, the current DFS level is too coarse and we need to go deeper.

The scheme proposed by Barnes and Hut (1986) is widely used in astrophysics because of its efficiency and computability. While both algorithms are $O(N \log N)$ complexity, tree-based methods tend to perform more slowly in practice (Springel, 2005). Xu (1995) introduced a scheme to combine both the short-range accuracy of tree methods with the efficiency of FFT-based methods. This TreePM method has been widely successful at handling short range forces with a tree method and long range forces with particle mesh techniques. The trick is forcing consistency between the two methods at intermediate distances. GADGET-3 combines a high degree of optimization with the TreePM algorithm to produce a highly efficient algorithm.

Before proceeding to talk about the complications of executing TreePM on distributed systems like the Linux clusters worked with in this thesis, we would be remiss in not mentioning field expansion methods. Typically these take the form of an expansion of the potential in spherical harmonics using a set of radial basis functions. A brief discussion of these methods is presented in Chapter 2.9.4 of Binney and Tremaine (2008). These methods have great historical significance, and have even seen a recent resurgence in helping understand the structure of dark matter haloes (Lilley et al., 2018a,b).

To summarize, there are a number of ways to find gravitational forces in a simulation that all amount to solving Poisson's Equation, (2.4). The most accurate way is to compute all pairwise forces, but efficient algorithms have been developed to accurately estimate forces from gravity. The force calculation together with a time stepping scheme for N-body realizations forms the main components of an N-body simulation, and solving Eqs. (2.8) and (2.9) to estimate $f(\mathbf{r}, \mathbf{v}, t)$ is what we mean when we say we ran a simulation.

2.1.6 Complications on Distributed Systems

Modern high performance computing is largely done on compute clusters which are groups of smaller computers (nodes) connected with some high speed connection (Gigabit Ethernet, InfiniBand). The nodes form a distributed system in the sense that they do not share memory addresses. Each node may have multiple processes running (typically up to the number of logical cores on the node's CPU). Processes do

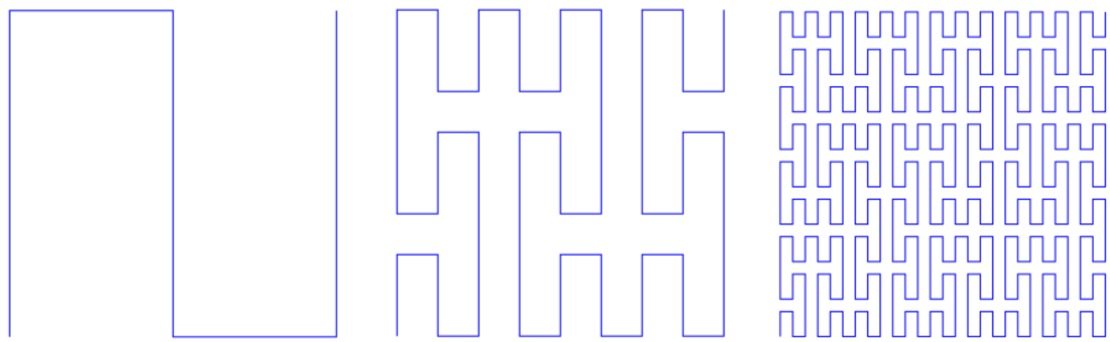

Figure 2.1: Several examples of the Peano space filling curve in 2D. The level of refinement increases left-to-right. Obtained from de Campos (2019) and reproduced under the Creative Commons Attribution-Share Alike 3.0 Unported license.

not share data[6], and must communicate through a protocol like the Message Passing Interface (MPI) (Lusk et al., 1996).

Specifically, in an N-body simulation, will have a subset of all of the particles, and a subset of the total tree structure. A naive DFS of an Octree simply cannot be done since no process will have all of the particles. When a process requires particles from another process, this reduces the efficiency gained from increasing the number of processors, and one might even get an overall slowdown. Another potential problem is that an individual process may get a higher work load than other processes, causing the other processes to wait for it to finish. We talk about how both of these problems are solved here.

To reduce the need to explicitly transfer particles between processes, Gadget-3 notes that pairwise forces will only be needed for nearby particles. These represent the bulk of the tree force calculation. Any scheme which puts nearby particles on the

[6]Processes do not share data in a fully distributed model of parallel computing. Shared memory models like OpenMP (Basumallik et al., 2007) share data between processes on a single node. MPI 3 even has similar shared memory support (MPI Forum, 2015). Gadget-3 was initially designed to not use these paradigms, and our intention is not to give a complete overview of all of parallel computing, so we relegate clarification to this footnote and references.

same processor will reduce the overall communication time in the force calculation phase. One way to accomplish efficient load balancing is to partition the simulation space using a space filling curve. Fig. 2.1 shows the Peano space-filling curve at several levels of refinement in 2D. This is the curve GADGET-3 uses. A level of refinement is selected, and estimates of the computational cost in each cube are added up along the space filling curve to equally distribute the computational load. This results in nearby particles being on the same process, and in the processes having roughly equal work loads. Springel (2005) shows that this is highly effective at reducing communication cost in the simulation, and it goes into more detail about how TreePM is carried out on distributed systems.

2.2 Phase Space and Initial Conditions

In §2.1 we outlined the underlying theory behind representing stars and dark matter in an N-body simulation. The focus of this thesis is studying the behavior of stellar discs in cosmological environments, and the first step towards that understanding is the construction of a pristine, equilibrium N-body model. Ultimately, in the course of running an N-body simulation, these pristine systems will diverge to higher entropy[7] states, initially due to random errors in the N-body representation. Nonetheless, these models give us an understanding of how perfectly unperturbed galaxies will evolve due to the fact that real galaxies are also made of a finite number of particles.

[7] The Shannon entropy is a commonly used measure for self-gravitating systems. See Binney and Tremaine (2008) for more details.

2.2.1 Modelling Approaches

The DF represents the 6D phase space information and completely describes an N-body system. In a simple disc-halo system, there is a flattened axisymmetric component (the disc), and a spheroidal component (the dark matter halo) each with their own DF. These are made self-consistent by the separate DFs' incorporation of their combined gravitational potential.

However, the DF is not the quantity that is observed in external galaxies. Astronomers are not typically working with a 6D phase space description of the structures they observe. Luminosity (density) profiles are one observable , as well as circular velocities (rotation curves) for discs, and also the spread of line of sight (LOS) velocities of disc stars. A modelling approach that takes our understanding of these observables as input is conceptually easier to understand than a DF which may or may not be unique (Binney and Tremaine, 2008).

In this spirit, Jeans (1915)[8] laid out a framework to describe galaxy evolution in terms of the *moments* of the distribution function. Specifically, the idea is to multiply the CBE (Eq. (2.3)) by each of $(1, \mathbf{v}_i)$ and integrate over the velocity part of phase space. These together yield the second-order Jeans equations (Binney and Tremaine, 2008),

$$\frac{\partial \nu}{\partial t} + \frac{\partial \nu \langle v_i \rangle}{\partial x_i} = 0 \tag{2.17}$$

$$\nu \frac{\partial \langle v_j \rangle}{\partial t} + \nu \langle v_i \rangle \frac{\partial \langle v_j \rangle}{\partial x_i} = -\nu \frac{\partial \Phi}{\partial x_j} - \frac{\partial \nu \sigma_{ij}^2}{\partial x_i} \tag{2.18}$$

[8]Notably before the famous 1920 Curtis-Shapley debate (Trimble, 1995), a climax of the ongoing debate over whether so-called "spiral nebulae" were actually external galaxies. Hubble's distance measurements to variable stars in M31 a few years later resolved the debate finally.

where $i, j \in (1,2,3)$, $\langle \cdot \rangle$ denotes expectation over f, $\mathbb{E}_f[\cdot]$, ν is the number density of particles, and $\sigma^2_{ij} = \langle v_i v_j \rangle - \langle v_i \rangle \langle v_j \rangle$ is the velocity dispersion tensor. In equilibrium for spherical systems, the second equation is often written as (Binney and Tremaine, 2008),

$$\frac{\partial \nu \langle v_r^2 \rangle}{\partial r} + \nu \left(\frac{\partial \Phi}{\partial r} + \frac{2\langle v_r^2 \rangle - \langle v_\theta^2 \rangle - \langle v_\phi^2 \rangle}{r} \right) \tag{2.19}$$

where θ is the polar angle, ϕ is the azimuthal angle, and r is the spherical radius[9]. Note that there is only one scalar equation. Symmetries in the velocity dispersion tensor for spherical systems require that the cross moments are zero (Binney and Tremaine, 2008). For axisymmetric systems, the equilibrium Jeans equations are often written (Binney and Tremaine, 2008),

$$\begin{aligned}
\frac{\partial \nu \langle v_R^2 \rangle}{\partial R} + \frac{\partial \nu \langle v_R v_z \rangle}{\partial z} + \nu \left(\frac{\langle v_R^2 \rangle - \langle v_\phi^2 \rangle}{R} + \frac{\partial \Phi}{\partial R} \right) &= 0 && (2.20) \\
\frac{1}{R} \frac{\partial R \nu \langle v_R v_z \rangle}{\partial R} + \frac{\partial \nu \langle v_z^2 \rangle}{\partial z} + \nu \frac{\partial \Phi}{\partial z} &= 0 && (2.21) \\
\frac{1}{R^2} \frac{\partial R^2 \nu \langle v_R v_\phi \rangle}{\partial R} + \frac{\partial \nu \langle v_z v_\phi \rangle}{\partial z} &= 0 && (2.22)
\end{aligned}$$

where z is the Cartesian z, R is the cylindrical radius, and ϕ is the polar angle. These equations look suspiciously like Euler's equations for fluid dynamics with a missing energy equation. Jeans (1915) did not magically solve the statistical mechanical issues mentioned in §2.1; given a number density and potential, we still have an unknown velocity dispersion tensor with six elements, and only 4 independent equations. In the simplified spherical case, we have three unknown elements and two independent equations.

[9]Note a slight abuse of notation. We said that v_i has $i \in (1,2,3)$, but here we use symbols to represent specific coordinate systems. The point is that the indices have three unique values.

We have also thrown out information about the DF by using moments and stopping at second order. Higher order Jeans equations can be appended to this system by multiplying the CBE by $v_i v_j v_k$ to obtain the third order equations, and so on. These get progressively more complicated, and we would require more additional equations to evaluate the equilibrium Jeans equations (Binney and Tremaine, 2008).

Despite these shortcomings, more information can be imposed on the system to make these equations applicable. Hernquist (1993) presented one of the first successful applications of Jeans modelling to creating equilibrium galaxies with bulges, discs, and dark matter haloes. In the case of the dark matter halo for a disc-halo system, one only has to specify the function,

$$\beta(r) = 1 - \frac{\langle v_\theta^2 \rangle + \langle v_\phi^2 \rangle}{2\langle v_R^2 \rangle}. \tag{2.23}$$

This parameter measures anisotropy in the velocity ellipsoid defined by σ_{ij} at each radius; $\beta = -\infty$ if all orbits are circular, $\beta = 0$ if the system is isotropic, and $\beta = 1$ if orbits are purely radial. Together with an assumed density-potential pair, continuity equation, and the spherical second-order Jeans equation, the spherical halo's velocity structure is specified. At the time of writing, Hernquist (1993) did not have much information about the dark matter distribution in galaxies (recall (Navarro et al., 1997) followed this work in establishing a common density profile for dark matter haloes). As such, we will not talk about their uninformed choice of halo, and it really is not important.

In the case of the axisymmetric disc, Hernquist (1993) based their model on the observations at the time which suggested that stellar discs had an exponential radial density profile (Freeman, 1970). This motivated a density profile commonly used today,

$$\rho_d(r) = \frac{M_d}{4\pi R_d^2 z_d} e^{-R/R_d} \mathrm{sech}^2\left(\frac{z}{z_d}\right). \tag{2.24}$$

Here, M_d is the mass of the disc, R_d is the radial scale length, and z_d is the vertical scale length. Observations support the idea that the second radial velocity moment also has an exponential profile (van der Kruit and Searle, 1981; Lewis and Freeman, 1989),

$$\langle v_R^2 \rangle = \sigma_{R,0} e^{-R/R_\sigma}. \tag{2.25}$$

Here, R_σ is the radial dispersion scale length, and $\sigma_{R,0}$ is a free velocity scale (on the order of 100 km/s for the Milky Way). In principle, any radial scale length can be used for $\langle v_R^2 \rangle$, but it is generally accepted to be a longer scale length than R_d. The vertical dispersion and second velocity moment are determined from the assumption of the disc being isothermal,

$$\langle v_z^2 \rangle = \pi G \Sigma z_d \tag{2.26}$$

where Σ_d is the surface density as a function of radius. Finally, a relation between $\langle v_\phi^2 \rangle$ and the other second moments is needed to fully solve the second order system. Jeans modelling for discs injects the intuition behind a theoretical development known as the *epicycle approximation.*

The main idea is that stars in discs are on roughly circular and planar orbits, so a reasonably accurate description of their orbits can be obtained by taking the equations of motion in a truncated series expansion about a circular orbit at the guiding radius, R_g. This is better understood in terms of the effective potential in the rotating reference frame in which a star rotating at R_g is stationary. For a star on the x-axis, the $\hat{x}$ direction represents the radial direction, the $\hat{y}$ direction is the same as $\hat{\phi}$ in the original frame, and $\hat{z}$ is unchanged. The equations of motion are (Binney and Tremaine, 2008),

$$\frac{\mathrm{d}^2 x}{\mathrm{d}t^2} = \frac{\partial \Phi_{eff}}{\partial R} \tag{2.27}$$

$$\frac{\mathrm{d}^2 y}{\mathrm{d}t^2} = 0 \tag{2.28}$$

$$\frac{\mathrm{d}^2 z}{\mathrm{d}t^2} = \frac{\partial \Phi_{eff}}{\partial z} \tag{2.29}$$

where $\Phi_{eff} = \Phi(R, z) + L_z^2/2R^2$ is the effective potential in the accelerating (rotating) reference frame, and L_z is the z-component of the angular momentum. These equations can be written in a first order expansion as,

$$\frac{\mathrm{d}^2 x}{\mathrm{d}t^2} = \kappa^2 x \tag{2.30}$$

$$\frac{\mathrm{d}^2 y}{\mathrm{d}t^2} = 0 \tag{2.31}$$

$$\frac{\mathrm{d}^2 z}{\mathrm{d}t^2} = \nu^2 z \tag{2.32}$$

where,

$$\kappa^2(R_g) = \left(R \frac{\partial \Omega^2}{\partial R} + 4\Omega^2 \right)_{R=R_g, z=0}, \tag{2.33}$$

with the circular frequency Ω,

$$\Omega^2(R_g) = \frac{1}{R_g} \left(\frac{\partial \Phi}{\partial R} \right)_{R=R_g, z=0} = \frac{L_z^2}{R_g^4}, \tag{2.34}$$

and,

$$\nu^2(R_g) = \left(\frac{\partial \Phi}{\partial z} \right)_{R=R_g, z=0}. \tag{2.35}$$

That is, a star's orbit is described by three frequencies: its rotational frequency Ω, a radial oscillation frequency, κ, and a vertical oscillation frequency, ν. This view is accurate so long as the vertical motion does not deviate far from the disc midplane. The actual values of these constants in Galactic astronomy are related to a problem known as the *Oort Problem*, and we believe that for the Sun (Binney and Tremaine, 2008),

$$\frac{\kappa}{\Omega} \approx 1.35 \tag{2.36}$$

$$\frac{\nu}{\kappa} \approx 2 \tag{2.37}$$

The fact that the orbit is described by three distinct frequencies that are unequal for the Sun means that the Sun's orbit does not close. If the Milky Way potential never changed, the path of the Sun would fill an annulus centered around R_g (Binney and Tremaine, 2008). That is to say, the orbit looks like it forms a rosette pattern.

By assuming the epicycle approximation, we are able to form a complete solution to the Jeans equations for the disc. This is done by looking at a dynamical property of disc star orbits called *asymmetric drift*, which is the velocity defined by (Binney and Tremaine, 2008),

$$v_a = v_c - \langle v_\phi \rangle \tag{2.38}$$

where $v_c = R\Omega$. We have yet to discuss how we find $\langle v_\phi^2 \rangle$, whose non-zero nature explains why we have asymmetric drift in the first place. By evaluating the asymmetric drift with the assumptions of the epicycle approximation, we get (Hernquist, 1993),

$$\sigma_\phi^2 = \langle v_\phi^2 \rangle = \langle v_R^2 \rangle \frac{\kappa^2}{4\Omega^2}, \tag{2.39}$$

where the fraction in the product contains quantities solely determined from the potential, and the coefficient is determined from the assumed radial dispersion profile. This fully solves a disc-halo system. In practice, the system is realized by sampling the spatial density profile (by rejection sampling, for instance) and assigning velocities assuming Gaussians with means $\langle v_i \rangle$ and variances $\langle v_i^2 \rangle$.

2.2.2 DF-based Models

Although Jeans modelling is used to set up initial conditions for galaxies because it does not require a DF to be known ahead of time, the best initial conditions are generated from DFs [10]. In general, the equilibrium DF is a function of six variables. However, there are some quantities, called *integrals of motion*, which do not change along a star's orbit in a potential. For an axisymmetric potential, these are the total energy, $\mathcal{E}$, L_z and a third quantity, I_3. For spherical systems, up to five integrals of motion are admitted by the system, but the simplest *ergodic* models simply have $f_h(\mathcal{E})$ for the DF.

If we assume the epicycle approximation, then $I_3 \approx E_z = \Phi(R,0) - \Phi(R,z) + \frac{1}{2}v^2$, where v is the velocity of an orbit (Kuijken and Dubinski, 1995). The vertical energy, E_z, is conserved so long as the disc is razor thin. Jeans showed that a DF that is a function of the integrals of motion describes an equilibrium distribution. More specifically, quoting from Binney and Tremaine (2008),

Theorem 2.2.1 (The Jeans Theorem)**.** *Any steady-state solution of the collisionless Boltzmann equation depends on the phase-space coordinates only through integrals of*

[10] That is not to say that no one uses Jeans modelling to set up ICs. Approaches like the one presented in Hernquist (1993) were enormously successful and still used today.

motion in a given potential, and any function of the integrals yields a steady-state solution of the collisionless Boltzmann equation.

Proof of this theorem can be obtained in Jeans (1915) and in Chapter 4.2 of Binney and Tremaine (2008), although it essentially amounts to observing that the time derivative of a function of time-independent quantities is zero by the chain rule. Now that we know that any DF of the integrals of motion gives a steady state solution, and that using the epicyclic approximation gives us three known integrals of motion, we can ask ourselves what kinds of DFs describe the NFW haloes and exponential discs that are easily obtained from Jeans modelling.

We talk about the case of an ergodic halo and DF yielding an exponential disc at length here. For the remainder of the thesis, we primarily generate our initial conditions in this way. For any ergodic DF, a chosen density profile may be inverted by the Eddington inversion formula (Binney and Tremaine, 2008),

$$f(\mathcal{E}) = \int_0^{\mathcal{E}} \frac{\mathrm{d}\Psi}{\sqrt{\mathcal{E}-\Psi}} \frac{\mathrm{d}\nu}{\mathrm{d}\Psi} \tag{2.40}$$

where $\Psi = -\Phi$. Note that the combined potential need not be spherical, only the overall density of the spheroidal halo. We choose a truncated NFW profile (Navarro et al., 1997),

$$\nu_h(r) \sim \rho_h(r) = \frac{\rho_0 R_s^3}{r(R_s + r)^2} \tag{2.41}$$

where ρ_0 is a scale density and R_s is the halo scale length as our target halo density. By obtaining the 1D DF from Eq. (2.40), we can sample halo orbits given the combined disc-halo potential.

For the disc DF, we use a DF that yields exponential discs presented in Kuijken and Dubinski (1995). Noting that if E_z is an integral of motion that $E_p = \mathcal{E} - E_z$ is also an integral of motion, we use,

$$f_d(E_p, L_z, E_z) = \frac{\Omega(R_c)}{(2\pi^3)^{1/2}\kappa(R_c)} \frac{\tilde{\rho_d}}{\tilde{\sigma_R}^2(R_c)\tilde{\sigma_z}(R_c)} \exp\left[-\frac{E_p - E_c(R_c)}{\tilde{\sigma_R}^2(R_c)} - \frac{E_z}{\tilde{\sigma_z}^2(R_c)}\right]. \tag{2.42}$$

Note that the quantities Ω and κ have their usual definitions, the tilde functions are free choices to tune the disc properties (although they are qualitatively understood as velocity dispersions), and E_c is the energy of a circular orbit. Note that the R_c-dependent quantities do not violate the sole dependence on integrals of motion, since R_c is uniquely obtained in a one-to-one fashion from L_z.

For the tilde functions, we choose them to yield the closest thing to an exponential-sech^2 density profile with and exponential radial velocity dispersion as possible. Assuming an exponential radial dispersion profile, a disc density is obtained by iteratively adjusting $\tilde{\sigma_z}$ and $\tilde{\rho}$ such that (Kuijken and Dubinski, 1995),

$$\rho_d(R, z) = \frac{M_d}{8\pi R_d^2 z_d} e^{-R/R_d} \text{erfc}\, \left(\frac{R - R_{out}}{\sqrt{2}\delta R_{out}}\right) \exp\left[-0.8676 \frac{\Psi_z(R, z)}{\Psi_z(R, z_d)}\right] \tag{2.43}$$

Here, M_d is a parameter that is approximately equal to the mass of the disc, R_{out} is a truncation radius, δR_{out} is a parameter determining the sharpness of the truncation, and Ψ_z is the negative vertical potential, $\Phi(R, 0) - \Phi(R, z)$. The motivation behind the last term in the product is to yield a dropoff of vertical density close to $\text{sech}^2(z/z_d)$.

Similar to the Jeans models, we actualize these systems by sampling their combined spatial densities. At every sampled point, we draw a velocity from the DF that is constructed in the combined potential. This does not require us to, for example, use a Gaussian distribution for the velocity dispersions as in Jeans models. This kind of model is as accurate as the assumption that E_z is an integral of motion is (as accurate as the epicycle approximation is). A more detailed discussion about how self-consistent systems are realized from DFs can be found in Kuijken and Dubinski (1995), and this work forms the basis for the GalactICS code used in this thesis.

2.2.3 Action-Angle Variables and the Strong Jeans Theorem

Of course, E_z is only approximately an integral of motion for axisymmetric, nearly planar systems. Although not a substantial element of this thesis, it is worth mentioning a different approach to approximating integrals of motion. Instead of explicitly assuming we are working with an axisymmetric, static system and deducing the conserved quantities, let's ask more generally, *for any system*, what are the conserved quantities? Integrals of motion have the property that orbits may be viewed as single points in a space with dimension of the number of integrals. The only thing unique about them is where they are in the phase of the orbit.

With this in mind, we introduce the actions (Binney and Tremaine, 2008),

$$\mathbf{J} = \oint \mathbf{p} \cdot \mathrm{d}^n \mathbf{q} \tag{2.44}$$

where $\mathbf{J}$ are the actions, and $\mathbf{p}$ and $\mathbf{q}$ are canonical coordinates. The closed path over which this integral is evaluated yields a unique set of actions. If the system is axisymmetric and the path we have chosen is a circle of radius R, it is straightforward to see that the radial component of the action is just $L_z = Rv_c$, which depends on the potential.

Turning the definition of the actions into a transformation from a physically motivated conjugate coordinate system is difficult in general. Closed form solutions for axisymmetric systems exist if the potential is of the Stäckel from[11], but in general, these transformations do not exist. A commonly used technique is to locally approximate the potential as being of the Stäckel form Binney (2012). In practice, one is reduced to approximating the potential instead of the third integral of motion as in the case of GalactICS. For nearly planar disc systems, the differences are insignificant, but become more relevant as one wants to initialize a thicker disc (Vasiliev, 2018; Bauer and Widrow, 2018).

2.3 Cosmology's Implications for Simulations

Our discussion up to this point has focused on simulating isolated systems. Complications arise when we move to a fully cosmological environment. The purpose of this section is to briefly review relevant cosmology, and to explain what numerical methods must be modified and used to simulate cosmological systems. We conclude this section with a brief commentary on identifying substructure in simulations.

2.3.1 FRW Cosmology: Large Scale Properties

In words, the ΛCDM paradigm described in Chapter 1 prescribes a Universe comprised of four fundamental substances: baryons, radiation, dark matter, and dark energy. On large scales, the Universe is also believed to be isotropic and homogeneous, meaning the patch we occupy is the exact same as any other patch. General Relativity provides a mechanism for us to meaningfully compute distances between patches is this scenario. The so-called Friedmann-Robertson-Walker metric tells us that the *proper distance* between two points at different positions in space and at

[11] For more detail, see Chapter 3.5.3 of Binney and Tremaine (2008).

different times is (Kolb and Turner, 1990; Dodelson, 2003),

$$\mathrm{d}\,s^2 = c^2 \mathrm{d}\,t^2 + a^2(t)\left(\frac{\mathrm{d}\,r^2}{1-kr^2} + r^2 \mathrm{d}\,\Omega^2\right). \tag{2.45}$$

Here, c is the speed of light, t is the time coordinate, a is the scale factor of the Universe which is equal to 1 at present day and 0 at the Big Bang, k describes the spatial curvature, and r and Ω have their standard spherical coordinate definitions. The case used for the whole thesis is where $k = 0$, a flat Universe. Assuming this metric, and that all substances in the Universe behave like perfect fluids, it can be shown with General Relativity that the large scale evolution of the Universe is described by the following, the Friedmann Equations (Kolb and Turner, 1990; Dodelson, 2003),

$$\left(\frac{\dot{a}}{a}\right)^2 = \frac{8\pi G}{3}\rho \tag{2.46}$$

$$\frac{\ddot{a}}{a} = -\frac{4\pi G}{3}\left(\rho + \frac{3p}{c^2}\right). \tag{2.47}$$

Here ρ is the density of the Universe, p is the pressure of the Universe, and we introduce the definition $H(t) = \dot{a}/a$, the Hubble parameter. With the definition of the Hubble parameter, the first of the Friedmann equations is commonly expressed,

$$\left(\frac{H(t)}{H_0}\right)^2 = a^{-4}\Omega_{R,0} + a^{-3}\Omega_{M,0} + \Omega_{\Lambda,0} \tag{2.48}$$

where $\Omega_{R,0}$, $\Omega_{M,0}$, and $\Omega_{\Lambda,0}$ are the relative contributions of radiation, dark and baryonic matter, and dark energy at present day, respectively. Also, H_0 is the present-day Hubble parameter. Every flat ΛCDM universe has these as free parameters, and we can choose them to be anything we like. The different powers of a reflect how radiation, matter, and dark energy contribute differently to the energy as the Universe expands, and can be deduced under relatively few assumptions (Kolb and Turner, 1990; Dodelson, 2003).

When simulating a ΛCDM universe, we can choose to work in a frame where relative distances between fixed points remain fixed. This is the proper coordinate system. The distance between two objects in a proper coordinate system, d, for a flat Universe is simply,

$$d(t) = a(t)r \tag{2.49}$$

where r is the proper distance. An interesting notable consequence of this is,

$$\begin{aligned} \dot{d} &= \dot{a}r + a\dot{r} && (2.50) \\ \frac{\dot{d}}{a} &= \frac{\dot{a}}{a}r + \dot{r} && (2.51) \\ &= H(t)r + \dot{r}. && (2.52) \end{aligned}$$

If two objects are at rest with respect to the proper coordinate system at present day ($\dot{r} = 0$), we measure a non-zero proper velocity,

$$\dot{d} = H_0 r. \tag{2.53}$$

This effect was first described by Hubble (1929), and explains why distant galaxies appear to be moving away from us. More generally, we call this term in the proper velocity the *Hubble flow*.

Following up on this concept, we introduce the notion of *redshift*. The term derives from the fact that as objects become more distant, we expect the Hubble flow to cause the emitters to move away from the observer. Photons emitted by a stationary object with a wavelength, λ, are observed with wavelength $a(t_{emit})\lambda$, and we define the redshift, z,

$$1 + z = \frac{1}{a} \tag{2.54}$$

in analogy to this phenomenon. This is a decreasing unit of time that is often used interchangeably with the scale factor, a.

2.3.2 FRW Cosmology: Cosmological ICs

Of course, the Universe is not actually homogeneous on small scales. As we suggested in Chapter 1, small scale fluctuations are present in the early Universe which collapse to form galaxies. Initially, these fluctuations evolve independently of each other in the so-called *linear regime*. Initial conditions for ΛCDM simulations rely on this fact to generate the initial perturbations for the simulation.

The prevailing view in cosmology is that the Big Bang was followed by the development of a primordial perturbation field. As the Universe expanded, interactions with baryons and radiation modified the initial distribution of perturbation scales. Mathematically, we take the the perturbation field $\delta(\mathbf{r}, t)$, which describes the deviation from the Universe's mean density at some position and time, and find its Fourier transform. The result is a statistical distribution, called the *power spectrum*, that describes the scale of perturbations (Hahn and Abel, 2013),

$$P(k) = \alpha k^{n_s} \mathcal{T}^2(k) \tag{2.55}$$

where α is a normalization constant, n_s is a spectral index describing the original inflationary produced perturbations, and $\mathcal{T}$ is a scale-dependent *transfer function* that describes deviations from a power law at different scales. For reference, low k corresponds to larger perturbations in the same way that low frequency corresponds to larger time gaps. The smallest structures occur at high k.

While a detailed discussion of how the transfer function is computed can be found in Hahn and Abel (2013), we will simply say that it is a reflection of the idea that perturbations only grow when matter becomes dominant. It reflects how we believe that perturbations of different scales grew at different rates in the early Universe. However, once it is known at some desired time (redshift), we can sample a Gaussian density field with the right statistical characteristics. This spatial sample with corresponding velocities obtained via something called 2nd Order Lagrangian Perturbation Theory[12] form the initial conditions for our ΛCDM simulation.

2.3.3 Numerical Methods: Time Integration

Two big problems are present for applying N-body techniques as described. The first, and maybe most obvious of these, is in how we step through time. The time integration scheme worked out in §2.1.4 makes a critical assumption: the Hamiltonian and its separable components are time independent! Eq. (2.49) forces us to re-express the leapfrog scheme. For primed quantities as proper (comoving), we have our new

[12] See Hahn and Abel (2013) for a detailed description of this technique.

system(Quinn et al., 1997),

$$\dot{\mathbf{v}}' + 2H(t)\mathbf{v}' = -\frac{\nabla'\phi'}{a^3} \tag{2.56}$$

$$\dot{\mathbf{r}}' = \mathbf{v}' \tag{2.57}$$

$$\nabla'^2\phi' = 4\pi G\left(\rho' - \rho_b'\right) \tag{2.58}$$

where $\mathbf{r}'$ is the comoving position, $\mathbf{v}'$ is the comoving velocity, ϕ' is the comoving potential, ρ' is the comoving mass density, and ρ_b' is the mean comoving background mass density. The new drift/kick operators are then defined implicitly (Quinn et al., 1997),

$$D_t(\Delta t) : \begin{cases} \mathbf{r}_i' & \longrightarrow \mathbf{r}_i' + \mathbf{v}_i'\Delta t \\ \mathbf{v}_i' & \longrightarrow \mathbf{v}_i' \end{cases}, \tag{2.59}$$

and,

$$K_t(\Delta t) : \begin{cases} \mathbf{r}_i' & \longrightarrow \mathbf{r}_i' \\ \mathbf{v}_i' & \longrightarrow \mathbf{v}_i' \frac{1-H(t)\Delta t}{1+H(t)\Delta t} + \frac{\nabla'\phi'(\mathbf{r}_i')\Delta t}{a^3(t)(1+H(t)\Delta t)} \end{cases}. \tag{2.60}$$

The problem is that there does not appear to be a way to work forward from a separable Hamiltonian to these operators. Thus, any integration scheme constructed from these operators will not be free of energy drift. To get around this, we ask if there is some canonical transformation that can give us a symplectic integrator. Via a derivation in Quinn et al. (1997), we find that for a choice of $\mathbf{r}'$ as our coordinate system, the canonical momentum is $\mathbf{p}' = a^2\mathbf{v}'$. The Hamiltonian is,

$$H = \frac{\mathbf{p}'}{2a^2} + \frac{\phi'}{a}, \tag{2.61}$$

for $\phi' = a\phi + \frac{1}{2}\ddot{a}a\mathbf{r}'^2$. This is a separable Hamiltonian with drift and kick operators,

$$D_t(\Delta t) : \begin{cases} \mathbf{r}'_i & \longrightarrow \mathbf{r}'_i + \mathbf{p}'_i \int_t^{t+\Delta t} \frac{\mathrm{d}\, t}{a^2(t)} \\ \mathbf{p}'_i & \longrightarrow \mathbf{v}'_i \end{cases}, \tag{2.62}$$

and,

$$K_t(\Delta t) : \begin{cases} \mathbf{r}'_i & \longrightarrow \mathbf{r}'_i \\ \mathbf{p}'_i & \longrightarrow \mathbf{p}'_i - \nabla'\phi' \int_t^{t+\Delta t} \frac{\mathrm{d}\, t}{a(t)} \end{cases} \tag{2.63}$$

Since these operators derive directly from a separable Hamiltonian, this integrator is symplectic. Even though the energy of our cosmological system is not conserved, there will be no drift about the continuum system's actual energy. This is the integration scheme used in Gadget-3 for cosmological simulations.

2.3.4 Numerical Methods: Gravity Calculation

Beyond the coordinate systems and time stepping scheme used in cosmological simulations, there is also the issue that the actual Universe, the system we are trying to simulate, extends over vast distances. Typically, only a box, a few tens to hundreds of Mpc per side is simulated. Gravity is a long range force, and there will be a contribution at any point in the simulation box from distant, massive objects. The way that this handled in modern cosmological simulations is to impose periodic boundary conditions when we solve Poisson's equation. This is essentially like viewing our simulation box cloned infinitely many times along each axis, shifted by its length along each axis.

For forces computed using an FFT-based technique like particle mesh, periodic boundary conditions are assumed. The DFT by its nature implies the density signal in the box repeats forever. For non-grid based techniques, this is not so trivial. Normally, GADGET-3 will use a DFT to compute long range forces. However, it does implement a way to use its tree code for long range calculations (Springel, 2005). While for this thesis, the particle mesh grid functionality is used for long range forces, a description of how GADGET-3 implements its tree code with periodic boundary conditions can be found in Hernquist et al. (1991).

2.3.5 Identifying Substructure in Simulations

The picture of a simulated ΛCDM universe has been conceptually and quantitatively described up to this point. The key concept tying simulations of ΛCDM to isolated galaxy simulations is the presence of substructure. Here, we describe how we identify substructure in these complicated simulations.

First and foremost, the question of finding substructure in data is not unique to astrophysics. More generally, we are solving an unsupervised machine learning problem called *clustering*. Solutions to clustering problems take unlabeled data, such as particle masses, positions, and velocities, and identify significant groups within the data (James et al., 2014).

Although there are many techniques that one can use to find clusters in data, we focus on *hierarchical clustering* methods, which as the name suggests, are meant to build hierarchies of clusters. Since ΛCDM simulations produce subhaloes within haloes, we expect a such a structure in these clusters.

There are two general approaches to hierarchical clustering (James et al., 2014). Agglomerative methods initially place each particle in their own cluster, and will merge two clusters if they meet some kind of *linkage criterium*. For example, given clusters C_1 and C_2, the complete-linkage approach will merge the two clusters if $\max\{d(c_1, c_2) : c_1 \in C_1 \wedge c_2 \in C_2\} < l$, for some distance metric[13], d, and a linking length, l that is a free parameter. Other common metrics include the single-linkage criterion, $\min\{d(c_1, c_2) : c_1 \in C_1 \wedge c_2 \in C_2\} < l$, and the average linkage criteria $\langle d(c_1, c_2)\rangle\,(c_1 \in C_1 \wedge c_2 \in C_2) < l$.

The other approach to hierarchical clustering is divisive clustering, which starts with all of the particles in the same cluster (James et al., 2014). Divisive clustering splits the top cluster into objects of maximum dissimilarity until each object is its own cluster. Here, dissimilarity is defined by some metric chosen ahead of time.

Regardless of which approach to hierarchical clustering one uses, the end result is a tree-like structure called a *dendrogram*, with large clusters at the top and individual particles at the bottom. In simulations of cosmology, we construct these at every timestep to determine which haloes merged with other haloes. There is a long literature on this subject described in Behroozi et al. (2013), although we use their implementation, the ROCKSTAR code, in this thesis.

The main idea behind the algorithm implemented in ROCKSTAR is to first apply a divisive scheme to the 3D data to create more manageable subclusters that get

[13]Common distance metrics are the Euclidean metric or the Mahalanobis distance (James et al., 2014).

piped to an agglomerative 6D scheme. A big issue in the literature has been finding distance metrics which work with 6D phase space information in an acceptable manner (Behroozi et al., 2013). In addition to the naive hierarchical clustering algorithm, ROCKSTAR also removes unbound particles from clusters and implements a clever scheme to tell when haloes have merged in a snapshot.

The resultant data structure after applying this algorithm sequentially to all snapshots is a dendrogram of dendrograms at all later times. A node in the last snapshot represents the merging history of a single galaxy. In such a data structure, we see smaller haloes coming together to form a Milky Way mass object at redshift $z = 0$. By applying this technique to the raw particle data, we can pick out dark matter haloes in our simulations.

Bibliography

Barnes, J. and Hut, P. (1986). A hierarchical O(N log N) force-calculation algorithm. *Nature*, 324:446–449.

Basumallik, A., jai Min, S., and Eigenmann, R. (2007). Programming distributed memory sytems using openmp. In *Parallel and Distributed Processing Symposium, International 0*, page 207.

Bauer, J. S. and Widrow, L. M. (2018). Can Stellar Discs in a Cosmological Setting Avoid Forming Strong Bars? *ArXiv e-prints*, page arXiv:1809.00090.

Behroozi, P. S., Wechsler, R. H., and Wu, H.-Y. (2013). The ROCKSTAR Phase-space Temporal Halo Finder and the Velocity Offsets of Cluster Cores. *ApJ*, 762:109.

Binney, J. (2012). Actions for axisymmetric potentials. *MNRAS*, 426:1324–1327.

Binney, J. and Merrifield, M. (1998). *Galactic Astronomy*.

Binney, J. and Tremaine, S. (2008). *Galactic Dynamics: Second Edition*. Princeton University Press.

Cooley, J. W. and Tukey, J. W. (1965). An algorithm for the machine calculation of complex fourier series. *Mathematics of Computation*, 19(90):297–301.

de Campos, A. M. (2019). Image of Peano Space-Filling Curve. `https://commons.wikimedia.org/wiki/File:Peanocurve.svg`.

Dodelson, S. (2003). *Modern cosmology*.

Freeman, K. C. (1970). On the Disks of Spiral and S0 Galaxies. *ApJ*, 160:811.

Frenk, C. S., White, S. D. M., and Davis, M. (1983). Nonlinear evolution of large-scale structure in the universe. *ApJ*, 271:417–430.

Hahn, O. and Abel, T. (2013). MUSIC: MUlti-Scale Initial Conditions. Astrophysics Source Code Library.

Hénon, M. (1970). Le problème des N-corps en astronomie et en physique des plasmas plus Experiments with a cylindrical galaxy (film de R. Hockney). In *Physique Fondamentale et Astrophysique*, pages C3–27.

Hernquist, L. (1993). N-body realizations of compound galaxies. *ApJS*, 86:389–400.

Hernquist, L., Bouchet, F. R., and Suto, Y. (1991). Application of the Ewald method to cosmological N-body simulations. *ApJS*, 75:231–240.

Hubble, E. (1929). A Relation between Distance and Radial Velocity among Extra-Galactic Nebulae. *Proceedings of the National Academy of Science*, 15:168–173.

James, G., Witten, D., Hastie, T., and Tibshirani, R. (2014). *An Introduction to Statistical Learning: With Applications in R*. Springer Publishing Company, Incorporated.

Jeans, J. H. (1915). On the theory of star-streaming and the structure of the universe. *MNRAS*, 76:70–84.

Klypin, A. A. and Shandarin, S. F. (1983). Three-dimensional numerical model of the formation of large-scale structure in the Universe. *MNRAS*, 204:891–907.

Kolb, E. W. and Turner, M. S. (1990). *The early universe.*

Kuijken, K. and Dubinski, J. (1995). Nearly Self-Consistent Disc / Bulge / Halo Models for Galaxies. *MNRAS*, 277:1341.

Lewis, J. R. and Freeman, K. C. (1989). Kinematics and chemical properties of the old disk of the Galaxy. *AJ*, 97:139–162.

Lilley, E. J., Sanders, J. L., and Evans, N. W. (2018a). A two-parameter family of double-power-law biorthonormal potential-density expansions. *MNRAS*, 478:1281–1291.

Lilley, E. J., Sanders, J. L., Evans, N. W., and Erkal, D. (2018b). Galaxy halo expansions: a new biorthogonal family of potential-density pairs. *MNRAS*, 476:2092–2109.

Lusk, E., Doss, N., and Skjellum, A. (1996). A high-performance, portable implementation of the mpi message passing interface standard. *Parallel Computing*, 22:789–828.

Lynden-Bell, D. (1999). Negative Specific Heat in Astronomy, Physics and Chemistry. *Physica A Statistical Mechanics and its Applications*, 263:293–304.

MPI Forum (2015). MPI: A Message-Passing Interface Standard Version 3.1. In *Message Passing Interface Forum.*

Navarro, J. F., Frenk, C. S., and White, S. D. M. (1997). A Universal Density Profile from Hierarchical Clustering. *ApJ*, 490:493–508.

Padmanabhan, T. (1990). Statistical mechanics of gravitating systems. *Phys. Rep.*, 188:285–362.

Press, W. H., Teukolsky, S. A., Vetterling, W. T., and Flannery, B. P. (1992). *Numerical recipes in FORTRAN. The art of scientific computing.*

Quinn, T., Katz, N., Stadel, J., and Lake, G. (1997). Time stepping N-body simulations. *arXiv Astrophysics e-prints.*

Sethna, J. P. (2006). Statistical mechanics: Entropy, order parameters, and complexity. In *Oxford Master Series in Physic*. Univ. Press.

Springel, V. (2005). The cosmological simulation code GADGET-2. *MNRAS*, 364:1105–1134.

Trimble, V. (1995). The 1920 Shapley-Curtis Discussion: Background, Issues, and Aftermath. *PASP*, 107:1133.

van der Kruit, P. C. and Searle, L. (1981). Surface photometry of edge-on spiral galaxies. I - A model for the three-dimensional distribution of light in galactic disks. *A&A*, 95:105–115.

Vasiliev, E. (2018). Agama reference documentation. *arXiv e-prints.*

Xu, G. (1995). A New Parallel N-Body Gravity Solver: TPM. *ApJS*, 98:355.

Chapter 3

A Method for Studying Discs in Cosmological Haloes

This chapter contains a reproduction of a paper published in Monthly Notices of the Royal Astronomical Society as: Jacob S. Bauer, Lawrence M. Widrow, and Denis Erkal. Disc-halo interactions in ΛCDM. *Monthly Notices of the Royal Astronomical Society*, 476:198-209, 2018.

3.1 Abstract

We present a new method for embedding a stellar disc in a cosmological dark matter halo and provide a worked example from a ΛCDM zoom-in simulation. The disc is inserted into the halo at a redshift $z = 3$ as a zero-mass rigid body. Its mass and size are then increased adiabatically while its position, velocity, and orientation are determined from rigid-body dynamics. At $z = 1$, the rigid disc is replaced by an N-body disc whose particles sample a three-integral distribution function (DF). The simulation then proceeds to $z = 0$ with live disc and halo particles. By comparison, other methods assume one or more of the following: the centre of the rigid disc during the growth phase is pinned to the minimum of the halo potential, the orientation of the rigid disc is fixed, or the live N-body disc is constructed from a two rather than three-integral DF. In general, the presence of a disc makes the halo rounder, more centrally concentrated, and smoother, especially in the innermost regions. We find that methods in which the disc is pinned to the minimum of the halo potential tend to overestimate the amount of adiabatic contraction. Additionally, the effect of the disc on the subhalo distribution appears to be rather insensitive to the disc insertion method. The live disc in our simulation develops a bar that is consistent with the bars seen in late-type spiral galaxies. In addition, particles from the disc are launched or "kicked up" to high galactic latitudes.

3.2 Introduction

The structure and evolution of galaxies are determined by the spectrum of primordial density perturbations, the dynamics of stars and dark matter, and baryonic physics.

Over the past two decades, there has been a concerted effort to incorporate the latter into cosmological simulations (e.g. Katz et al., 1996; Springel and Hernquist, 2003; Stinson et al., 2006; Roškar et al., 2010; Pakmor and Springel, 2013; Gómez et al., 2016). While these simulations have enhanced our understanding of galaxy formation, their computational cost is high. Adding to the challenge is the complex and sub-grid nature of star formation, supernova feedback, and other baryonic processes, which require *ad hoc* parametric models.

In this work, we focus on the dynamics of disc galaxies. Our goal is to study the nature of disc-halo interactions where it is advantageous to be able to control properties of the disc such as its mass, size, and internal kinematics. Such control is not possible in *ab initio* simulations.

Simulations of isolated disc galaxies provide an alternative arena to study galactic structure and dynamics. Moreover, many aspects of disc-halo interactions can be understood by considering the collisionless dynamics of stars and dark matter while ignoring gas physics. For example, simulations of stellar disc-bulge systems embedded in dark haloes have proved indispensable in studies of bar and spiral structure formation (See Sellwood (2013) and references therein). These simulations typically begin with systems that are in equilibrium, or nearly so. For this reason, they usually assume axisymmetric initial conditions, which are manifestly artificial. In short, discs do not come into existence as formed, highly symmetric objects but rather build up through the combined effects of gas accretion, star formation, and feedback (Vogelsberger et al., 2013; Schaye et al., 2015). Moreover, the haloes in which the real discs reside are almost certainly triaxial and clumpy (Navarro et al., 1997; Moore et al., 1999; Klypin et al., 1999).

There now exists a long history of attempts to bridge the gap between simulations of isolated disc-bulge-halo systems, with their pristine initial conditions, and cosmological simulations. Kazantzidis et al. (2008), for example, followed the evolution of a Milky Way-like disc in its encounter with a series of satellites whose properties were motivated by cosmological simulations. They found that the satellites "heated" the disc and prompted the formation of a bar and spiral structure. Along similar lines, Purcell et al. (2011) modeled the response of the Milky Way to the gravitational effects of the Sagittarius dwarf galaxy (Sgr) by simulating disc-satellite encounters for different choices of the satellite mass. They concluded that Sgr may have triggered the development of the spiral structure seen in the Milky Way today. Continuing in this vein, Laporte et al. (2016) studied the influence of the Large Magellanic Cloud and Sgr on the Milky Way disc and found that they can create similar warps to what has been observed. The effect of a time-dependent triaxial halo was investigated in Hu and Sijacki (2016) where they found it can trigger grand-design spiral arms.

Of course, the disc of the Milky Way lives within a population of satellite galaxies and, quite possibly, pure dark matter subhaloes (Moore et al., 1999; Klypin et al., 1999). With this in mind Font et al. (2001) simulated the evolution of an isolated disc-bulge-halo model where the halo was populated by several hundred subhaloes. They concluded that that substructure played only a minor role in heating the disc, a result that would seem at odds with those of Kazantzidis et al. (2008). Numerical simulations by Gauthier et al. (2006) and Dubinski et al. (2008) shed some light on this discrepancy. In those simulations, 10% of the halo mass in an isolated disc-bulge-halo system was replaced by subhaloes with a mass distribution motivated by the cosmological studies of Gao et al. (2004). Gauthier et al. (2006) found that a modest amount of disc heating occurred during the first 5 Gyr, at which point satellite interactions prompted the formation of a bar, which in turn heated the disc more significantly. Not surprisingly, the timing of bar formation varied from 1 Gyr to 10 Gyr when the experiment was repeated with different initial conditions for the satellites.

The aforementioned simulations have several drawbacks. First, most of them do not allow for halo triaxiality. Second, the disc is initialized at its present-day mass whereas real discs form over several Gyr. Finally, the subhaloes are inserted into the halo in an *ad hoc* fashion. Several attempts have been made to grow a stellar disc in a cosmological halo in an effort to address these shortcomings (Berentzen and Shlosman, 2006; DeBuhr et al., 2012; Yurin and Springel, 2015). The general scheme proceeds in three stages. During the first stage, a cosmological simulation is run with pure dark matter and a suitable halo is selected. In the second, a rigid disc potential is grown slowly in the desired halo, thus allowing the halo particles to respond adiabatically to the disc's time-varying potential. In the third stage, the rigid disc is replaced by a live one and the simulation proceeds with live disc and halo particles.

DeBuhr et al. (2012) used such a scheme to introduce stellar discs into dark matter haloes from the Aquarius Project (Springel et al., 2008). They added a rigid disc at a redshift $z = 1.3$ with a mass parameter for the disc that grew linearly with the scale factor from an initial value of zero to its final value at $z = 1$. The disc was initially centered on the potential minimum of the halo and oriented so that its symmetry axis pointed along either the minor or major axis of the halo. During the rigid disc phase, the motion of the disc centre of mass was determined from Newton's 3rd law.

To initialize the live disc, DeBuhr et al. (2012) approximate the halo potential as a flattened, axisymmetric logarithmic potential and then determine the disc distribution function (DF) by solving the Jeans equations.

Yurin and Springel (2015) introduced a number of improvements to this scheme. Most notably, they use GALIC to initialize the live disc (Yurin and Springel, 2014). This code is based on an iterative scheme for finding stationary solutions to the collisionless Boltzmann equation. The general idea for iterative codes is to begin with a set of particles that has the desired spatial distribution and some initial guess for the velocity distribution. The velocities are then adjusted so as to achieve stationarity, as measured by evolving the system and computing a certain merit function. In Yurin and Springel (2015) the initial disc was assumed to be axisymmetric with a DF that depended on two integrals of motion, the energy, E, and angular momentum, L_z. One striking, if not puzzling, result from this work is the propensity of the discs to form very strong bars. These bars are especially common in models without bulges even in cases where the disc is submaximal.

In this paper, we introduce an improved scheme for inserting a live disc in a cosmological halo. In particular, the centre of mass *and* orientation of the rigid disc are determined by solving the standard equations of rigid body dynamics. Thus, our rigid disc can undergo precession and nutation. The angular and linear velocities of the rigid disc at the end of the growth phase are incorporated into the live disc initial conditions. As in Yurin and Springel (2015) we use an axisymmetric approximation for the halo potential when constructing the disc DF. However, our DF is constructed from an analytic function of E, L_z, and the vertical energy E_z, which is an approximate integral of motion used in GALACTICS (Dubinski and Kuijken, 1995;

Widrow et al., 2008). By design, the disc DF yields a model whose density has the exponential-sech^2 form. And with a three-integral DF, we have sufficient flexibility to model realistic Milky Way-like discs. As discussed below, the initial disc DF may be crucial in understanding the formation of the bar.

As a demonstration of our method we grow a Milky Way-like disc in an approximately $10^{12}\,h^{-1}\,M_\odot$ halo from a cosmological zoom-in simulation. We discuss both disc dynamics and the effect our disc has on the population of subhaloes. Discs have been invoked as a means of depleting halo substructure and thus alleviating the Missing Satellite Problem, which refers to the underabundance of observed Milky Way satellites relative to the number of Cold Dark Matter subhaloes seen in simulations (Moore et al., 1999; Klypin et al., 1999). An earlier study by D'Onghia et al. (2010) found that when a disc potential is grown in a Milky Way-size cosmological halo, the abundance of substructure in the mass range $10^7\,M_\odot$ to $10^9\,M_\odot$ was reduced by a factor of $2-3$. Similar results were found by Sawala et al. (2017) and Garrison-Kimmel et al. (2017).

The organization of the paper is as follows. In Section 2, we outline our method for inserting a live disc into a cosmological simulation. We also present results from a test-bed simulation where a disc is inserted into an isolated flattened halo. We next apply our method to a cosmological zoom-in simulation. In Section 3, we focus on disc dynamics and find that the disc develops a bar, spiral structure and a warp. In addition, disc-halo interactions appear to "kick" stars out of the disc and into regions normally associated with the stellar halo. In Section 4, we present our results for the spherically-averaged density profile and shape of the dark matter halo as well as the distribution of subhaloes. Particular attention is paid to the sensitivity of these

	DMO	MN	FO	RD	LD
$M_d\,(M_\odot)$	–	7.2×10^{10}	7.2×10^{10}	7.2×10^{10}	7.2×10^{10}
$R_{d,0}$ (kpc)	–	3.7	3.7	3.7	3.7
N_d	–	–	10^6	10^6	10^6
z_g	–	3.0	3.0	3.0	–
z_l	–	1.0	1.0	1.0	1.0
N_r	4096	4096	4096	4096	4096
$L_{box}(\text{ Mpc}\,h^{-1})$	50	50	50	50	50

Table 3.1: A summary of the simulation parameters, as discussed in the text. M_d is the final disk mass, $R_{d,0}$ is the final disk scale radius, N_d is the number of particles used to simulate the disk, z_g and z_l are the redshifts when the disk beings to grow and when it becomes live (respectively), N_r is the effective resolution in the zoom-in region, and L_{box} is the comoving size of the box.

results to the disc insertion scheme. We conclude in Section 5 with a summary and discuss possible applications of this work.

3.3 Inserting a Stellar Disc into a Cosmological Halo

In this section, we detail our method for inserting a live stellar disc into a cosmological simulation. We begin with an overview of our approach and the five main simulations presented in this paper. We then describe some of the more technical aspects of the method.

3.3.1 Overview of Simulation Set

Our simulations are performed with the N-body component of GADGET-3, which is an updated version of GADGET-2 (Springel, 2005). For the cosmological simulations, we implement the zoom-in technique of Katz et al. (1994) and Navarro et al. (1994), broadly following the recommendations of Oñorbe et al. (2014), which allows us to achieve very high spatial and mass resolution for a single halo while still accounting for the effects of large-scale tidal fields. For the cosmological parameters, we use the results from Planck 2013 (Planck Collaboration et al., 2014) with $h = 0.679$, $\Omega_b = 0.0481$, $\Omega_0 = 0.306$, $\Omega_\Lambda = 0.694$, $\sigma_8 = 0.827$, and $n_s = 0.962$.

We begin by simulating a $50\,h^{-1}$Mpc box with $N_r = 512^3$ particles, where N_r is the effective resolution, each with a mass of $\sim 7.9 \times 10^7\,h^{-1}M_\odot$. We identify a Milky Way-like halo in the present-day snapshot, that is, a $\sim 10^{12}\,M_\odot$ halo which has experienced no major mergers since $z = 1$ and which has no haloes with $2h^{-1}$ Mpc more than half the mass of the MW-analogue. We then run an intermediate zoom-in simulation targeting all particles within 10 virial radii of the low resolution halo. The initial conditions for this simulation are generated with MUSIC (Hahn and Abel, 2013), which creates five nested regions from a coarse resolution of $N_r = 128^3$ in the outskirts to an effective $N_r = 2048^3$ resolution in the targeted region. After this simulation reaches $z = 0$, we select all particles within 7.5 virial radii and regenerate initial conditions with one more level of refinement, giving six nested zoom regions, where now, the highest effective resolution is $N_r = 4096^3$. Our final halo is composed of approximately 10^7 particles, each with a mass of $1.54 \times 10^5\,h^{-1}M_\odot$. The softening lengths were selected using the criteria in Power et al. (2003) with a softening of 719 comoving pc for the highest resolution particles in the final zoom-in simulation. We found that this repeated zoom-in technique results in remarkably little contamination from coarse resolution particles within the targeted halo, giving a clean region of size $1.9h^{-1}$ Mpc at $z = 0$.

The dark matter only (DMO) simulation not only serves as the basis for four simulations with discs but also provides a control "experiment" for our study of the effect discs have on halo properties. In each of our disc simulations, the potential of a rigid disc is introduced at the "growing disc" redshift z_g. The mass parameter of the disc is then increased linearly with the scale factor $a = 1/(1+z)$ from zero to its final value M_d at the "live disc" redshift z_l. As described in Sec. 3.3.5, the radial and vertical scale lengths of the disc are also increased between z_g and z_l to account for the fact that discs grow in scale as well as mass while they are being assembled.

In the first of our disc-halo simulations, dubbed MN, we introduce a rigid Miyamoto-Nagai disc (Miyamoto and Nagai, 1975), whose gravitational potential is given by

$$\Phi(R,\, z) = -\frac{GM_d}{\left(R^2 + \left(R_d + (z^2 + z_d^2)^{1/2}\right)^2\right)^{1/2}}\ . \tag{3.1}$$

For this simulation, which was meant to mimic the scheme in D'Onghia et al. (2010), we assume that the centre of the disc tracks the minimum of the halo potential while the orientation of the disc is fixed to be aligned with the z-axis of the simulation box. Note that this is effectively a random direction for the halo.

In the remaining three disc simulations, we grow an exponential-sech^2 rigid disc potential in our halo with mass and scale-length parameters that grow in time. For our fixed-orientation (FO) simulation, the position and velocity of the disc's centre of mass are determined from Newtonian dynamics while the spin axis of the disc is initially aligned with the minor axis of the halo at $z = z_g$ and kept fixed in the simulation box frame thereafter. In this respect, the simulation is similar to the ones presented in DeBuhr et al. (2012) and Yurin and Springel (2015). For the rigid-disc (RD) simulation the disc's orientation, which is now a function of time, is determined from Euler's rigid body equations.

In the MN, FO, and RD runs, we continue the simulation to the present epoch ($z = 0$) with the assumed rigid disc potential where the mass and scale length parameters are held fixed and the position and orientation are calculated as they were during the growth phase. For our final live disc (LD) simulation, we swap a live disc for the RD disc at z_l. Thus, the RD and LD simulations are identical prior to z_l. All of our discs have a final mass of $M_d = 7.2 \times 10^{10} M_\odot$, a final scale radius of 3.7 kpc, and a final scale height of 0.44 kpc. Our simulation parameters can be found summarized in Table 3.1.

3.3.2 Summary of Live Disc Insertion Scheme

The first step in our disc insertion scheme is to calculate an axisymmetric approximation to the gravitational potential of the DMO halo at $z = 0$. We do so using an expansion in Legendre polynomials as described below. We then generate a particle representation of a stellar disc that is in equilibrium with this potential using the GALACTICS code (Kuijken and Gilmore, 1989; Widrow et al., 2008). Though GALACTICS allows one to generate the phase space coordinates of the disc stars, at this stage, we only need the positions of the stars, which we use to represent the "rigid disc". At the z_g snapshot, we incorporate the disc particles into the mass distribution of the system with the disc centered on the potential minimum of the halo. We then rerun the simulation from z_g to z_l with the following provisos. First, the mass of the disc is increased linearly with a from zero to its final value. Second, the size of the disc increases with time, which we account for by having the positions of the disc particles, as measured in the disc frame, expand with time to their final values at z_l.

Finally, the center of mass and orientation of the disc are determined by integrating the equations of rigid-body dynamics. At redshift z_l, the DF of the disc is recalculated assuming the same structural parameters as before but with an axisymmetric approximation to the new halo potential. An N-body disc is generated from this DF and the simulation proceeds with live disc particles. In this paper, we choose $z_g = 3$ and $z_l = 1$ so that the growth period lasts from 2.2 Gyr to 5.9 Gyr after the Big Bang. This period in time roughly corresponds to the epoch of peak star formation in Milky Way-like galaxies (e.g. van Dokkum et al., 2013).

Our simulations during this epoch can be used to study the effect of a disc potential on the evolution of substructure. On the other hand, our simulations of the live disc epoch ($z_l > z > 0$) can also be used to study disc dynamics in a cosmologically-motivated dark halo.

3.3.3 Halo Potential

Our method requires an axisymmetric approximation to the halo potential centred on the disc. This approximation is found using an expansion in spherical harmonics (see Binney and Tremaine (2008)) where only the $m = 0$ terms are included. The potential is then expressed as an expansion in Legendre polynomials. We divide the region that surrounds the disc into spherical shells and calculate the quantities

$$m_{l,i} = \sum_{n \in S_i} m_n P_l(\cos\theta_n), \tag{3.2}$$

where the sum is over the halo particles of mass m_n in the i'th shell (S_i), P_l are the Legendre polynomials, and (r, θ, ϕ) are spherical polar coordinates centred on the disc. The axisymmetric approximation to the potential is then

$$\Phi_h\left(r,\,\theta\right) = \sum_{l=0}^{\infty} A_l\left(r\right) P_l\left(\cos\theta\right) \tag{3.3}$$

where

$$A_l(r) = -G\left(\frac{1}{r^l}\int_0^r dr' r'^{l+2} m_l(r') + r^{l+1}\int_0^r dr' r'^{1-l} m_l(r')\right) \tag{3.4}$$

and m_l is given by Eq. (3.2) for sufficiently small radial bins.

3.3.4 Disc DFs

Armed with an axisymmetric approximation to the halo potential, we construct a self-consistent DF for the disc following the method outlined in Dubinski and Kuijken (1995). This DF is an analytic function of E, L_z, and E_z. By construction, the DF yields a density law for the disc which is, to a good approximation, given by

$$\rho_d\left(R,\,z\right) \simeq \frac{M_d}{4\pi R_d^2 z_d} e^{-R/R_d} \mathrm{sech}^2\left(z/z_d\right) T\left(R_t, \Delta_t\right) \tag{3.5}$$

where M_d, R_d, and z_d are the mass, radial scale length and vertical scale height of the disc and $R = \sqrt{r^2 - z^2}$. The truncation function T insures that the density falls rapidly to zero at a radius $R_t + \Delta_t$. The square of the radial velocity dispersion is chosen to be proportional to the surface density, that is, $\sigma_R = \sigma_{R0}\exp\left(-R/2R_d\right)$. The central velocity dispersion σ_{R0} controls, among other things, the Toomre Q parameter and thus the susceptibility of the disc to instabilities in the disc plane. The azimuthal velocity dispersion is calculated from the radial velocity dispersion through the epicycle approximation (for details see Binney and Tremaine, 2008) while the vertical velocity dispersion is adjusted to yield a constant scale height z_d. We stress that although the density law is written as a function of R and z, which are not integrals of motion, the underlying DF is a function of E, L_z, and E_z, which are integrals of motion to the extent that the epicycle approximation is valid and that the potential can be approximated by an axisymmetric function.

3.3.5 Rigid Disc Dynamics

During the disc growth phase, the disc mass is given by

$$M(a) = M_d \left(\frac{a - a_g}{a_l - a_g} \right) \ , \tag{3.6}$$

where a_g is the scale factor evaluated at z_g. The positions of the disc particles expand self-similarly in disc or body coordinates. That is, the comoving position of a disc particle in body coordinates is given by $\mathbf{s}_i(a) = b(a)\mathbf{s}_i(a_l)$ where $\mathbf{s}_i(a)$ is the comoving position of the i'th disc particle in the body frame

$$b(a) = b_g + (1 - b_g) \left(\frac{a - a_g}{a_l - a_g} \right) \ , \tag{3.7}$$

where $b_g = b(a_g)$, an we choose $b_g = 0.1$. The angular velocity of the disc is described by the vector $\boldsymbol{\omega} = (\omega_x, \omega_y, \omega_z)$ where ω_z corresponds to the spin of the disc about its symmetry axis. We assume that

$$\omega_z(a) = \omega_z(a_l) \left(\frac{M(a)}{M_d} \right)^{1/\alpha} b(a) \ , \tag{3.8}$$

which insures that the disc tracks the Tully-Fisher relation, $M_d \propto V_d^\alpha \propto (\omega_3 R_d)^\alpha$ (Torres-Flores et al., 2011). In this work we set $\alpha = 3.5$.

The orientation of the disc is described by its Euler angles. We follow the convention of Thornton and Marion (2008) and use ϕ, θ, and ψ where the matrix

$$\mathcal{R} = \mathcal{R}_z(\phi)\mathcal{R}_y(\theta)\mathcal{R}_z(\psi) \tag{3.9}$$

describes the transformation from the disc body frame to the simulation frame. Here $\mathcal{R}_i(\alpha)$ is the matrix for a rotation by angle α about the i'th axis. Physically, changes in ϕ and θ correspond to precession and nutation, respectively while ψ is a degenerate rotation about the disc's symmetry axis. The equations of motion for the Euler angles and angular velocity of the disc, which must account for the time-dependence of the disc's moment of inertia as well as the fact that GADGET-3 uses comoving coordinates, are derived in Appendix 3.6. These equations allow us to solve for the orientation of the disc under the influence of torque due to dark matter.

At the end of the growth phase, we initialize the disc with a DF that is recalculated using GALACTICS. As we will see, during the growth phase the motion of the disc involves a mix of precession and nutation. In general, a live disc is not able to support the sort of rapid nutation seen in the rigid disc, essentially because different parts of the disc respond to torques from the halo and the disc itself differently. We therefore initialize the live disc with an orientation and precessional motion given by a fixed-window moving average of the rigid disc coordinates.

3.3.6 Test-bed Simulation of an Isolated Galaxy

We test our method by growing a stellar disc in an isolated, flattened halo in a non-cosmological simulation. To initialize the flattened halo we first generate a particle realization of a truncated, spherically symmetric NFW halo (Navarro et al., 1997) whose density profile is given by

$$\rho(r) = \frac{v_h^2 a_h}{4\pi G} \frac{1}{r\left(r + a_h\right)^2} \tag{3.10}$$

with $a_h = 8\,\mathrm{kpc}$ and $v_h = 400\,\mathrm{km\,s^{-1}}$. The halo is truncated at a radius much larger than the radius of the disc. The z and v_z coordinates are then reduced by a factor of two and the system is evolved until it reaches approximate equilibrium. The result is an oblate halo with an axis ratio of ~ 0.8 and a symmetry axis that coincides with the z-axis of the simulation box. We next grow a rigid disc over a period of 1 Gyr to a final mass of $4.9 \times 10^{10}\,M_\odot$ and final radial and vertical scale lengths of $R_d = 2.5\,\mathrm{kpc}$ and $z_d = 200\,\mathrm{pc}$, respectively. The disc is grown at an incline of 30° relative to the symmetry plane of the halo. Doing so allows us to check the rigid body integration scheme for a case when the symmetry axes of the disc and halo are initially misaligned. At $t = 1\,\mathrm{Gyr}$ we replace the rigid disc with a live one and evolve the system for an additional 1 Gyr. In a separate simulation, we also follow the evolution of the rigid disc over the same time period, allowing us to compare the evolution of the live and rigid disc.

Fig. 3.1 shows the Euler angles and angular velocity components for the rigid and live discs as a function of time. The time-dependence of ω_x and ω_y is characterized by an interference pattern between short $\sim 125\,\mathrm{Myr}$ period nutations and a decaying long-period precessional motion. Note that θ and ϕ for the live disc track

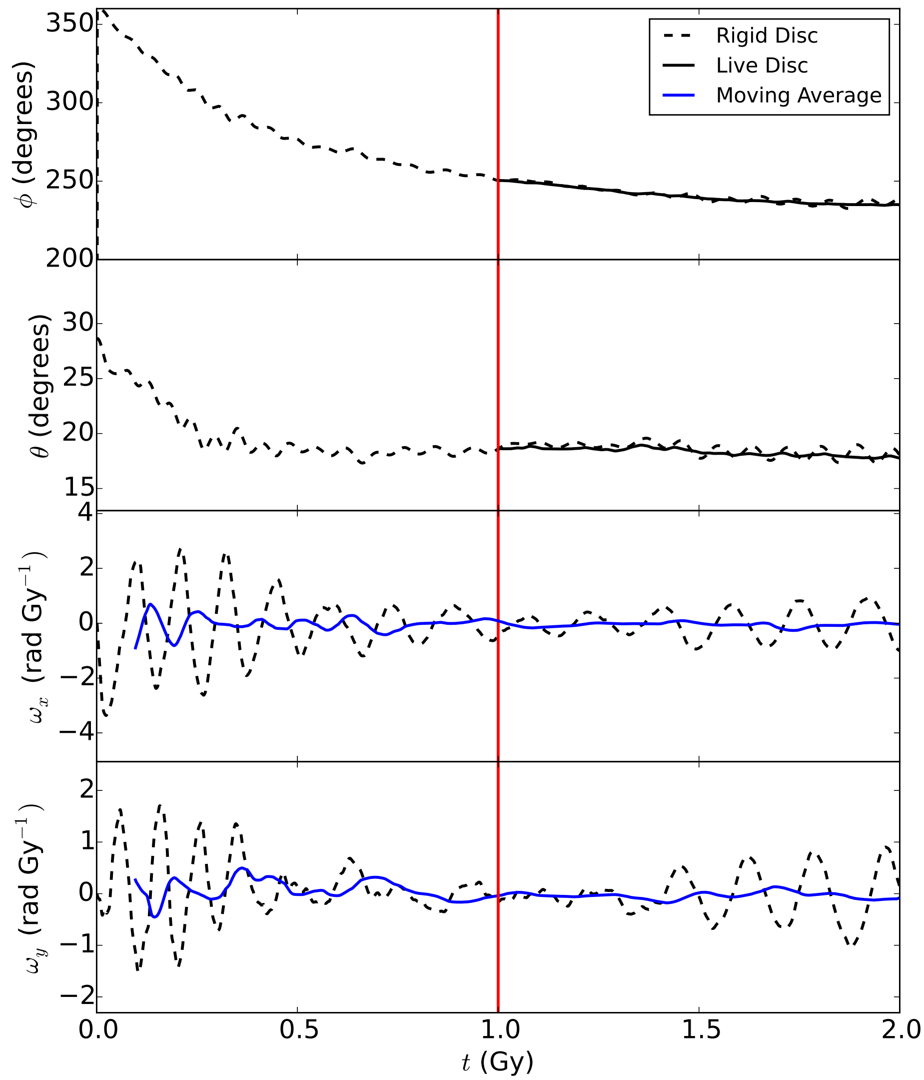

Figure 3.1: Kinematic variables for the rigid and live discs in an isolated, flattened halo as a function of time. The upper two panels show the Euler angles θ and ϕ for the rigid disc (dashed curves) and live disc (solid curves) where the live disc is introduced at $t = 1\,\mathrm{Gyr}$ (red vertical line). The bottom two panels show the x and y components of the angular velocity, as measured in the body coordinate system. In these two panels the solid curves show the $\delta t \sim 150\,\mathrm{My}$ moving average, which is used to initialize the live disc.

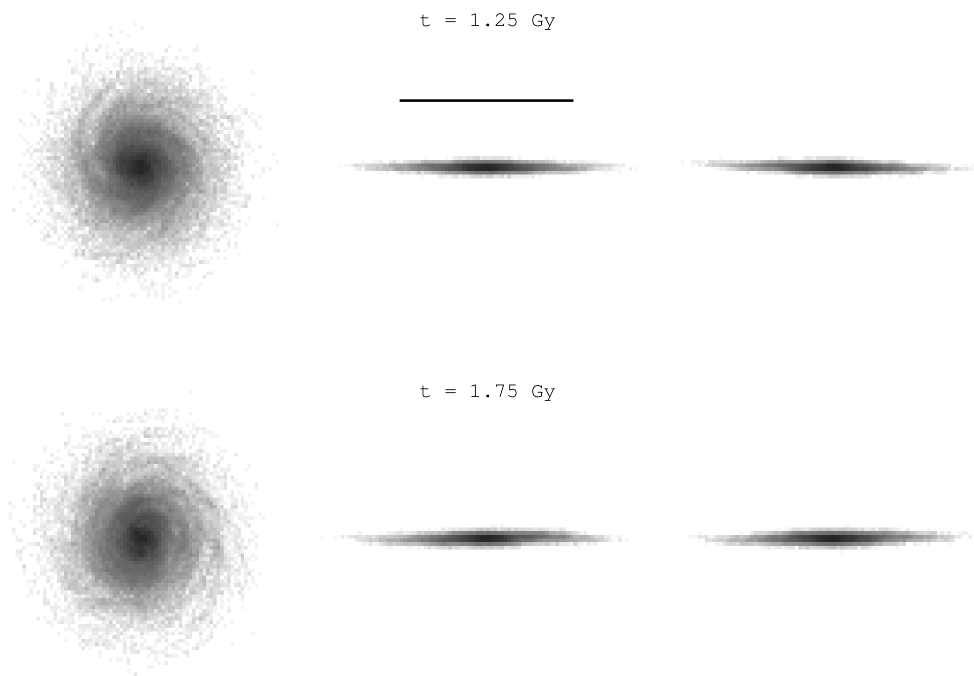

Figure 3.2: Face-on projections of the particle distribution for two snapshots of a live disc in a flattened halo. The solid line for scale is 25 kpc with a centre coincident with the disc's.

the corresponding values for the rigid disc for $t > 1\,\mathrm{Gyr}$. By initializing the live disc with the angular velocity of the rigid disc, we capture the (small) precessional motion of $\sim 10°\mathrm{Gyr}^{-1}$ between $t = 1\,\mathrm{Gyr}$ and $2\,\mathrm{Gyr}$. The disc settles into a preferred plane within the first 300 Myr that is intermediate between its initial symmetry plane and the initial symmetry plane of the halo. More precisely, the vector of the new minor axis is $\mathbf{c} = [-0.159, 0.146, 0.976]$ measured at 20 kpc, 12.5° from the original flattening axis.

Fig. 3.2 shows surface density maps for the disc at two snapshots. The disc develops a weak warp due to its interaction with the halo. The development of the warp is also evident in the surface density, vertical velocity dispersion, and scale

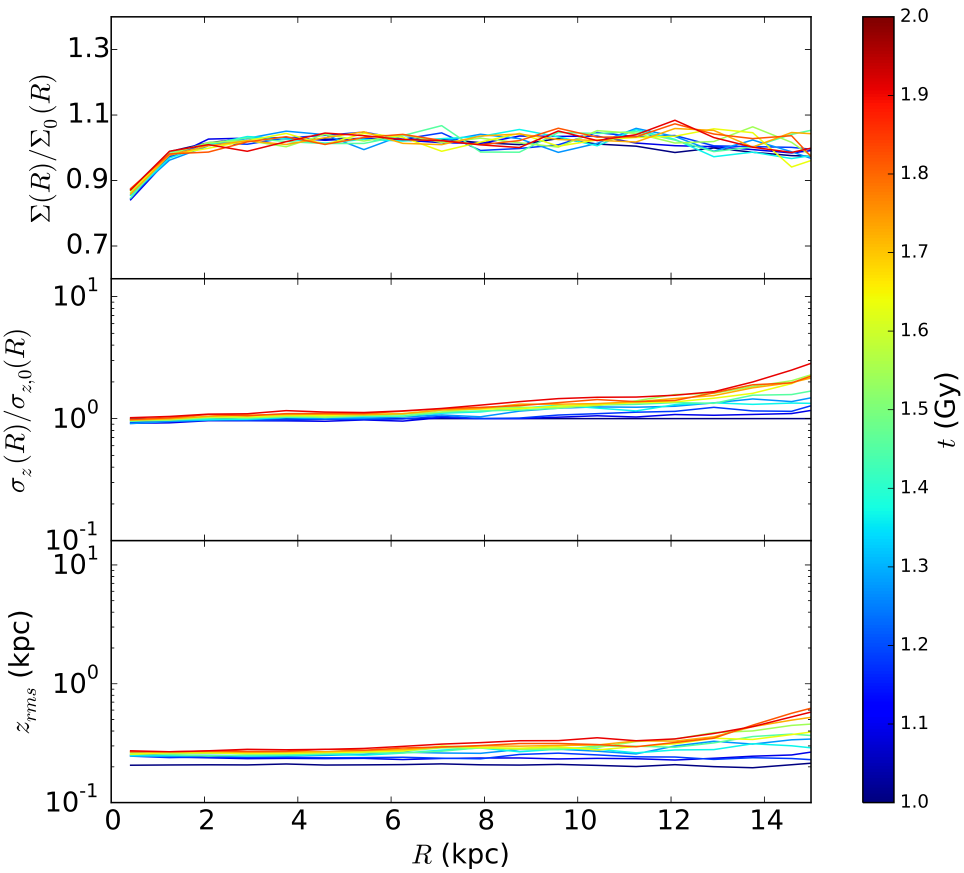

Figure 3.3: Surface density, vertical velocity dispersion, and scale height profiles as a function of Galactocentric radius R for 10 snapshots equally spaced in time. The top panel shows the surface density $\Sigma(R)$ divided by $\Sigma_0(R) = (M_d/2\pi R_d^2)\exp\left[-(R/R_d)\right]$ in order to highlight departures from a pure exponential disc. Likewise, in the middle panel, we show the ratio $\sigma_z(R)/\sigma_{z,0}(R)$ where $\sigma_{z,0} = \exp(-R/2R_d)$. The bottom panel shows the RMS z as a function of R.

height profiles shown in Fig. 3.3. We see that the surface density within $\sim 15\,\mathrm{kpc}$ or $6R_d$ is essentially unchanged while at larger radii, there are $10-20\%$ time-dependent fluctuations. The scale height $\langle z^2 \rangle^{1/2}$ increases with time and radius. At early times, the increase is most prominent beyond $\sim 15\,\mathrm{kpc}$ while at late times, the scale height increases more smoothly from the center to the edge of the disc.

3.4 Cosmological Simulations

We now use our method to insert a live disc with prescribed structural properties into a cosmological halo. In this section, we focus on disc dynamics while in the next, we consider the effect the disc has on the dark halo.

In Fig. 3.4 we show the kinematic variables for the rigid and live discs in the RD and LD simulations. The two simulations are identical prior to $z = 1$ $(a = 0.5)$ when the live disc is swapped in for the rigid one. The short period (300 Myr) oscillations in ω_1 and ω_2 are nutations. To initialize the live disc, we use the fixed-window moving average of ω_x and ω_y. By and large, the Euler angles of the rigid and live disc's track one another for $z < 1$, indicating that the rigid disc is a reasonable model for a live one, at least in terms of the disc's orientation.

In Fig. 3.5 we show the circular speed curves at $z = 1$ and $z = 0$ for our four simulations. We see that the disc in our model is submaximal. To be precise, we have $V_d/V_c \simeq 0.68$ at $R = 2.2R_d$ where V_d is the circular speed due to the disc and V_c is the total circular speed. In short, the contributions from the disc and halo to the centrifugal force are approximately equal at a radius where the disc contribution reaches its peak value. By comparison, a maximal disc is generally defined to have $V_d/V_c > 0.85$ (Sackett, 1997). If we use V_d/V_c at $2.2R_d$ as the defining characteristic

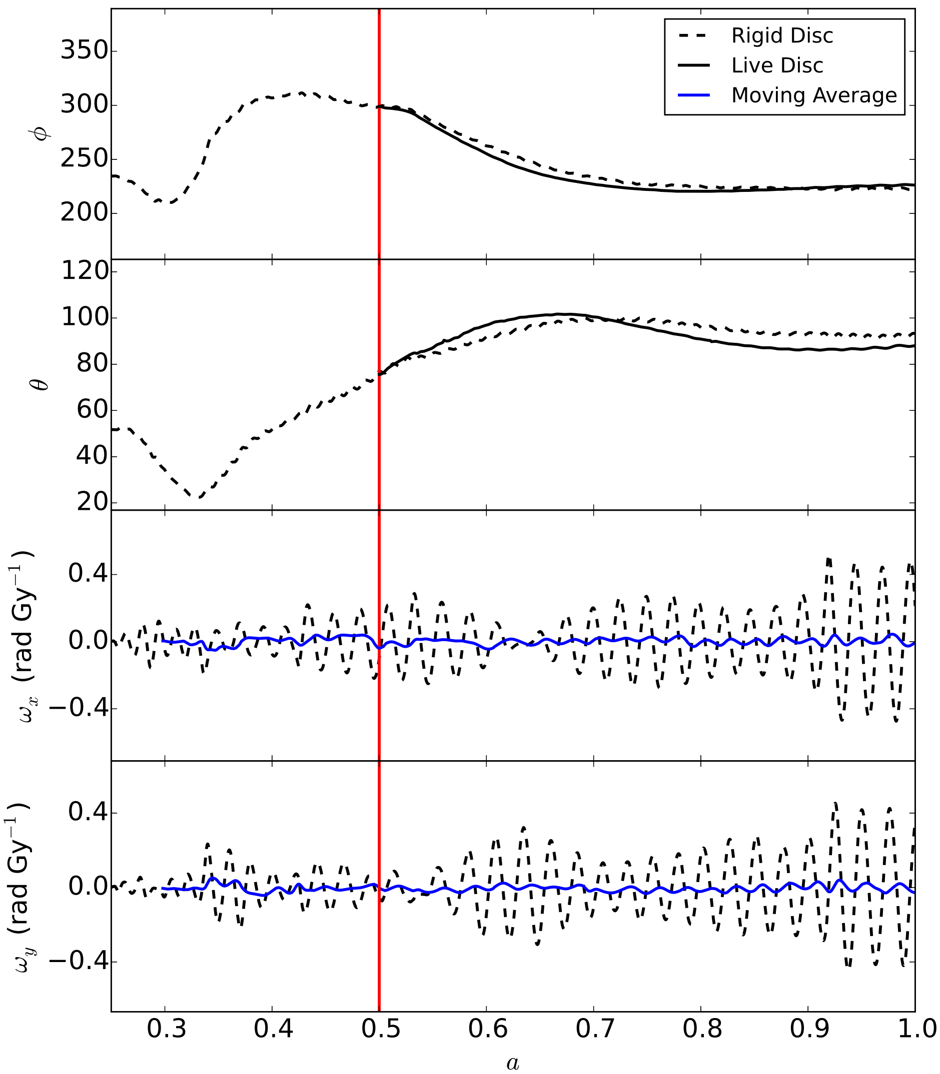

Figure 3.4: Kinematic variables for the rigid and live discs in our cosmological halo as a function of scale factor a. Line types are the same as in Fig. 3.1. The live disc is introduced at a redshift $z = 1$ when the scale factor is $a = 0.5$ (red vertical line). The blue line shows the $\delta a \sim 0.04$ moving average calculated by averaging the last 300 points in the disc integration routine.

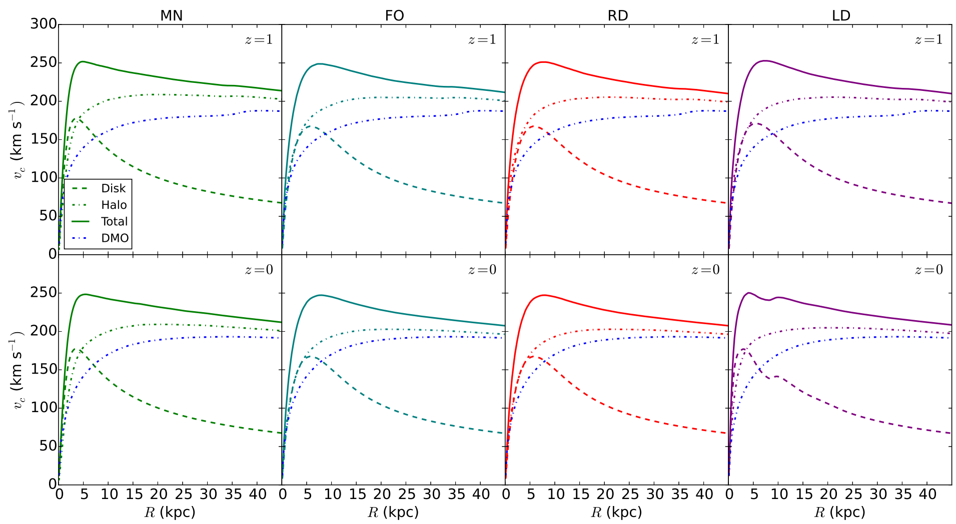

Figure 3.5: Circular speed curve decompositions at $z = 1$ (top row) and $z = 0$ (bottom row) for (from left to right) our MN, FO, RD, and LD simulations. Halo contributions are represented as dot-dashed lines, disc contributions are represented by dashed lines, and the total rotation curve is given by a solid line. For reference, we have included the circular speed curve for the DMO halo (dot-dashed curve).

of the model, then our simulations match up with the F-5 simulation of Yurin and Springel (2015), although our discs are slightly warmer, with a Toomre Q-parameter of 1.4 as compared with $Q \simeq 0.9$ for their discs and our discs are thinner (200 pc vs. 600 pc). We note that in a two-integral disc DF, Q and the disc thickness are linked whereas in a three-integral DF, they can be set independently. The method of Yurin and Springel (2014) can be extended to consider a three-integral DF, but these models were not considered in Yurin and Springel (2015). Moreover, their two-integral model, which imposes $\sigma_R = \sigma_z$, violates the epicycle approximation, leading to transient system behaviour at early times when disc bars first form.

The circular speed curves in Fig. 3.5 show little change exterior to $\sim 2R_d$ after z_l, thus providing another indication that the live disc was close equilibrium when it was swapped in for the rigid one. The formation of a bar is evident in the circular speed, and we can infer the bar contributes substantially inside $2.2R_d \simeq 8\,\mathrm{kpc}$. The halo contribution at $R = 2.2R_d$ is about 20% larger in the four disc runs than in the DMO one due to adiabatic contraction. Interestingly, the halo in the MN run shows somewhat more contraction than in the RD and LD runs. We note that in the MN run, the disc potential tracks the potential minimum of the halo whereas in the RD/LD case, the disc's position is determined from Newtonian dynamics. In general, the centre of the disc tracks the halo potential minimum so long as the potential changes slowly with time. However, during a major merger (and indeed, just such an event occurs at $z = 2$) there are rapid changes in the halo potential and the position of the disc, as determined by Newtonian dynamics, can differ significant from the minimum of the halo potential. Evidently, the *ad hoc* prescription of growing a disc at the halo's potential minimum may, in some cases, over-estimate the effect of adiabatic contraction.

3.4.1 Bar Formation

In Fig. 3.6 we show orthogonal projections of the disc density in our LD simulation at four epochs between $z = 1$ (lookback time of 7.9 Gyr) and the present epoch. During the first billion years of live disc evolution, the disc develops a bar and spiral structure. In addition, there is a warp in the outer disc extending several kiloparsecs above the midplane of the inner disc. By the present epoch, the bar has grown in length and intensified and the edge-on view shows the classic X-pattern.

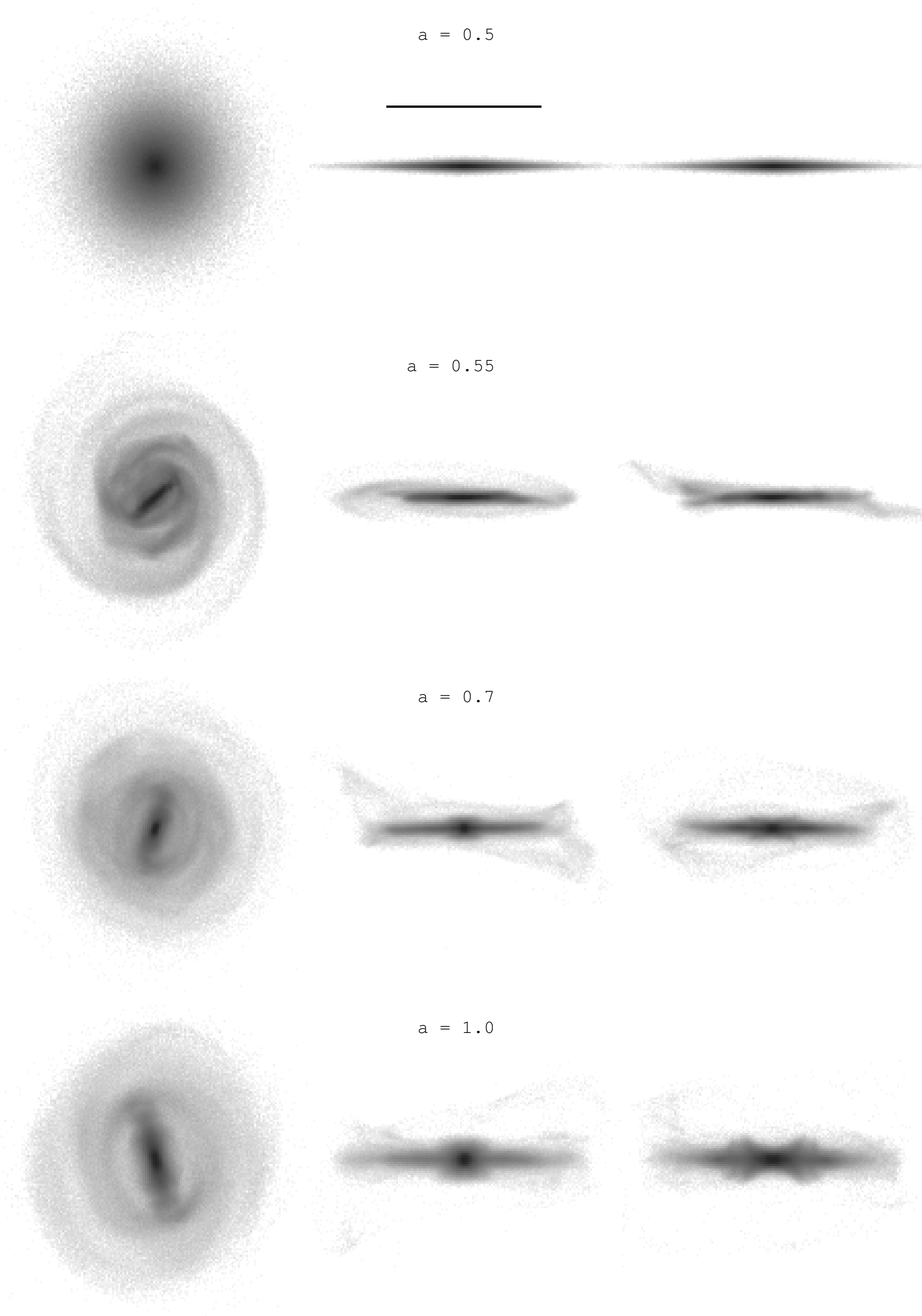

Figure 3.6: Projected density along three orthogonal directions for the live disc at four epochs between $z = 1$ and $z = 0$. The projections are presented in physical units. The solid line for scale is 37 kpc with a centre coincident with the disc's.

We consider the usual parameter bar strength $A_2 = |c_2|$ where

$$c_m = \frac{1}{M_S} \sum_{j \in S} m_j e^{im\phi_j} \ . \tag{3.11}$$

Here, S is some circularly-symmetric region of the disc (e.g., a circular annulus) and the sum is over all particles labeled by j and with mass m_j that are inside S. We find that A_2 for the inner $2R_d$ of the disc reaches 0.43 at $t = 6.7\,\mathrm{Gyr}$, decreases to 0.36 by $t = 9.2\,\mathrm{Gyr}$, presumably because the bar has buckled, and then increases to 0.47 by the present epoch. On the other hand, A_2 for the entire disc increases to 0.27, decreases to 0.23, and then increases to 0.28 for the same epochs. Note that the inner $2R_d$ of the disc contains 60% of the mass. Thus, the fact that $A_{2,2R_d}/A_{2,\mathrm{tot}} \simeq 0.6$ implies that most of the bar mass resides within the inner $2R_d$.

The bars in Yurin and Springel (2015) seem to be stronger then then ones in our simulations — they find $A_2 \simeq 0.6$ but use a non-standard formula for A_2. Moreover, their bars appear to extend across most of the disc. In terms of disc dynamics, the main difference between our simulations is the fact that we use a three-integral DF for the disc whereas they use a two-integral DF. In the latter, the velocity dispersion in the radial and vertical directions are the same. Thus, the radial dispersion, which fixes the Toomre Q parameter, also determines the thickness of the disc. We note that their initial discs are a factor of two or three thicker than ours. We speculate that the bars that develop in these thick discs are less susceptible to buckling and therefore able to grow stronger and longer. These ideas will be investigated in more detail in a future publication.

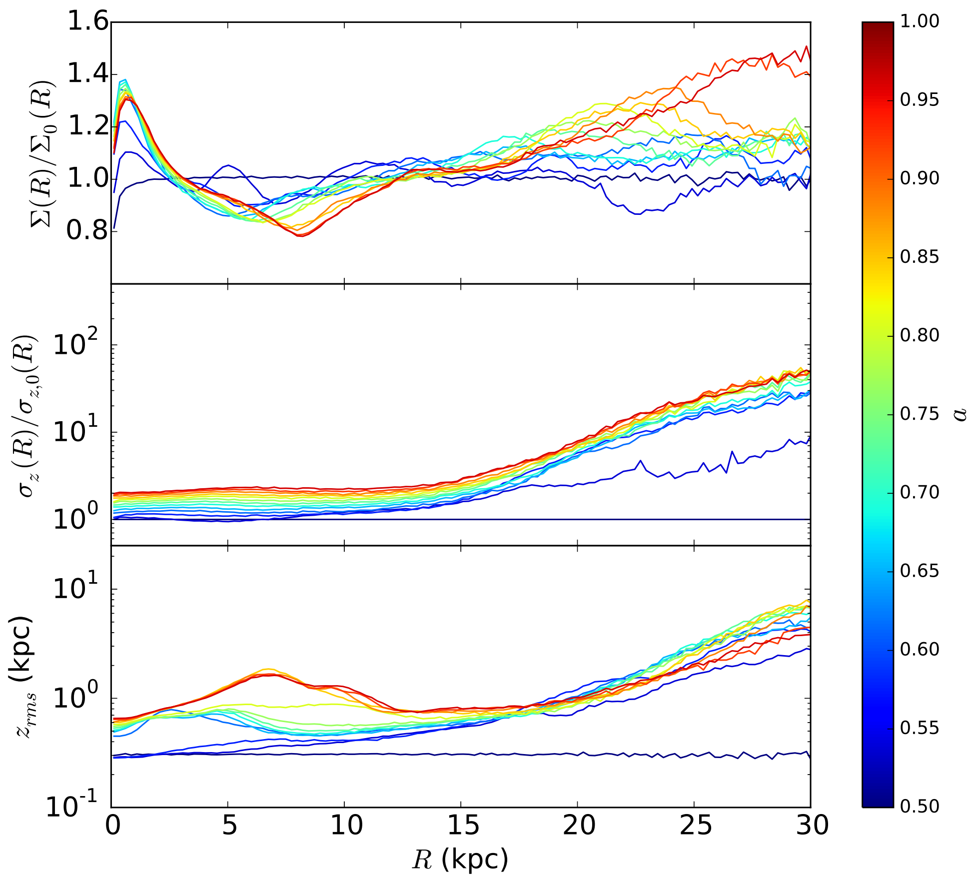

Figure 3.7: Surface density, vertical velocity dispersion, and scale height profiles of the live disc for 10 snapshots equally spaced in scale factor a between $a = 0.5$ ($z = 1$) and $a = 1$ (present epoch). Panels are the same as in Fig. 3.3.

3.4.2 Kicked-up Stars and Disc Heating

The outer part of the disc suffers considerable disruption and warping presumably through its interaction with the main halo or substructure. The right-most panel of the $a = 0.55$ snapshot in Fig. 3.6, for example, shows a classic integral-sign warp. The other snapshots show that a significant number of disc particles have orbits that now take them to high galactic latitudes.

The impressions one has from the density projections are borne out in Fig. 3.7 where we show the surface density and scale height profiles at different times. Bar formation redistributes mass in the disc leaving a deficit (relative to the initial exponential disk) between 5 and 15 kpc. The disc becomes thicker and its vertical velocity dispersion increases though a combination of disc-halo interactions and the effects of the bar and spiral structure (Gauthier et al., 2006; Dubinski et al., 2008; Kazantzidis et al., 2008).

A striking feature of the simulations are the streams of disc stars well above the disc plane. These stars may represent an example of a kicked-up disc, which has been seen in other N-body simulations (Purcell et al., 2010; McCarthy et al., 2012) and invoked to explain kinematic and spectroscopic observations of M31 (Dorman et al., 2013) and the Monoceros Ring (e.g. Newberg et al., 2002; Ibata et al., 2003). The idea is that interactions between the disc and both satellite galaxies and halo substructure liberate stars from the disc, launching them to regions of the galaxy normally associated with the stellar halo. Our live disc simulation corroborates this hypothesis and is in broad agreement with previous numerical work.

Finally, we note that the $a = 1$ panel of Fig. 3.6 shows a relatively thin, stream-like structure, above the disc which is qualitatively similar to the Anti-centre Stream (ACS, Grillmair, 2006). While the ACS is believed to be due to the disruption of a globular cluster (e.g. Grillmair, 2006), Fig. 3.6 suggests that perturbations to the disc can create similar features. Intriguingly, (de Boer et al., 2017) recently found that the ACS is rotating in the same sense as the Milky Way disc.

3.5 Halo Substructure in the Presence of a Disc

In this section, we consider the effect of a disc on a halo's structural properties such as its spherically-averaged density profile, its shape, and its subhalo population. An examination of the DMO simulation shows that the halo we have selected builds up through a series of mergers and accretion events, but that by $z = 1$ it has settled into a relatively relaxed state with an NFW profile that evolves very little between $z = 1$ and $z = 0$ within the inner 100 kpc. Our sequence of simulations, (MN, FO, RD, and LD) allow us to tease out the effects of different disc insertion methods. The MN simulation, for example, pins the centre of the disc to the minimum of the halo potential, whereas the other simulations dynamically evolve the position and velocity of the disc potential via Newtonian mechanics. The MN and FO simulations both assume that the orientation of the disc potential during the growth phase is fixed whereas RD and LD solve for the orientation using rigid body dynamics.

3.5.1 Global Properties of the Halo

In Fig. 3.8 we show the ratio of the spherically-averaged density profile in the four disc runs to that from the DMO run. At $z = 1$ the haloes in the FO, RD, and MN runs show evidence for adiabatic contraction with the density in the inner $\sim 30\,\mathrm{kpc}$ increasing by a factor of $1.2 - 2.1$. The effect is strongest in the MN simulation, which is to be expected since the halo in that case always sees the disc potential at the minimum of its potential. Of course, this prescription is unphysical. In general, and especially during a major merger, the disc and halo potential minimum will not necessarily coincide.

Between $z = 1$ and $z = 0$, the mass of the disc is constant. Adiabatic contraction

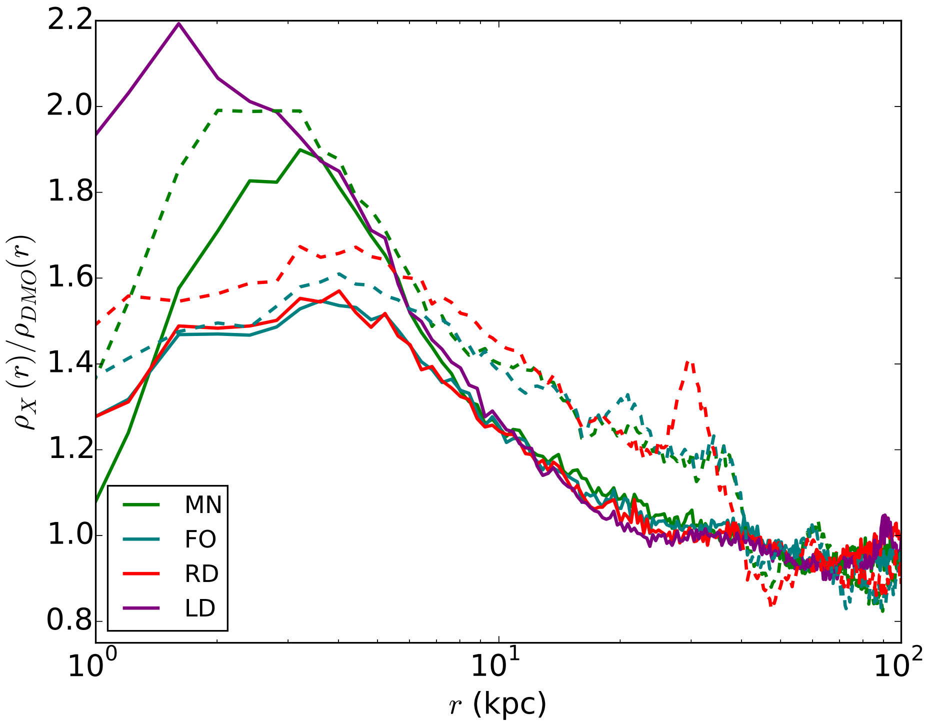

Figure 3.8: The ratio of halo density to the DMO simulation for MN (green), FO (teal), RD (red), and LD (purple) at $z = 1$ (dashed) and $z = 0$ (solid). The presence of the disc significantly increases the central concentration of the halo.

ceases but the halo still responds to the time-varying disc potential. Interestingly, at intermediate radii (between $\sim 10 - 40\,\mathrm{kpc}$) the density profile of the halo settles back to a state close to that found in the DMO run. Perhaps most striking is the fact that the halo in the LD run becomes more centrally concentrated than the halo in any of the other cases. One possible explanation is that dynamical friction from the disc drags dark matter subhaloes toward the centre of the halo where they are tidally disrupted.

In Fig. 3.9 we show the minor-to-major (c_r/a_r) and intermediate-to-major (b_r/a_r) axis ratios as a function of radius for both the $z = 1$ and $z = 0$ snapshots. The axis

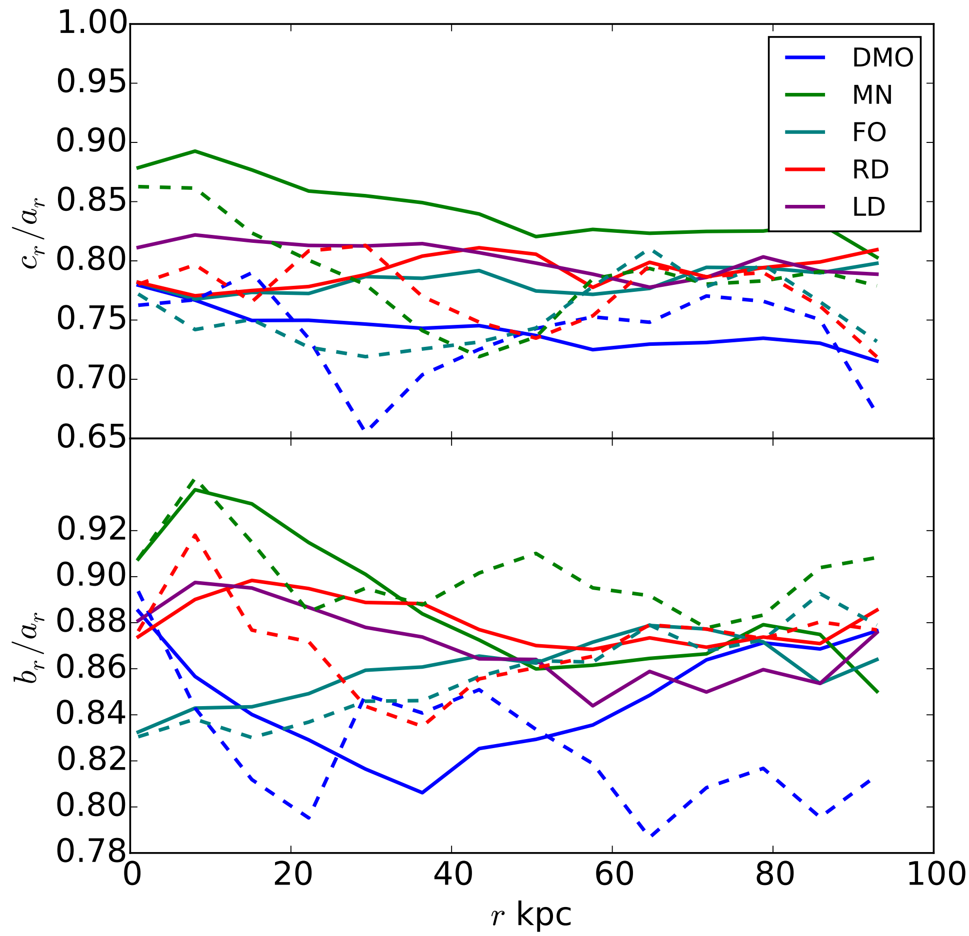

Figure 3.9: Axis ratios as a function of radius. Shown are the minor-to-major axis ratio (top panel) and the intermediate-to-major axis ratio (bottom panel) at $z = 1$ (dashed curves) and $z = 0$ (solid curves). Blue corresponds to DMO, green to MN, teal to FO, red to RD, and purple to LD.

ratios are calculated by diagonalizing the moment of inertia tensor in linearly-spaced radial shells. The DMO halo is triaxial with $c_r/a_r \simeq 0.75$ and $b_r/a_r \simeq 0.85$. Note that the axis ratio profiles are smoother at $z = 0$ than at $z = 1$, which supports the observation that the halo has settled into a more relaxed state over the past 7 or so billion years. In general, discs tend to make haloes more spherical, a result that has been known for some time from both collisionless and hydrodynamical simulations (e.g. Dubinski, 1994; Zemp et al., 2012).

Evidently, the MN halo is rounder, especially in the inner part, than the FO halo. Recall that the main difference between these two cases is that the MN disc is pinned to the potential minimum of the halo. It is perhaps not surprising then that, as with adiabatic contraction, it has a stronger effect on the halo's shape. We also note that the axis ratio profiles for the RD and LD simulations are fairly similar.

3.5.2 Subhalo Populations

We now turn our attention to halo substructure. We identify subhaloes and determine their positions and masses using ROCKSTAR (Behroozi et al., 2013), which employs a friends-of-friends algorithm in six phase space dimensions. We consider only those subhaloes with mass m_s between $m_{\rm min} = 10^{7.5}\,M_\odot$ and $m_{\rm max} = 10^{10.5}\,M_\odot$. Subhaloes at the lower end of this range are marginally resolved with ~ 100 particles, above which the subhalo mass can be trusted (e.g. Onions et al., 2012), while those at the upper end contain $\sim 3\%$ of the halo's virial mass.

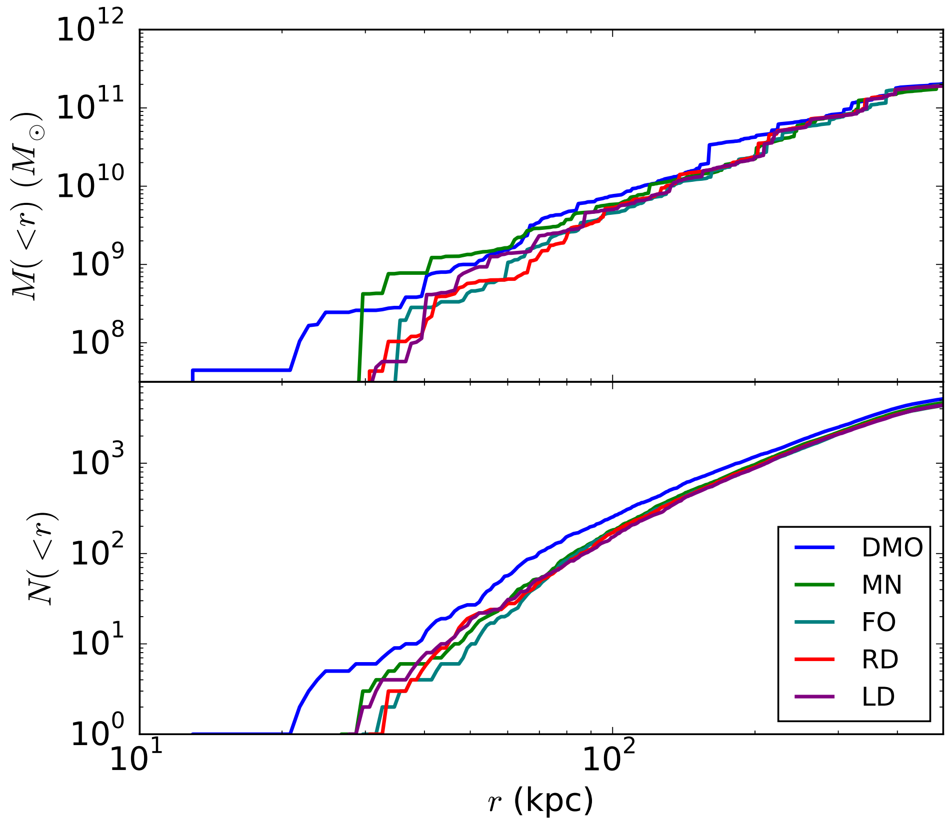

Figure 3.10: Cumulative mass in subhaloes inside a radius r (upper panel) and cumulative number of subhaloes (lower panel). We consider only subhaloes within 500 kpc of the halo centre and with a mass above $10^{7.5} M_\odot$. The curves are blue (DMO), green (MN), teal (FO), red (RD), and purple (LD).

In Fig. 3.10 we show the cumulative mass in subhaloes as a function of Galactocentric radius:

$$M_s\,(<r) = \int_0^r dr \int_{m_{\min}}^{m_{\max}} dm_s\, m_s\, \frac{d^2N}{dm_s\, dr} \tag{3.12}$$

We also show the cumulative number of subhaloes. In general, the presence of a disc depletes substructure inside about 30 kpc but leaves the outer substructures

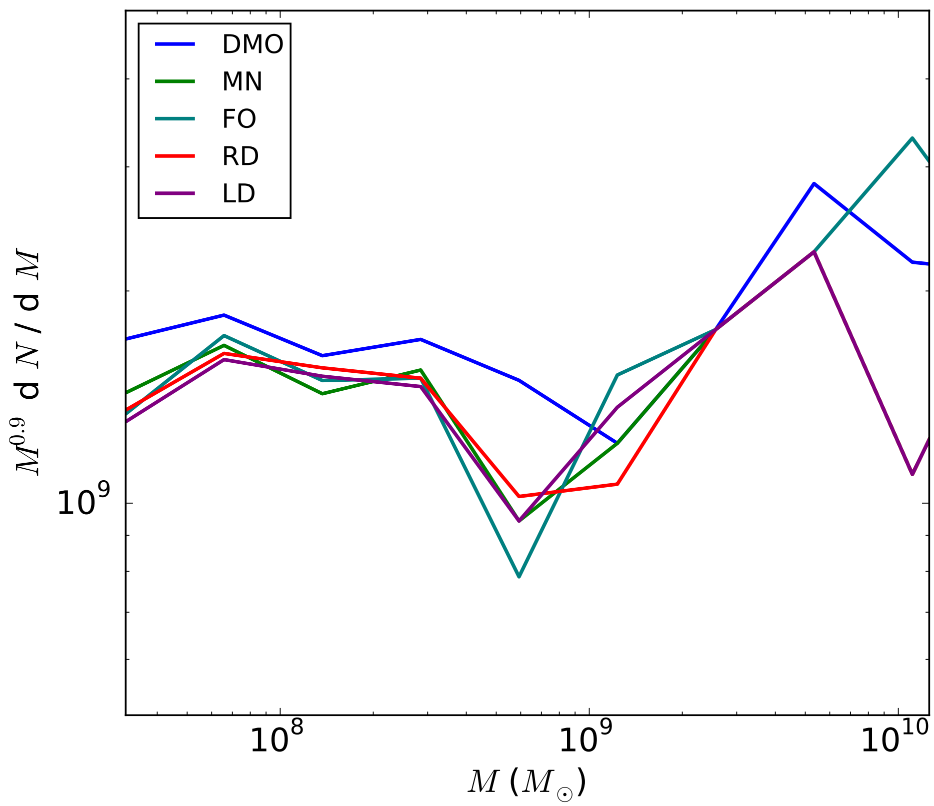

Figure 3.11: Differential mass distribution multiplied by $M^{0.9}$ for subhaloes above $10^{7.5} M_\odot$. We make an outer radius cut at 500 kpc. The curves are blue (DMO), green (MN), teal (FO), red (RD), and purple (LD).

unaffected.

We next consider the differential mass distribution as a function of subhalo mass. Recall that for a pure dark matter halo, $dN/d\ln(m_s) \propto m_s^{-p}$ where $p \simeq 0.9$ (e.g. Gao et al., 2004). In Fig. 3.11, we therefore show the quantity $m^{0.9}\, dN/d\ln(m_s)$ in order to enhance the differences between the different disc runs. We see that the halo population between $m_s \simeq m_{\rm min}$ and $m_s \simeq 10^9\, M_\odot$ is depleted, but only by about $20 - 30\,\%$. Taken together, Fig. 3.10 and Fig. 3.11 imply that the main depletion of the subhaloes occurs within the inner regions of the parent halo, in agreement

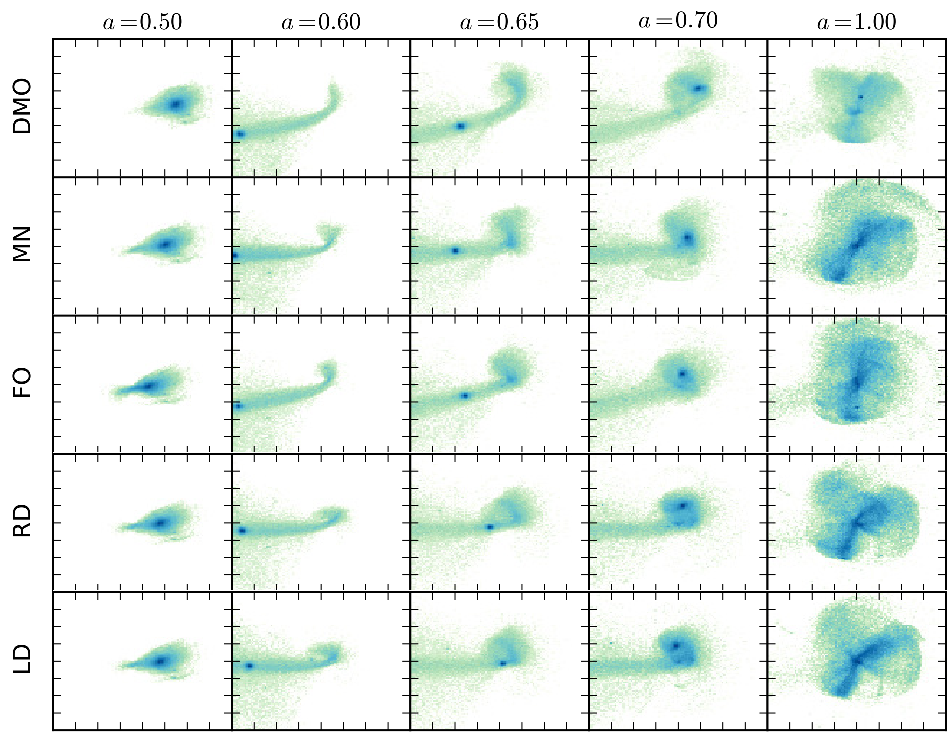

Figure 3.12: X-Y projections for a selected Sagittarius-like dwarf galaxy. The rows from top to bottom are no disc, a fixed Miyamoto-Nagai disc, a rigid disc, and a live disc. The scale factors in columns from left to right are 0.5, 0.55, 0.6, 0.65, and 0.7. The frame edges are 295 kpc on each side.

with D'Onghia et al. (2010); Sawala et al. (2017); Garrison-Kimmel et al. (2017). That said, the depletion of subhaloes seems rather insensitive to the disc insertion method, although we caution that only a single halo was used. Our results, being mainly in agreement with previous work, should still be viewed with caution due the consideration of a single host halo.

3.5.3 Case Study: A Sagittarius-like Dwarf

Observations of the Milky Way's dwarf galaxies and associated tidal streams provide a potentially powerful probe of the Galactic potential and thus the Galaxy's dark halo. One of the best-studied examples is the Sagittarius dwarf Ibata et al. (1994). Fortunately, our simulation has a satellite galaxy with similar properties, namely, a dark matter mass of $1.8 \times 10^{10}\, M_{\odot}$ at $z = 1.0$ and an orbit that takes it close to the disc. We identify this object in the five simulations using the ROCKSTAR halo catalogues. We then gather a list of IDs for all the bound particles at an early time before the dwarf is disrupted and follow these same particles in later snapshots using a binary search tree look-up scheme. In Fig. 3.12 we show the evolution of this subhalo between redshift $z_l = 1$ and $z = 0$. The first row shows the baseline evolution in our DMO simulation. The dwarf develops leading and trailing tidal tails during the first few billion years. By the present epoch, the tidal debris has dispersed throughout the halo.

The next four rows show the same satellite in our disc simulations. Perhaps the most noticeable result is that there are stronger features in the tidal debris at the present epoch once a disc is included. The detailed morphology of the tidal debris is certainly different from one disc simulation to the next. By eye, debris in MN and FO look somewhat similar as does the debris in RD and LD. Perhaps the most noticeable result is that the tidal debris extends to larger galactocentric radii when a disc is included. The detailed morphology of the tidal debris clearly depends on the disc insertion method. By eye, tidal debris appears more isotropic in MN and FO than in RD and LD. The implication is that fixed potentials are more efficient at disrupting massive satellites than a potential which can respond to the satellite's presence. However, we have only a single example of massive satellite disruption, and we caution that more examples of this behaviour are needed to test this hypothesis.

3.6 Conclusions

Simulations in which a stellar disc is inserted “by hand” into a cosmological N-body halo provide a compromise between simulations of isolated disc-halo systems and cosmological simulations that include gasdynamics and star formation. Our method builds on the scheme used by Berentzen and Shlosman (2006); DeBuhr et al. (2012) and refined by Yurin and Springel (2015). The basic idea is to introduce, at a redshift z_g, a rigid disc with zero mass into a halo within a cosmological zoom-in simulation. Between z_g and z_l the disc is treated as an external potential with a mass and size that increase adiabatically to their present day values. At z_l, the rigid disc is replaced by an N-body one and the simulation proceeds to the present epoch with live disc and halo particles.

Our method improves upon previous ones in two important ways. First, during the growth phase ($z_g > z > z_l$) the position and orientation of the disc evolve according to the standard equations of rigid-body dynamics. Thus, the disc in our scheme receives its linear and angular momentum with the halo in a self-consistent fashion and is therefore able to move, precess, and nutate due to torques from the halo. While previous methods introduced aspects of rigid-body dynamics during the growth phase none appear to have implemented the full dynamical equations have done here (D’Onghia et al., 2010; DeBuhr et al., 2012; Yurin and Springel, 2015).

Our sequence MN, FO, RD, and LD of simulations highlights where the details of the disc insertion scheme are important and where they are not. For example, schemes in which the disc tracks the minimum of the halo potential tend to overestimate the effects of adiabatic contraction. On the other hand, the effect of the depletion of halo substructure seems to be rather insensitive to the details of how the disc is introduced into the simulation.

Disc insertion schemes such as the one introduced in this paper, provide an attractive arena for studies of galactic dynamics. In particular, they allow one to study the interaction between a stellar disc and a realistic dark halo with computationally inexpensive simulations while maintaining some level of control over the structural parameters of the disc. We fully intend to leverage these advantages in future work.

Appendix A: Euler's Equations in Comoving Coordinates

The time-evolution of the angular momentum vector $\mathbf{L}$ of a rigid body acted upon by a torque $\boldsymbol{\tau}$ is given by

$$\left(\frac{d\mathbf{L}}{dt}\right)_f = \left(\frac{d\mathbf{L}}{dt}\right)_b + \boldsymbol{\omega} \times \mathbf{L} = \boldsymbol{\tau} \tag{3.13}$$

where the subscripts f and b denote the frame of the simulation box and the body frame, respectively. In physical coordinates, $\mathbf{L} = \mathbf{r} \times \mathbf{p}$. Alternatively, we can write $\mathbf{L} = \mathbf{s} \times \mathbf{q}$ where $\mathbf{s} = a^{-1}\mathbf{r}$ refer to comoving coordinates and $\mathbf{q} = a^2\dot{\mathbf{s}}$ is the conjugate momentum to $\mathbf{s}$ (see Quinn et al. (1997)).

For a rigid body, the components of the angular momentum are given by $L_i = I_{ij}\omega_j$ where i, j run over x, y, z and there is an implied sum over j. Since GADGET-3 uses comoving coordinates, we write $I_{ij} = a^2 J_{ij}$ where J is the moment of inertia tensor written in terms of the comoving coordinates, $\mathbf{s}$, rather than the physical coordinates, $\mathbf{r}$. For convenience, we define a "comoving" angular velocity $\boldsymbol{\varpi} = a^{-2}\boldsymbol{\omega}$. We then have $L_i = J_{ij}\varpi_j$. Note that because of the symmetry of our disc, the moment of inertia tensor is diagonal with $J_{xx} = J_{yy} = J_{zz} \equiv J/2$. The equations of motion for the Euler angles and the disc angular velocity are then given by the standard Euler equations of rigid body dynamics, modified to account for the time-dependence of the disc's moment of inertia:

$$\frac{d\phi}{dt} = a^{-2} \sin^{-1}\theta \left(\varpi_x \sin(\psi) + \varpi_y \cos(\psi)\right) \ , \tag{3.14}$$

$$\frac{d\theta}{dt} = a^{-2} \left(\varpi_1 \cos(\psi) - \varpi_y \sin(\psi)\right) \ , \tag{3.15}$$

$$J\frac{\varpi_x}{dt} + \varpi_x \frac{dJ}{dt} + J\varpi_y\varpi_z = \tau_x \ , \tag{3.16}$$

and

$$\frac{\varpi_y}{dt} + \varpi_y \frac{dJ}{dt} - J\varpi_x\varpi_z = \tau_y \ . \tag{3.17}$$

We have omitted the equations for ψ (rotations in the body frame about the symmetry axis) and ϖ_z since these are determined directly from Eq. 3.8.

Bibliography

Behroozi, P. S., Wechsler, R. H., and Wu, H.-Y. (2013). The ROCKSTAR Phase-space Temporal Halo Finder and the Velocity Offsets of Cluster Cores. *ApJ*, 762:109.

Berentzen, I. and Shlosman, I. (2006). Growing Live Disks within Cosmologically Assembling Asymmetric Halos: Washing Out the Halo Prolateness. *ApJ*, 648:807–819.

Binney, J. and Tremaine, S. (2008). *Galactic Dynamics: Second Edition*. Princeton University Press.

de Boer, T. J. L., Belokurov, V., and Koposov, S. E. (2017). The fall of the Northern Unicorn: Tangential motions in the Galactic Anti-centre with SDSS and Gaia. *ArXiv e-prints*.

DeBuhr, J., Ma, C.-P., and White, S. D. M. (2012). Stellar discs in Aquarius dark matter haloes. *MNRAS*, 426:983–999.

D'Onghia, E., Springel, V., Hernquist, L., and Keres, D. (2010). Substructure Depletion in the Milky Way Halo by the Disk. *ApJ*, 709:1138–1147.

Dorman, C. E., Widrow, L. M., Guhathakurta, P., Seth, A. C., Foreman-Mackey, D., Bell, E. F., Dalcanton, J. J., Gilbert, K. M., Skillman, E. D., and Williams,

B. F. (2013). A New Approach to Detailed Structural Decomposition from the SPLASH and PHAT Surveys: Kicked-up Disk Stars in the Andromeda Galaxy? *ApJ*, 779:103.

Dubinski, J. (1994). The effect of dissipation on the shapes of dark halos. *ApJ*, 431:617–624.

Dubinski, J., Gauthier, J.-R., Widrow, L., and Nickerson, S. (2008). Spiral and Bar Instabilities Provoked by Dark Matter Satellites. In Funes, J. G. and Corsini, E. M., editors, *Formation and Evolution of Galaxy Disks*, volume 396 of *Astronomical Society of the Pacific Conference Series*, page 321.

Dubinski, J. and Kuijken, K. (1995). The settling of warped disks in oblate dark halos. *ApJ*, 442:492–503.

Font, A. S., Navarro, J. F., Stadel, J., and Quinn, T. (2001). Halo Substructure and Disk Heating in a Λ Cold Dark Matter Universe. *ApJ*, 563:L1–L4.

Gao, L., White, S. D. M., Jenkins, A., Stoehr, F., and Springel, V. (2004). The subhalo populations of ΛCDM dark haloes. *MNRAS*, 355:819–834.

Garrison-Kimmel, S., Wetzel, A. R., Bullock, J. S., Hopkins, P. F., Boylan-Kolchin, M., Faucher-Giguere, C.-A., Keres, D., Quataert, E., Sanderson, R. E., Graus, A. S., and Kelley, T. (2017). Not so lumpy after all: modeling the depletion of dark matter subhalos by Milky Way-like galaxies. *ArXiv e-prints*.

Gauthier, J.-R., Dubinski, J., and Widrow, L. M. (2006). Substructure around M31: Evolution and Effects. *ApJ*, 653:1180–1193.

Gómez, F. A., White, S. D. M., Grand, R. J. J., Marinacci, F., Springel, V., and Pakmor, R. (2016). Warps and waves in fully cosmological models of galactic discs. *ArXiv e-prints*.

Grillmair, C. J. (2006). Substructure in Tidal Streams: Tributaries in the Anticenter Stream. *ApJ*, 651:L29–L32.

Hahn, O. and Abel, T. (2013). MUSIC: MUlti-Scale Initial Conditions. Astrophysics Source Code Library.

Hu, S. and Sijacki, D. (2016). Stellar spiral structures in triaxial dark matter haloes. *MNRAS*, 461:2789–2808.

Ibata, R. A., Gilmore, G., and Irwin, M. J. (1994). A dwarf satellite galaxy in Sagittarius. *Nature*, 370:194–196.

Ibata, R. A., Irwin, M. J., Lewis, G. F., Ferguson, A. M. N., and Tanvir, N. (2003). One ring to encompass them all: a giant stellar structure that surrounds the Galaxy. *MNRAS*, 340:L21–L27.

Katz, N., Quinn, T., Bertschinger, E., and Gelb, J. M. (1994). Formation of Quasars at High Redshift. *MNRAS*, 270:L71.

Katz, N., Weinberg, D. H., and Hernquist, L. (1996). Cosmological Simulations with TreeSPH. *ApJS*, 105:19.

Kazantzidis, S., Bullock, J. S., Zentner, A. R., Kravtsov, A. V., and Moustakas, L. A. (2008). Cold Dark Matter Substructure and Galactic Disks. I. Morphological Signatures of Hierarchical Satellite Accretion. *ApJ*, 688:254–276.

Klypin, A., Kravtsov, A. V., Valenzuela, O., and Prada, F. (1999). Where Are the Missing Galactic Satellites? *ApJ*, 522:82–92.

Kuijken, K. and Gilmore, G. (1989). The mass distribution in the galactic disc. I - A technique to determine the integral surface mass density of the disc near the sun. *MNRAS*, 239:571–603.

Laporte, C. F. P., Gómez, F. A., Besla, G., Johnston, K. V., and Garavito-Camargo, N. (2016). Response of the Milky Way's disc to the Large Magellanic Cloud in a first infall scenario. *ArXiv e-prints*.

McCarthy, I. G., Font, A. S., Crain, R. A., Deason, A. J., Schaye, J., and Theuns, T. (2012). Global structure and kinematics of stellar haloes in cosmological hydrodynamic simulations. *MNRAS*, 420:2245–2262.

Miyamoto, M. and Nagai, R. (1975). Three-dimensional models for the distribution of mass in galaxies. *PASJ*, 27:533–543.

Moore, B., Ghigna, S., Governato, F., Lake, G., Quinn, T., Stadel, J., and Tozzi, P. (1999). Dark Matter Substructure within Galactic Halos. *ApJ*, 524:L19–L22.

Navarro, J. F., Frenk, C. S., and White, S. D. M. (1994). Accretion of Satellite Galaxies and the Density of the Universe. *MNRAS*, 267:L1.

Navarro, J. F., Frenk, C. S., and White, S. D. M. (1997). A Universal Density Profile from Hierarchical Clustering. *ApJ*, 490:493–508.

Newberg, H. J., Yanny, B., Rockosi, C., Grebel, E. K., Rix, H.-W., Brinkmann, J., Csabai, I., Hennessy, G., Hindsley, R. B., Ibata, R., Ivezić, Z., Lamb, D., Nash,

E. T., Odenkirchen, M., Rave, H. A., Schneider, D. P., Smith, J. A., Stolte, A., and York, D. G. (2002). The Ghost of Sagittarius and Lumps in the Halo of the Milky Way. *ApJ*, 569:245–274.

Oñorbe, J., Garrison-Kimmel, S., Maller, A. H., Bullock, J. S., Rocha, M., and Hahn, O. (2014). How to zoom: bias, contamination and Lagrange volumes in multimass cosmological simulations. *MNRAS*, 437:1894–1908.

Onions, J., Knebe, A., Pearce, F. R., Muldrew, S. I., Lux, H., Knollmann, S. R., Ascasibar, Y., Behroozi, P., Elahi, P., Han, J., Maciejewski, M., Merchán, M. E., Neyrinck, M., Ruiz, A. N., Sgró, M. A., Springel, V., and Tweed, D. (2012). Subhaloes going Notts: the subhalo-finder comparison project. *MNRAS*, 423:1200–1214.

Pakmor, R. and Springel, V. (2013). Simulations of magnetic fields in isolated disc galaxies. *MNRAS*, 432:176–193.

Planck Collaboration, Ade, P. A. R., Aghanim, N., Armitage-Caplan, C., Arnaud, M., Ashdown, M., Atrio-Barandela, F., Aumont, J., Baccigalupi, C., Banday, A. J., and et al. (2014). Planck 2013 results. XVI. Cosmological parameters. *A&A*, 571:A16.

Power, C., Navarro, J. F., Jenkins, A., Frenk, C. S., White, S. D. M., Springel, V., Stadel, J., and Quinn, T. (2003). The inner structure of ΛCDM haloes - I. A numerical convergence study. *MNRAS*, 338:14–34.

Purcell, C. W., Bullock, J. S., and Kazantzidis, S. (2010). Heated disc stars in the stellar halo. *MNRAS*, 404:1711–1718.

Purcell, C. W., Bullock, J. S., Tollerud, E. J., Rocha, M., and Chakrabarti, S. (2011). The Sagittarius impact as an architect of spirality and outer rings in the Milky Way. *Nature*, 477:301–303.

Quinn, T., Katz, N., Stadel, J., and Lake, G. (1997). Time stepping N-body simulations. *ArXiv Astrophysics e-prints*.

Roškar, R., Debattista, V. P., Brooks, A. M., Quinn, T. R., Brook, C. B., Governato, F., Dalcanton, J. J., and Wadsley, J. (2010). Misaligned angular momentum in hydrodynamic cosmological simulations: warps, outer discs and thick discs. *MNRAS*, 408:783–796.

Sackett, P. D. (1997). Does the Milky Way Have a Maximal Disk? *ApJ*, 483:103–110.

Sawala, T., Pihajoki, P., Johansson, P. H., Frenk, C. S., Navarro, J. F., Oman, K. A., and White, S. D. M. (2017). Shaken and stirred: the Milky Way's dark substructures. *MNRAS*, 467:4383–4400.

Schaye, J., Crain, R. A., Bower, R. G., Furlong, M., Schaller, M., Theuns, T., Dalla Vecchia, C., Frenk, C. S., McCarthy, I. G., Helly, J. C., Jenkins, A., Rosas-Guevara, Y. M., White, S. D. M., Baes, M., Booth, C. M., Camps, P., Navarro, J. F., Qu, Y., Rahmati, A., Sawala, T., Thomas, P. A., and Trayford, J. (2015). The EAGLE project: simulating the evolution and assembly of galaxies and their environments. *MNRAS*, 446:521–554.

Sellwood, J. A. (2013). *Dynamics of Disks and Warps*, page 923. Springer.

Springel, V. (2005). The cosmological simulation code GADGET-2. *MNRAS*, 364:1105–1134.

Springel, V. and Hernquist, L. (2003). Cosmological smoothed particle hydrodynamics simulations: a hybrid multiphase model for star formation. *MNRAS*, 339:289–311.

Springel, V., Wang, J., Vogelsberger, M., Ludlow, A., Jenkins, A., Helmi, A., Navarro, J. F., Frenk, C. S., and White, S. D. M. (2008). The Aquarius Project: the subhaloes of galactic haloes. *MNRAS*, 391:1685–1711.

Stinson, G., Seth, A., Katz, N., Wadsley, J., Governato, F., and Quinn, T. (2006). Star formation and feedback in smoothed particle hydrodynamic simulations - I. Isolated galaxies. *MNRAS*, 373:1074–1090.

Thornton, S. T. and Marion, J. B. (2008). *"Classical Dynamics of Particles and Systems"*. "Cengage Learning", 5 edition.

Torres-Flores, S., Epinat, B., Amram, P., Plana, H., and Mendes de Oliveira, C. (2011). GHASP: an Hα kinematic survey of spiral and irregular galaxies - IX. The near-infrared, stellar and baryonic Tully-Fisher relations. *MNRAS*, 416:1936–1948.

van Dokkum, P. G., Leja, J., Nelson, E. J., Patel, S., Skelton, R. E., Momcheva, I., Brammer, G., Whitaker, K. E., Lundgren, B., Fumagalli, M., Conroy, C., Förster Schreiber, N., Franx, M., Kriek, M., Labbé, I., Marchesini, D., Rix, H.-W., van der Wel, A., and Wuyts, S. (2013). The Assembly of Milky-Way-like Galaxies Since z ~ 2.5. *ApJ*, 771:L35.

Vogelsberger, M., Genel, S., Sijacki, D., Torrey, P., Springel, V., and Hernquist, L. (2013). A model for cosmological simulations of galaxy formation physics. *MNRAS*, 436:3031–3067.

Widrow, L. M., Pym, B., and Dubinski, J. (2008). Dynamical Blueprints for Galaxies. *ApJ*, 679:1239–1259.

Yurin, D. and Springel, V. (2014). GALIC: Galaxy initial conditions construction. Astrophysics Source Code Library.

Yurin, D. and Springel, V. (2015). The stability of stellar discs in Milky Way-sized dark matter haloes. *MNRAS*, 452:2367–2387.

Zemp, M., Gnedin, O. Y., Gnedin, N. Y., and Kravtsov, A. V. (2012). The Impact of Baryon Physics on the Structure of High-redshift Galaxies. *ApJ*, 748:54.

Chapter 4

Cosmological Bar Formation: Nature vs Nurture

This chapter contains a reproduction of a paper published in Monthly Notices of the Royal Astronomical Society as: Jacob S. Bauer and Lawrence M. Widrow. Can stellar discs in a cosmological setting avoid forming strong bars?. *Monthly Notices of the Royal Astronomical Society*, 476:523-537, 2019.

4.1 Abstract

We investigate the connection between the vertical structure of stellar discs and the formation of bars using high-resolution simulations of galaxies in isolation and in the cosmological context. In particular, we simulate a suite of isolated galaxy models that have the same Toomre Q parameter and swing amplification parameter but that differ in the vertical scale height and velocity dispersion. We find that the onset of bar formation occurs more slowly in models with thicker discs. Moreover, thicker discs and discs in simulations with larger force softening are found to be more resilient to buckling, which acts to regulate the length and strength of bars. We simulate disc-halo systems in the cosmological environment using a disc-insertion technique developed in a previous paper. In this case, bar formation is driven by the stochastic effects of a triaxial halo and subhalo-disc interactions and the initial growth of bars appears to be relatively insensitive to the thickness of the disc. On the other hand, thin discs in cosmological haloes do appear to be more susceptible to buckling than thick ones and therefore bar strength correlates with disc thickness as in the isolated case. Thus, one can form discs in cosmological simulations with relatively weak bars or no bars at all provided the discs as thin as the discs we observe and the softening length is smaller than the disc scale height.

4.2 Introduction

The problem of bar formation in disc galaxies tests our understanding of cosmological structure formation and galactic dynamics. In principle, theories of galaxy formation should yield predictions for the fractional distribution of bars in terms of their strength, length, and pattern speed. While it is often difficult to make precise, quantitative statements about bars from observations, general properties of their distribution have emerged (See Sellwood and Wilkinson (1993), Sellwood (2013) and Binney and Tremaine (2008) for reviews). Roughly 25-30 per cent of disc galaxies exhibit strong bars (that is bars that dominate the disc luminosity) and another 20 per cent or more have relatively weak bars (Barazza et al., 2008; Aguerri et al., 2009; Masters et al., 2010; Sellwood, 2013). The bar fraction appears to increase with time. Approximately one tenth of disc galaxies between $0.5 \leq z \leq 2$ have visually identifiable strong bars, which is a factor of 3-4 smaller than the fraction in the local Universe (see Simmons et al. (2014) and references therein).

The bar fraction also varies with galaxy type. Masters et al. (2010) find that 70 ± 5 per cent of the so-called passive red spirals have bars as compared to a 25 ± 5 per cent bar fraction for blue spirals. Since the red spirals are interpreted as old galaxies that have used up their star-forming gas, this result is consistent with a bar fraction that increases with time.

Further evidence of a colour correlation with galaxy bar fractions was presented in Masters et al. (2011). They also found an increased bar fraction in galaxies with dominant bulges. Other correlations were explored by Nair and Abraham (2010), who found correlations between bar fractions galaxies of different morphological types and characteristic masses. They also found that central mass concentrations were correlated with different strong bar fractions depending on the morphological type and mass of the galaxies considered. In the same line of thought, Masters et al. (2012) found a correlation between the gas content of a galaxy and the likelihood of a strong bar being present.

Putting all of these observations together, disc galaxies in the local Universe divide into three roughly equal bins: those with strong bars, those with weak bars, and those with no detectable bar. These observations suggest that bars are capable of forming at a wide range of cosmic times, but once formed are difficult to destroy. Though bars can, in theory, be destroyed through an increased central mass concentration, the requisite mass exceeds typical masses for supermassive black holes (Athanassoula et al., 2005).

Intuition tells us that properties of a bar should depend on the properties of its host galaxy and the environment in which that galaxy lives. Theoretical arguments indicate that cold, thin discs are susceptible to local "Toomre" instabilities (Binney and Tremaine, 2008). Furthermore, discs that are strongly self-gravitating, that is discs that contribute the bulk of the gravitational force required to maintain their rotational motion, are susceptible to global instabilities. Thus, one can construct initially axisymmetric galaxy models that form bars with vastly different properties (or no bars at all) by changing the internal disc dynamics or trading off disc mass for bulge and halo mass. The implication is that the structure of bars provides an indirect means for inferring a disc's kinematics and mass-to-light ratio as well as the distribution of mass in a galaxy's dynamically "hot" components, namely its bulge and dark matter halo. However, it is difficult to infer the mass distribution of a galaxy from bar strengths alone since it depends on the halo velocity dispersion, which cannot be observed directly (Athanassoula, 2003).

A galaxy's ability to resist local instabilities is typically expressed in terms of the (kinetic) Toomre Q-parameter (see Eq. (4.1)) (Toomre, 1964) while its ability to resist global instabilities is encapsulated in the swing-amplification X-parameter (see Eq. (4.2)) (Goldreich and Tremaine, 1978, 1979). Both parameters are defined so that large values imply a more stable disc. The hypothesis that they determine a galaxy's susceptibility to bar formation has been tested by simulations of isolated, idealized galaxy models (Ostriker and Peebles, 1973; Zang and Hohl, 1978; Combes and Sanders, 1981; Sellwood, 1981). Typically, the initial galaxy is represented by an N-body (Monte Carlo) realization of an equilibrium solution to the collisionless Boltzmann equation comprising a disc, dark matter halo, and often, a bulge. Equilibrium does not imply stability, and a galaxy can develop spiral structure and a bar through instabilities that are seeded by shot noise (Efstathiou et al., 1982) and amplified by feedback loops such as swing amplification (Sellwood, 2013). A common way to suppress the mechanisms which give rise to these effects is by increasing either Q or X. For example, in dynamically warm discs (that is, discs with high Q) perturbations are randomized on timescales short enough to prevent the feedback loop from starting (Athanassoula and Sellwood, 1986). Likewise, submaximal discs, that is, discs with high X, avoid the bar instability presumably because the disc lacks the self-gravity to drive the bar instability (Efstathiou et al., 1982; Christodoulou et al., 1995; Sellwood, 2013).

As one might imagine, the parameters Q and X do not uniquely describe a galaxy's susceptibility to bar formation. Widrow et al. (2008) present a grid of models in the $Q-X$ plane that all satisfy observational constraints for the Milky Way. These simulations confirm the basic notion that susceptibility to instabilities increases with decreasing Q and X. However, a careful study of bar strength and length as a function of time across these simulations suggests a more complicated picture. In particular, the bar strength is not a perfectly monotonic function of X at fixed Q or vice versa. The implication is that additional parameters are required to fully predict how bar formation will proceed from some prescribed initial conditions. In short, bar formation may proceed very differently within a family of models that have the same Q and X but vary in other ways.

One property of a disc not captured by either Q or X is its thickness, or alternatively, its vertical velocity dispersion. (The Toomre parameter depends only on the radial velocity dispersion.) Klypin et al. (2009) use a suite of simulations to demonstrate that the thickness of the disc plays a profound role in the development of a bar. In particular, their thick disc model forms a stronger and more slowly rotating bar as compared with the bar that forms in a thin disc model with the same initial radial dispersion profile and rotation curve decomposition. Moreover, simulation parameters such as mass resolution and time step also influence the growth of the bar instability and slowdown of the bar due to angular momentum transfer with the dark halo (Dubinski et al., 2009).

Of course, galaxies are neither isolated nor born as axisymmetric, equilibrium systems. In N-body realizations of these idealized systems, instabilities are seeded from the shot noise of the particle distribution. On the other hand, interactions in real galaxies can be driven by interactions with the given galaxy's environment. As such, the process of bar formation may be very different in idealized galaxies as compared with galaxies in a cosmological setting. For example, halo substructure in the form of satellite galaxies and dark matter subhaloes can pass through and perturb the disc. Gauthier et al. (2006), Kazantzidis et al. (2008), and Dubinski et al. (2009) showed that an apparently stable disc galaxy model can develop a bar when a fraction of the "smooth" halo is replaced by substructure in the form of subhaloes. The effect is stochastic; subhalo-triggered bar formation seems to require subhaloes whose orbits take them into the central regions of the disc in a prograde sense. More recently, Purcell et al. (2011) showed that Sagittarius dwarf alone could have been responsible for the Milky Way's spiral structure and bar.

Cosmological haloes also possess large-scale time-dependent tidal fields, which impart torques to the disc and cause it to precess, nutate, and warp (Dubinski and Kuijken, 1995a; Binney et al., 1998; Dubinski and Chakrabarty, 2009; Bauer et al., 2018). In turn, stellar discs can reshape the inner parts of the dark matter haloes via adiabatic contraction and dynamical friction (Blumenthal et al., 1986; Ryden and Gunn, 1987; Dubinski, 1994; Dubinski and Kuijken, 1995b; DeBuhr et al., 2012; Yurin and Springel, 2015; Bauer et al., 2018). In principle, one can turn to *ab initio* hydrodynamic cosmological simulations to capture the effects of both triaxiality and substructure. Indeed, galaxy formation studies in the cosmological environment that include the formation of supermassive black holes, stars, and the feedback from these objects on galaxy formation have had remarkable success over the last decade (See, for example Vogelsberger et al. (2013); Schaye et al. (2015)). Unfortunately, feedback techniques are extremely computationally expensive. Moreover, the simulator cannot control the properties of the disc such as its mass and radial scale length that form within a particular haloes. This restriction makes it difficult to explore the "nature vs. nurture" question: Do bars reflect the structure of their host galaxy, substructure interactions of the disc's lifetime, or large-scale tidal fields from the dark halo?

Techniques developed by Berentzen and Shlosman (2006), DeBuhr et al. (2012), Yurin and Springel (2015), Bauer et al. (2018) and others allow one to insert a collisionless disc into a dark matter halo. These techniques provide a compromise between fully cosmological simulations and simulations of isolated galaxies. In general, the first step is to run a pure dark matter simulation of a cosmological volume and select a halo suitable for the galaxy one intends to study. The simulation is then rerun with a rigid disc potential that is adiabatically grown from some early epoch (say redshift $z = 3$) and an intermediate one (say $z = 1$). Doing so allows the halo to respond to "disc formation". At the intermediate redshift, a suitable N-body disc that is approximately in equilibrium is swapped in for the rigid disc potential and the simulation continues, now with live disc and halo particles.

Perhaps the most striking and perplexing result to come from recent disc-insertion simulations is the prevalence of strong bars. Yurin and Springel (2015), for example, find that all of the discs in their bulge-less simulations for strong bars even though some of these discs are decidedly submaximal. In addition, over half of the discs in simulations with classical bulges form strong bars. Their results suggest that discs in the cosmological setting are more prone to forming strong bars and that bulges play an essential role in explaining the presence of disc galaxies with weak bars or no bars at all.

Though the Yurin and Springel (2015) models vary in Q and X they share two important properties. First, the ratio of the radial and vertical velocity dispersion is set to unity throughout the disc. Second, the ratio of the vertical and radial scale lengths is fixed at 0.2, which is roughly a factor of two larger than that of the Milky Way's thin disc. In addition, the gravitational softening length in their simulations is fixed at 680 pc. Thus, the discs in their simulations are thicker and (vertically) warmer than what one might expect for Milky Way-like galaxies. The results from Klypin et al. (2009) suggest that these properties rather than (or together with) halo substructure and triaxiality are responsible for the preponderance of strong bars in the Yurin and Springel (2015) models.

In this paper, we attempt to isolate the different effects that determine whether a galaxy forms a strong bar, a weak one, or no bar at all. The core of the paper is a a sequence of N-body simulations that include simulations of isolating disc galaxies and galaxies in cosmological haloes. Our choice of models is meant to complement those of Yurin and Springel (2015). In particular, we choose models that have the same Q and X but that vary in their vertical structure.

We begin in section §4.3 by discussing the dimensionless parameters that arise when one constructs equilibrium disc galaxy models. These include the aforementioned Q and X parameters as well as the ratio of the vertical and radial velocity dispersion and the ratio of the vertical and radial scale lengths. We also discuss possible effects of gravitational softening. In 4.4 we describe our sequence of simulations and discuss how they fit in with previous work. We discuss results for our isolated galaxy simulations in §4.4.1 and our cosmological ones in §4.6. We conclude with a discussion of the implications of our results in §4.7.

4.3 Theoretical Considerations

In this section, we consider the structural properties of disc-halo models with an eye toward understanding the formation of bars in these systems. We begin with the Q and X parameters and then discuss the vertical structure of the disc as defined by its scale height, vertical velocity dispersion, and surface density. Finally, we consider the effect softening might have on bar formation.

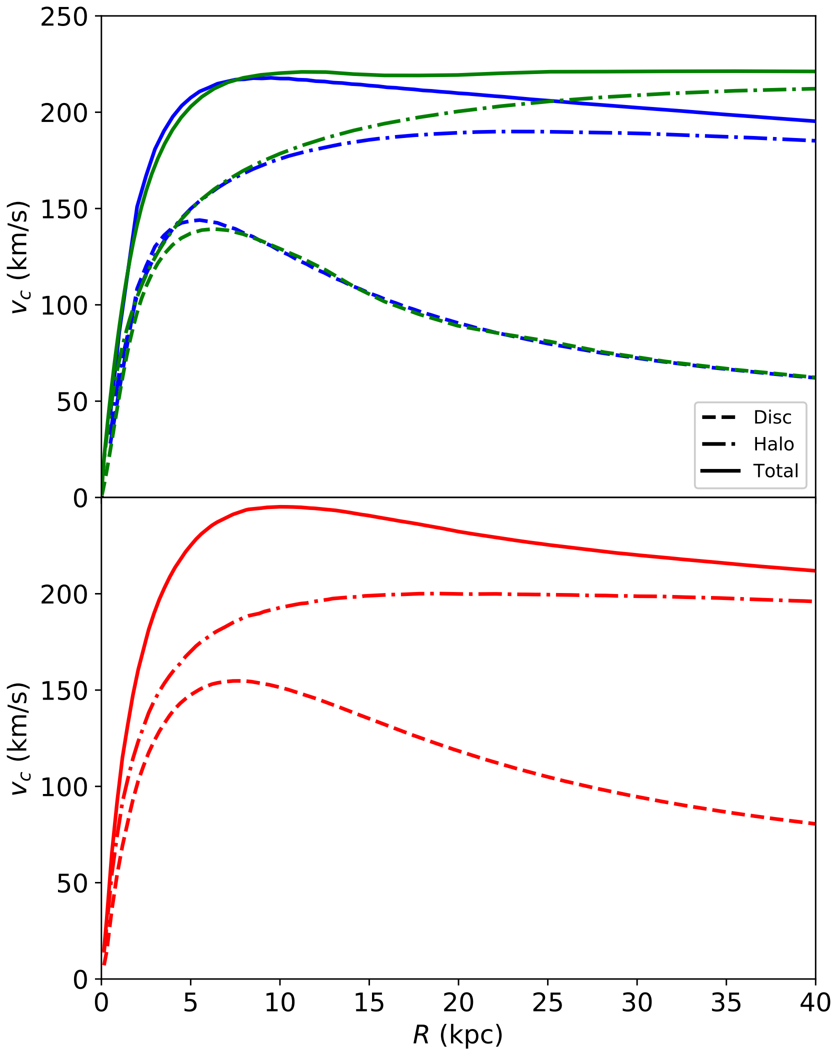

Figure 4.1: Rotation curve decomposition for our models. Total rotation curves are shown as solid lines while the separate contributions from the disc and halo are shown as dashed and dot-dashed curves, respectively. Blue curves in the top panel are for the isolated galaxy simulations with GALACTICS initial conditions while the green curves are for the simulations C.I.Ag run with AGAMA initial conditions. Bottom panel shows initial rotation curve decomposition for the runs D.I and E.II.

	M_d	R_d	V_c	σ_R	z_d/R_d	σ_R/σ_z	X	Q	ρ_h/ρ_0	ϵ	Description
A.I/A.III	3.49	2.50	216	25.3	0.10	1.27	2.34	1.00	0.14	0.15	Thin, Fiducial / Thin, Isotropized
A.II	3.49	2.50	216	25.3	0.10	1.27	2.34	1.00	0.14	0.50	Thin, High Softening
B.I/B.III	3.49	2.50	213	25.3	0.20	0.97	2.34	1.00	0.28	0.15	Mid, Fiducial / Mid, Isotropized
B.II	3.49	2.50	213	25.3	0.20	0.97	2.34	1.00	0.28	0.50	Mid, High Softening
C.I	3.49	2.50	208	25.3	0.40	0.77	2.34	1.00	0.50	0.15	Thick, Fiducial
C.I.Ag	3.49	2.50	216	25.3	0.40	0.77	2.34	1.00	0.50	0.15	Thick, AGAMA ICs
D.I	5.82	3.70	245	25.2	0.10	1.14	2.45	1.00	0.29	0.18	Thin, Cosmological
E.II	5.82	3.70	245	27.4	0.25	0.72	2.45	1.00	0.73	0.74	Thick, High Softening, Cosmological
YS15.A5	5.00	3.00	263	30.7	0.2	1.00	3.22	1.38	0.21	0.68	–
YS15.B5	5.00	3.00	211	26.6	0.2	1.00	2.06	0.96	0.11	0.68	–
YS15.C5	5.00	3.00	270	30.3	0.2	1.00	3.31	1.42	0.23	0.68	–
YS15.D5	5.00	3.00	236	26.6	0.2	1.00	2.58	1.12	0.16	0.68	–
YS15.E5	5.00	3.00	233	27.1	0.2	1.00	2.58	1.11	0.15	0.68	–
YS15.F5	5.00	3.00	219	27.0	0.2	1.00	2.22	1.02	0.11	0.68	–
YS15.G5	5.00	3.00	227	28.2	0.2	1.00	2.45	1.09	0.13	0.68	–
YS15.H5	5.00	3.00	244	28.6	0.2	1.00	2.85	1.21	0.16	0.68	–
G06	7.77	5.57	226	17.1	0.06	1.80	2.78	1.43	0.10	0.15	–

Table 4.1: Summary of parameters for the simulations considered in this paper, the disc-halo simulations considered in Yurin and Springel (2015) (labeled YS15) and the Gauthier et al. (2006) (G06). M_d is the final disc mass in units of $10^{10}\,M_\odot$, R_d is the disc scale radius in units of kpc, and V_c and σ_R are the circular speed and radial velocity dispersion in units of $\mathrm{km\,s^{-1}}$ and evaluated at $R_p = 2.2R_d$. For the disc aspect ratio, we quote z_d/R_d where z_d is the sech^2-scale length. The velocity dispersion ratio σ_R/σ_z, the X and Q parameters, the ratio of the halo density in the midplane to that of the disc, and the logarithmic derivative of the circular speed are also measured at R_p. Finally, the softening length ϵ is given in units of kpc. Simulations A.III and B.III are the same as A.I and B.I except that they are run with vertical motions isotropized so as to shut off the buckling instability.

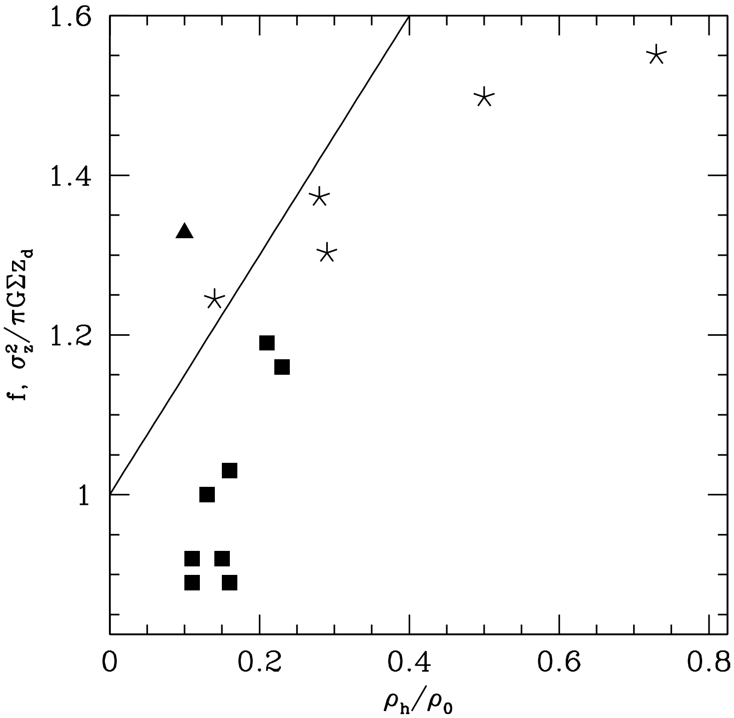

Figure 4.2: The dimensionless ratio $\sigma_z^2/\pi G\Sigma z_d$ as a function of ρ_h/ρ_0 for the models considered in this paper (stars), the disc-halo models from Yurin and Springel (2015) (filled squares) and the model from Gauthier et al. (2006) (filled triangle). The straight line is the function $f = 1 + (2\pi/3)^{1/2}\, \rho_h/\rho_0$ discussed in the text.

4.3.1 Q and X

The stability of a stellar disc is generally thought to be determined by the Toomre-Q parameter (Toomre, 1964)

$$Q \equiv \frac{\sigma_R \kappa}{3.36 G\Sigma} \tag{4.1}$$

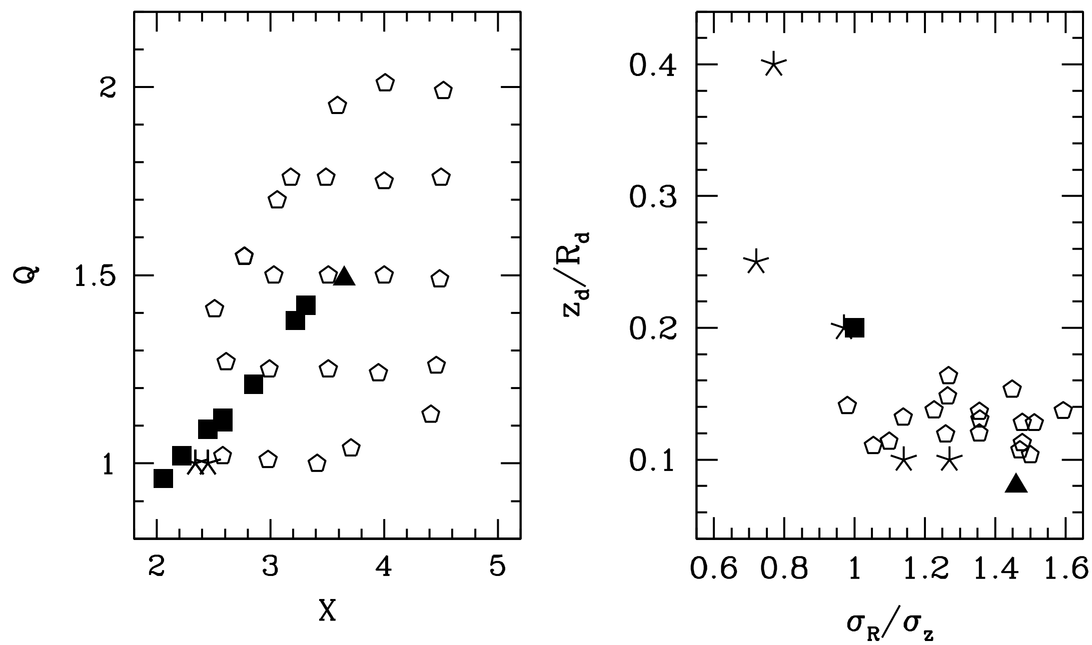

Figure 4.3: Distribution of simulations considered in this paper in the $Q-X$ and the $z_d/R_d - \sigma_R/\sigma_z$ planes. Stars are simulations run for this paper (A-E); filled squares denote the series of simulations described in Yurin and Springel (2015); the filled triangle denotes the simulation of M31 run in Gauthier et al. (2006); open pentagons denote the simulations described in Widrow et al. (2008).

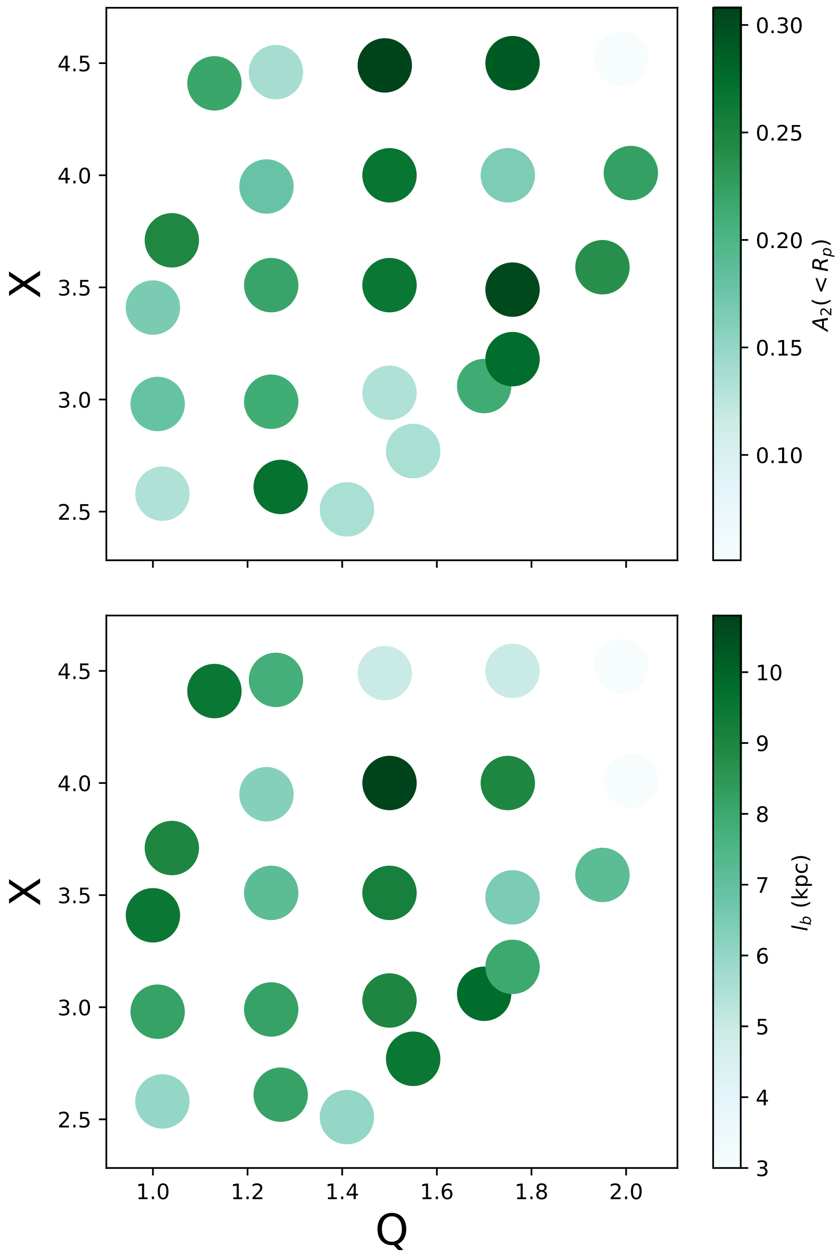

Figure 4.4: Strength and length of bars for the simulations considered in Widrow et al. (2008). The twenty-five models span the Q-X plane. Top panel shows the A_2 parameter while the bottom panel shows the bar length, l_b. Both are measured at 5 Gyr (the final snapshot of the simulations). The bar length is the full bar length.

and the Goldreich-Tremaine (swing amplification) parameter (Goldreich and Tremaine, 1978, 1979)

$$X_m \equiv \frac{\kappa^2 R}{2\pi m G\Sigma} \tag{4.2}$$

where R is the Galactocentric radius of a cylindrical (R, ϕ, z) coordinate system, Σ is the surface density of the disc, σ_R is the radial velocity dispersion of the disc, and m is the azimuthal mode number. The epicyclic radial frequency κ is given by

$$\kappa^2 = \frac{2V_c^2}{R^2}\left(1 + \frac{d\ln V_c}{d\ln R}\right) \tag{4.3}$$

where V_c is the circular speed. We assume an exponential disc with mass M_d, radial scale length R_d, and surface density

$$\Sigma(R) = \frac{M_d}{2\pi R_d^2} e^{-R/R_d} \ . \tag{4.4}$$

Note that κ, σ_R, Σ, V_c, Q, and X_m are functions of R. In what follows, we consider the radius R_p at which the contribution to the rotation curve from the disc, V_d reaches a peak value. For an exponential disc, $R_p \simeq 2.2R_d$ and $V_d(R_p) \simeq 0.62\,(GM_d/R_d)^{1/2}$ (Binney and Tremaine, 2008).

Roughly speaking, Q describes the susceptibility of a disc to local instabilities. Cold discs with low velocity dispersion and $Q < 1$ are unstable to local perturbations. On the other hand, X_m describes the vigour with which a global perturbation with an m-fold azimuthal symmetry undergoes swing amplification. Since we are interested in bar formation, we set $m = 2$ and note that X_2^{-1} is a measure of disc self-gravity.

To see this, we use Eq. (4) and the expression for $V_{d,p}$ to find

$$X_2(R_p) \simeq 0.79 \left.\frac{V_c^2}{V_d^2}\right|_{R_p} \tag{4.5}$$

where we have assumed that the logarithmic derivative in Eq.(4.3) is zero.

For simplicity, we define

$$X \equiv \left.\frac{V_c^2}{V_d^2}\right|_{R_p} . \tag{4.6}$$

Therefore $X = 2$ when the contribution of the disc to the circular speed curve at its peak is equal to the combined contributions of the dynamically hot components, namely the bulge and halo. Following Efstathiou et al. (1982), Yurin and Springel (2015), use $Q_{\rm bar} = V_{\rm max}/\left(GM_d/R_d\right)^{1/2}$ where $V_{\rm max}$ is the maximum circular speed. If we assume that $V_{\rm max} \simeq V_c(R_p)$, then $Q_{\rm bar}^2 \simeq 0.387X$ and the stability criterion from Efstathiou et al. (1982), $Q_{\rm bar} > 1.1$, becomes $X > 3.13$.

4.3.2 Vertical Structure of Stellar Discs

As discussed in Klypin et al. (2009) the vertical structure of a stellar disc plays a key role in determining the properties of any bar that forms. In general, the vertical structure is characterized by the vertical velocity dispersion σ_z, surface density Σ, and scale height. For a self-gravitating plane-symmetric isothermal disc these quantities are connected through the relation $\sigma_z^2 = \sqrt{12}G\Sigma z_{\rm rms}$ where $z_{\rm rms}$ is the root mean square distance of "stars" from the midplane, and z_d is the disc scale height (See §4.5 and Spitzer (1942); Camm (1950)).

We can incorporate the effects of dark matter by modifying the Poisson equation

$$\begin{aligned}\frac{d^2\Phi}{dz^2} &= 4\pi G\left(\rho_d(z)+\rho_h(z)\right)\\ &= 4\pi G\rho_0\left(e^{-\Phi/\sigma_z^2}+\rho_h/\rho_0\right)\end{aligned} \tag{4.7}$$

where ρ_d and ρ_h are the densities of the disc and halo, respectively, and ρ_0 is the density of the disc in the midplane. In the second line we assume, as is done in the pure self-gravitating case, that the disc stars are vertically isothermal with velocity dispersion σ_z. We also assume that the halo density is constant in the region of the disc. We then solve Eq. 4.7 numerically. The result is well-described by the relation

$$\sigma_z^2 = \sqrt{12}G\Sigma z_{\rm rms}\left(1+\alpha\rho_h/\rho_0\right) \tag{4.8}$$

where the factor $\alpha = \sqrt{2\pi/3}$ provides a simple interpolation between the pure self-gravitating case and the case where disc particles are test particles in the (harmonic) potential of a constant density halo. We plot the simulations to be presented in this paper, along with others, in Fig. 4.2. We see variation about a line with slope α of the simulations detailed in Table 4.1. Simulations deviate from this trendline substantially as the disc scale height is increased and the planar model we considered becomes less accurate.

As discussed in the next section Eq. 4.8 holds at the 10 per cent level for our equilibrium models. Departures from Eq. 4.8 might come from radial gradients and the rotation of the disc. (See, for example, Read (2014)).

Combining Eqs. 4.1, 4.6, 4.8 we find following relation:

$$\frac{Q^2}{X} = 3.103\,\frac{\sigma_R^2}{\sigma_z^2}\,\frac{z_{\rm rms}}{R_d}\,f\left(1+\frac{d\ln V_c}{d\ln R}\right)\ . \tag{4.9}$$

This expression can be interpreted in several ways. First, if the ratios of σ_R to σ_z and $z_{\rm rms}$ to R_d are fixed, then there is a linear relation between Q^2 and X. On the other hand, if one considers a family of models in which the only variation is in the vertical structure of the disc, then the scale height varies roughly linearly with the vertical velocity dispersion, apart from corrections due to the contribution of the halo to the vertical force.

4.3.3 Effect of Gravitational Softening

Numerical effects can significantly alter the development of bars in simulated galaxies. For example, in simulations of an isolated galaxy that is initially in equilibrium, the onset of bar formation is delayed when mass resolution is increased (Dubinski et al., 2009) essentially because the bar instability is seeded by shot noise. The importance of mass resolution as well as force resolution and time stepping have been discussed in Klypin et al. (2009).

In this section, we focus on the effects of force softening. Gravitational softening is necessary to avoid large (possibly infinite) forces that arise from Newtonian two-body interactions. Equilibrium models, such as the ones used as initial conditions in isolated galaxy simulations, satisfy the collisionless Boltzmann and Poisson equations. When evolved with force softening, they will begin slightly out of equilibrium. This effect should be most noticeable when the softening length is comparable to or larger than the thickness of the disc. Detailed discussions of the effect softened gravity has on the secular evolution of N-body galaxies can be found in Romeo (1994); Athanassoula and Sellwood (1986); Merritt (1996); Weinberg (1996); Romeo (1997, 1998).

To gain some intuition as to this extent of this effect we the Poisson equation in one dimension. The potential for a mass distribution with vertical density profile of $\rho(z)$ can be calculated by convolving ρ with the Green's function:

$$\Phi(z) = 4\pi G \int_{-\infty}^{\infty} \mathcal{G}(z' - z)\rho(z')\mathrm{d}z' \ . \tag{4.10}$$

For Newtonian gravity, $\mathcal{G} = |z|/2$. For softened gravity, we replace $\mathcal{G}$ with $\mathcal{G}_s = \frac{1}{2}\left(z^2 + \epsilon^2\right)^{1/2}$ where ϵ is the softening length. (The motivation for this expression is as follows: Begin with a system of Plummer-softened particles, that is, a system where point-like particles are replaced by particles whose spherical density profile is proportional to $\left(r^2 + \epsilon^2\right)^{-5/2}$. If the particles are confined to a plane, then the vertical density profile will be $\rho(z) \propto \left(z^2 + \epsilon^2\right)^{-3/2}$. The one-dimensional potential with this $\rho(z)$ is indeed proportional to $\left(z^2 + \epsilon^2\right)^{1/2}$.) The integral Eq. 4.10 and the related integral for the vertical force, $f(z)$, can be evaluated numerically. As expected, the potential energy per unit area of the system, $W \equiv \int dz\, \rho(z) z f(z)$ is smaller than that of the same system found assuming Newtonian gravity. Hence, a system that is set up to be in equilibrium under the assumption of Newtonian gravity, will be too "warm" for a softened gravity simulation and will "puff up". To an excellent approximation, we find that the virial ratio between the kinetic energy per unit area and W is given by $2T/W \simeq (1 + (a\epsilon/z_{\rm rms})^2)^b$ where $a = 1.25$ and $b = 0.25$. Roughly speaking, simulations run with a softening length equal to $z_{\rm rms}$ will have a virial ratio of 1.25.

Softening may have other effects on the development of the bar. In principle, softening should suppress the Toomre instability on small scales. However, this instability develops on scales comparable to or larger than the Jeans length, which is typically much larger than the thickness of the disc and hence larger than the softening length for most simulations. On the other hand, softening may suppress buckling, a bending instability, which is strongest on small scales. As discussed below, buckling appears to be responsible for regulating the growth of bars.

4.4 Models and Simulations

4.4.1 Initial Conditions for Isolated Galaxy Simulations

We follow the evolution of isolated disc-halo systems using the N-body code GADGET-3 (Springel, 2005). The initial conditions for most of our isolated galaxy simulations are generated with GalactICS (Kuijken and Dubinski, 1995; Widrow et al., 2008), which allows users to build multicomponent, axisymmetric equilibrium systems with prescribed structural and kinematic properties. Disc particles are sampled from a distribution function (DF) that is a semi-analytic function of the total energy E, the angular momentum about the disc symmetry axis L_z, and the vertical energy $E_z = \Phi(R,0)-\Phi(R,z)+\frac{1}{2}v_z^2$, where Φ is the gravitational potential and v_z is an orbit's vertical velocity. By design, the disc DF yields a density law in cylindrical (R, ϕ, z) coordinates given, to a good approximation, by $\rho(R,z) = \Sigma(R)\,\mathrm{sech}^2(z/z_d)$. Here $\Sigma(R)$ is exponential surface density profile (Eq. 4.4) and z_d is the scale height. Note that $z_{\rm rms} = \pi/\sqrt{12}z_d$ while the "half-mass" scale height used in Yurin and Springel (2015) is given by $z_{1/2} \simeq 0.549z_d \simeq 0.605z_{\rm rms}$. The disc DF is also constructed to yield a radial velocity dispersion profile that is exponential in R with scale length $2R_d$. The halo DF is designed to yield a truncated NFW profile (Navarro et al., 1997) as described in Widrow et al. (2008).

While E_z used in the GalactICS disc DF is conserved to a good approximation for nearly circular orbits it varies considerable for stars that make large excursions in R and z. Thus, the initial conditions for "thick" or "warm" discs will not represent true equilibrium solutions to the dynamical equations. To test whether non-conservation of vertical energy affects our results, we compare a thick disc model with GalactICS initial conditions with a similar one where the initial conditions are generated with AGAMA (Vasiliev, 2018), an action-based code that does not rely on the epicycle approximation. AGAMA initial conditions should be closer to the true equilibrium than GalactICS models, especially for the thick discs. In principle, this action-based code should yield initial conditions that are closer to a true equilibrium system than ones based on E_z especially for thick discs.

4.4.2 Description of Simulations

In this section, we describe a suite of simulations where Q and X are fixed and where the velocity dispersion and scale length ratios are allowed to vary. Our aim is to test the hypothesis that scale height plays a key role in the development of bars. The parameters for our simulations are summarized in Table 4.1. Our suite of isolated galaxy simulations form a sequence A, B, C in increasing thickness. The models have the same rotation curve decomposition, which is shown in the top panel of Fig. 4.1. By design, the contribution to the rotation curve from the disc is slightly below that of the halo at R_p. Therefore our models have X slightly greater than 2 and should be susceptible to global instabilities.

The fiducial simulations are run with a softening length of 184, pc, which is about two thirds of the scale height of our thinnest model (A.I). The simulations A.II and B.II use a softening length of 736 pc, which is close to the value assumed in Yurin and

Springel (2015). The simulation C.I.Ag is similar to C.I (large scale height) but run with AGAMA initial conditions. A comparison of its rotation curve decomposition with that for model C.I is shown in the top panel of Fig. 4.1. The contributions from the discs in the two models are nearly the same and the contributions from the haloes differ significantly only beyond $\sim 10\,\mathrm{kpc}$. The simulations A.III and B.III use a scheme to isotropize vertical motions and effectively shut off buckling and are discussed in §4.5.4.

In addition to these isolated galaxy simulations we run two cosmological simulations using the disc insertion scheme described in Bauer et al. (2018). The initial conditions for these models, labeled D.I and E.II, are identical except for the vertical scale height and softening length, which are larger in E.II. Thus, these models are cosmological analogs to A.I and B.II. The rotation curves for these models are shown in the bottom panel of Fig. 4.1. The models themselves are discussed in Section §4.6.

4.4.3 Comparison with Previous Work

While the parameters Q and X allow one to predict the rapidity and vigour with which instabilities develop in disc galaxies that are actually imperfect predictors of the strength and length of bars at late times. The point is illustrated in Widrow et al. (2008) where results for a suite of 25 simulations that explore the $Q-X$ plane are presented. By design, the initial conditions for the models satisfy observational constraints for the Milky Way such as the rotation curve, the local vertical force, and the velocity dispersion toward the bulge. (See Hartmann et al. (2014) for a further analysis of these simulations.) As expected, the onset of the bar instability is delayed in models with large initial values for Q and/or X. However, the dependence on these parameters of the bar strength and length is more complicated. In Fig. 4.3, we show the distribution of models in the $Q - X$ and $z_d/R_d - \sigma_R/\sigma_z$ planes from a few papers which consider Milky Way like galaxies. It is common for bar formation studies to consider only a small subset of the total parameter space. As we will see, models which are close together in Q and X may exhibit very different bar formation behaviour.

In Fig.4.4, we show the bar strength parameter A_2 and length of the bar across the models considered in Widrow et al. (2008). Evidently, the models that form the strongest and longest bars have intermediate values of Q and X. The implication is that models where the instabilities grow too quickly lead to weaker and somewhat shorter bars. Bar formation appears to be a self-regulating process.

Table 4.1 gives the relevant parameters for the eight disc-halo models from Yurin and Springel (2015) as well as the disc-bulge-halo model for M31 from Gauthier et al. (2006). In the Yurin and Springel (2015) simulations discs are inserted into dark matter haloes from the cosmological Aquarius simulation. In this respect, they are similar to the disc-insertion simulations described in Section §4.6. The initial discs in these models all have a scale height to scale length ratio of 0.2 and a radial to vertical velocity dispersion ratio of 1. As discussed above, these choices mean that their discs were chosen from a one-parameter family of models within the $Q - X$ parameter space.

4.5 Isolated Galaxy Simulations

4.5.1 Morphology of Bar Forming Galaxies

Face on surface density maps for models A.I, A.II, B.I, B.II, C.I, and C.I.Ag are shown in Fig. 4.5. All discs form bars by the end of the simulation ($t = 10\,\mathrm{Gyr}$). However, bar formation appears to be delayed in models B.I and C.I relative to that in model A.I while the final bar in A.I is shorter than those in B.I and C.I. Other $m = 2$ features are also evident. These include two-armed spiral structure, most clearly seen in A.I and B.III and elliptical rings, as, for example, in C.I.

Evidently, the dominant mode for in-plane perturbations is $m = 2$ Nevertheless, there are strong $m = 3$ structures in the 1.5 Gyr snapshot of the A.I and A.II simulations and hints of a weak $m = 3$ structure in the same snapshot of B.II.

A larger softening length seems to lead to stronger bars at intermediate times. We see this in the comparison of A.I and A.II or B.I and B.II in the 3.0 Gyr and 4.5 Gyr snapshots.

4.5.2 Bar Strength Parameter A_2

It is convenient to think of the azimuthal distribution of particles in a given radial bin as a Fourier series. We use the canonical definition for the coefficient of the Fourier component with m-fold azimuthal symmetry (see Debattista and Sellwood (2000a), for instance),

$$c_m = \frac{1}{M_S} \sum_{j \in S} \mu_i e^{im\phi} \tag{4.11}$$

where μ_i is the mass of the i-th particle, S is a circularly symmetric region of the disc, and M_S is the mass in this region. The normalization is chosen so that a distribution of particles along a line through the origin will have $|c_m| = 1$ for all m even. Moreover, for a uniform distribution of particles, $c_0 = 1$ and $c_m = 0$ for all $m > 0$. The amplitude and phase for the m-th Fourier coefficient are given by $A_m \equiv |c_m|$ and $\phi_m = \arg\,(c_m)$, respectively. Note that both of these quantities depend on the region S

Fig. 4.6 shows a plot of the mean A_2 inside the radius R_p as a function of time for the fiducial simulations, the two simulations with high softening, and the thick disc simulation with initial conditions from AGAMA. Consider first the fiducial (low-softening) simulations. Initially, A_2 grows roughly exponentially with a growth rate that decreases with increasing thickness. In simulations A.I and B.I, the end of exponential growth is followed by a decrease in A_2 after which A_2 again increases, now, approximately linearly with time. In the thick disc case (C.I) exponential growth transitions directly to linear growth. The trend is for exponential growth to end at later times as one goes to thicker discs. It is worth noting that the value of A_2 at 10 Gyr is similar in the three low-softening simulations.

In the thin disc case, an increase in softening appears to delay the onset of exponential growth as well as the time at which exponential growth ends. Furthermore, the drop in A_2 is less severe. Though the value of A_2 at the end of the simulation is approximately the same in the low and high softening cases, the bar strength, as measured by A_2 is larger in the high-softening case at intermediate times between 4 and 8 Gyr. For the intermediate thickness case (B.I and B.II) softening has little effect on the initial growth rate of A_2. But as in the thin disc case, softening allows exponential growth to continue to later times and the final bar is about twenty per cent stronger as compared with the low-softening case. Once again we see that the effect of high softening is to produce stronger bars at intermediate times.

The evolution of A_2 for the thick disc runs with GalactICS and agama initial conditions are fairly similar. In particular, the initial growth rate is almost identical as are the final values.

Fig. 4.6 encapsulates bar strength into a single number, the mean $m = 2$ Fourier amplitude inside 2.2 disc scale lengths, or about 5.5 kpc. A more complete picture of bar strength is presented in Fig. 4.7 where we plot A_2 as a function of R and t. The figure is constructed by calculating c_2 (Eq. 4.11) for cylindrical rings of radius 200 pc. Also shown is the corotation radius, which is determined from the pattern speed Ω_p and rotation curve. The former is given by a numerical estimate of $\mathrm{d}\phi_2/\mathrm{d}t$; corotation is found by determining the radius at which $\Omega_p = V_c/R$. Thus, since our galaxy models have roughly flat rotation curves beyond 5 kpc, the corotation essentially gives the inverse pattern speed or pattern period.

From Fig. 4.7 we see that the corotation radius tends to grow with time and provides an envelope for the bar and other $m = 2$ structures such as two-armed spirals and elliptical rings. The bar pattern speed is therefore decreasing with time, presumably due to dynamical friction between the bar and both the disc and dark halo (Debattista and Sellwood, 1998, 2000b). It is worth noting that the corotation radius increases more rapidly in simulations with high softening. The naive interpretation is that softening somehow increases the frictional coupling between the bar and disc or halo particles. A more likely explanation is that with a high softening length comes stronger bars. Since the acceleration on the bar due to dynamical friction scales as the mass of the bar, stronger bars should spin down more rapidly.

As in Fig. 4.6 we see that bar formation is delayed in models with thicker discs. Bar formation is well underway by 2 Gyr in A.I but doesn't really take hold until

4 Gyr in C.I. Moreover, the first hints of $m = 2$ power in C.I arise further out at radii closer to 5 kpc.

The dip in bar strength is clearly seen between $2.5 - 3$ Gyr in A.I and between $3.5 - 4$ Gyr in B.I. As discussed below, we attribute this dip to buckling.

4.5.3 Vertical Structure and Velocity Dispersion

Fig. 4.8 shows the $z_{\rm rms}$ radial profiles for a sequence of snapshots in various models. The evolution of $z_{\rm rms}$ is studied during the initial 500 Myr of the simulation. The top panels show the $z_{\rm rms}$ profiles for simulations A.I and A.II and illustrate the effect softening has on the evolution from "equilibrium" initial conditions. As discussed in §2, a system that is initialized to be in equilibrium under the assumption of Newtonian gravity will be out of equilibrium if evolved with softened gravity. In particular, the mean potential energy will be systematically low and the system will puff up. For our thin disc model, $z_{\rm rms} \simeq 230$ pc. In the high softening case, $\epsilon = 736\,{\rm pc} \simeq 2.2 z_{\rm rms}$, we estimate the virial ratio for the vertical structure to be $2T/W \simeq 1.7$. Of course, the excess kinetic energy will redistribute itself into both kinetic and potential energy. The upshot is that the system quickly settles into a new state with a thickness somewhat larger than the initial one as seen in the right hand panel. One might be tempted to suggest that a high softening implies that a disc behaves like a thicker disc. This picture is not quite correct, since a thicker disc will not substantially redistribute energy if it is initialized in equilibrium.

The bottom panels in Fig. 4.8 provide a comparison of $z_{\rm rms}$ profiles for the thick disc simulations with GalactICS and AGAMA initial conditions. We first note that $z_{\rm rms}$ is approximately constant in the C.I but varies by about 200 pc in C.I.Ag. This difference is simply a reflection in how the initial conditions are set up. In both cases, the scale height depends implicitly on the functional form of the DFs, which are written in terms of either E, E_z, and L_z or the actions. The GalactICS case does exhibit transient wavelike perturbations with a peak to trough amplitude of 100 pc at radii $R > 4$ kpc. A plausible explanation for these oscillations is that they are due to the fact that E_z is not a true constant of motion. In any case, the system quickly settles to to a new equilibrium state not too different from the initial one.

Fig. 4.9 shows profiles for z_{rms} and the diagonal components of the velocity dispersion tensor, σ_z, σ_R, and σ_ϕ. All models exhibit significant in-plane heating across the disc and throughout the simulations. While the initial radial velocity dispersion profiles are exponential in R the final profiles are relatively flat within the central 5 kpc. Thus, the greatest increase in radial velocity dispersion is at about this radius, which corresponds to the end of the bar. Likewise the σ_ϕ profile develops a "bump" around $R \simeq 5 - 10$ kpc.

Vertical heating and thickening also appear to be connected with bar formation. The σ_z profile increases in the A.I/A.II and B.I/B.II simulations such that by 10 Gyr, the central value is 100 km/s. This value is roughly equal to the initial value in the C.I and C.I.Ag (thick disc) simulations. Note as well that vertical heating in the inner disc occurs rapidly beginning around 3-4 Gyr, roughly when the bar is forming. By contrast, vertical heating of the outer disc occurs gradually over the entire simulation.

The bottom row in Fig. 4.9 shows the z_{rms} profiles for the different simulations. Again, we see that the inner disc in the A.I/A.II and B.I/B.II simulations begins to thicken around 3-4 Gyr. Moreover, the thickness of the inner disc increases with R reaching a maximum at around $R \sim 5 - 7$ kpc. Curiously enough, the innermost

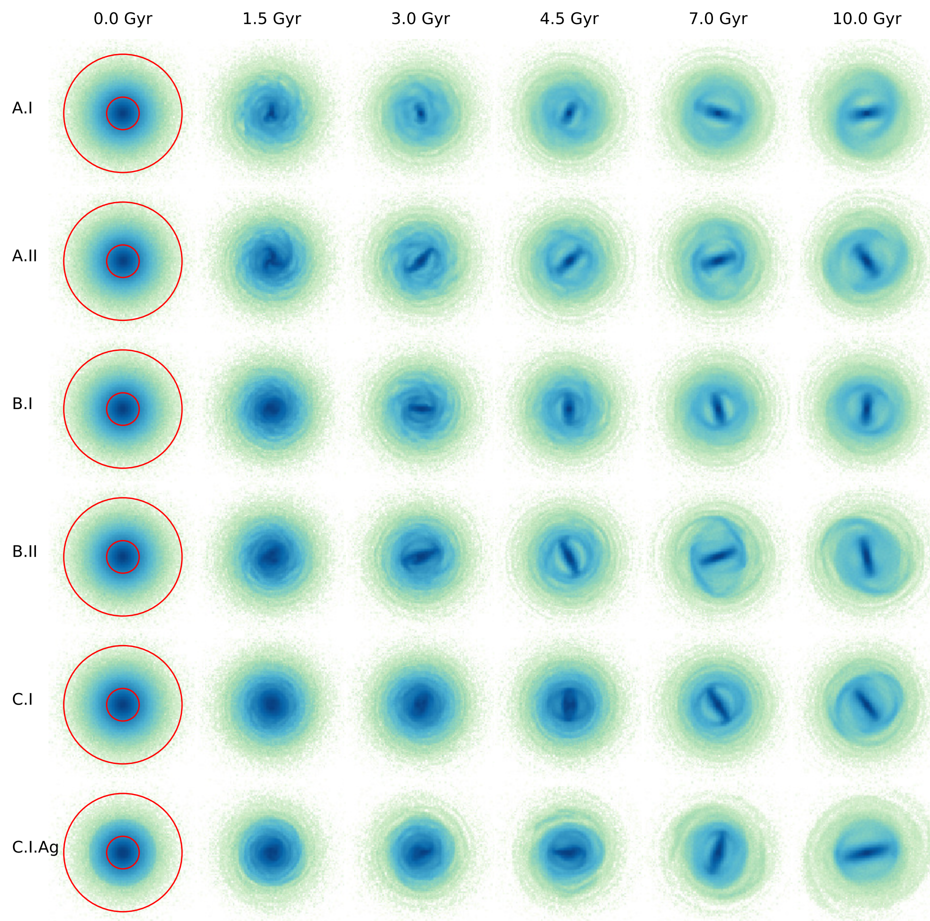

Figure 4.5: Surface density maps for isolated galaxy simulations at select times. Time proceeds from 0 to 10 Gyr, left-to-right, and the models span top-to-bottom in order of their appearance in Table 4.1. The overlaid red circles have radii $R_p = 5.5\,\mathrm{kpc}$ and 20 kpc. Recall $R_P = 2.2R_d$, the radius of peak circular velocity.

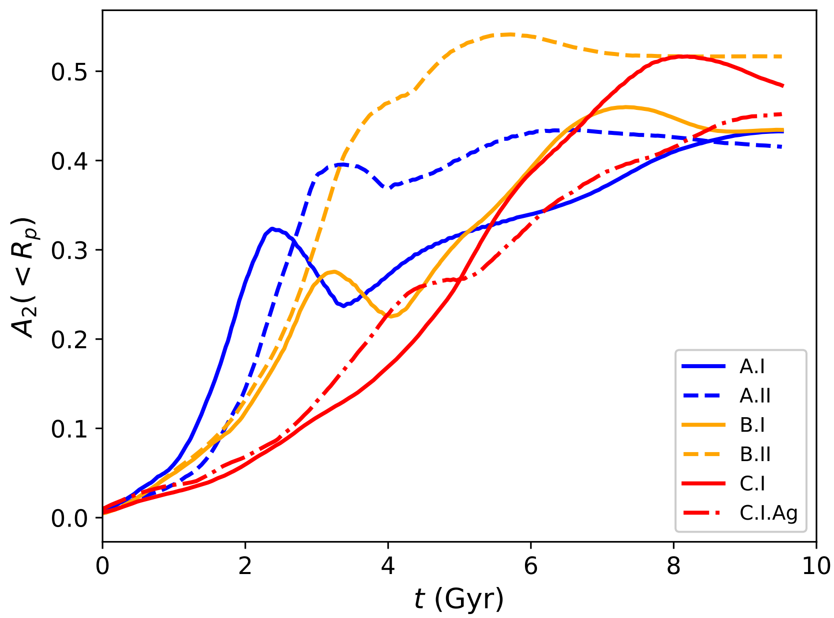

Figure 4.6: Mean bar strength parameter inside a cylindrical radius R_p, $A_2(< R_p)$, as a function of time. Curves are smoothed in time with a top-hat moving window of width 1 Gyr. Line colours are blue, red, and orange for models A, B, and C, respectively. Results for the fiducial runs A.I, B.I, and C.I are shown as solid curves while the results for the runs with high softening length, A.II and B.II, are shown as dashed curves. The AGAMA model C.I.Ag is shown as a dot-dashed curve.

region of the discs in C.I and C.I.Ag decrease with time. As with σ_z, the thickness of the discs for $R \simeq 0$ at late times are all approximately the same. Evidently, bar formation tends to drive the innermost regions of the host disc to a common vertical structure.

Fig. 4.10 provides a different perspective on these results. Here we plot σ_R, σ_ϕ, σ_z, and z_{rms} as a function of time for three representative radii. From the upper three rows, we see that the increase in velocity dispersion is most abrupt in the inner disc, implying that heating there is driven by bar formation. Furthermore, the vertical velocity dispersion in the thick disc models is very nearly time-independent. As in

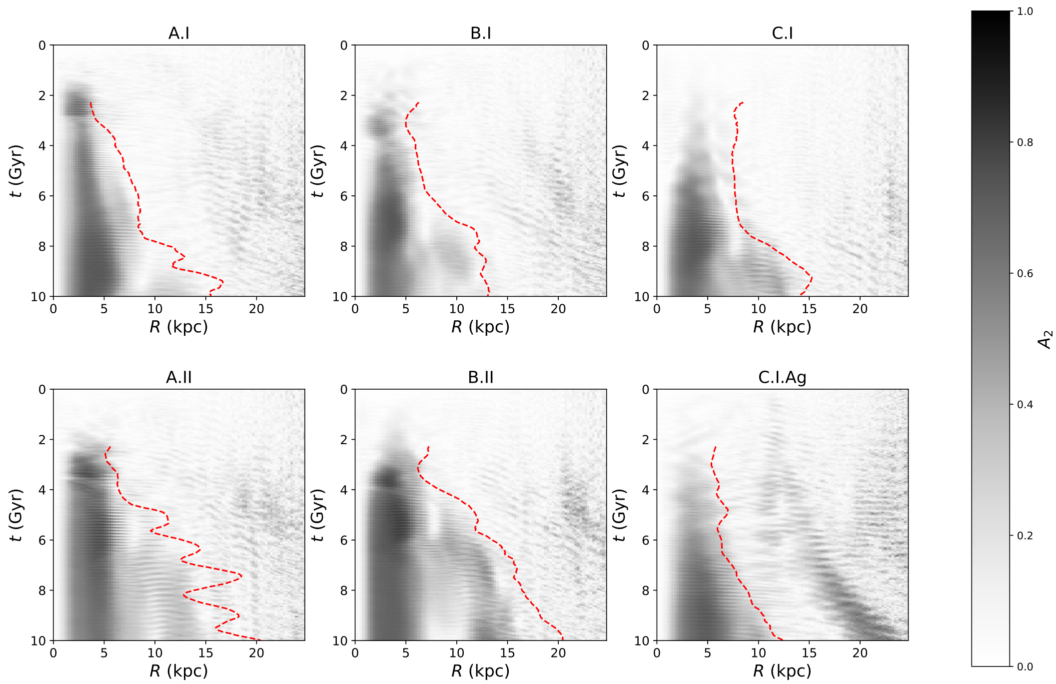

Figure 4.7: Bar strength parameter A_2 as a function of radius and time. The trajectory of corotation is shown by the dashed red line.

Fig. 4.9, we see that the discs in all simulations are thickest for $R \simeq 2.2\, R_d \simeq 5 - 6$ kpc. Finally, we again observe that in the thick disc simulations, the inner disc becomes thinner with time.

4.5.4 Simulations Where Buckling is Suppressed

Buckling is a well-known phenomena often seen in simulations of bar-forming galaxies where the bar bends in and out of the disc plane. Eventually, these coherent oscillations are converted to random vertical motions (Binney and Tremaine, 2008).

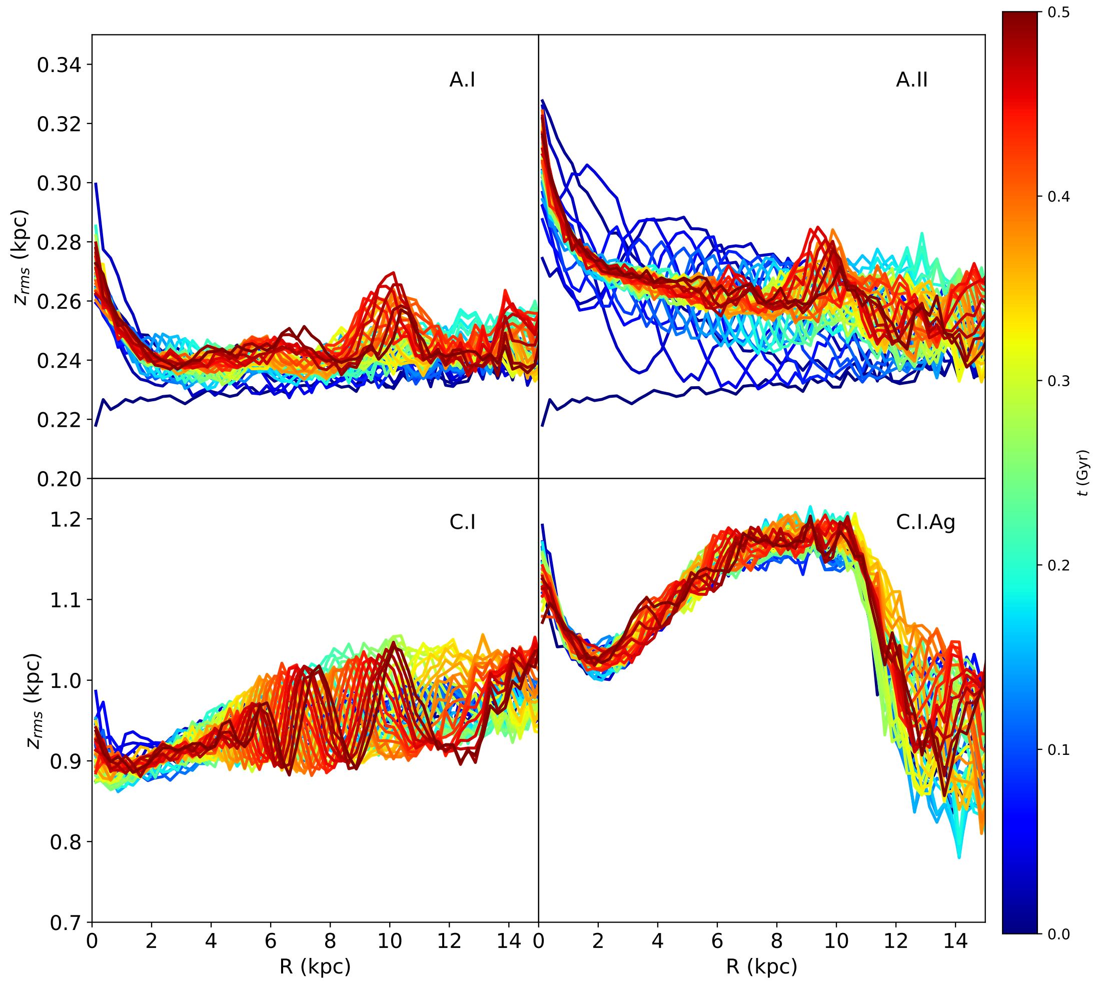

Figure 4.8: Root mean square height z_{rms} as a function of cylindrical radius R for ten snapshots equally spaced over the first 500 Myr. Panels are for simulations A.I (upper left), A.II (upper right), C.I (lower left) and C.I.Ag (lower right).

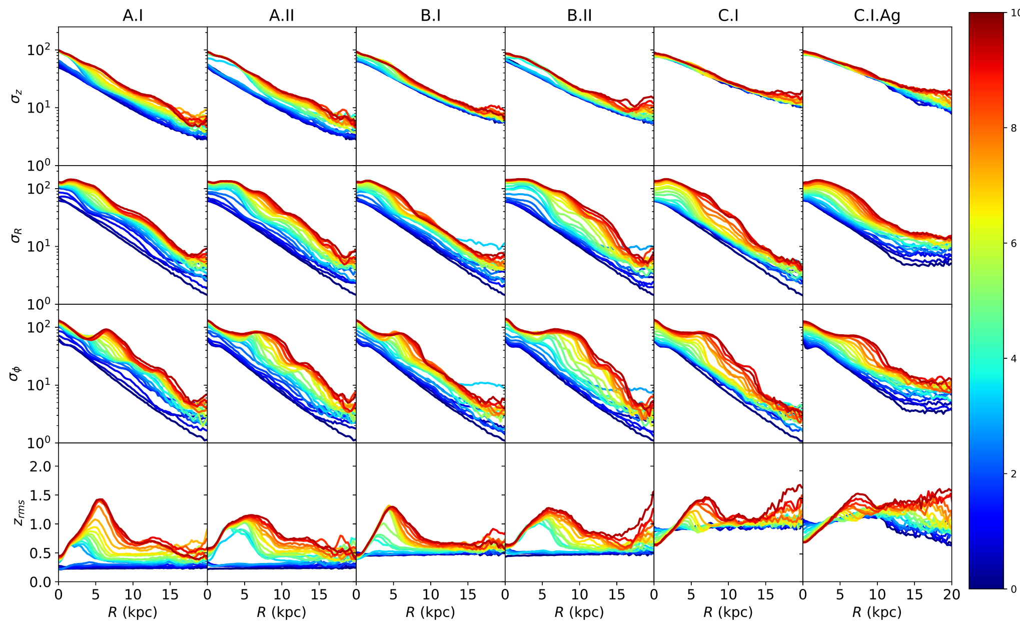

Figure 4.9: Diagonal components of the velocity dispersion tensor and $z_{\rm rms}$ as a function of R for different snapshots between 0 and 10 Gyr. Shown, from to to bottom, are profiles for $z_{\rm rms}$, σ_z, σ_R, and σ_ϕ for the same size models included in Fig. 4.5.

Buckling typically leads to shorter and weaker bars (Martinez-Valpuesta and Shlosman, 2004; Debattista et al., 2006)

To isolate the effects of buckling we implement a simple scheme that prevents the instability from taking hold. Essentially, at each timestep, we reverse the vertical components of the position, velocity, and acceleration for a fraction p of disc particles. In practice, we choose $p = 0.25$ though the results are insensitive to the exact value.

Fig. 4.11 shows the effect suppressing buckling has on the disc evolution. In the thin disc case, the bar instability develops a bit faster when buckling is suppressed. More importantly, the drop in A_2 seen in simulation A.I is not as strong,

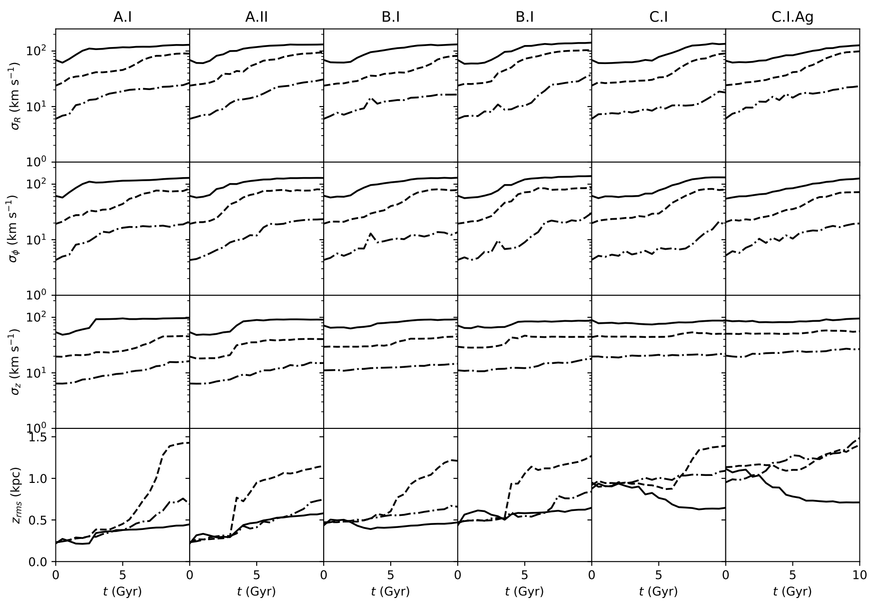

Figure 4.10: The velocity dispersions, σ_R, σ_ϕ, and σ_z, and z_{rms} as a function of time for our six fiducial models. The lines are averaged in the circular region of radius 0.25 kpc (solid), an annulus of width 0.25 kpc centered near 2.2 R_d (dashed), and a 0.25 kpc width annulus centered at around 5 R_d (dot-dashed).

thus confirming the notion that buckling regulates the strength of bars. Buckling has a similar effect on our intermediate thickness runs. Furthermore, the effect of suppressing buckling is similar, in some respects, to the effect of increasing softening as can be seen by noting similarities between A.II and B.III. Finally, we note that buckling doesn't appear to occur in our thick disc simulations.

4.6 Cosmological Simulations

Disc galaxies simulated from axisymmetric, equilibrium initial conditions, as was done in the previous section, form bars at rates and with strengths that depend on their

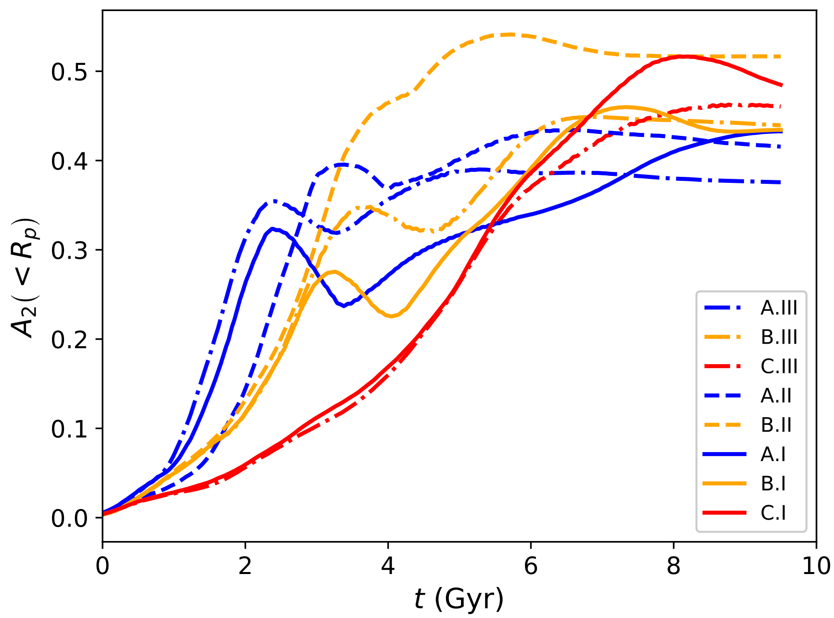

Figure 4.11: Mean bar strength parameter inside the cylindrical radius R_p, $A_2(< R_p)$, as a function of time. The figure is essentially the same as Fig. 4.6 though this time we include simulations A.III, B.III, and C.III where buckling is suppressed.

intrinsic scale height of the disc and on the force resolution of the simulation. In this section, we investigate the extent to which these results hold in a cosmological environment. In particular we follow the evolution of a thin disc with moderate softening and a thick disc with high softening that are embedded in identical cosmological haloes.

4.6.1 Simulation Setup; Inserting Discs into Cosmological Haloes

We model a stellar disc in a cosmological halo using the disc insertion scheme described in Bauer et al. (2018). This scheme, which builds on the methods developed

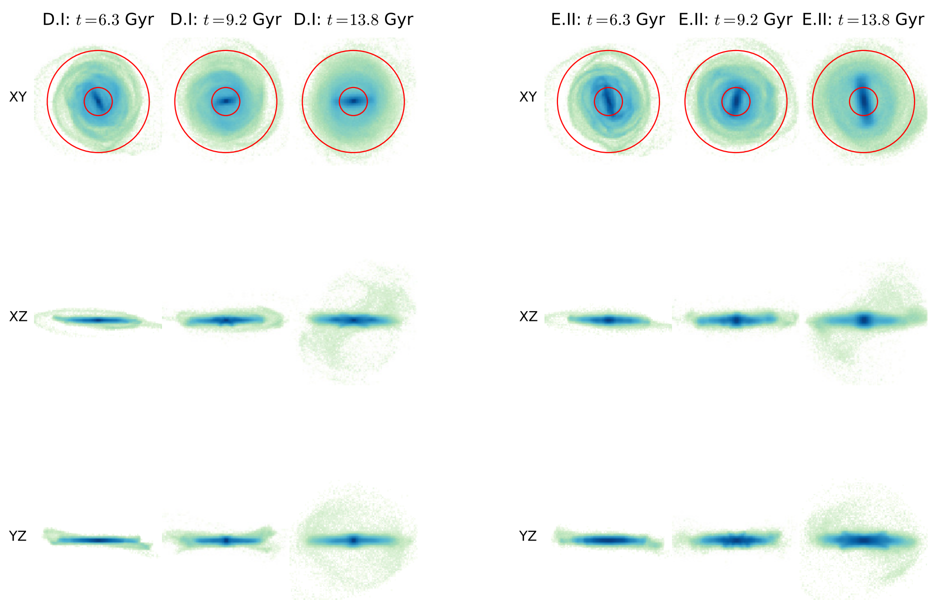

Figure 4.12: Projections for the D.I (left three columns) and E.II (right three columns). The three columns for each simulation correspond,from left to right, to 2.2 Gyr, 5.9 Gyr, and 13.7 Gyr after the Big Bang. The overlaid red circles have radii R_p and 20 h^{-1} kpc.

by Berentzen and Shlosman (2006), DeBuhr et al. (2012), and Yurin and Springel (2015) uses an iterative procedure to initialize the disc. The first step is to run a pure dark matter simulation and identify a suitable halo. The system is then rerun from redshift z_g to z_l, this time with a disc potential that grows slowly in mass and radius. Doing so allows the halo particles to respond to the gravitational field of the would-be disc. At z_l, the rigid disc is replaced by an N-body system and the "live" disc-halo system is evolved to the present epoch.

For our pure dark matter simulation, we implement the zoom-in technique of

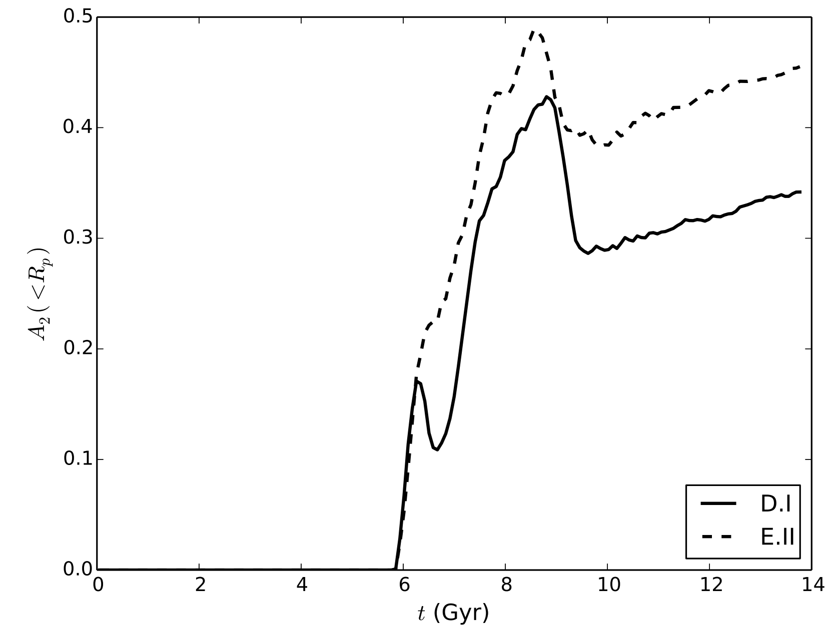

Figure 4.13: $A_2(< R_p)$ as a function of the age of the Universe for simulations D.I (solid curve) and E.II (dashed curve).

Katz et al. (1994) and Navarro et al. (1994), broadly following the recommendations of Oñorbe et al. (2014), which allows us to achieve very high spatial and mass resolution for a single halo while still accounting for the effects of large-scale tidal fields. We choose cosmological parameters based on the results from Planck 2013 (Planck Collaboration et al., 2014) with $H_0 = 67.9\,\mathrm{km\,s^{-1}\,kpc^{-1}}$, $\Omega_b = 0.0481$, $\Omega_0 = 0.306$, $\Omega_\Lambda = 0.694$, $\sigma_8 = 0.827$, and $n_s = 0.962$. N-body initial conditions for the dark matter particles are generated with the MUSIC code (Hahn and Abel, 2013). We select a suitably-sized halo for a Milky Way-like galaxy, namely one with a $z = 0$ mass of $1.23 \times 10^6\, h^{-1} M_\odot$ that comprises 10^6.

During its growth phase from $z_g = 3$ to $z_l = 1$, the disc is treated as a rigid body whose orientation and center-of-mass position evolve according to the standard

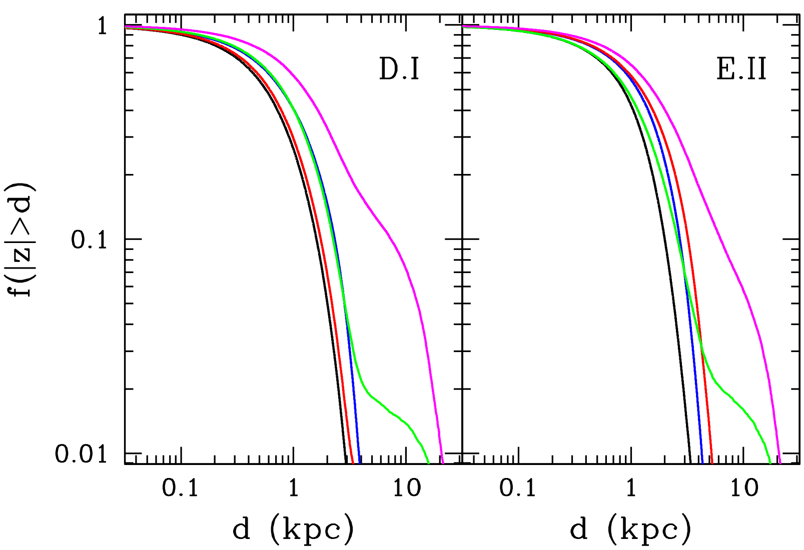

Figure 4.14: Fraction of particles with distance from the midplane greater than some distance d as a function of d. The difference colours correspond to different bins in cylindrical radius R: $0 < R < 5\,\mathrm{kpc}$ — black; $5\,\mathrm{kpc} < R < 10\,\mathrm{kpc}$ — blue; $10\,\mathrm{kpc} < R < 15\,\mathrm{kpc}$ — red; $15\,\mathrm{kpc} < R < 20\,\mathrm{kpc}$ — green; $20\,\mathrm{kpc} < R\,\mathrm{kpc}$ — magenta.

equations of rigid body dynamics. At z_l, we swap a live disc for the rigid one using the GalactICS code (Kuijken and Gilmore, 1989; Widrow et al., 2008), which generates a three-integral DF disc in the best axisymmetric approximation to the halo Bauer et al. (2018).

We run two simulations, D.I, which assumes a thin disc with a softening length of 184 pc and E.II, which assumes a thick disc with a softening length of 736 pc. The softening length chosen for D.I is in accord with the criteria outlined in Power et al. (2003). The simulations D.I and E.II roughly correspond to A.I and B.II, respectively. As well, E.II is similar to the discs considered by DeBuhr et al. (2012), Yurin and Springel (2015) and Bauer et al. (2018), whereas D.I is more consistent with typical discs considered in isolated galaxy suites like Widrow et al. (2008).

4.6.2 Results

Results from our two cosmological simulations are displayed in Figs. 4.12 and 4.13. The former shows projections of the mass density at three epochs while the latter gives $A_2(< R_p)$ as a function of time. Evidently, the discs in both cases roughly follow the same evolutionary sequence that was seen in the isolated galaxy simulations: rapid growth of the bar strength followed by a period where the bar strength decreases, presumably due to buckling, and finally steady strengthening of the bar. The three epochs chosen in Fig. 4.12 correspond to the initial growth phase of the bar ($a = 0.6,\ t = 6.3\,\mathrm{Gyr}$), an epoch after buckling ($a = 0.7,\ t = 9.2\,\mathrm{Gyr}$), and the present epoch at $t = 13.8\,\mathrm{Gyr}$. Visually, the bar appears to be stronger and longer in the E.II run than D.I one at each of these epochs but perhaps most notably in the final one. Indeed, the disc in E.II looks very similar to those seen in the simulations of DeBuhr et al. (2012), Yurin and Springel (2015), and Bauer et al. (2018). The fact that the bar in D.I is weaker than the one in E.II is consistent with the results from our isolated galaxy simulations that thicker discs produce stronger bars (see Fig. 4.5).

The most significant difference between bar formation in the cosmological setting and bar formation in isolated galaxies concerns the initial growth of the bar. For isolated galaxies, Fig. 4.6 clearly shows that the onset of bar formation is delayed for thicker discs. Conversely, in the cosmological case, A_2 rapidly grows to a value of ~ 0.17 within the first few hundred Myr after the disc "goes live" regardless of the disc thickness. At this point, the bar in the thin disc model decreases in strength with A_2 dropping to ~ 0.11 before resuming its growth. By contrast, the bar in the thick disc model continues to grow monotonically. As in the isolated galaxy simulations, self-regulating processes such as buckling are more efficient in the thin disc case and so A_2 in simulation D.I lags behind that of E.II. We note that in both cases, A_2 drops significantly at around $t = 7.5\,\mathrm{Gyr}$ and grows steadily thereafter.

Our interpretation of these results is as follows: In isolation, where discs start from axisymmetric initial conditions, the only source of the $m = 2$ perturbations that drive bar formation is shot noise from the N-body distribution. Evidently, making a disc thicker slows the growth of these perturbations. On the other hand, $m = 2$ perturbations abound in the cosmological environment where haloes are clumpy and triaxial. The initial growth of the bar may, in fact, be relatively insensitive to the thickness of the disc, once discs are placed in a cosmological setting. On the other hand, disc thickness does effect the resilience of the bar to self-regulating processes, such that buckling and therefore thick discs tend to have stronger bars.

Finally, we note that in both D.I and E.II, a significant number of particles are found at high galactic latitudes. These particles represent stars "kicked-up" from the disc presumably by the large-scale tidal fields of the halo and interactions between the disc and halo substructure. Kicked-up stars have been seen in cosmological simulations by Purcell et al. (2010), McCarthy et al. (2012) and Tissera et al. (2013). Their existence was inferred in a combined analysis of kinematic and photometric data for the Andromeda galaxy (Dorman et al., 2013). Furthermore, the idea of kicked-up stars has been invoked by (Price-Whelan et al., 2015) to explain the Triangulum-Andromeda stellar clouds (Rocha-Pinto et al., 2003; Martin et al., 2014) and by (Sheffield et al., 2018; Laporte et al., 2018) to explain the Monoceros Ring (Yanny et al., 2000; Newberg et al., 2002) and associated A13 stellar overdensity (Sharma et al., 2010).

In Fig. 4.14 we show the fraction of stars with $|z| > d$ for different regions of the discs in our two cosmological simulations. The results are strikingly similar for the two simulations as is already evident from a visual inspection of Fig. 4.12. The implication is that the processes by which stellar orbits are perturbed out of the disc plane are relatively insensitive to the vertical structure of the disc. We see that very few of the stars with cylindrical radius $R < 15\,\mathrm{kpc}$ and only $1-2\,\%$ of the stars between 15 and 20 kpc are kicked-up to distances greater than 3 kpc though some stars from the $15-20\,\mathrm{kpc}$ region do end up with $|z| > 10\,\mathrm{kpc}$. On the other hand, $20\,\%$ of the stars from the region beyond 20 kpc end up with $|z| > 3\,\mathrm{kpc}$ from the midplane and 10 10 kpc. Of course, the actual number of stars is certainly larger since a fraction of the kicked-up stars will be passing through the disc with large vertical velocities.

4.7 Conclusions

We briefly summarize our findings as:

- Bar strength in a cosmological setting depends on X and Q, as well as additional properties such as thickness and vertical dispersion.
- In isolation, thick discs appear more resilient to buckling.

- In a cosmological setting, environment appears to be a much larger driver of bar formation than internal disc dynamics.
- Disc scale height has little-to-no impact on the number of stars being kicked out of a stellar disc.

The seminal work of Ostriker and Peebles (1973) introduced the notion that disc dynamics provides a powerful constraint on the structure of discs and the haloes in which they reside. In short, discs that are dynamically cold and that account for a substantial fraction of the gravitational force that keeps their stars on nearly circular orbits are unstable to the formation of strong bars and spiral structure. The existence of galaxies with weak bars or no bars at all tells us that at least some discs are relatively low in mass (i.e., submaximal) and/or dynamically warm.

The theoretical analysis presented in Section 2 showed with a few simple assumptions (e.g., exponential surface density profile) one can derive a relation among the structural parameters of a disc in approximate equilibrium and thus a constraint on initial conditions that one might choose for simulations. For example, if one fixes z_d/R_d and σ_R/σ_z, as was done in Yurin and Springel (2015), then there is an approximately one-to-one relationship between Q and X. Likewise, fixing Q and X implies a relationship between z_d/R_d and σ_R/σ_z. These results have important implications for applying disc dynamics as a constraint on models of galaxy formation. In particular, inconsistencies between bar demographics in a galaxy formation model and in observational surveys may reflect differences in the scale height and vertical velocity dispersion of model and real galaxies.

One lesson from our work and the work of others is that the relation between structural parameters of galaxies and bar strength and length is often rather complicated. This observation is no doubt due, at least in part, to the self-regulating nature of bar formation. When bars develop rapidly, they tend to buckle, which leads to weaker and shorter bars (Martinez-Valpuesta and Shlosman, 2004). Thick discs appear to be more resilient to buckling, which may explain why bars in these models often end up stronger and longer than bars in thin-disc models (Klypin et al., 2009). For similar reasons, gravitational softening can affect the development and ultimate strength of bars.

In simulations of isolated galaxies from "pristine" equilibrium initial conditions, bar formation is seeded by the shot noise of the N-body distribution. On the other hand, bars in a cosmological environment are subjected to large perturbations including the $m = 2$ ones that drive bar formation. Thus, the fact that bar formation is delayed in thick disc models of isolated galaxies may be purely academic — bar formation in the cosmological environment will be initiated by a variety of stochastic effects regardless of the thickness of the disc. On the other hand, the resilience of thick discs to buckling *is* relevant in the cosmological setting and may explain why thick discs tend to form strong bars. The upshot is that a proper understanding the distribution of bars in cosmological models must go hand-in-hand with a proper understanding of the vertical structure of discs.

Clearly, a more exhaustive exploration of the model parameter space is in order. One might, for example, include galaxy scaling relations to further constrain the space of models. In addition, it would be of interest to insert different discs (and for that matter, nearly identical ones) into different haloes in order to explore the random nature of disc-halo interactions. Ultimately, improvements in observations together with a more complete survey of models via simulations should allow us to fully exploit bars in discs as a means of testing and constraining theories of structure formation.

Acknowledgements

LMW and JSB are supported by a Discovery Grant with the Natural Sciences and Engineering Research Council of Canada. JSB acknowledges the assistance of Matthew Chequers and Keir Darling in understanding the AGAMA program interface. The authors acknowledge the contributions of the Python scientific open source community, particularly the SciPy project (Jones et al., 2001), NumPy (Oliphant, 2015), Pandas (McKinney, 2010), and matplotlib (Hunter, 2007).

Bibliography

Aguerri, J. A. L., Méndez-Abreu, J., and Corsini, E. M. (2009). The population of barred galaxies in the local universe. I. Detection and characterisation of bars. *A&A*, 495:491–504.

Athanassoula, E. (2003). What determines the strength and the slowdown rate of bars? *MNRAS*, 341:1179–1198.

Athanassoula, E., Lambert, J. C., and Dehnen, W. (2005). Can bars be destroyed by a central mass concentration?- I. Simulations. *MNRAS*, 363:496–508.

Athanassoula, E. and Sellwood, J. A. (1986). Bi-symmetric instabilities of the Kuz'min/Toomre disc. *MNRAS*, 221:213–232.

Barazza, F. D., Jogee, S., and Marinova, I. (2008). Bars in Disk-dominated and Bulge-dominated Galaxies at z ˜ 0: New Insights from ˜3600 SDSS Galaxies. *ApJ*, 675:1194–1212.

Bauer, J. S., Widrow, L. M., and Erkal, D. (2018). Disc-Halo Interactions in {\Lambda}CDM. *ArXiv e-prints*.

Berentzen, I. and Shlosman, I. (2006). Growing Live Disks within Cosmologically Assembling Asymmetric Halos: Washing Out the Halo Prolateness. *ApJ*, 648:807–819.

Binney, J., Jiang, I.-G., and Dutta, S. (1998). The Persistence of WARPS in Spiral Galaxies with Massive Haloes. *MNRAS*, 297:1237–1244.

Binney, J. and Tremaine, S. (2008). *Galactic Dynamics: Second Edition*. Princeton University Press.

Blumenthal, G. R., Faber, S. M., Flores, R., and Primack, J. R. (1986). Contraction of dark matter galactic halos due to baryonic infall. *ApJ*, 301:27–34.

Camm, G. L. (1950). Self-gravitating star systems. *MNRAS*, 110:305.

Christodoulou, D. M., Shlosman, I., and Tohline, J. E. (1995). A new criterion for bar-forming instability in rapidly rotating gaseous and stellar systems. 2: Nonaxisymmetric form. *ApJ*, 443:563–569.

Combes, F. and Sanders, R. H. (1981). Formation and properties of persisting stellar bars. *A&A*, 96:164–173.

Debattista, V. P., Mayer, L., Carollo, C. M., Moore, B., Wadsley, J., and Quinn, T. (2006). The Secular Evolution of Disk Structural Parameters. *ApJ*, 645:209–227.

Debattista, V. P. and Sellwood, J. A. (1998). Dynamical Friction and the Distribution of Dark Matter in Barred Galaxies. *ApJ*, 493:L5–L8.

Debattista, V. P. and Sellwood, J. A. (2000a). Constraints from Dynamical Friction on the Dark Matter Content of Barred Galaxies. *ApJ*, 543:704–721.

Debattista, V. P. and Sellwood, J. A. (2000b). Constraints from Dynamical Friction on the Dark Matter Content of Barred Galaxies. *ApJ*, 543:704–721.

DeBuhr, J., Ma, C.-P., and White, S. D. M. (2012). Stellar discs in Aquarius dark matter haloes. *MNRAS*, 426:983–999.

Dorman, C. E., Widrow, L. M., Guhathakurta, P., Seth, A. C., Foreman-Mackey, D., Bell, E. F., Dalcanton, J. J., Gilbert, K. M., Skillman, E. D., and Williams, B. F. (2013). A New Approach to Detailed Structural Decomposition from the SPLASH and PHAT Surveys: Kicked-up Disk Stars in the Andromeda Galaxy? *ApJ*, 779:103.

Dubinski, J. (1994). The effect of dissipation on the shapes of dark halos. *ApJ*, 431:617–624.

Dubinski, J., Berentzen, I., and Shlosman, I. (2009). Anatomy of the Bar Instability in Cuspy Dark Matter Halos. *ApJ*, 697:293–310.

Dubinski, J. and Chakrabarty, D. (2009). Warps and Bars from the External Tidal Torques of Tumbling Dark Halos. *ApJ*, 703:2068–2081.

Dubinski, J. and Kuijken, K. (1995a). The settling of warped disks in oblate dark halos. *ApJ*, 442:492–503.

Dubinski, J. and Kuijken, K. (1995b). The settling of warped disks in oblate dark halos. *ApJ*, 442:492–503.

Efstathiou, G., Lake, G., and Negroponte, J. (1982). The stability and masses of disc galaxies. *MNRAS*, 199:1069–1088.

Gauthier, J.-R., Dubinski, J., and Widrow, L. M. (2006). Substructure around M31: Evolution and Effects. *ApJ*, 653:1180–1193.

Goldreich, P. and Tremaine, S. (1978). The excitation and evolution of density waves. *ApJ*, 222:850–858.

Goldreich, P. and Tremaine, S. (1979). The excitation of density waves at the Lindblad and corotation resonances by an external potential. *ApJ*, 233:857–871.

Hahn, O. and Abel, T. (2013). MUSIC: MUlti-Scale Initial Conditions. Astrophysics Source Code Library.

Hartmann, M., Debattista, V. P., Cole, D. R., Valluri, M., Widrow, L. M., and Shen, J. (2014). The effect of bars on the $\mathrm{M}_{\mathrm{ffl}}$-$\sigma_e$ relation: offset, scatter and residuals correlations. *MNRAS*, 441:1243–1259.

Hunter, J. D. (2007). Matplotlib: A 2d graphics environment. *Computing In Science & Engineering*, 9(3):90–95.

Jones, E., Oliphant, T., Peterson, P., et al. (2001). SciPy: Open source scientific tools for Python. [Online; accessed ¡today¿].

Katz, N., Quinn, T., Bertschinger, E., and Gelb, J. M. (1994). Formation of Quasars at High Redshift. *MNRAS*, 270:L71.

Kazantzidis, S., Bullock, J. S., Zentner, A. R., Kravtsov, A. V., and Moustakas, L. A. (2008). Cold Dark Matter Substructure and Galactic Disks. I. Morphological Signatures of Hierarchical Satellite Accretion. *ApJ*, 688:254–276.

Klypin, A., Valenzuela, O., Colín, P., and Quinn, T. (2009). Dynamics of barred galaxies: effects of disc height. *MNRAS*, 398:1027–1040.

Kuijken, K. and Dubinski, J. (1995). Nearly Self-Consistent Disc / Bulge / Halo Models for Galaxies. *MNRAS*, 277:1341.

Kuijken, K. and Gilmore, G. (1989). The mass distribution in the galactic disc. I - A technique to determine the integral surface mass density of the disc near the sun. *MNRAS*, 239:571–603.

Laporte, C. F. P., Johnston, K. V., Gómez, F. A., Garavito-Camargo, N., and Besla, G. (2018). The influence of Sagittarius and the Large Magellanic Cloud on the stellar disc of the Milky Way Galaxy. *MNRAS*, 481:286–306.

Martin, N. F., Ibata, R. A., Rich, R. M., Collins, M. L. M., Fardal, M. A., Irwin, M. J., Lewis, G. F., McConnachie, A. W., Babul, A., Bate, N. F., Chapman, S. C., Conn, A. R., Crnojević, D., Ferguson, A. M. N., Mackey, A. D., Navarro, J. F., Peñarrubia, J., Tanvir, N. T., and Valls-Gabaud, D. (2014). The PAndAS Field of Streams: Stellar Structures in the Milky Way Halo toward Andromeda and Triangulum. *ApJ*, 787:19.

Martinez-Valpuesta, I. and Shlosman, I. (2004). Why Buckling Stellar Bars Weaken in Disk Galaxies. *ApJ*, 613:L29–L32.

Masters, K. L., Mosleh, M., Romer, A. K., Nichol, R. C., Bamford, S. P., Schawinski, K., Lintott, C. J., Andreescu, D., Campbell, H. C., Crowcroft, B., Doyle, I., Edmondson, E. M., Murray, P., Raddick, M. J., Slosar, A., Szalay, A. S., and Vandenberg, J. (2010). Galaxy Zoo: passive red spirals. *MNRAS*, 405:783–799.

Masters, K. L., Nichol, R. C., Haynes, M. P., Keel, W. C., Lintott, C., Simmons, B., Skibba, R., Bamford, S., Giovanelli, R., and Schawinski, K. (2012). Galaxy Zoo and ALFALFA: atomic gas and the regulation of star formation in barred disc galaxies. *MNRAS*, 424:2180–2192.

Masters, K. L., Nichol, R. C., Hoyle, B., Lintott, C., Bamford, S. P., Edmondson, E. M., Fortson, L., Keel, W. C., Schawinski, K., Smith, A. M., and Thomas, D. (2011). Galaxy Zoo: bars in disc galaxies. *MNRAS*, 411:2026–2034.

McCarthy, I. G., Font, A. S., Crain, R. A., Deason, A. J., Schaye, J., and Theuns, T. (2012). Global structure and kinematics of stellar haloes in cosmological hydrodynamic simulations. *MNRAS*, 420:2245–2262.

McKinney, W. (2010). Data structures for statistical computing in python. In van der Walt, S. and Millman, J., editors, *Proceedings of the 9th Python in Science Conference*, pages 51 – 56.

Merritt, D. (1996). Optimal Smoothing for N-Body Codes. *AJ*, 111:2462.

Nair, P. B. and Abraham, R. G. (2010). On the Fraction of Barred Spiral Galaxies. *ApJ*, 714:L260–L264.

Navarro, J. F., Frenk, C. S., and White, S. D. M. (1994). Accretion of Satellite Galaxies and the Density of the Universe. *MNRAS*, 267:L1.

Navarro, J. F., Frenk, C. S., and White, S. D. M. (1997). A Universal Density Profile from Hierarchical Clustering. *ApJ*, 490:493–508.

Newberg, H. J., Yanny, B., Rockosi, C., Grebel, E. K., Rix, H.-W., Brinkmann, J., Csabai, I., Hennessy, G., Hindsley, R. B., Ibata, R., Ivezić, Z., Lamb, D., Nash,

E. T., Odenkirchen, M., Rave, H. A., Schneider, D. P., Smith, J. A., Stolte, A., and York, D. G. (2002). The Ghost of Sagittarius and Lumps in the Halo of the Milky Way. *ApJ*, 569:245–274.

Oñorbe, J., Garrison-Kimmel, S., Maller, A. H., Bullock, J. S., Rocha, M., and Hahn, O. (2014). How to zoom: bias, contamination and Lagrange volumes in multimass cosmological simulations. *MNRAS*, 437:1894–1908.

Oliphant, T. E. (2015). *Guide to NumPy*. CreateSpace Independent Publishing Platform, USA, 2nd edition.

Ostriker, J. P. and Peebles, P. J. E. (1973). A Numerical Study of the Stability of Flattened Galaxies: or, can Cold Galaxies Survive? *ApJ*, 186:467–480.

Planck Collaboration, Ade, P. A. R., Aghanim, N., Armitage-Caplan, C., Arnaud, M., Ashdown, M., Atrio-Barandela, F., Aumont, J., Baccigalupi, C., Banday, A. J., and et al. (2014). Planck 2013 results. XVI. Cosmological parameters. *A&A*, 571:A16.

Power, C., Navarro, J. F., Jenkins, A., Frenk, C. S., White, S. D. M., Springel, V., Stadel, J., and Quinn, T. (2003). The inner structure of ΛCDM haloes - I. A numerical convergence study. *MNRAS*, 338:14–34.

Price-Whelan, A. M., Johnston, K. V., Sheffield, A. A., Laporte, C. F. P., and Sesar, B. (2015). A reinterpretation of the Triangulum-Andromeda stellar clouds: a population of halo stars kicked out of the Galactic disc. *MNRAS*, 452:676–685.

Purcell, C. W., Bullock, J. S., and Kazantzidis, S. (2010). Heated disc stars in the stellar halo. *MNRAS*, 404:1711–1718.

Purcell, C. W., Bullock, J. S., Tollerud, E. J., Rocha, M., and Chakrabarti, S. (2011). The Sagittarius impact as an architect of spirality and outer rings in the Milky Way. *Nature*, 477:301–303.

Read, J. I. (2014). The local dark matter density. *Journal of Physics G Nuclear Physics*, 41(6):063101.

Rocha-Pinto, H. J., Majewski, S. R., Skrutskie, M. F., and Crane, J. D. (2003). Tracing the Galactic Anticenter Stellar Stream with 2MASS M Giants. *ApJ*, 594:L115–L118.

Romeo, A. B. (1994). How faithful are N-body simulations of disc galaxies? *A&A*, 286:799–806.

Romeo, A. B. (1997). Dynamical effects of softening in N-body simulations of disc galaxies. Method and first applications. *A&A*, 324:523–533.

Romeo, A. B. (1998). Modelling gravity in N-body simulations of disc galaxies. Optimal types of softening for given dynamical requirements. *A&A*, 335:922–928.

Ryden, B. S. and Gunn, J. E. (1987). Galaxy formation by gravitational collapse. *ApJ*, 318:15–31.

Schaye, J., Crain, R. A., Bower, R. G., Furlong, M., Schaller, M., Theuns, T., Dalla Vecchia, C., Frenk, C. S., McCarthy, I. G., Helly, J. C., Jenkins, A., Rosas-Guevara, Y. M., White, S. D. M., Baes, M., Booth, C. M., Camps, P., Navarro, J. F., Qu, Y., Rahmati, A., Sawala, T., Thomas, P. A., and Trayford, J. (2015). The EAGLE project: simulating the evolution and assembly of galaxies and their environments. *MNRAS*, 446:521–554.

Sellwood, J. A. (1981). Bar instability and rotation curves. *A&A*, 99:362–374.

Sellwood, J. A. (2013). *Dynamics of Disks and Warps*, page 923.

Sellwood, J. A. and Wilkinson, A. (1993). Dynamics of barred galaxies. *Reports on Progress in Physics*, 56:173–256.

Sharma, S., Johnston, K. V., Majewski, S. R., Muñoz, R. R., Carlberg, J. K., and Bullock, J. (2010). Group Finding in the Stellar Halo Using M-giants in the Two Micron All Sky Survey: An Extended View of the Pisces Overdensity? *ApJ*, 722:750–759.

Sheffield, A. A., Price-Whelan, A. M., Tzanidakis, A., Johnston, K. V., Laporte, C. F. P., and Sesar, B. (2018). A Disk Origin for the Monoceros Ring and A13 Stellar Overdensities. *ApJ*, 854:47.

Simmons, B. D., Melvin, T., Lintott, C., Masters, K. L., Willett, K. W., Keel, W. C., Smethurst, R. J., Cheung, E., Nichol, R. C., Schawinski, K., Rutkowski, M., Kartaltepe, J. S., Bell, E. F., Casteels, K. R. V., Conselice, C. J., Almaini, O., Ferguson, H. C., Fortson, L., Hartley, W., Kocevski, D., Koekemoer, A. M., McIntosh, D. H., Mortlock, A., Newman, J. A., Ownsworth, J., Bamford, S., Dahlen, T., Faber, S. M., Finkelstein, S. L., Fontana, A., Galametz, A., Grogin, N. A., Grützbauch, R., Guo, Y., Häußler, B., Jek, K. J., Kaviraj, S., Lucas, R. A., Peth, M., Salvato, M., Wiklind, T., and Wuyts, S. (2014). Galaxy Zoo: CANDELS barred discs and bar fractions. *MNRAS*, 445:3466–3474.

Spitzer, Jr., L. (1942). The Dynamics of the Interstellar Medium. III. Galactic Distribution. *ApJ*, 95:329.

Springel, V. (2005). The cosmological simulation code GADGET-2. *MNRAS*, 364:1105–1134.

Tissera, P. B., Scannapieco, C., Beers, T. C., and Carollo, D. (2013). Stellar haloes of simulated Milky-Way-like galaxies: chemical and kinematic properties. *MNRAS*, 432:3391–3400.

Toomre, A. (1964). On the gravitational stability of a disk of stars. *ApJ*, 139:1217–1238.

Vasiliev, E. (2018). AGAMA: Action-based galaxy modelling architecture. *ArXiv e-prints*.

Vogelsberger, M., Genel, S., Sijacki, D., Torrey, P., Springel, V., and Hernquist, L. (2013). A model for cosmological simulations of galaxy formation physics. *MNRAS*, 436:3031–3067.

Weinberg, M. D. (1996). High-Accuracy Minimum Relaxation N-Body Simulations Using Orthogonal Series Force Computation. *ApJ*, 470:715.

Widrow, L. M., Pym, B., and Dubinski, J. (2008). Dynamical Blueprints for Galaxies. *ApJ*, 679:1239–1259.

Yanny, B., Newberg, H. J., Kent, S., Laurent-Muehleisen, S. A., Pier, J. R., Richards, G. T., Stoughton, C., Anderson, Jr., J. E., Annis, J., Brinkmann, J., Chen, B., Csabai, I., Doi, M., Fukugita, M., Hennessy, G. S., Ivezić, Ž., Knapp, G. R., Lupton, R., Munn, J. A., Nash, T., Rockosi, C. M., Schneider, D. P., Smith, J. A., and York, D. G. (2000). Identification of A-colored Stars and Structure in the

Halo of the Milky Way from Sloan Digital Sky Survey Commissioning Data. *ApJ*, 540:825–841.

Yurin, D. and Springel, V. (2015). The stability of stellar discs in Milky Way-sized dark matter haloes. *MNRAS*, 452:2367–2387.

Zang, T. A. and Hohl, F. (1978). Computer experiments on the effect of retrograde stars in disk galaxies. *ApJ*, 226:521–539.

Chapter 5

Forming Vertical Structure in ΛCDM Discs

This chapter contains a draft of a paper submitted to Monthly Notices of the Royal Astronomical Society. Its current manuscript ID is MN-19-3241-MJ.

5.1 Abstract

We perform numerical experiments where stellar discs are inserted into dark matter haloes in a ΛCDM simulation after which the fully-live disc-halo systems are evolved until the present epoch. Prior it its insertion, a disc is treated as a growing, rigid potential whose position and orientation are determined from rigid-body dynamics. When the disc goes live, the disc-halo system is in approximate equilibrium. The discs develop structures such as bars, warps, and bending waves. Not surprisingly, we find that when we insert the disc at a redshift $z = 1$, it develops more structure and exhibits more clearly signs of disequilibrium then when it is inserted later. We identify populations of stars kicked out of the disc to high latitudes that are qualitatively similar what is observed in the Milky Way. An in-depth attempt is made to disentangle the effects of bar buckling, tidal fields due to the generally triaxial halo and from distant subhaloes, and the passage of subhaloes through the inner disc. While our results are consistent with the hypothesis the the kicked-out-disc was produced by a very massive satellite galaxy, we also find that they can arise from the interaction of the disc with its halo. We conclude that in the Milky Way a wide variety of cosmological environments are able to explain disc structures like Monoceros, A13, and TriAnd.

5.2 Introduction

The HI discs of late-type galaxies, when observed edge-on, often exhibit pronounced warps (see, for example, Sancisi (1976); Bosma (1991); García-Ruiz et al. (2002) and reviews by Binney (1992) and Sellwood (2013)). Indeed, the HI warp in the Milky

Way has been known since the work of Oort et al. (1958). There is also evidence for a stellar warp in the Milky Way, which roughly traces that of the HI disc (Cox et al., 1996; Reylé et al., 2009).

The prevalence of warps suggests that a typical stellar disc experiences perturbations normal to its midplane. Recent surveys, particularly of the stellar content in the Galaxy, have revealed other manifestations of vertical perturbations. For example, surveys such as the Sloan Extension for Galactic Understanding and Exploration (SEGUE) and Gaia Data Release 2 (GDR2) have uncovered an asymmetry with respect to the Galactic midplane in stellar number counts in the vicinity of the Sun (Widrow et al., 2012; Yanny and Gardner, 2013; Bennett and Bovy, 2019). In addition, bulk motions of stars normal to the midplane have been found in data from SEGUE, the Radial Velocity Experiment (RAVE), the LAMOST survey, and GDR2 (Widrow et al., 2012; Williams et al., 2013; Carlin et al., 2013; Pearl et al., 2017; Carrillo et al., 2018; Gaia Collaboration et al., 2018). Furthermore, a corrugation in stellar number counts with a wavelength of $\sim 5\,\mathrm{kpc}$ and an amplitude of $\sim 100\,\mathrm{pc}$ has been detected between 10 and 15 kpc in Galactocentric radii (Xu et al., 2015). Corrugations in the velocity field of gas discs in external galaxies have also been observed (Matthews and Uson, 2008; Sánchez-Gil et al., 2015, for example).

In addition to waves and corrugations, several stream-like stellar structures in the Milky Way may have originated within the disc. In the past, these structures were thought to comprise stars tidally stripped from disrupted dwarf galaxies or globular clusters. Recently, the idea that some of the streams are actually stars 'kicked out' of the disc has gained traction. One example is the Monoceros ring (Newberg et al., 2002; Yanny et al., 2003), also called the Galactic Anticentre Stellar

Structure (GASS) (Crane et al., 2003; Rocha-Pinto et al., 2003), which is located at low latitudes towards the Galactic anti-centre at a Galactocentric distance of about 18 kpc. The coincidence in position and velocity of GASS and disc stars suggests that a disc origin may be a more likely explanation than tidal stripping (Deason et al., 2018; Sheffield et al., 2018). Similar structures have been found in the outer disc, most notably the Triangulum-Andromeda clouds (TriAnd) (Rocha-Pinto et al., 2004) and A13 (Sharma et al., 2010). There is also evidence for kicked-out stars in M31 (Richardson et al., 2008; Dorman et al., 2013; Bernard et al., 2015) and M33 (McConnachie et al., 2006, 2010). (For a review of the kicked-out-disc hypothesis, see Johnston et al. (2017).)

There is now a concerted effort to explain vertical disequilibria in Milky Way-like galaxies. Much of this effort has focused on the hypothesis that a single massive subhalo, such as the Sagittarius dwarf spheroidal galaxy (Sgr dSph) (Ibata et al., 1994), is responsible for much of the vertical structure in the Milky Way. Simulations of a single satellite encounter with an isolated galaxy have been used to study this hypothesis (Purcell et al., 2011; Gómez et al., 2013; Widrow et al., 2014; Feldmann and Spolyar, 2015; de la Vega et al., 2015; D'Onghia et al., 2016; Laporte et al., 2016, 2018a,b, for example). While many of the observed features are easily reproduced in the simulations, it appears that a very massive ($10^{11}\,M_\odot$) Sgr dSph-like satellite is required to explain the extraplanar streams in the outer disc (Laporte et al., 2018b).

The single-satellite encounter is a rather idealized scenario; disc-environment interactions in real galaxies will, of course, be more complicated. In particular, discs may be continually perturbed by any number of satellites or dark matter subhaloes whose orbits take them into the disc region of the galaxy. Early steps toward a more realistic model were taken by Font et al. (2001) and Gauthier et al. (2006) who allowed for a system of subhaloes. In particular, Gauthier et al. (2006) simulated an M31-like disc in a dark halo where roughly 10% of the smooth halo mass was replace by dark subhaloes with a mass spectrum motivated by cosmological ΛCDM simulations. They found that one or more of the subhaloes triggered the formation of a bar. Further analyses of this simulation and a similar one by Chequers et al. (2018) found that the system of subhaloes could excite a plethora of vertical structure. However, these simulations failed to create the streams of disc stars described above.

When a satellite passes through the plane of disc, it interacts with the disc through a process akin to dynamical friction. Essentially, disc stars fall in behind the satellite, disrupting and ultimately heating the disc (Sellwood et al., 1998). On the other hand a distant but very massive satellite can excite bending modes via differential acceleration. In the simple example of a satellite falling toward the disc along its spin axis, the acceleration of the disc toward the satellite decreases with radius. Thus, as the satellite passes through the centre of the disc, it will set up axisymmetric bending modes as seen in Sellwood (1996).

Finally, we note that dark haloes in ΛCDM cosmologies are thought to be aspherical and will therefore exert torques on the disc that can cause it to bend and warp. The effect is due to a misalignment of the disc symmetry axis with any of the approximate symmetry axes of the halo. For example, Hu and Sijacki (2016) embed discs in triaxial haloes. In their appendix, strong warps can be seen in discs which are substantially misaligned from their haloes. Gómez et al. (2017) found that vertical structure was ubiquitous in their hydrodynamical cosmological simulations, some of which did not have discs in a stable orientation to their host halo.

In this paper, we study the vertical structure that develops in discs embedded in realistic ΛCDM haloes. We use a disc insertion scheme to set up initial conditions where a stellar disc is in approximate equilibrium with a cosmological halo (Berentzen and Shlosman, 2006a; DeBuhr et al., 2012; Yurin and Springel, 2015; Bauer et al., 2018; Hu and Sijacki, 2018). Our scheme affords us more control over the structural properties of the disc than would be possible in fully self-consistent hydrodynamical simulations and was successfully used to study bar formation in a cosmological context in Bauer and Widrow (2018). In fact, bar buckling is another mechanism for exciting vertical structure in stellar discs (Khoperskov et al., 2018), a point we return to later in this paper.

Our paper is organized as follows: In §5.3 we present two toy models that serve to illustrate the mechanisms by which satellites can excite bending modes in a stellar disc. An overview of the cosmological simulations is given in §5.4 while the time evolution and key structural features of the discs in these simulations are discussed in §5.5. In §5.6 we examine how stars are kicked out of discs. We relate our key results to other studies in §5.7 and present a summary and some concluding remarks in §5.8.

5.3 Single satellite simulations

In this section, we illustrate some of the factors driving vertical structure in stellar discs through two toy models where a disc interacts with a single subhalo.

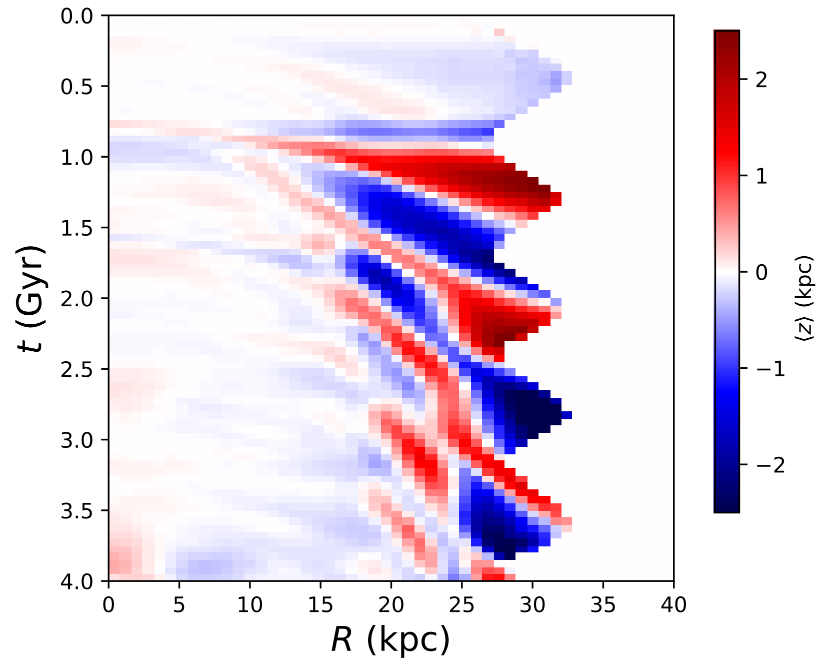

Figure 5.1: Mean vertical displacement, $\langle z \rangle$, of the disc for the toy model described in §5.3.1 as a function of R and t.

5.3.1 Axisymmetric subhalo encounter

In our first experiment, the subhalo is initially at rest and positioned 100 kpc from the centre of the disc along its symmetry axis. We generate the initial conditions for the disc, halo, and subhalo using the GalactICS code (Kuijken and Gilmore, 1989; Widrow et al., 2008). The disc has an exponential surface density with scale length $R_d = 3.7\,\mathrm{kpc}$ and mass $M_d = 4 \times 10^{10}\,M_\odot$. The halo has an NFW density profile (Navarro et al., 1997), with scale length $R_h = 33.2\,\mathrm{kpc}$, virial mass $M_h = 1.1 \times 10^{12}$, and concentration $c = 6.7$. We use 10^6 halo particles and 3.5×10^6 disc particles. The subhalo is also assumed to have an NFW profile with scale length $R_h = 1.70\,\mathrm{kpc}$, virial mass $M_h = 2.7 \times 10^{10}$, and concentration $c = 38.1$. The choice

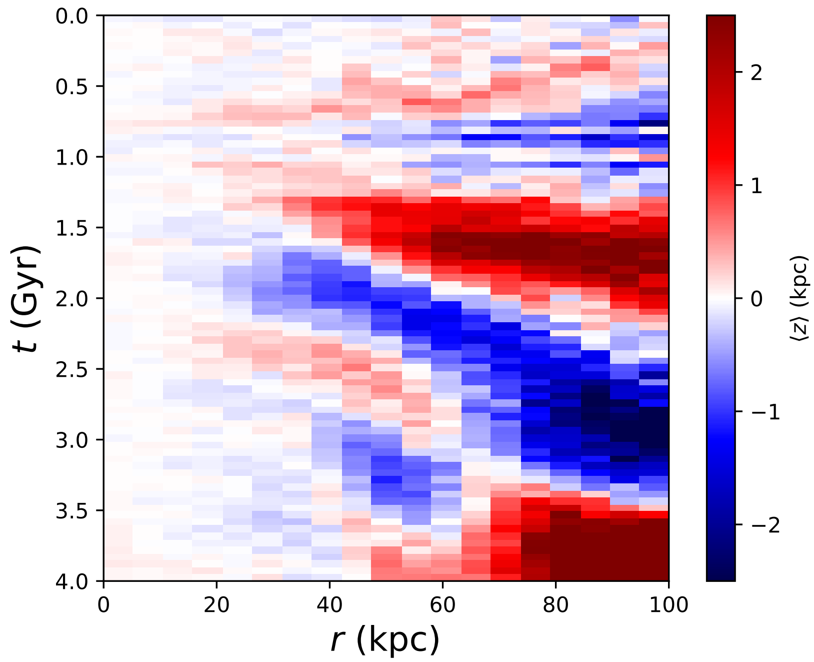

Figure 5.2: Mean vertical displacement of the halo in the toy model described in §5.3.1 as a function of spherical radius r and t.

of parameters for the disc, halo, and subhalo are motivated by examples from our suite of cosmological simulations. The simulation is performed using GADGET-3, a privately released version of the popular GADGET-2 code (Springel, 2005).

In Fig. 5.1 we show the azimuthally averaged vertical displacement, $\langle z \rangle(R, t)$. The displacement is relative to the disc midplane, defined by the mean z of all the particles. This quantifies axisymmetric vertical perturbations, that is, $m = 0$ vertical perturbations where m is the azimuthal mode number. More generally, for a quantity

Θ, we define the m-fold symmetric Θ_m,

$$\Theta_m = \frac{1}{M_S} \int_S \mathrm{d}^3\mathbf{r}\mathrm{d}^3\mathbf{v} f(\mathbf{r},\mathbf{v})\Theta(\mathbf{r},\mathbf{v})e^{im\phi_j} \tag{5.1}$$

$$\approx \frac{1}{M_S} \sum_{j\in S} m_j \Theta(\mathbf{r}_j,\mathbf{v}_j)e^{im\phi_j} \tag{5.2}$$

where M_S is the mass in a region S, $f(\mathbf{r},\mathbf{v})$ is the phase space distribution function, ϕ_j is the azimuthal angle of the j-th particle in S, and m_j is the mass of the j-th particle in S.

At first the disc is relatively unperturbed; the subhalo is so far away that it exerts an approximately uniform acceleration across the disc. Only in the very outer disc do we see slight disc flapping, that is, a lagging of the outer disc relative to the inner one. The lag is more pronounce as the subhalo makes its first pericentric passage. After the subhalo has passed through the disc, at about 1 Gyr, the pattern reverses as the center of the disc is pulled back down. The resulting lag of the outer disc then shows up as a positive signal. The disc develops a corrugation pattern as seen in the alternating red and blue bands (positive and negative $\langle z\rangle$). These bending waves propagate outward (bands stretch down and to the right in the figure.) Over time, the wavelength decreases as does the speed of propagation. Note that the strong (> 1 kpc) flapping of the disc beyond 20 kpc persists for many dynamical times (see, also Sellwood (1996)) and weaker corrugation patters are seen further in.

Qualitatively similar behaviour is seen in the halo. In Fig. 5.2 we show $\langle z\rangle$, this time averaged in spherical shells in the halo. At early times, the halo is dragged along with the subhalo. Eventually, we get a sloshing back and forth of the halo.

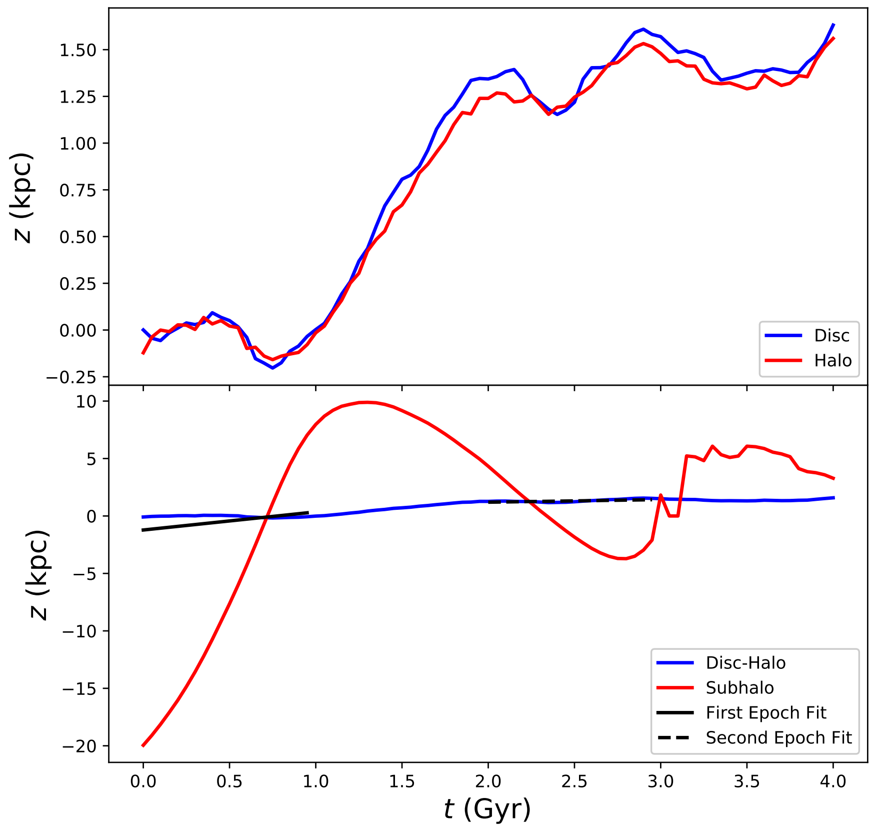

Figure 5.3: Top panel: Orbit of the disc (blue) and inner halo (red) in the toy model described in §5.3.2. Only the z-components of the disc and halo position vectors are shown. Bottom panel: Orbits of the disc and inner halo (blue) and subhalo density peak (red). The black lines show the fits for the two epoch as described in the text.

5.3.2 Off-axis subhalo encounter

In our second experiment, the satellite is again initialized at rest 100 kpc from the centre of the disc, but this time at an angle of just 12° from the disc plane. The choice of orbit is motivated by a satellite in one of our cosmological simulations. The parameters for the disc, halo, and subhalo are the same as in §5.3.1.

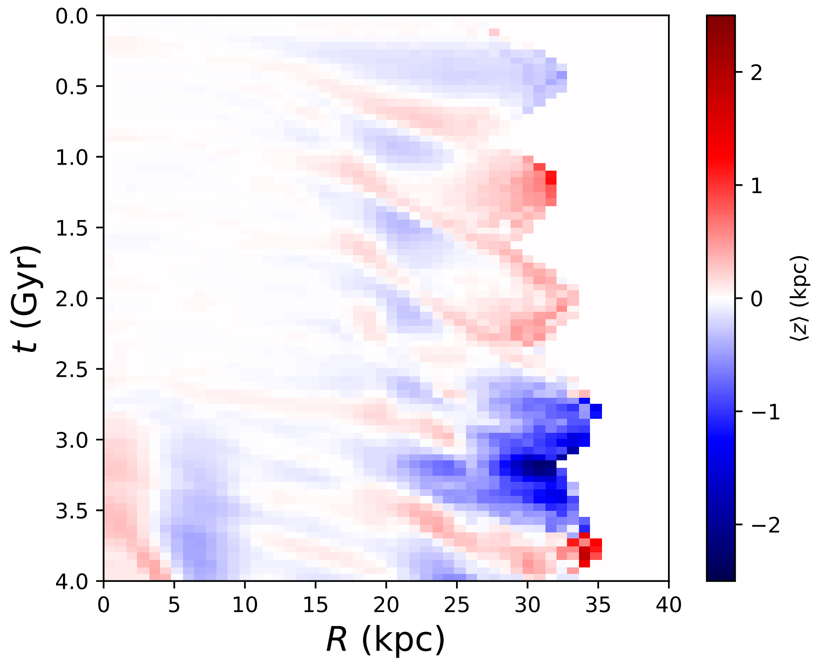

Figure 5.4: Mean height, $\langle z \rangle$, of the disc for the toy model described in §5.3.2 as a function of R and t.

In the upper panel of Fig. 5.3 we plot the z coordinates of the position vector $\mathbf{r}_d$ of the disc and $\mathbf{r}_h$, the position vector of the peak halo density. Evidently, the halo density peak and centre of the disc closely track one another. We next define a common position vector for the disc and inner halo:

$$\mathbf{r}_{dh} = \frac{M_d \mathbf{r}_d + M_{h,20} \mathbf{r}_{h,20}}{M_d + M_{h,20}} \tag{5.3}$$

where we have arbitrarily used 20 kpc to define the inner halo. Given the closeness of $\mathbf{r}_d$ and $\mathbf{r}_h$, the choice of this definition shouldn't effect the results that follow.

Our working hypothesis is that during periods between perigalactic passages, the subhalo and the combination of the disc and inner halo can be treated as a two-body system. That is, $\mathbf{r}_{dh}$ and $\mathbf{r}_{sh}$, where the latter is the position vector for the peak of the subhalo, satisfy the equation

$$\frac{M_{dh}\mathbf{r}_{dh} + M_{sh}\mathbf{r}_{sh}}{M_{dh} + M_{sh}} = \mathbf{r}_{c,0} + \mathbf{v}_{c,0}t \tag{5.4}$$

where M_{dh} and M_{sh} are the effective disc-halo and subhalo masses.

To test our hypothesis, we maximize the likelihood function

$$\ln \mathcal{L} = -\frac{\chi^2}{2\sigma_d^2} - N \ln \sigma_d/\mathrm{kpc} \tag{5.5}$$

over the parameters $\mathbf{r}_{c,0}$, $\mathbf{v}_{c,0}$, M_{dh}, and M_{sh}. Here, N is the number of snapshots, σ_d is the RMS difference between the model and the data, and

$$\chi^2 = \left| \frac{M_{dh}\mathbf{r}_{dh} + M_{sh}\mathbf{r}_{sh}}{M_{dh} + M_{sh}} - (\mathbf{r}_{c,0} + \mathbf{v}_{c,0}t) \right|^2 . \tag{5.6}$$

Maximization is done in two 1 Gyr epochs centered on 0.5 Gyr and 2 Gyr, respectively. These windows are chosen to avoid the pericentric passages at 0.85 Gyr and 3 Gyr, when the subhalo is losing the most mass when the system will be poorly described by a two-body model. The center-of-mass motion lines, $\mathbf{r}_{c,0} + \mathbf{v}_{c,0}t$ for the two epochs are shown in Fig. 5.3. The inferred effective mass ratios $M_{sh} : M_{dh}$ are 16:1 and 85:1, respectively. Thus, the effective mass of the subhalo has been reduced by a factor of ~ 5, presumably due to tidal stripping. We also find that $\sigma_d = 190\,\mathrm{pc}$ and $290\,\mathrm{pc}$ for the two epochs. The fact that the values for σ_d are as small as they are supports our hypothesis of a two-body model for the disc-halo/subhalo system.

In Fig. 5.4 we plot the mean height across the disc as a function of radius and time. The general corrugation pattern is similar to the one seen in our first experiment though the amplitude is smaller. The difference in amplitude is no doubt due to the fact that we are averaging over azimuth in an experiment that lacks azimuthal symmetry.

5.4 Simulations

In this section, we summarize our cosmological simulations beginning with a brief description of our disc insertion scheme.

5.4.1 Disc Insertion Technique

Our disc insertion scheme (Bauer et al., 2018) expands upon the method introduced by Berentzen and Shlosman (2006b), DeBuhr et al. (2012), and Yurin and Springel (2015). It uses an iterative procedure to initialize an axisymmetric, smooth disc in a cosmological halo, that is generally clumpy and triaxial. The first step is to run a pure dark matter simulation and identify a suitable halo. We then rerun the simulation with a rigid disc potential that grows from zero to that of the fully formed disc between an initial scale factor, a_g, to a final scale factor, a_l. When the simulation reaches a_l, the rigid disc is replaced by an N-body system and the "live" disc-halo system is evolved to the present epoch at $a = 1$.

For our pure dark matter simulation, we implement the zoom-in technique of Katz et al. (1994) and Navarro et al. (1994). We select Milky Way-like haloes with no major mergers and use the results of Oñorbe et al. (2014) to ensure minimal contamination of low-resolution particles. Our choice of cosmological parameters is based on the

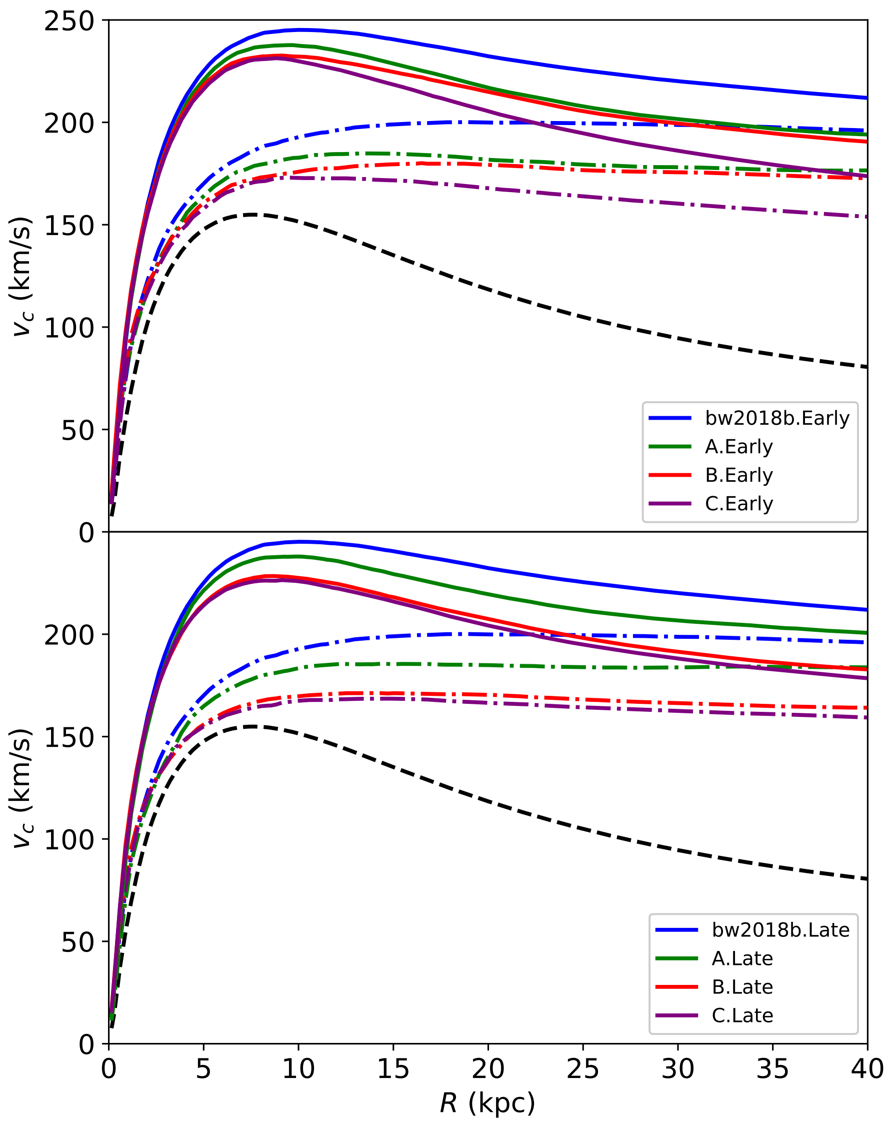

Figure 5.5: Circular speed curves for cosmological models. The same disc is used in all runs, and its rotation curve contribution is shown by the black dashed line. The halo contributions for the Early and Warm subsuites are shown in the top panel as dot-dashed lines, while the total rotation curves are shown as solid curves. The bottom panel shows the same for the Late subsuite.

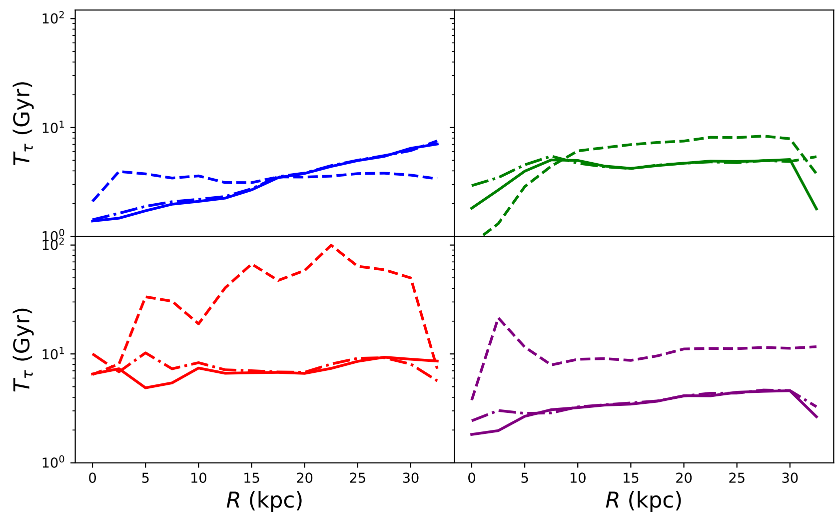

Figure 5.6: The torque timescale, T_τ, at initialization as a function of R. Colours are the same as in Fig. 5 with bauer2018b in the upper left panel, A in the upper right, B in the lower left, and C in the lower right. Line types are Early (solid), Warm (dot-dashed), and Late (dashed).

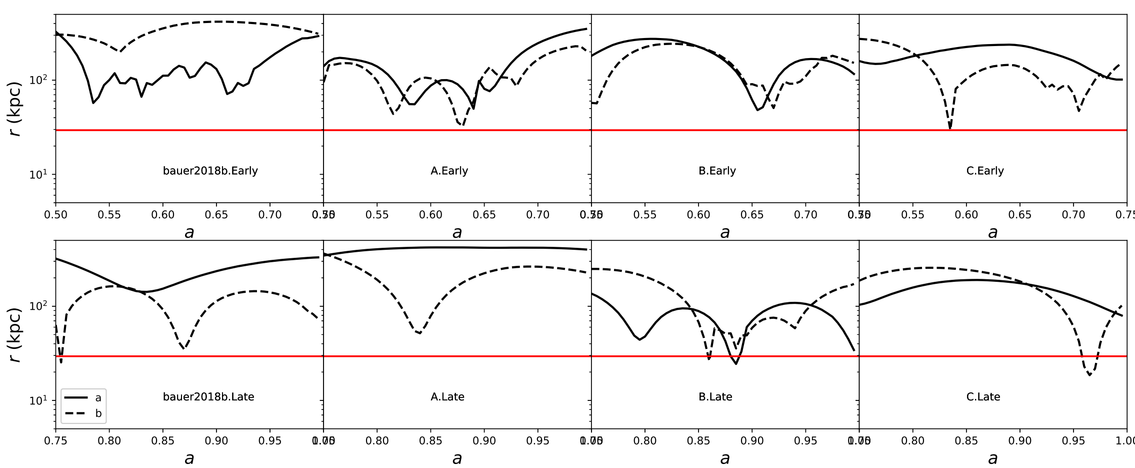

Figure 5.7: Orbits of the most massive subhalo (solid curve) and second most massive subhalo (dashed curve) for the fiducial suite (top panel) and late insertion suite (bottom). These are the substructures listed as the top two entries for each simulation in Table 5.2. The red line denotes $20\,h^{-1}\,\mathrm{kpc} = 29.5\,\mathrm{kpc}$.

results from Planck 2013 (Planck Collaboration et al., 2014): $H_0 = 67.9\,\mathrm{km\,s^{-1}\,kpc^{-1}}$, $\Omega_b = 0.0481$, $\Omega_0 = 0.306$, $\Omega_\Lambda = 0.694$, $\sigma_8 = 0.827$, and $n_s = 0.962$. N-body initial conditions for the dark matter particles are generated with the MUSIC code (Hahn and Abel, 2013).

During its growth phase from $a_g = 0.25$ to $a_l = 0.5$[1], the disc is treated as a rigid body whose orientation and center-of-mass position evolve according to the standard equations of rigid body dynamics. Bauer et al. (2018) found that the rigid disc assumption is actually quite true to the orientation and center of mass evolution of a pure stellar disc. At a_l, we swap a live disc for the rigid one using a modified version of GalactICS (Kuijken and Gilmore, 1989; Widrow et al., 2008), which generates a three-integral DF disc in the best axisymmetric approximation to the halo Bauer et al. (2018).

5.4.2 Numerical Experiments

We present a concise description of our cosmological models in Table 5.1. The haloes are chosen such that the total circular speed curves are similar to the Milky Way's. Note that the bauer2018b simulations use a halo from Bauer and Widrow (2018). The haloes used in the A, B, and C simulations are previously unpublished. In the simulations denoted as X.Early, the disc is inserted at $a_l = 0.5$; for those denoted X.Lake, $a_l = 0.75$. One of the benefits of disc insertion techniques is the ability to modify disc properties in the same halo. We exploit this capability in our third suite, denoted as X.Warm, where we increase the disc's dynamical temperature as measured by the Toomre Q parameter (Toomre, 1964).

[1] For reference, $a = 0.25$ is 2.2 Gyr after the Big Bang, $a = 0.5$ is 5.9 Gyr after the Big Bang, and $a = 0.75$ is 10.0 Gyr after the Big Bang. The age of this Universe at present day is 13.8 Gyr.

Fig. 5.5 shows the circular speed curves for all disc-halo combinations. There are relatively small variations in the circular speed for $R < 5\,\mathrm{kpc}$ where the disc dominates. The variations are significant ($\sim 10\,\mathrm{km\,s^{-1}}$) near the peak of the circular speed curve and even larger beyond the disc where the halo dominates the gravitational potential. In all cases, the disc is submaximal. In particular, the ratio of the square of the disc contribution to the rotation curve and square of the total rotation curve measured at $2.2\,R_d$, $V_d^2/V_{tot}^2|_{R=2.2\,R_d}$, ranges between 0.37 and 0.46. These values are well below the lower bound for a maximal disc advocated by Sackett (1997).

In the discussion that follow, we focus on three archetypal simulations:

1. **strong disc-subhalo interaction:** In B.Late the disc has close interactions with two subhaloes but no substantial disc-halo misalignment. One of these subhaloes passes twice through the plane of the disc.

2. **disc-halo misalignment:** C.Early presents a case a substantial misalignment from its host halo (see below) but relatively modest subhalo interactions with the disc.

3. **distant massive subhaloes:** The disc in A.Early is relatively well aligned to its host halo, but its most massive substructures do not interact closely with the disc.

To illustrate how the simulations differ, consider Fig. 5.8 where we plot the component of the torque perpendicular to the spin axis of the disc across the disc plane. In B.late, we have the localized effect of a subhalo that passes through the plane of the disc. On the other hand, in C.Early, we have a strong $m = 2$ torque due to the large-scale structure of the halo and misalignment of the disc with any of the halo's approximate symmetry axes.

5.4.3 Halo Environments

To further quantify the effect of the halo environment we define a torque timescale:

$$T_\tau(R) = \frac{L(R)}{\tau_\perp(R)}, \tag{5.7}$$

where $L(R)$ is the magnitude of the angular momentum in a ring centered at radius R and $\tau_\perp(R)$ is the azimuthally-averaged component of the torque that is perpendicular to the spin axis of the disc. The greater the misalignment between disc and halo, the larger the torque of the halo on the disc, and the shorter the timescale T_τ. In Fig. 5.6, we plot T_τ as a function of radius at initialization for our models. In general, the effect of tidal torques from the halo are smaller at late times when much of the substructure and triaxiality of the halo has been washed out. We also infer that the effect of the halo in torquing the disc is largest in C.Early.

In Table 5.2, we list the five most massive (at initialization) substructures for each of our simulations while the orbits of the two most massive substructures are shown in Fig. 5.7. The orbits present a wide variety of behaviour. For example, the subhaloes in bauer2018b.Early spend most of their lives in the outer halo on roughly tangential orbits. By contrast, the second most mass subhalo in C.late orbits to within $\sim 20\,\mathrm{kpc}$ of the disc centre. The subhaloes in A.early are more massive but never reach to within $30\,\mathrm{kpc}$.

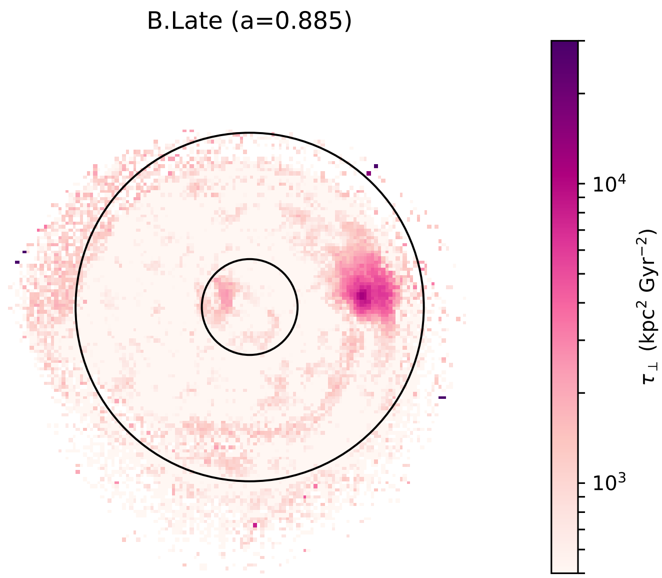

(a)

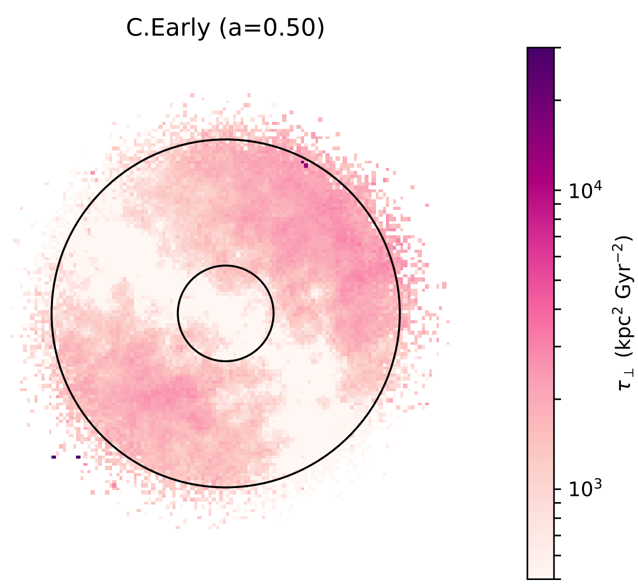

(b)

Figure 5.8: The component of the torque perpendicular to the spin axis of the disc across the disc plane. Top panel is for B.Late at $a = 0.885$ when the most massive subhalo is at pericentre. The bottom panel is for C.Early at initialization ($a = 0.5$). The circles correspond to $R_p = 2.2\,R_d = 8.1\,\text{kpc}$ and $20\,h^{-1}\,\text{kpc} = 29.5\,\text{kpc}$.

Table 5.1: Table of simulations run in the main experiment. M_h is the virial mass of the host halo, R_h is the NFW scale length of the host halo, c is the NFW concentration parameter of the host halo, a_l is the live disc insertion scale factor, $\delta\Theta_{h,20}$ is the halo misalignment angle for the 20 kpc shell, N_d is the number of disc particles, Q is the Toomre stability parameter of the disc at initialization, and f_{kud} is the fraction of disc mass that gets classified as kicked-out-disc (KOD) stars measured at present day with $\eta = 8$.

	M_h ($M_\odot$)	R_h (kpc)	c	a_l	N_d	Q	$\cos\delta\Theta_{h,20}$	f_{kud}
bauer2018.Early	1.0×10^{12}	15.9	9.84	0.50	1.0×10^{6}	1.1	0.16	1.2×10^{-2}
bauer2018.Warm	1.0×10^{12}	15.9	9.84	0.50	1.0×10^{6}	1.1	0.16	1.1×10^{-2}
bauer2018.Late	1.2×10^{12}	15.2	15.4	0.75	1.0×10^{6}	1.8	0.93	4.2×10^{-3}
A.Early	9.4×10^{11}	17.8	8.56	0.50	3.5×10^{6}	1.3	0.97	3.7×10^{-3}
A.Warm	9.4×10^{11}	17.8	8.56	0.50	3.5×10^{6}	1.8	0.97	1.6×10^{-3}
A.Late	1.1×10^{12}	18.5	12.1	0.75	3.5×10^{6}	1.3	0.98	6.8×10^{-5}
B.Early	5.9×10^{11}	10.4	12.6	0.50	3.5×10^{6}	1.3	0.91	8.5×10^{-4}
B.Warm	5.9×10^{11}	10.4	12.6	0.50	3.5×10^{6}	1.8	0.91	1.2×10^{-3}
B.Late	1.1×10^{12}	33.2	6.70	0.75	3.5×10^{6}	1.3	0.99	9.2×10^{-4}
C.Early	4.3×10^{11}	8.33	14.1	0.50	3.5×10^{6}	1.3	0.84	5.3×10^{-3}
C.Warm	4.3×10^{11}	8.33	14.1	0.50	3.5×10^{6}	1.8	0.84	5.6×10^{-3}
C.Late	6.7×10^{11}	13.6	14.0	0.75	3.5×10^{6}	1.3	0.92	1.0×10^{-4}

Table 5.2: Table of the five most massive substructures at a_l in all of the simulations detailed in Table 5.1. The virial mass, M_s, and NFW scale radius, R_s, are given.

Subhalo Name ($z = 1$)	$M_s\,(M_\odot)$	R_s (kpc)	c	Subhalo Name ($z = 0.333$)	$M_s\,(M_\odot)$	R_s (kpc)	c
bauer2018b.Early.a	1.4×10^{10}	3.75	9.92	bauer2018b.Late.a	1.6×10^{10}	3.35	16.5
bauer2018b.Early.b	1.0×10^{10}	1.02	32.8	bauer2018b.Late.e	0.7×10^{10}	0.27	154.
bauer2018b.Early.c	0.5×10^{10}	2.60	10.1	bauer2018b.Late.c	0.3×10^{10}	0.07	485.
bauer2018b.Early.d	0.4×10^{10}	1.51	15.7	bauer2018b.Late.d	0.3×10^{10}	1.06	29.8
bauer2018b.Early.e	0.2×10^{10}	0.28	69.0	bauer2018b.Late.e	0.2×10^{10}	0.38	76.7
A.Early.a	1.8×10^{10}	2.69	15.3	A.Late.a	1.3×10^{10}	2.62	19.6
A.Early.b	1.2×10^{10}	1.26	28.4	A.Late.b	0.9×10^{10}	0.61	74.8
A.Early.c	1.0×10^{10}	0.71	47.9	A.Late.c	0.5×10^{10}	0.77	46.4
A.Early.d	0.7×10^{10}	2.29	13.0	A.Late.d	0.4×10^{10}	1.69	19.7
A.Early.e	0.5×10^{10}	1.73	13.2	A.Late.e	0.2×10^{10}	1.25	21.5
B.Early.a	1.1×10^{10}	1.76	19.4	B.Late.a	2.7×10^{10}	1.70	38.1
B.Early.b	0.2×10^{10}	0.41	47.5	B.Late.b	1.2×10^{10}	2.27	22.0
B.Early.c	0.2×10^{10}	0.67	28.4	B.Late.c	0.6×10^{10}	2.67	14.4
B.Early.d	0.2×10^{10}	1.81	10.3	B.Late.d	0.4×10^{10}	1.42	24.0
B.Early.e	0.2×10^{10}	0.54	34.0	B.Late.e	0.4×10^{10}	1.13	29.7
C.Early.a	1.0×10^{10}	1.78	18.5	C.Late.a	0.5×10^{10}	0.18	194.
C.Early.b	0.6×10^{10}	0.92	30.0	C.Late.b	0.4×10^{10}	6.37	5.46
C.Early.c	0.3×10^{10}	2.24	10.2	C.Late.c	0.4×10^{10}	0.75	46.2
C.Early.d	0.1×10^{10}	0.91	18.7	C.Late.d	0.3×10^{10}	1.26	26.1
C.Early.e	0.1×10^{10}	0.25	60.3	C.Late.e	0.3×10^{10}	6.78	4.81

5.5 Structure and Evolution of Simulation Models

In this section we summarize the evolution of the models in our simulations. We begin with a discussion of bar formation and then turn to bending and warping of the discs.

5.5.1 Bar Formation

In isolation, a disc-halo system forms a bar when $m = 2$ density instabilities, seeded by shot noise-induced perturbations, exponentially grow (Efstathiou et al., 1982). Factors such as the relative contribution of the disc to the rotation curve, radial velocity dispersion, and the disc scale height broadly determine formation rate, strength, and length of the bar (Athanassoula and Sellwood, 1986; Christodoulou et al., 1995; Klypin et al., 2009; Sellwood, 2013; Bauer and Widrow, 2018). Strong environmental perturbers such as halo substructure and tides can induce bar formation even in discs that resist bar formation in isolation (Gauthier et al., 2006; Kazantzidis et al., 2008; Purcell et al., 2011).

DeBuhr et al. (2012); Yurin and Springel (2015) used a disc insertion scheme similar to the one used here and found that in the absence of a classical bulge stellar discs always formed bars in a cosmological environment, even if they are submaximal. In a previous paper, we argued that these simulations overestimated the susceptibility of a disc to forming strong bars (Bauer and Widrow, 2018). This argument stems from the observation that the discs in DeBuhr et al. (2012) and Yurin and Springel (2015) were too thick by a factor of ~ 2 as compared with the thickness of the Milky Way and similar galaxies. We found that the more realistic thin discs grow bars more quickly that then buckle. Since buckling regulates the strength of the bar, the net

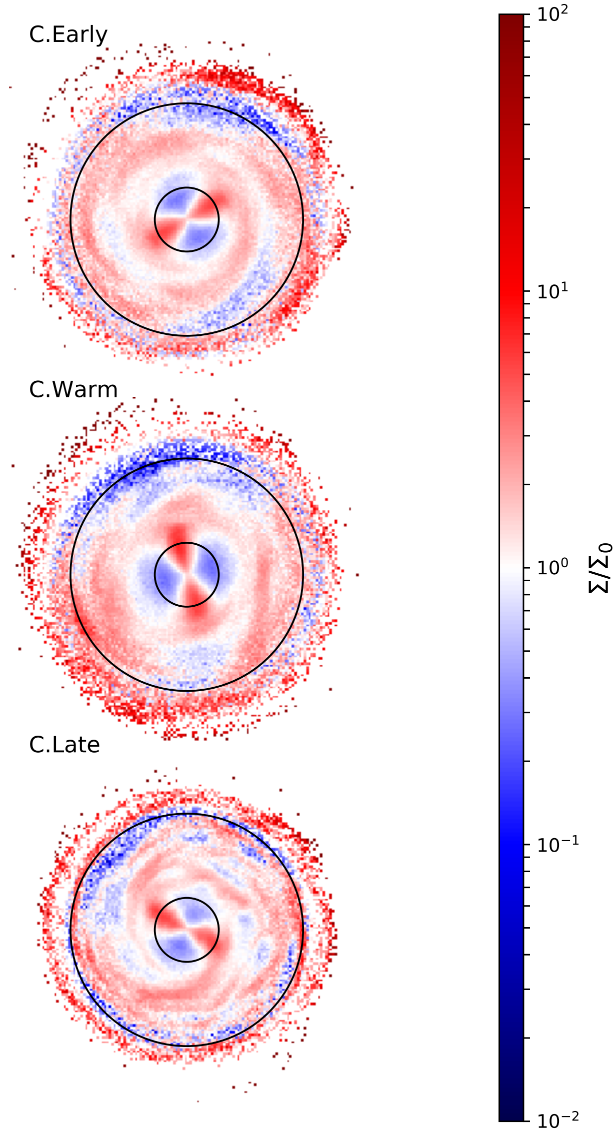

Figure 5.9: The ratio of surface density, Σ, to azimuthally averaged surface density, Σ_0 for the C.Early, C.Warm, and C.Late models. The circles correspond to $R_p = 2.2\,R_d = 8.1\,\mathrm{kpc}$ and $20\,h^{-1}\,\mathrm{kpc} = 29.5\,\mathrm{kpc}$.

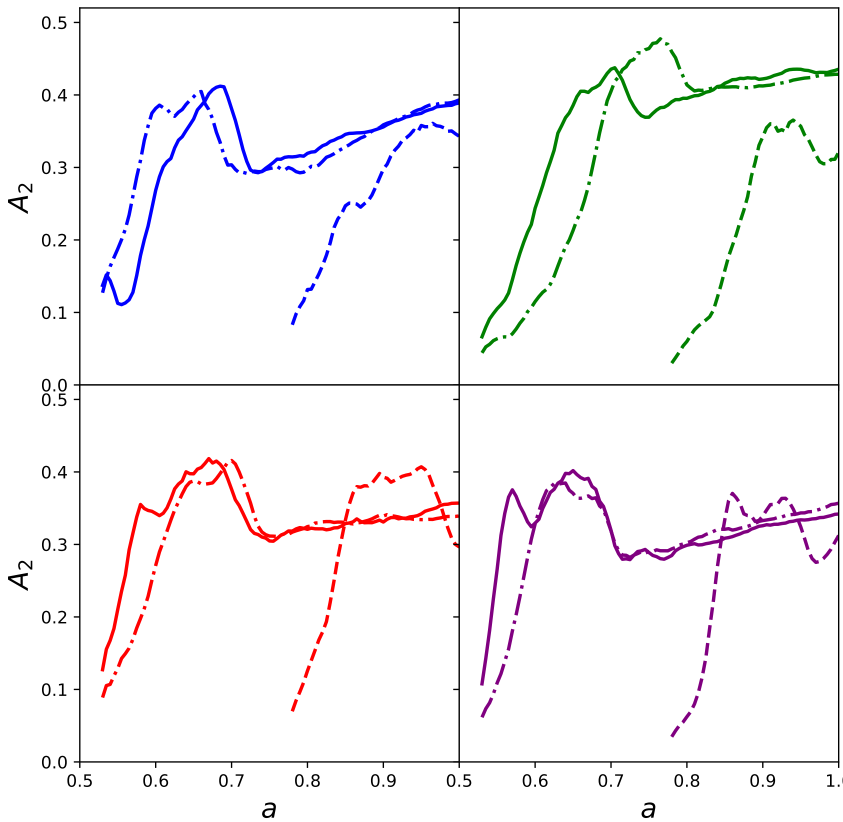

Figure 5.10: Bar strength as measured by $A_2(< R_p)$ as a function of time for all models.

result is that bars in thin discs end up being weaker than those in thick discs (Klypin et al., 2009; Bauer and Widrow, 2018).

In Fig. 5.9 we show the ratio of the surface density across the face of the disc to the azimuthally-averaged surface density for the final snapshots of the C.Early, C.Warm, and C.Late simulations. Similar results are obtained for the bauer2018, A, and B simulations. Bars form in all three simulations, as evidenced by the X-pattern at the centre of the disc. The bar connects with a two-armed spiral in C.Early and

C.Late. The bar-spiral arm connection is less obvious in the C.Warm simulation.

In Fig. 5.10, we plot the bar strength parameter ($\Theta = 1$ in Eq. (5.2)) evaluated in the region $R < 2.2R_p$ (Debattista and Sellwood, 2000). We see that all models experience some kind of buckling event, which reduces A_2 by $20 - 30\%$. With the exception of bauer2018b, bar formation and buckling is delayed in the warm disc simulations relative to the cold disc ones.

Broadly speaking, our simulations form bars similar to that of the Milky Way's bar in strength and length. The bulk of the bar mass in all simulations appears contained to within $R_p = 2.2\,R_d$ The late-insertion suite shows a reduced bar length, bolstering an idea presented in Bauer and Widrow (2018) that for similar galaxies, one might be able to use the bar length to compare relative ages of stellar discs.

5.5.2 Disc Heating

Vertical heating and thickening in stellar discs is a well-studied phenomenon, which can be driven by bars and spiral structure (McMillan and Dehnen, 2007; Sellwood, 2013) or by interactions of the disc with its satellites and its dark halo (Lacey and Ostriker, 1985; Toth and Ostriker, 1992; Sellwood et al., 1998; Bauer and Widrow, 2018, for example). These effects suggest that disc in a cosmological environment should thicken with time, and indeed, this is confirmed in our simulations. Fig. 5.11 shows the evolution of z_{rms} for each disc in the fiducial and warm suites. We see that substantial heating follows bar buckling in each simulation, a result consistent with Gauthier et al. (2006); Kazantzidis et al. (2008); Yurin and Springel (2015); Bauer and Widrow (2018). We note that the warm suite exhibits up to 25% more disc heating. There is little to say about disc heating in the late-insertion simulations

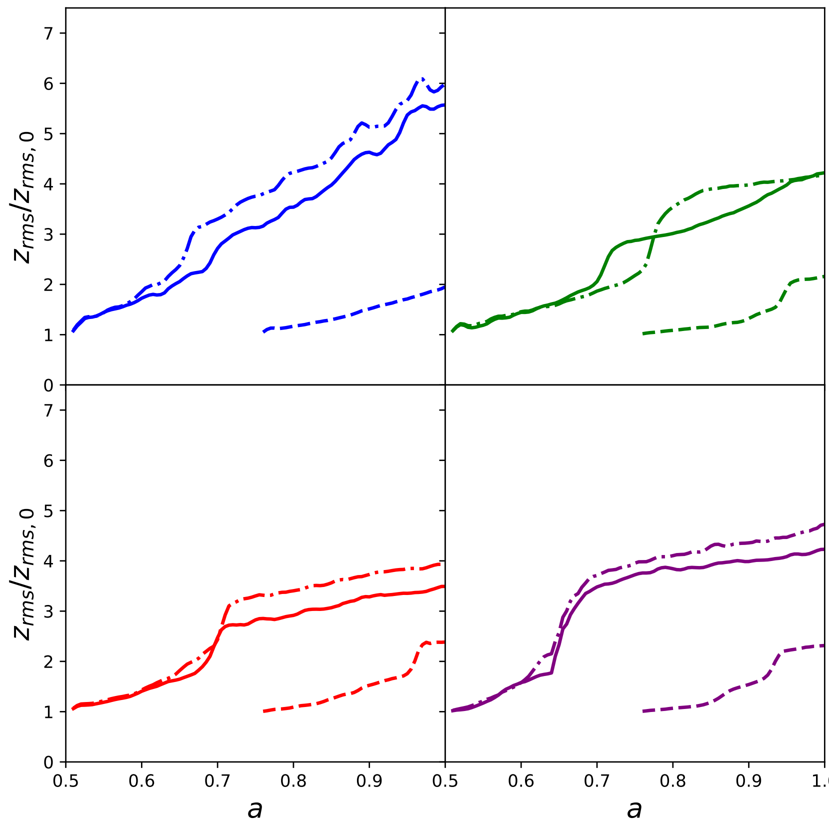

Figure 5.11: Disc height as measured by $z_{rms}/z_{rms,0}$ as a function of time for all models.

except that the discs approximately double in thickness over the simulation time. These simulations end as the buckling is just beginning.

5.5.3 Bending waves in Cosmological Discs

In Fig. 5.12 we show mean vertical displacement ($\langle z \rangle$) maps for a single snapshot for our twelve simulations. We choose $a = 0.625$ for the early insertion runs and

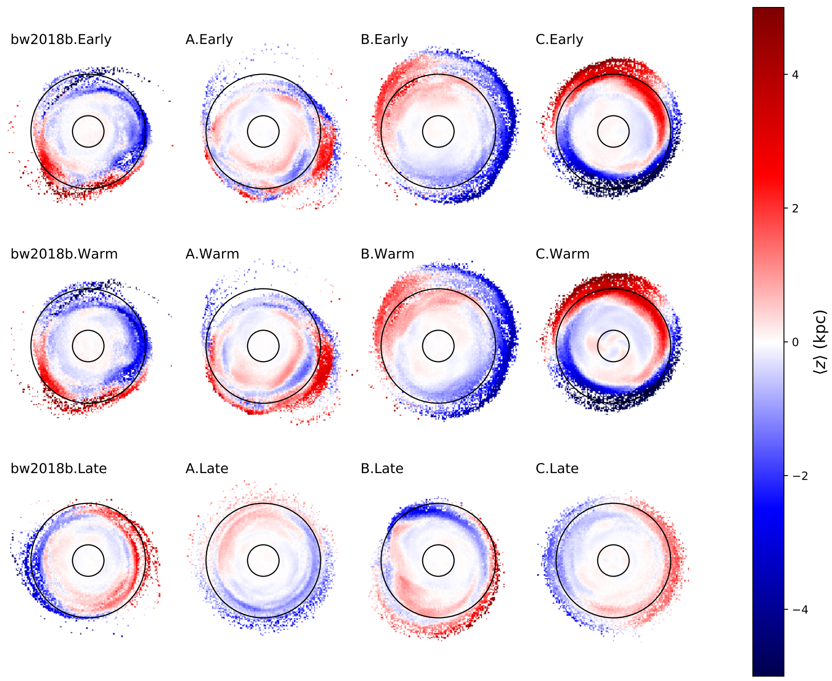

Figure 5.12: Mean displacement above or below the disc at $a = 0.625$ for the top two rows, and $a = 0.875$ for the bottom row (late-insert suite). The circles correspond to $2.2\,R_d = 8.1\,\mathrm{kpc}$ and $20\,h^{-1}\,\mathrm{kpc} = 29.5\,\mathrm{kpc}$.

$a = 0.875$ for the late insertion runs. Significant warping in the outer discs with midplane displacements of a few kiloparsecs is seen in all simulations. However, the morphology of the warps varies considerably. The C and bauer2018b simulations show a clear $m = 1$ pattern, while the pattern in A and B is more complicated. Though the strongest bending features are beyond 20 kpc there is clear evidence for bending waves with amplitudes below 1 kiloparsec further in.

In Fig. 5.13 we show the azimuthally-averaged ($m = 0$) bending of the disc as a function of radius and time for three of our simulations. The B.Late simulation,

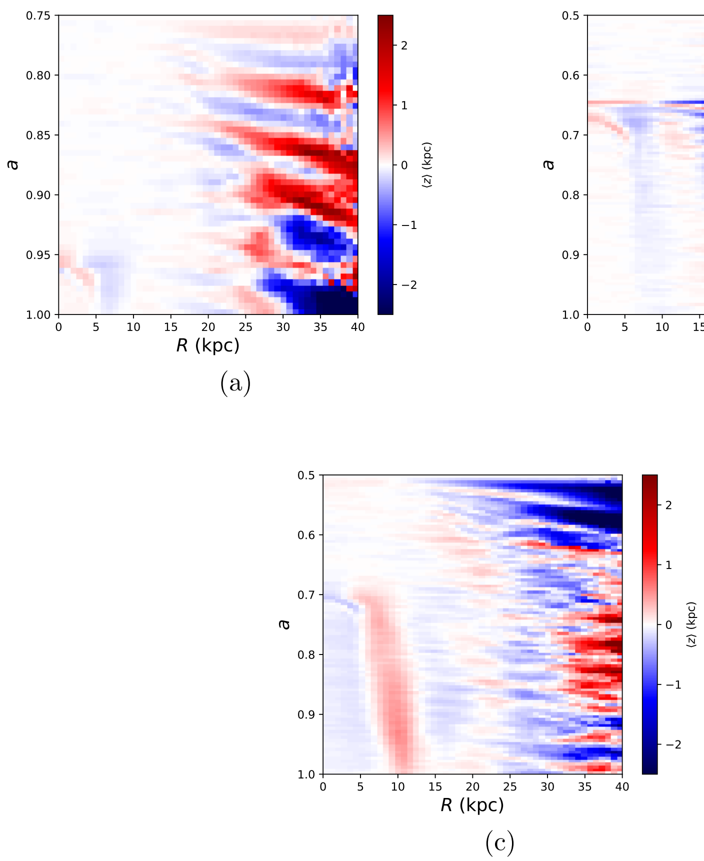

Figure 5.13: The $m = 0$ bending mode for B.Late (a), C.Early (b), and A.Early (c) as a function of radius and scale factor.

where a satellite similar to the Sgr dSph interacts with the disc shows a pattern of bending waves similar to what we saw in the toy model presented in §5.3.2 Monoceros-scale fluctuations interior to 20 kpc occur early on and persist throughout the entire simulation.

The evolution of $\langle z \rangle(R)$ is rather different in the C.Early simulation, where disc-halo misalignment is driving the dynamics. In this case, the bending waves are more like standing waves (horizontal rather than sloping down and to the right). In addition, there are bending waves extending all the way to the centre of the disc,

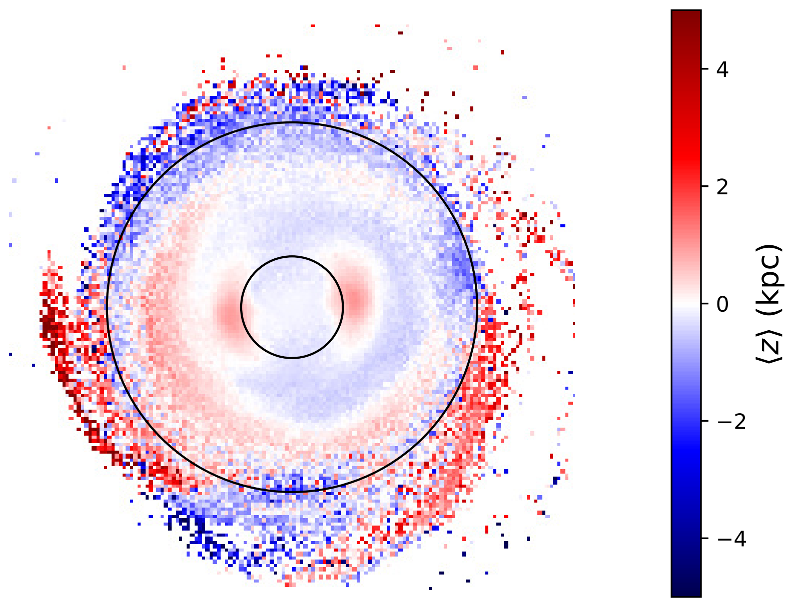

Figure 5.14: The mean height, $\langle z \rangle$, map for A.Early at $a = 0.875$.

beginning when $a \simeq 0.65$. We attribute these waves the the buckling of the bar.

Finally, we consider A.Early where the disc interacts with a relatively massive but more distant subhalo. Bending waves set up in the outer disc almost immediately while sub-kiloparsec corrugations persist throughout the disc over the entire simulation. Moreover, at $a = 0.5$ a long-lived feature develops in the inner disc. To explore this model further, we show a face-on vertical displacement map in Fig. 5.14 for $a = 0.875$. We interpret this feature as a 'banana bar', that is, a bar that exibits a permanent bend along its long axis.

In addition to flapping $m = 0$ modes, we detect strong $m = 1$ warp signatures ($\Theta = z$ in Eq. (5.2)) in our three detailed examples. In the case of the strong satellite encounter, B.Late, we see a sub-kpc warp present in Fig. 5.15a during the first half of

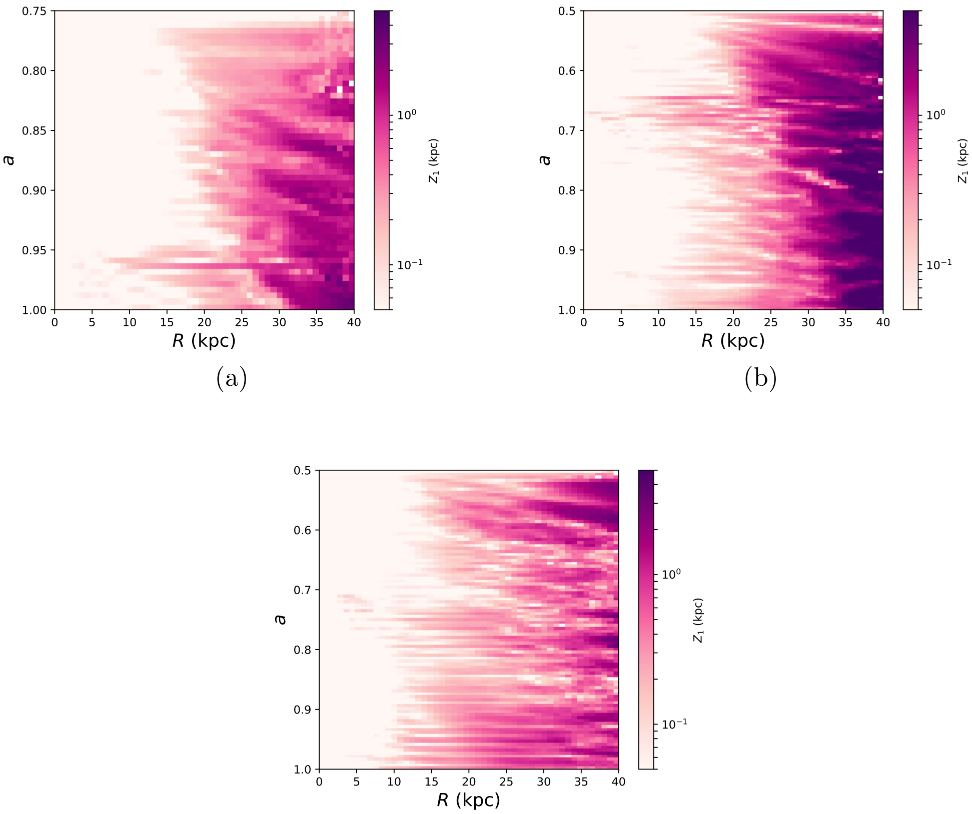

(c)

Figure 5.15: The $m = 1$ bending mode for B.Late (a), C.Early (b), and A.Early (c) as a function of radius and scale factor.

the simulation. As the substructure orbit continues, a close pass excites stronger $m = 1$ structures. In contrast, the strong misalignment case, C.Early show in Fig. 5.15b, exhibits kiloparsec-scale $m = 1$ bending modes in the outer disc. Furthermore, the strong $m = 1$ signal extends inside of 25 kpc at the beginning of the simulation where there is relatively little $m = 0$ signature, and also where B.Late has relatively low $m = 1$ signal. The contour of the $m = 1$ bending mode post-buckling roughly traces the $m = 0$ contour with a similar magnitude, suggesting a superposition of effects brought on by the environment's coupling to the buckling event.

The intermediate case, A.Early shown in Fig. 5.15c, presents something qualitatively between B.Late and C.Early. While the outer disc is initially excited, this behaviour subsides as the halo equilibrates. We then find consistent, several hundred pc signal in the inner and outer disc over the simulation. Lastly, buckling has a less drastic impact on the $m = 1$ signature for A.Early than it did for the $m = 0$.

5.6 KOD Dynamics

In this section, we focus on stars that are kick out of the disc. We begin with a definition of a KOD star and then discuss the kicked-out populations in our simulations.

5.6.1 Definition of a KOD star

We a define a kicked-out star as one where the distance from the midplane, $|z(t)|$, exceeds some threshold, $\eta z_{\rm rms}$:

$$|z(t)| > \eta \, z_{\rm rms}(t) \tag{5.8}$$

where η is a dimensionless parameter and $z_{rms}(R, t)$ is the time-dependent thickness of the disc, as estimated in an annulus at $2.2R_d$. Clearly, the choice of η determines the number of stars identified as being kicked out of the disc. For example, $\eta = 4$ yields 216K KOD stars or 6.2% of the total stellar content of the disc. Likewise, $\eta = 8$ and $\eta = 12$ yield 19K KOD stars (0.53%) and 4,302 KOD stars (0.069%), respectively. These percentages can be compared with the percentages of stars in an exponential disc that satisfy our KOD criteria, namely 1.8%, 0.034%, and 6×10^{-4}%, for $\eta = 4$, 8, and 12, respectively. We see that for $\eta = 8$ and $\eta = 12$, the number of

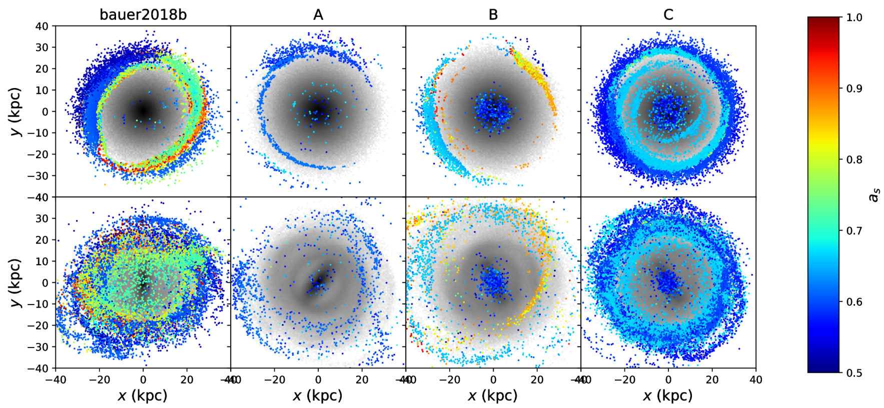

(a)

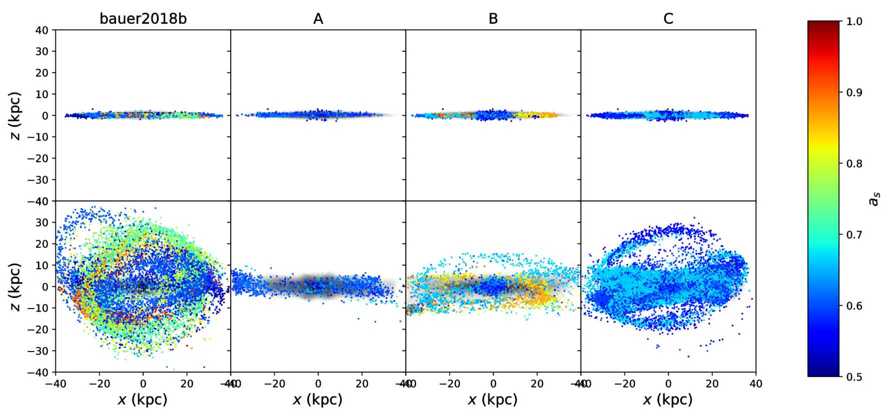

(b)

Figure 5.16: KOD stars are shown for the fiducial suite in face-on (a) and edge-on (b) projections in the initial disc (upper panel) and final snapshot (lower panel). The stars not kicked out of the disc are shown as a histogram and the KOD stars are coloured by the time satisfying Eq. 5.8. Each column is one of the haloes considered in this paper.

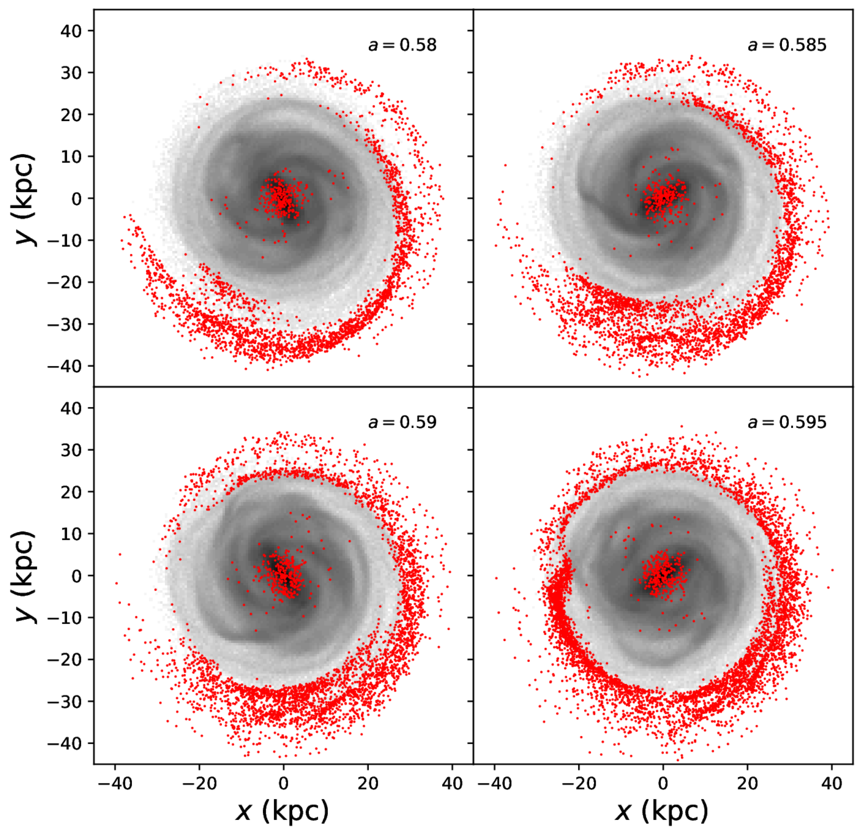

Figure 5.17: KOD stars are plotted for C.Early at the labeled times. Note the association with spiral arms, suggesting a similar mechanism to Laporte et al. (2019).

stars identified as being kicked out exceeds the number expected in an exponential disc by over an order of magnitude.

5.6.2 KOD Star Dynamics

We now turn our attention to the dynamics of KOD stars, identified via Eq. 5.8 with $\eta = 8$ in the final snapshot. Fig. 5.16 shows the KOD stars in our fiducial suite at the

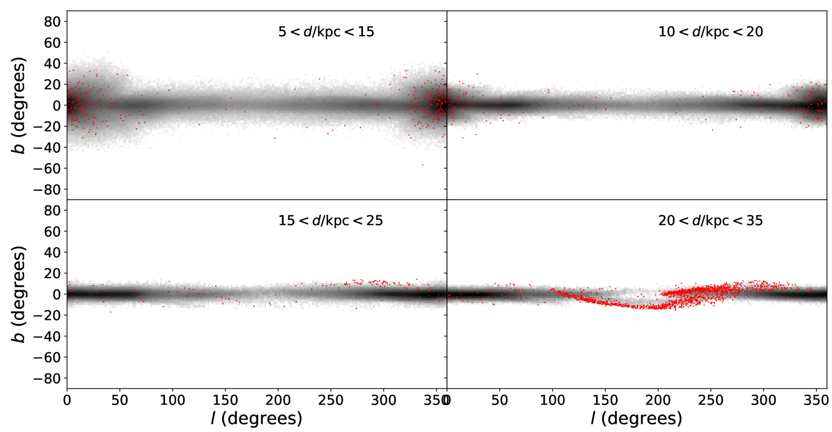

(a)

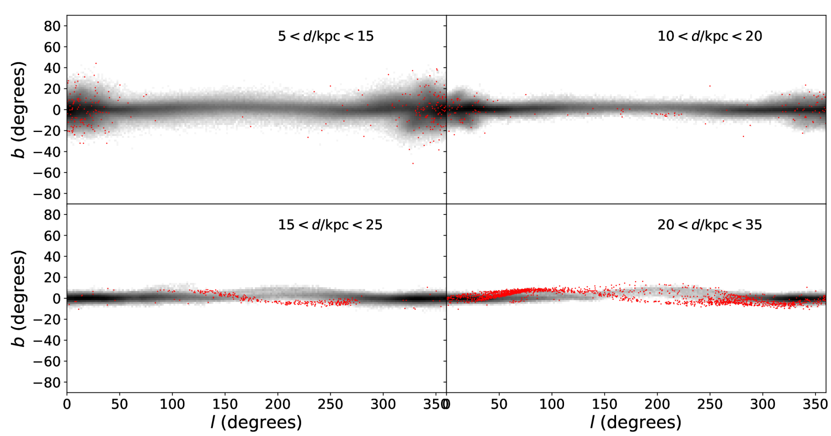

(b)

Figure 5.18: Heliocentric views of KOD stars in several different distance shells. The top panel depicts this for C.Early at $a = 0.775$. The bottom panel shows the same for B.Late at $a = 0.975$.

final snapshot. In addition, we show the same stars traced back to their position in the initial snapshot. The stars are color-coded by the time at which they are kicked out of the disc. We immediately see that the KOD structures vary markedly across our simulations. For example, A.Early shows a relatively small KOD population. Moreover, the KOD structure it does have exists at very low latitudes and was kicked out fairly early in the simulation. B.Early has a few streams of KOD stars, which were kicked out of the disc at roughly the time when the disc had its close encounters with massive subhaloes. Indeed, there appear to be two distinct populations of KOD stars. Finally, bauer2018b.Early and C.Early show the most significant populations of KOD stars. These simulations correspond to the simulations with the most significant disc-halo misalignment and shortest T_τ. In both cases, we see a continuous range of times over which stars were kicked out. Moreover, in C.Early, many of the KOD stars were originally in the inner disc.

The mechanism in C.Early by which stars from the inner disc can be kicked out is highlighted in Fig. 5.17. Each new round of KOD stars appears to be associated with a spiral pattern of small pitch angle. Together with Fig. 5.16, we are left with the picture that KOD stars generally originate in the outer disc though in some cases, such as C.Early, strong spiral structure transfers stars outward and into strong warps. Stars in these warps can then be easily stripped from the disc. The stripped stars in turn phase mix to form the high-latitude structures seen in the final snapshot of C.Early. Stars associated with the features seen in Fig. 5.17 form filamentary structures with a characteristic bifurcation, which Laporte et al. (2019) referred to as “feathers”.

In Fig. 5.18a, we see the KOD stars in C.Early as they appear from the Solar neighborhood at $a = 0.775$. The stars form the top and bottom feather structure described in Laporte et al. (2019), and are undoubtedly associated with grand design spiral structure. The similarities suggest that large-scale tidal fields create observable, stream-like structures at low-to-mid Galactic latitudes, extending along the length of the sky. We contrast this with B.Late, where there is a moderate-mass ($10^{10}\,M_{\odot}$) Sgr interaction. From the perspective of the Sun, KOD structures present in B.Late and shown in Fig. 5.18b appear at relatively low latitudes. Thus a moderate-mass Sgr dSph does not appear to be capable of exciting high latitude structures on a short timescale.

5.7 Discussion

5.7.1 Disc Flapping

Perhaps the most novel effect that we have explored is the generation of flapping modes from differential acceleration of the disc by distant subhaloes and other mass concentrations in a ΛCDM cosmology. Sellwood (1996) presented the first in-depth study of this phenomenon in isolated galaxies. We find that the disc flapping naturally arises in the cosmological environment and can be due to one of three mechanisms: two-body interaction of the disc and inner halo with a subhalo, buckling of the bar, and torquing of the disc by its smooth, triaxial halo.

There is reason to think that the first of these mechanisms is is secondary to the others. Gómez et al. (2017) ran MHD simulations where they note a lack of U-shaped ($m = 0$) warps, which would presumably be caused by flapping. Conversely, they found that S-shaped ($m = 1$) warps were fairly common. In our suite of simulations, B.Late provides the best example where flapping modes from a distant subhalo can be seen as the dominant effect; it has no buckling bar and is initialized in a quiet halo. For both A.Early and C.Early, we would be hard pressed to say that we see the same kind of behaviour, especially where the disc is decently resolved.

The bar buckling generation mechanism for flapping modes is prominently displayed in C.Early. After the bar buckles, we see axisymmetric fluctuations in the mean height, as well as substantial flapping in the region of Monoceros. C.Early is clearly an outlier in this respect, and we suggest that bar buckling in conjunction with triaxility is a viable mechanism for corrugations in cosmological simulations. The general effect of bar buckling appears to introduce a signal in mean height, consistent with the simulation in Khoperskov et al. (2018).

5.7.2 Bending waves, KOD stars and feathers

Consistent with Gómez et al. (2017), we find that halo misalignment is not a likely source of bending in the inner disc. Rather, most of the $m = 0$ and $m = 1$ waves in the inner disc appear to be associated with bar buckling. However, the outer disc is most definitely affected by the smooth halo's tides. We see this in C.Early's $m = 1$ profile, which is much stronger than that in either B.Late or A.Early.

Laporte et al. (2018b) and Laporte et al. (2019) found that a massive Sgr-like dwarf ($M \simeq 8{\times}10^{10}\,M_{\odot}$ and above) whose orbit passes through the Galactic midplane several times can produce populations of KOD stars consistent with those observed in the Milky Way. It is worth noting that their proposed mass is at the higher end of estimates for the mass of the Sgr dSph progenitor, and twice the mass of the stellar disc in our simulations. Our B.Late simulation provides an example of an encounter with a 3×10^{10} subhalo that passes through the disc plane at $a = 0.875$ on an orbit that is similar to model L1 in Laporte et al. (2018b). Consistent with their findings, it appears that even this quite massive perturber cannot excite the requisite structures. On the other hand, we do find KOD stars in other simulations within our suite where the main disc-environment effects come from large-scale tidal fields. Indeed, the simulations in which KOD stars reach their highest latitudes are the ones with substantial inner-halo-disc axis misalignment, namely C.Early and bauer2018b.Early. These are also the simulations with the highest $m = 1$ bending signature in the outer disc. Thus, kicking stars to higher latitudes either requires an extremely massive perturber or substantial misalignment with the host halo.

Our results are consistent with those of Laporte et al. (2019) who found that KOD stars remain close to each other in phase space. For instance, in B.Late stars are kicked out of the disc at two discrete times from narrow regions of the disc. By the end of the simulation, these stars are still closely associated with each other. We can also infer from our simulations that for some mono-abundant chemical population at $z = 1$, we would expect to see dynamically coherent (as supported by how stars are clustered by their kick-up time in the final snapshot) structures with a consistent chemical abundance. This result is consistent with observations by Bergemann et al. (2018), who found narrow abundance spreads for M-giants in A13 and TriAnd. The clustering of stars by their kickup time is true whether they were kicked by substructure, as in B.Late, or by the smooth halo, as in C.Early.

5.8 Conclusions

We have presented a suite of simulations in which stellar discs are inserted into cosmological haloes. These haloes are, in general, triaxial and clumpy and drive the disc from its initial axisymmetric and near equilibrium state to one of disequilibrium. The key findings are summarized as:

- All discs all form bars, even though buckling can regulate their strengths.
- All discs exhibit some kind of bending and warping.
- Disc flapping is a major manifestation of disequilibrium in the cosmological environment.
- Subhaloes with a mass lower than that of the disc are unlikely to generate KOD populations.

It is not surprising that the discs in our simulations bend and warp. In addition, we find large populations of stars kicked out of the disc. These departures from planarity signal a state of disequilibrium likely present in the Milky Way. We have identified several mechanisms for generating vertical structure, which include the well-studied interaction of the disc with a massive satellite, differential acceleration of the disc due to tidal fields of the halo or a distant massive satellite, and the buckling bar. The first two mechanisms can produce large warps (amplitudes of order 1-3 kpc) in the outer disc along with smaller amplitude waves that extend further in. On the other hand, the buckling bar is efficient at producing bending waves and corrugation patterns in the inner disc.

Absent substantial global tides, the KOD populations we see are not able to reach high latitudes. As such, our findings are consistent with the idea that a subhalo less massive than the disc is unlikely to be responsible for even low latitude streams seen in the Milky Way. On the other hand, disc-halo misalignment can generate these populations quite easily. Taken in whole, our analysis suggests that studies which focus on only one mechanism of vertical structure generation are unlikely to capture the full picture. We have done out best to disentangle the different mechanism of disequilibrium. Future work will attempt to determine which ones dominate in the Milky Way.

Acknowledgements

LMW and JSB are supported by a Discovery Grant with the Natural Sciences and Engineering Research Council of Canada.

Bibliography

Athanassoula, E. and Sellwood, J. A. (1986). Bi-symmetric instabilities of the Kuz'min/Toomre disc. *MNRAS*, 221:213–232.

Bauer, J. S. and Widrow, L. M. (2018). Can Stellar Discs in a Cosmological Setting Avoid Forming Strong Bars? *ArXiv e-prints*, page arXiv:1809.00090.

Bauer, J. S., Widrow, L. M., and Erkal, D. (2018). Disc-halo interactions in ΛCDM. *MNRAS*, 476:198–209.

Bennett, M. and Bovy, J. (2019). Vertical waves in the solar neighbourhood in Gaia DR2. *MNRAS*, 482:1417–1425.

Berentzen, I. and Shlosman, I. (2006a). Growing Live Disks within Cosmologically Assembling Asymmetric Halos: Washing Out the Halo Prolateness. *ApJ*, 648:807–819.

Berentzen, I. and Shlosman, I. (2006b). Growing Live Disks within Cosmologically Assembling Asymmetric Halos: Washing Out the Halo Prolateness. *ApJ*, 648:807–819.

Bergemann, M., Sesar, B., Cohen, J. G., Serenelli, A. M., Sheffield, A., Li, T. S., Casagrande, L., Johnston, K. V., Laporte, C. F. P., Price-Whelan, A. M., Schönrich, R., and Gould, A. (2018). Two chemically similar stellar overdensities on opposite sides of the plane of the Galactic disk. *Nature*, 555:334–337.

Bernard, E. J., Ferguson, A. M. N., Richardson, J. C., Irwin, M. J., Barker, M. K., Hidalgo, S. L., Aparicio, A., Chapman, S. C., Ibata, R. A., Lewis, G. F., McConnachie, A. W., and Tanvir, N. R. (2015). The nature and origin of substructure in the outskirts of M31 - II. Detailed star formation histories. *MNRAS*, 446:2789–2801.

Binney, J. (1992). WARPS. *ARA&A*, 30:51–74.

Bosma, A. (1991). Warped and Flaring HI Disks. In Casertano, S., Sackett, P. D., and Briggs, F. H., editors, *Warped Disks and Inclined Rings around Galaxies*, page 181.

Carlin, J. L., DeLaunay, J., Newberg, H. J., Deng, L., Gole, D., Grabowski, K., Jin, G., Liu, C., Liu, X., Luo, A.-L., Yuan, H., Zhang, H., Zhao, G., and Zhao, Y. (2013). Substructure in Bulk Velocities of Milky Way Disk Stars. *ApJ*, 777:L5.

Carrillo, I., Minchev, I., Kordopatis, G., Steinmetz, M., Binney, J., Anders, F., Bienaymé, O., Bland-Hawthorn, J., Famaey, B., Freeman, K. C., Gilmore, G., Gibson, B. K., Grebel, E. K., Helmi, A., Just, A., Kunder, A., McMillan, P., Monari, G., Munari, U., Navarro, J., Parker, Q. A., Reid, W., Seabroke, G., Sharma, S., Siebert, A., Watson, F., Wojno, J., Wyse, R. F. G., and Zwitter, T. (2018). Is the Milky Way still breathing? RAVE-Gaia streaming motions. *MNRAS*, 475:2679–2696.

Chequers, M. H., Widrow, L. M., and Darling, K. (2018). Bending waves in the Milky Way's disc from halo substructure. *MNRAS*, 480:4244–4258.

Christodoulou, D. M., Shlosman, I., and Tohline, J. E. (1995). A new criterion for bar-forming instability in rapidly rotating gaseous and stellar systems. 2: Nonaxisymmetric form. *ApJ*, 443:563–569.

Cox, A. L., Sparke, L. S., van Moorsel, G., and Shaw, M. (1996). Optical and 21 CM Observations of the Warped, Edge-On Galaxy UGC 7170. *AJ*, 111:1505.

Crane, J. D., Majewski, S. R., Rocha-Pinto, H. J., Frinchaboy, P. M., Skrutskie, M. F., and Law, D. R. (2003). Exploring Halo Substructure with Giant Stars: Spectroscopy of Stars in the Galactic Anticenter Stellar Structure. *ApJ*, 594:L119–L122.

de la Vega, A., Quillen, A. C., Carlin, J. L., Chakrabarti, S., and D'Onghia, E. (2015). Phase wrapping of epicyclic perturbations in the Wobbly Galaxy. *MNRAS*, 454:933–945.

Deason, A. J., Belokurov, V., and Koposov, S. E. (2018). Cresting the wave: proper motions of the Eastern Banded Structure. *MNRAS*, 473:2428–2433.

Debattista, V. P. and Sellwood, J. A. (2000). Constraints from Dynamical Friction on the Dark Matter Content of Barred Galaxies. *ApJ*, 543:704–721.

DeBuhr, J., Ma, C.-P., and White, S. D. M. (2012). Stellar discs in Aquarius dark matter haloes. *MNRAS*, 426:983–999.

D'Onghia, E., Madau, P., Vera-Ciro, C., Quillen, A., and Hernquist, L. (2016). Excitation of Coupled Stellar Motions in the Galactic Disk by Orbiting Satellites. *ApJ*, 823:4.

Dorman, C. E., Widrow, L. M., Guhathakurta, P., Seth, A. C., Foreman-Mackey, D., Bell, E. F., Dalcanton, J. J., Gilbert, K. M., Skillman, E. D., and Williams, B. F. (2013). A New Approach to Detailed Structural Decomposition from the SPLASH and PHAT Surveys: Kicked-up Disk Stars in the Andromeda Galaxy? *ApJ*, 779:103.

Efstathiou, G., Lake, G., and Negroponte, J. (1982). The stability and masses of disc galaxies. *MNRAS*, 199:1069–1088.

Feldmann, R. and Spolyar, D. (2015). Detecting dark matter substructures around the Milky Way with Gaia. *MNRAS*, 446:1000–1012.

Font, A. S., Navarro, J. F., Stadel, J., and Quinn, T. (2001). Halo Substructure and Disk Heating in a Λ Cold Dark Matter Universe. *ApJ*, 563(1):L1–L4.

Gaia Collaboration, Katz, D., Antoja, T., Romero-Gómez, M., Drimmel, R., Reylé, C., Seabroke, G. M., Soubiran, C., Babusiaux, C., Di Matteo, P., and et al. (2018). Gaia Data Release 2. Mapping the Milky Way disc kinematics. *A&A*, 616:A11.

García-Ruiz, I., Sancisi, R., and Kuijken, K. (2002). Neutral hydrogen and optical observations of edge-on galaxies: Hunting for warps. *A&A*, 394:769–789.

Gauthier, J.-R., Dubinski, J., and Widrow, L. M. (2006). Substructure around M31: Evolution and Effects. *ApJ*, 653:1180–1193.

Gómez, F. A., Minchev, I., O'Shea, B. W., Beers, T. C., Bullock, J. S., and Purcell, C. W. (2013). Vertical density waves in the Milky Way disc induced by the Sagittarius dwarf galaxy. *MNRAS*, 429:159–164.

Gómez, F. A., White, S. D. M., Grand, R. J. J., Marinacci, F., Springel, V., and Pakmor, R. (2017). Warps and waves in the stellar discs of the Auriga cosmological simulations. *MNRAS*, 465:3446–3460.

Hahn, O. and Abel, T. (2013). MUSIC: MUlti-Scale Initial Conditions. Astrophysics Source Code Library.

Hu, S. and Sijacki, D. (2016). Stellar spiral structures in triaxial dark matter haloes. *MNRAS*, 461:2789–2808.

Hu, S. and Sijacki, D. (2018). Impact of cosmological satellites on stellar discs: dissecting one satelliteat a time. *MNRAS*, 478:1576–1594.

Ibata, R. A., Gilmore, G., and Irwin, M. J. (1994). A dwarf satellite galaxy in Sagittarius. *Nature*, 370:194–196.

Johnston, K. V., Price-Whelan, A. M., Bergemann, M., Laporte, C., Li, T. S., Sheffield, A. A., Majewski, S. R., Beaton, R. S., Sesar, B., and Sharma, S. (2017). Disk Heating, Galactoseismology, and the Formation of Stellar Halos. *Galaxies*, 5:44.

Katz, N., Quinn, T., Bertschinger, E., and Gelb, J. M. (1994). Formation of Quasars at High Redshift. *MNRAS*, 270:L71.

Kazantzidis, S., Bullock, J. S., Zentner, A. R., Kravtsov, A. V., and Moustakas, L. A. (2008). Cold Dark Matter Substructure and Galactic Disks. I. Morphological Signatures of Hierarchical Satellite Accretion. *ApJ*, 688:254–276.

Khoperskov, S., Di Matteo, P., Gerhard, O., Katz, D., Haywood, M., Combes, F., Berczik, P., and Gomez, A. (2018). The echo of the bar buckling: phase-space spirals in Gaia DR2. *arXiv e-prints*, page arXiv:1811.09205.

Klypin, A., Valenzuela, O., Colín, P., and Quinn, T. (2009). Dynamics of barred galaxies: effects of disc height. *MNRAS*, 398:1027–1040.

Kuijken, K. and Gilmore, G. (1989). The mass distribution in the galactic disc. I - A technique to determine the integral surface mass density of the disc near the sun. *MNRAS*, 239:571–603.

Lacey, C. G. and Ostriker, J. P. (1985). Massive black holes in galactic halos ? *ApJ*, 299:633–652.

Laporte, C. F. P., Gómez, F. A., Besla, G., Johnston, K. V., and Garavito-Camargo, N. (2016). Response of the Milky Way's disc to the Large Magellanic Cloud in a first infall scenario. *ArXiv e-prints*.

Laporte, C. F. P., Gómez, F. A., Besla, G., Johnston, K. V., and Garavito-Camargo, N. (2018a). Response of the Milky Way's disc to the Large Magellanic Cloud in a first infall scenario. *MNRAS*, 473:1218–1230.

Laporte, C. F. P., Johnston, K. V., Gómez, F. A., Garavito-Camargo, N., and Besla, G. (2018b). The influence of Sagittarius and the Large Magellanic Cloud on the stellar disc of the Milky Way Galaxy. *MNRAS*, 481(1):286–306.

Laporte, C. F. P., Johnston, K. V., and Tzanidakis, A. (2019). Stellar disc streams as probes of the Galactic potential and satellite impacts. *MNRAS*, 483:1427–1436.

Matthews, L. D. and Uson, J. M. (2008). Corrugations in the Disk of the Edge-On Spiral Galaxy IC 2233. *ApJ*, 688:237–244.

McConnachie, A. W., Chapman, S. C., Ibata, R. A., Ferguson, A. M. N., Irwin, M. J., Lewis, G. F., Tanvir, N. R., and Martin, N. (2006). The Stellar Halo and Outer Disk of M33. *ApJ*, 647:L25–L28.

McConnachie, A. W., Ferguson, A. M. N., Irwin, M. J., Dubinski, J., Widrow, L. M., Dotter, A., Ibata, R., and Lewis, G. F. (2010). The Photometric Properties of a Vast Stellar Substructure in the Outskirts of M33. *ApJ*, 723:1038–1052.

McMillan, P. J. and Dehnen, W. (2007). Initial conditions for disc galaxies. *MNRAS*, 378:541–550.

Navarro, J. F., Frenk, C. S., and White, S. D. M. (1994). Accretion of Satellite Galaxies and the Density of the Universe. *MNRAS*, 267:L1.

Navarro, J. F., Frenk, C. S., and White, S. D. M. (1997). A Universal Density Profile from Hierarchical Clustering. *ApJ*, 490(2):493–508.

Newberg, H. J., Yanny, B., Rockosi, C., Grebel, E. K., Rix, H.-W., Brinkmann, J., Csabai, I., Hennessy, G., Hindsley, R. B., Ibata, R., Ivezić, Z., Lamb, D., Nash, E. T., Odenkirchen, M., Rave, H. A., Schneider, D. P., Smith, J. A., Stolte, A., and York, D. G. (2002). The Ghost of Sagittarius and Lumps in the Halo of the Milky Way. *ApJ*, 569:245–274.

Oñorbe, J., Garrison-Kimmel, S., Maller, A. H., Bullock, J. S., Rocha, M., and Hahn, O. (2014). How to zoom: bias, contamination and Lagrange volumes in multimass cosmological simulations. *MNRAS*, 437:1894–1908.

Oort, J. H., Kerr, F. J., and Westerhout, G. (1958). The galactic system as a spiral nebula (Council Note). *MNRAS*, 118:379.

Pearl, A. N., Newberg, H. J., Carlin, J. L., and Smith, R. F. (2017). A Map of the Local Velocity Substructure in the Milky Way Disk. *ApJ*, 847:123.

Planck Collaboration, Ade, P. A. R., Aghanim, N., Armitage-Caplan, C., Arnaud, M., Ashdown, M., Atrio-Barandela, F., Aumont, J., Baccigalupi, C., Banday, A. J., and et al. (2014). Planck 2013 results. XVI. Cosmological parameters. *A&A*, 571:A16.

Purcell, C. W., Bullock, J. S., Tollerud, E. J., Rocha, M., and Chakrabarti, S. (2011). The Sagittarius impact as an architect of spirality and outer rings in the Milky Way. *Nature*, 477:301–303.

Reylé, C., Marshall, D. J., Robin, A. C., and Schultheis, M. (2009). The Milky Way's external disc constrained by 2MASS star counts. *A&A*, 495:819–826.

Richardson, J. C., Ferguson, A. M. N., Johnson, R. A., Irwin, M. J., Tanvir, N. R., Faria, D. C., Ibata, R. A., Johnston, K. V., Lewis, G. F., McConnachie, A. W., and Chapman, S. C. (2008). The Nature and Origin of Substructure in the Outskirts of M31. I. Surveying the Stellar Content with the Hubble Space Telescope Advanced Camera for Surveys. *AJ*, 135:1998–2012.

Rocha-Pinto, H. J., Majewski, S. R., Skrutskie, M. F., and Crane, J. D. (2003). Tracing the Galactic Anticenter Stellar Stream with 2MASS M Giants. *ApJ*, 594:L115–L118.

Rocha-Pinto, H. J., Majewski, S. R., Skrutskie, M. F., Crane, J. D., and Patterson, R. J. (2004). Exploring Halo Substructure with Giant Stars: A Diffuse Star Cloud or Tidal Debris around the Milky Way in Triangulum-Andromeda. *ApJ*, 615:732–737.

Sackett, P. D. (1997). Does the Milky Way Have a Maximal Disk? *ApJ*, 483:103–110.

Sánchez-Gil, M. C., Alfaro, E. J., and Pérez, E. (2015). Corrugated velocity patterns in the spiral galaxies: NGC 278, NGC 1058, NGC 2500 & UGC 3574. *MNRAS*, 454:3376–3390.

Sancisi, R. (1976). Warped HI Disks in Galaxies. *A&A*, 53:159.

Sellwood, J. A. (1996). Axisymmetric Bending Oscillations of Stellar Disks. *ApJ*, 473:733.

Sellwood, J. A. (2013). *Dynamics of Disks and Warps*, page 923.

Sellwood, J. A., Nelson, R. W., and Tremaine, S. (1998). Resonant Thickening of Disks by Small Satellite Galaxies. *ApJ*, 506:590–599.

Sharma, S., Johnston, K. V., Majewski, S. R., Muñoz, R. R., Carlberg, J. K., and Bullock, J. (2010). Group Finding in the Stellar Halo Using M-giants in the Two Micron All Sky Survey: An Extended View of the Pisces Overdensity? *ApJ*, 722:750–759.

Sheffield, A. A., Price-Whelan, A. M., Tzanidakis, A., Johnston, K. V., Laporte, C. F. P., and Sesar, B. (2018). A Disk Origin for the Monoceros Ring and A13 Stellar Overdensities. *ApJ*, 854:47.

Springel, V. (2005). The cosmological simulation code GADGET-2. *MNRAS*, 364:1105–1134.

Toomre, A. (1964). On the gravitational stability of a disk of stars. *ApJ*, 139:1217–1238.

Toth, G. and Ostriker, J. P. (1992). Galactic Disks, Infall, and the Global Value of Omega. *ApJ*, 389:5.

Widrow, L. M., Barber, J., Chequers, M. H., and Cheng, E. (2014). Bending and breathing modes of the Galactic disc. *MNRAS*, 440:1971–1981.

Widrow, L. M., Gardner, S., Yanny, B., Dodelson, S., and Chen, H.-Y. (2012). Galactoseismology: Discovery of Vertical Waves in the Galactic Disk. *ApJ*, 750:L41.

Widrow, L. M., Pym, B., and Dubinski, J. (2008). Dynamical Blueprints for Galaxies. *ApJ*, 679:1239–1259.

Williams, M. E. K., Steinmetz, M., Binney, J., Siebert, A., Enke, H., Famaey, B., Minchev, I., de Jong, R. S., Boeche, C., Freeman, K. C., Bienaymé, O., Bland-Hawthorn, J., Gibson, B. K., Gilmore, G. F., Grebel, E. K., Helmi, A., Kordopatis, G., Munari, U., Navarro, J. F., Parker, Q. A., Reid, W., Seabroke, G. M., Sharma, S., Siviero, A., Watson, F. G., Wyse, R. F. G., and Zwitter, T. (2013). The wobbly Galaxy: kinematics north and south with RAVE red-clump giants. *MNRAS*, 436:101–121.

Xu, Y., Newberg, H. J., Carlin, J. L., Liu, C., Deng, L., Li, J., Schönrich, R., and Yanny, B. (2015). Rings and Radial Waves in the Disk of the Milky Way. *ApJ*, 801:105.

Yanny, B. and Gardner, S. (2013). The Stellar Number Density Distribution in the Local Solar Neighborhood is North-South Asymmetric. *ApJ*, 777:91.

Yanny, B., Newberg, H. J., Grebel, E. K., Kent, S., Odenkirchen, M., Rockosi, C. M., Schlegel, D., Subbarao, M., Brinkmann, J., Fukugita, M., Ivezic, Ž., Lamb, D. Q., Schneider, D. P., and York, D. G. (2003). A Low-Latitude Halo Stream around the Milky Way. *ApJ*, 588:824–841.

Yurin, D. and Springel, V. (2015). The stability of stellar discs in Milky Way-sized dark matter haloes. *MNRAS*, 452:2367–2387.

Chapter 6

Summary and Conclusions

In this chapter, we summarize the main findings of this thesis and talk about future work.

6.1 Disc-Halo Interactions

6.1.1 Summary

One of the key contributions of this thesis is the understanding of how the dynamic nature of stellar discs affects halo properties, as studied in Chapter 3. Some halo properties, such as the distribution of mass in the inner halo, depend a lot on how the disc is modelled. This is very evident in the differences in adiabatic contraction between the rigid and live discs. Specifically, we find the formation of a bar led to a more concentrated halo mass distribution. On the whole, these results suggest that if one is interested in the Core-Cusp problem, this should be studied with fully live models of stellar discs.

The intermediate-to-outer halo is less effected by the dynamics of the inner halo. While some differences between our disc potential models were observed in the halo mass functions, these differences were minor. The details of how satellites are disrupted appear to be at least weakly dependent on how the disc is modelled, and stream studies should consider as realistic of a disc as possible. This last aspect of our work has informed some design decisions by others, namely in the work of Read and Erkal (2019). If one is just interested in subhalo population statistics, it is sufficient to model baryons as fixed potentials in a pure dark matter halo.

The global picture painted by our work is that modelling the disc as a rigid body does well in determining how the disc settles (i.e. its angular motion), a result consistent with Dubinski and Kuijken (1995). It appears that the formation of a bar in the live disc is the most substantial difference between the rigid and live discs' effects on the inner halo, a difference that only becomes significant *after* the the live disc

6.1.2 Insertion Scheme and Future Work

Our algorithm makes optimizations over previous disc insertion schemes. The optimizations we made are by no means exhaustive, and a detailed discussion of potential optimizations is given in Chapter A. We focus here on scientific concerns with our algorithm, rather than performance optimizations.

The scheme as specified has the undesirable property of adding angular momentum and mass to the halo. This happens when the disc grows, and we fail to extract mass and angular momentum from the halo[1]. A potential improvement which extracts mass and angular momentum from the halo particles during the disc growth phase would alleviate these concerns. This may have a sizable impact on our conclusions about the disc's effect on adiabatic contraction, since both the disc and halo are dominant in the inner galaxy.

We might also consider a scheme which initializes the disc with some gas component. Deg et al. (2019) modified GalactICS to allow for the inclusion of gas. This, combined with modifying halo particle masses, should allow us to more accurately compare our results to fully hydrodynamical *ab initio* simulations.

A valid criticism of our disc insertion technique is that all of the stars are initialized simultaneously. This is unrealistic, and allowing stars to gradually form out

[1]Note that dark matter particles dark matter only simulations include the baryon mass of the Universe.

of the rigid disc potential might show a more complicated dependence on the initial conditions parameter space. In fact, Aumer et al. (2016) grow discs in a similar fashion and find that slowly growing the disc along with gas physics impacts important properties like bar formation. In some cases it may even shut off bar formation, which we believe would substantially impact our conclusions about adiabatic contraction.

Even with the current algorithm, there is more we can do on the study of disc-halo interactions. A possible project would be to study the effect of varying disc properties in the same halo. We might also consider adding a spheroidal bulge component to see how high baryonic mass concentrations change our results. We might also look for more detailed evidence of the halo's response to the disc in our existing simulations in the form of wakes. This kind of response was explored in one of our toy models in Chapter 5, and it seems natural to extend this analysis to our cosmological simulations.

6.2 Bar Formation

6.2.1 Summary

We discuss our contributions to understanding how bars form in stellar discs in Chapter 4. The paper unifies previous work on disc insertion schemes by viewing them through a lens of a common parameter space. Through placing our models and the models of Yurin and Springel (2015) in this space, we are able to contextualize the very large bars formed in their study. In particular, we show that a commonly discounted variable, the disc thickness, is a primary driver of bar strength in a cosmological setting. We show that, in general, the length of a bar at present day for cosmological stellar discs is largely a function of the initial disc thickness. This effect is not numerical, as we show through our application of the AGAMA code (Vasiliev, 2018).

The importance of being cautious about the choice of gravitational softening length is also illustrated. Since disc thickness appears to play a major role in bar formation in ΛCDM, we must be careful that we are resolving our discs' vertical structure.

On the whole, we show that it is difficult to suppress the formation of bars in a cosmological setting. While the bar more closely resemble the Milky Way's when we start with a thinner disc, we find strong bars form nonetheless. As such, there is still a discrepancy in accounting for the observed bar fraction without invoking classical bulges or non-collisionless phenomena. Our work has proved useful in illustrating this, and we are credited for furthering discussion of this issue in Sellwood et al. (2019).

We manage to bolster this result in Chapter 5, where we ran twelve simulations in four haloes. Although all of the haloes had the same total mass as the Milky Way, they varied widely in terms of their other properties. Despite the differences in the haloes, the bars formed by embedded discs were quite similar. Additionally, there is a nontrivial dependence on Toomre Q in terms of when the bar buckles, but the final bar strength depends very weakly on this parameter, contrary to Yurin and Springel (2015). Rather, the trend Yurin and Springel (2015) sees in Q is likely due to the presence of their bulge simulations, which would increase Q as well as provide a stabilizing central mass.

6.2.2 Further Exploration

In Chapter 5, bar formation is not the focus of the study. Now that we have a sample of bars forming in different cosmological environments, we can position the discs in the parameter space described in Chapter 4. A proper synthesis with previous literature on this topic should be performed.

An interesting feature of our simulations is the existence of "banana bars" in some of the simulations. Understanding why we get banana bars in some simulations versus a more traditional X-shaped pattern might provide an observational constraint for the Milky Way. This topic should be explored in more detail.

It would also be interesting to see how implementing a hydrodynamical, growing disc described in §6.1.2 would change our results. An interesting conclusion from Aumer et al. (2016) was that bar formation could be suppressed by GMCs. It is worth noting that these simulations also included a compact bulge, and the result might be different for a pure disc-halo system in a fully cosmological environment. The author's view is that moving in this direction is the next logical step for disc-insertion schemes.

6.3 Vertical Structure

6.3.1 Summary

The main focus of Chapter 5 is how discs form vertical structure in ΛCDM environments. We showed that there are a wide variety of Milky Way-mass haloes that form vertical structure consistent with structure observed in the solar neighborhood. In particular, we showed that this structure can be formed without a massive satellite encounter in a cosmological setting. This position is bolstered by the fact that we see Monoceros-like structure in all twelve of our simulations.

We also find that consistent perpendicular torques on the disc are required to explain features in the outer disc. It is unlikely that substructures far below the 10^{11} solar mass regime are responsible for stars stripped to higher latitudes. Global tides from disc-halo axis misalignment seem to be the most effective way to create these populations of stars. We therefore suggest that streams originating from the outer disc may primarily depend on the Milky Way's interaction with the LMC. A massive merger like the one with the LMC can cause consistent perpendicular torques its own tides or by disturbing the existing smooth Milky Way halo mass.

6.3.2 More Accurate Milky Way Comparisons

A key flaw in this work is that we had no LMC analogues. An interesting experiment would be to compare the vertical structure caused by a future LMC merger and the vertical structure generated when a disc is misaligned in a triaxial halo. On the whole, future work should proceed in the same way as the work in Chapter 4. We should seek to relate the halo environments to a common parameter space.

We also might want to compare our simulations in the solar neighborhood to Gaia data through simulation-generated mock catalogues. Although not presented in this thesis, we have developed a code which allows us to generate initial conditions that are selectively upsampled in a specified annulus. In isolated galaxy simulations, the upsampled annulus remains mostly uncontaminated at late times. By resampling the solar neighborhood, and by using simulation-generated mock catalogues, we can compare our simulations more directly with observations.

6.4 Closing Remarks

This work presents an improved disc insertion scheme with applications to Galactic astronomy. We have successfully shown that we can set up and understand discs inserted into cosmological haloes. Future work is suggested, and we have no shortage of potential projects to improve our scheme. The long-term goal of this work is to bridge the gap with *ab initio* simulations, and we have presented a clear roadmap for doing so.

A common theme in our work is that both nature and nurture affect key aspects of the evolution of galaxies, namely in respect to the formation of bars and vertical structure. Future work will need to address this more quantitatively, as we work back to understanding our own Milky Way. In particular, we believe that disc insertion schemes will play a vital role in understanding the recently released Gaia DR2.

Additionally, as simulation resolutions and computing power improve, we may be forced to revisit the fundamentals at the beginning of Chapter 2. Simulation codes may need to be redesigned to accommodate ever-increasing needs to relate them to observations. Our hope is that disc insertion schemes will be at the heart of these discussions as a valuable tool in understanding observational data.

Our work represents a tangible leap forward, however small, in the field of Galactic dynamics. We hope that our work continues to inspire new developments, new comparisons, and more questions. In particular, we hope to see our work mature, and possibly tell us about the nature of the dark Universe in which we live. This is an incredibly exciting time for the field, one where we are proud to have played a small role.

Bibliography

Aumer, M., Binney, J., and Schönrich, R. (2016). The quiescent phase of galactic disc growth. *MNRAS*, 459(3):3326–3348.

Deg, N., Widrow, L. M., Randriamampandry, T., and Carignan, C. (2019). GALACTICS with gas. *MNRAS*, 486:5391–5399.

Dubinski, J. and Kuijken, K. (1995). The settling of warped disks in oblate dark halos. *ApJ*, 442:492–503.

Read, J. I. and Erkal, D. (2019). Abundance matching with the mean star formation rate: there is no missing satellites problem in the Milky Way above $M_{200} \sim 10^9 M_\odot$. *MNRAS*.

Sellwood, J. A., Shen, J., and Li, Z. (2019). The global stability of M33: still a puzzle. *MNRAS*, 486(4):4710–4723.

Vasiliev, E. (2018). Agama reference documentation. *arXiv e-prints*.

Yurin, D. and Springel, V. (2015). The stability of stellar discs in Milky Way-sized dark matter haloes. *MNRAS*, 452:2367–2387.

Appendix A

Implementing Disc Insertion Schemes in Gadget-3

This chapter is meant to provide more details on exactly how to implement the method described in Chapter 3. Example code is included where relevant, but the author believes it is a useful exercise for a new graduate student to implement this themselves, as it tests their understanding of the material in Chapter 2. For the purposes of this guide, we are going to assume that the reader has the copy of Gadget-3 used for this thesis and has a working understanding of how to use a compiler, MPI, and GalactICS[1].

A.1 Representing a Rigid Disk

A good deal of time was spent in the early development of the disc insertion scheme thinking about the best way to represent the rigid disc during the growth phase. There were two main approaches we considered.

The first was to not represent the disc as a physical object in the simulation, but simply as a smooth potential. In order to compute forces on such an object, one has to rely on Newton's third law. The force (torque) on the disc is equal and opposite to the force (torque) it exerts on every other particle in the simulation. The primary issue with this is that in a tree code or particle mesh code, Newton's third law is violated (Barnes and Hut, 1986; Hernquist et al., 1991; Springel, 2005). Furthermore, there is straightforward way to impose periodicity. Since this object exists outside of the tree or particle mesh calculations, it is not accounted for when Gadget-3 imposes periodic boundaries.

The second approach, and the one that we used, was to represent the disc as a

[1]You can reach the author at `jake.bauer.2.71828@gmail.com`. If a question is not answered well here, please reach out. The author is also happy to give direction on learning the prerequisite material.

series of massive particles. We wanted to avoid this initially, since this opens up a wide range of potential problems. The first of these is that you need to explicitly turn off the drift and kick operations for the rigid particles. The segments of code portrayed in Appendix C from `predict.c` and Appendix B from `kicks.c` handle the drift and kick shutoff for collisionless particles respectively.

In order to initially position the disc, you have to set the initial `DISK_X0`, `DISK_Y0`, `DISK_Z0` variables. The velocity is set by `DISK_VX0`, `DISK_VY0`, and `DISK_VZ0` in units of physical velocity divided by the scale factor (internal simulation units). The initial Euler angles are given as `DISK_PHI0`, `DISK_THETA0`, and `DISK_PSI0`.

A.1.1 Rigid Disk Initial Conditions

To generate the initial conditions, you need to have the zoom-in snapshot with the halo you want to extract. To set up the rigid disc, we have been using the last snapshot of the zoom-in to create the disc. Using the ROCKSTAR positions (converted to kpc) and velocities, run the code provided in Appendix D. Name the output file to be the path listed in the first line of `extpot.params`. **Make sure that the orientation for the rigid disk on the last line of this file is set to be toward the z-axis, or you will rotate the disk twice causing all sorts of bad things!**

Once the disk is finished generating, you need to merge it with the zoom-in particles. Place the unrotated disk at the origin, and the code will place the rigid disk upon initialization. You may use the C++ script we have provided in Appendix E. This file will reassign all of the particle IDs and types, so make sure if you use this script that you do not need to preserve the old ones. Make sure `#define append` and `#define GADGET_COSMOLOGY` are uncommented.

The disk position, velocity, angular position, and rate of Euler angle change are recorded in `disk_vars.txt`. The differences in these quantities from the last timestep are recorded in `disk_dvars.txt`. A variety of other quantities are written out into other log files that are pretty self explanatory. Apply `grep` to the code if you are unsure what a particular log file is. There should be comments.

A.2 Integrating the Rigid Body Equations

A.2.1 Initial Parameters and Timestep Selection

To integrate the disc, you need to set `RIGID_PARTICLE_DISK`, `ANALYTIC_LZ`, and a value for `TULLY_FISHER_A`. You will also need a timestep reduction factor, `TIMESTEP_REDUCTION_FACTOR`, which reduces the timestep size for the rigid disc integration. We have found that accurately capturing the nutation behavior for the disk generally requires a lower timestep than what Gadget-3 assigns from the acceleration.

On the topic of timesteps, you will need to force all of the disk particles into the same timestep bin. Recall how the time integration scheme was described; there is nothing preventing particles in the force tree that are all rigid disk particles from being assigned different timesteps. This is handled by the segment of code from `timestep.c` in Appendix F.

A.2.2 Integration

The actual integration scheme is handled in `rigiddisk.c`. The functions are self-explanatory and implement routines for generating the Euler rotation matrix. At runtime, the particles in the rigid disk have their relevant quantities (acceleration, torque, etc.) rotated into the frame where the disk axis is the z-axis. We solve the angular part of the disk dynamics in this frame using the implicit Euler method. For the actual timestep used in the integration method, make sure you use the time calculated in `update_halo_positions.c`. This is the actual time elapsed as formulated[2], not the drift or kick steps given for the conjugate positions and velocities. We apologize for the horrible mess that this section of code has become. Perhaps it would be instructive to write your own halo tracker.

A.3 Live Disk Setup and Initial Conditions

Here, we discuss the initialization of the live disk.

A.3.1 Creating Live Initial Conditions

The first thing needed for creating live disk ICs is the new halo at the insertion time. This can be extracted using the script provided in Appendix D, or something similar. This will be the halo to be passed to GalactICS. Make sure all units are physical, and not comoving quantities. Instead of setting the axis line in `extpot.params` to be the z-axis, set it to be the value in `disk_axis.txt` corresponding to the live disk insertion time.

Next, run GalactICS normally and tune the parameters in `in.diskdf` to get the particle coordinates in `Rdisk`. This disk is in the frame of the box. Comment out the `APPEND` option in the code provided in Appendix E and uncomment the `REASSIGN`

[2]You can check that you're using the right timestep by ensuring the total time elapsed corresponds to the time elapsed in that cosmology.

option, and recompile. Note that if you plan to use the scripts provided here, this disk must have the same number of particles as the rigid disk. You may want to relax this assumption, and there is nothing technical with GADGET-3 which prevents this.

A.3.2 Code Setup

To run the live disk, turn off the parameters you set for the rigid disk. Instead, set `LIVE_DISK`. You need to set an initial comoving position for the live disk, its comoving velocity[3]. These values are set with the same parameters used for the rigid disk. You will not need to set an initial rotation angle, as the disk is already rotated into the box frame in `Rdisk`.

You will, however, need to set the values of the initial angular velocities. These are set using the `DISK_OMEGA*` variables, which are the box frame values. For these, consider using a moving average the values in `disk_vars.txt`. Remember that a large portion of a rigid disk's angular velocity comes from nutations. You want to choose a window size that approximately averages over a nutation period. In practice, we have found that by initialization, there is very little net angular velocity. This step is probably not necessary, although the method paper describes it as an improvement.

A.4 Known Issues and Pet Peeves

As with most code developed in academia, individual researchers are largely responsible for the development, application, and maintenance of their codes. Balancing these priorities often means sacrificing on certain optimizations. Here, we list some

[3]Note the difference from the rigid disk setup. You can change the code to take a physical velocity if you wish. You can use the value in `disk_vars.txt` for the velocity if you wish

potential improvements to the existing algorithm that might be explored.

A.4.1 Choosing a Timestep and Integration Scheme

In the paper, we use a fixed timestep for the rigid disk that is based on the center-of-mass acceleration timescale. Often, this timescale is too long for the implicit Euler scheme that we use to integrate the rigid body equations. This is why we introduced a fixed `TIMESTEP_REDUCTION_FACTOR`. In reality, the timestep should be determined from the current magnitude of the torque and angular velocity. We would recommend experimenting with an adaptive timestep. One form that might be tried is,

$$\Delta t = \frac{2\pi\alpha}{|\boldsymbol{\omega}|} \tag{A.1}$$

where α is a constant for which lower values yield more accurate integration, and $\boldsymbol{\omega}$ is the angular velocity in the disk's body frame. There were a number of halos where we found the fixed timestep to be inadequate for capturing the angular evolution of the disk. This is especially an issue when the disk begins to settle in the host halo and sheds some of its angular velocity. An adaptive timestep would give us the low error required to resolve these scenarios as well as giving us efficiency when angular velocities are low.

We are also able to improve on the integration scheme. We use Implicit Euler, a first order integration scheme. By modifying the code to make use of the fact that GADGET-3 is already using a higher order leapfrog scheme, we may be able to improve the integration accuracy.

A.4.2 Damping

Another thing we looked at was the introduction of a damping factor in the equations of motion to cause the disk to return to a steady orientation (much like an air resistance term). The physical motivation behind this was that restoring forces in the disk would resist differential torquing. We never found a satisfactory way to do this, but we would submit that limiting the magnitude of the angular velocity might accomplish this. For example, one could apply a sigmoid function element-wise to the angular velocity of the disk to simulate this effect. This should have a positive effect on the stability of the angular integration.

A.4.3 Those Compile-Time Options

On the whole, the organization of the modified code is not the best. We highly suggest you implement the algorithm yourself because of this. One of the worst design decisions we made was to make the rigid disk variables compile time options. Frankly, this is confusing since we could simply load these values from a file.

Instead, we should create a parameter file with all of the initial entries for the disk coordinates, and load it in `init.c` and `begrun.c`. This way, you will not have to recompile the code every time you want to change the initial disk variables. Although this is a simple patch, we focused our immediate efforts on producing results from applying the code.

Another argument for rewriting the code stems from the compile-time options and the private nature of Gadget-3. To be honest, there are many options which stem from projects undertaken by other groups. This confuses our additions to the code, and we run the risk of messing with fundamental compile time logic required for the proper functioning of Gadget-3. Many N-body/SPH codes use similar algorithms, and it may be worthwhile implementing the algorithm in a more public code (like Gasoline).

A.4.4 Watch out for Single-Precision Floats

The last issue you may run into is in the fact that both GalactICS and Gadget-3 snapshots use single-precision floating point numbers by default. During one experiment where we extracted a cosmological halo and ran it as an isolated galaxy simulation, loss of precision errors actually resulted in some particles being placed in the same place. This is an issue because Barnes-Hut cannot possibly separate coincident particles into separate cells.

If this happens, Gadget-3 will continue increasing the tree allocation factor until you exceed available memory. The only ways around this are to either enforce double precision in the output or to resample the coincident particles. We have not found a functional issue with either approach in the experiment that we ran with the extracted halo.

Appendix B

Referenced Code: kicks.c

```
/*
  Don't kick the rigid disk.
*/

for(j = 0; j < 3; j++)  /* do the kick, only collisionless particles */
  {
    dvel[j] = P[i].GravPM[j] * dt_gravkick;
#ifndef SIDM_FREEZE
#ifdef EPSILON_MASS
            if(P[i].Type != 1){
#endif
#ifdef RIGID_PARTICLE_DISK
              if(P[i].Type != 2){
#endif
            P[i].Vel[j] += dvel[j];
            P[i].dp[j] += P[i].Mass * dvel[j];
#ifdef RIGID_PARTICLE_DISK
```

```
                        }
#endif
#ifdef EPSILON_MASS
                     }
#endif
#endif
    }
]
```

Appendix C

Referenced Code: predict.c

```
/*
  This section of code turns off the
  kick for rigid disk particles. The kick
  is handled by separate code.
*/


#ifndef SIDM_FREEZE
#ifdef EPSILON_MASS
if (P[i].Type != 1){
#endif // EPSILON_MASS
  #ifdef RIGID_PARTICLE_DISK
  if(P[i].Type != 2){
#endif // RIGID_PARTICLE_DISK
    for(j = 0; j < 3; j++)
      P[i].Pos[j] += P[i].Vel[j] * dt_drift;
    #ifdef RIGID_PARTICLE_DISK
  }
```

```
  #endif
  #ifdef EPSILON_MASS
 }

#endif // EPSILON_MASS
#endif

]
```

Appendix D

Referenced Code: extract_halo_ascii.py

```
import pynbody
import numpy as np
import sys


"""


Extracts halo particles in a spherical region in a
Gadget snapshot. Takes in the snapshot path as
first argument, 6D coordinates from halo finder,
and writes the ASCII file in GalactICS units to
the last argument.
```

```
"""

data = pynbody.load(sys.argv[1])
a = float(data.properties['time'])
X0 = float(sys.argv[2])
Y0 = float(sys.argv[3])
Z0 = float(sys.argv[4])
VX0 = float(sys.argv[5])
VY0 = float(sys.argv[6])
VZ0 = float(sys.argv[7])
out = sys.argv[8]


masses = []
posx   = []
posy   = []
posz   = []
velx   = []
vely   = []
velz   = []

i = 0
x_dm  = np.array(data.dm['pos'].T[0], dtype=np.float32)
y_dm  = np.array(data.dm['pos'].T[1], dtype=np.float32)
z_dm  = np.array(data.dm['pos'].T[2], dtype=np.float32)
vx_dm = np.array(data.dm['vel'].T[0], dtype=np.float32)
vy_dm = np.array(data.dm['vel'].T[1], dtype=np.float32)
vz_dm = np.array(data.dm['vel'].T[2], dtype=np.float32)
```

```
m_dm  = np.array(data.dm['mass'], dtype=np.float32)
print("Reading data...\n")
for x,y,z,vx,vy,vz,m in zip(x_dm,y_dm,z_dm, vx_dm, vy_dm, vz_dm, m_dm):
    r = np.array([x - X0, y - Y0, z - Z0])
    if (np.linalg.norm(r) < 250.):
        masses.append(m*4.302)
        posx.append(r[0]*a)
        posy.append(r[1]*a)
        posz.append(r[2]*a)
        velx.append(vx / (a * 100.))
        vely.append(vy / (a * 100.))
        velz.append(vz / (a * 100.))
    i = i + 1

print("Shifting arrays...\n")
masses = np.array(masses)
velx   = np.array(velx) - VX0/(100. * a)
vely   = np.array(vely) - VY0/(100. * a)
velz   = np.array(velz) - VZ0/(100. * a)



print("Writing Xhalo of length + " + str(len(posx))  + "...\n")
f = open(out, "w")
f.write(str(len(posx)) + " 0.000000\n")
for m,x,y,z,vx,vy,vz in zip(masses, posx, posy,\
                                posz, velx, vely, velz):
    f.write(str(float(m)) + " " + str(float(x)) + " " +\
            str(float(y)) + " " + str(float(z)) + \
            " " + str(float(vx)) + " " + str(float(vy)) +\
```

```
            " " + str(float(vz)) + "\n")

print("Done.")
f.close()

]
```

Appendix E

Referenced Code: merge_ics.cpp

```
#include <vector>
#include <iostream>
#include <fstream>
#include <stdlib.h>
#include <sstream>
#include <string>
#include <math.h>
#include <cstdlib>
#include <stdio.h>

/*
  Conversion script adapted from DiskStats code
  written by JSB
*/


#define GADGET2          // Currently no support for non-Gadget codes
#define USE_POTENTIALS // Comment this out if your snapshot
```

```
                        // doesn't have these
#define GADGET_COSMOLOGY
//#define  REASSIGN // Use if disk particles are in halo snap
#define APPEND    // Use if disk particles need to be added

/*
  Class header for a single particle
*/

struct Gadget_Header{
  int npart[6];
  double mpart_arr[6];
  double time;
  double redshift;
  int flag_sfr;
  int flag_feedback;
  int npart_cum[6];
  int num_snap_files;
  double boxSize;
  double omega0;
  double omegaLambda;
  double hubbleParam;
  char fill[96];  // The total header size is
                  // always 256 bytes (see user guide)
};//header;


class Snapshot{
 private:
```

```
  Gadget_Header header;
  int nparts;

  std::vector<int> IDs;
  std::vector<int> Types;
  std::vector<double> Masses;
  std::vector<std::vector<double> > Positions;
  std::vector<std::vector<double> > Velocities;
  std::vector<double> Densities;

#ifdef USE_POTENTIALS
  std::vector<double> Potentials;
#endif

 public:
  Snapshot(char * FILE_PATH, int n_files);

  /*
    Get private data
  */

  int NParts(){return nparts;}

  int ID(int idx){return IDs[idx];}
  int Type(int idx){return Types[idx];}
  double Mass(int idx){return Masses[idx];}
  double Rho(int idx){return Densities[idx];}
  double Pot(int idx){return Potentials[idx];}
```

```
std::vector<double> Pos(int idx){return Positions[idx];}
double PosX(int idx){return Positions[idx][0];}
double PosY(int idx){return Positions[idx][1];}
double PosZ(int idx){return Positions[idx][2];}

std::vector<double> Vel(int idx){return Velocities[idx];}
double VelX(int idx){return Velocities[idx][0];}
double VelY(int idx){return Velocities[idx][1];}
double VelZ(int idx){return Velocities[idx][2];}

double Time(){return header.time;}
double Redshift(){return header.redshift;}

/*
  Load data
*/

void LoadGadget2(char * FILE_PATH, int n_files);
void WriteGadget2(char * FILE_PATH);
void AppendDiskParticles(std::vector<double> &disk_x,\
                         std::vector<double> &disk_y,\
                         std::vector<double> &disk_z,\
                         std::vector<double> &disk_vx,\
                         std::vector<double> &disk_vy,\
                         std::vector<double> &disk_vz,\
                         std::vector<double> &disk_m,\
                         std::vector<int> &disk_ids);
```

```
  /*
    Print header to terminal
  */

  void PrintGadget2Header();

};

/*
  The constructor
*/
Snapshot::Snapshot(char * FILENAME, int n_snaps){

  #ifdef GADGET2
  LoadGadget2(FILENAME, n_snaps);
  #endif

}



/*
  Load a Gadget2 snapshot
*/

void Snapshot::LoadGadget2(char * FILENAME, int n_snaps){



  FILE * file;
```

```
int gadgetFortranBuffer; // See Gadget user manual for what this is

float empty3Array[3];
float emptyFloat;
int emptyInt;
int needMassArr;
int type;
int cumSum;


/*
  Try opening the file
*/

try{
  if(!(file = fopen(FILENAME, "r"))){
    throw std::exception();
  }
}
catch(std::exception &e){
  std::cout << "Exception: Cannot open file " << FILENAME << " for reading." << std
  exit(1);
}

std::cout << "Opened file " << FILENAME << " for reading.\n" << std::endl;


/*
  Header block
```

```
*/

std::cout << "Reading␣block␣1:␣Header" << std::endl;

// Read Fortran block buffer

fread(&gadgetFortranBuffer, 4, 1, file);

std::cout << "Buffer␣=␣"<< gadgetFortranBuffer << std::endl;
// Read the header

fread(&header, sizeof(Gadget_Header), 1, file);

// Get total particle number

nparts = 0.;
for (int i = 0; i < 6; i++){
  nparts += header.npart[i];
}

// Read Fortran block buffer

fread(&gadgetFortranBuffer, 4, 1, file);
std::cout << "Buffer␣=␣"<< gadgetFortranBuffer << std::endl;

/*
  Position block
*/
```

```
std::cout << "Reading block 2: Positions" << std::endl;

// Read Fortran block buffer

fread(&gadgetFortranBuffer, 4, 1, file);
std::cout << "Buffer = "<< gadgetFortranBuffer << std::endl;

// Read the positions

for (int i = 0; i < nparts; i++){
  fread(empty3Array, sizeof(float), 3, file);
  std::vector<double> newPos(3,0);
  newPos[0] = (double) empty3Array[0];
  newPos[1] = (double) empty3Array[1];
  newPos[2] = (double) empty3Array[2];

  if (newPos[0] != newPos[0] || newPos[1]
      != newPos[1] || newPos[2] != newPos[2]){
    std::cout << "NaN in positions." << std::endl;
    exit(2);
  }
  Positions.push_back(newPos);
}

// Read Fortran block buffer

fread(&gadgetFortranBuffer, 4, 1, file);
std::cout << "Buffer = "<< gadgetFortranBuffer << std::endl;
```

```
/*
  Read velocities
*/

std::cout << "Reading block 3: Velocities" << std::endl;


// Read Fortran block buffer

fread(&gadgetFortranBuffer, 4, 1, file);
std::cout << "Buffer = "<< gadgetFortranBuffer << std::endl;

// Get velocities

for (int i = 0; i < nparts; i++){
  fread(empty3Array, sizeof(float), 3, file);
  std::vector<double> newVel(3,0);
  newVel[0] = (double) empty3Array[0];
  newVel[1] = (double) empty3Array[1];
  newVel[2] = (double) empty3Array[2];
  Velocities.push_back(newVel);
}

// Read Fortran block buffer

fread(&gadgetFortranBuffer, 4, 1, file);
std::cout << "Buffer = "<< gadgetFortranBuffer << std::endl;
```

```
/*
  Get IDs
*/

std::cout << "Reading block 4: IDs" << std::endl;

// Read Fortran block buffer

fread(&gadgetFortranBuffer, 4, 1, file);
std::cout << "Buffer = "<< gadgetFortranBuffer << std::endl;

// Get IDs

for (int i = 0; i < nparts; i++){
  fread(&emptyInt, sizeof(int), 1, file);
  int newID = emptyInt;
  IDs.push_back(newID);
}

// Read Fortran block buffer

fread(&gadgetFortranBuffer, 4, 1, file);
std::cout << "Buffer = "<< gadgetFortranBuffer << std::endl;

/*
  Masses if needed
*/

needMassArr = 0;
```

```
for (int i = 0; i < 6; i++){
  if (header.npart[i] != 0 && header.mpart_arr[i] == 0)
    needMassArr = 1;
}

if (needMassArr == 1){
  std::cout << "Reading block 5: Masses" << std::endl;

  // Read Fortran buffer

  fread(&gadgetFortranBuffer, 4, 1, file);
  std::cout << "Buffer = "<< gadgetFortranBuffer << std::endl;

  // Get masses

  type = 0;
  for (int i = 0; i < nparts; i++){

    int j = 0;
    cumSum = 0;
    while (i >= cumSum){
      cumSum += header.npart[j];
      j++;
    }

    type = j - 1;

    if (header.mpart_arr[type] == 0){
      fread(&emptyFloat, sizeof(float), 1, file);
```

```
      double newMass = (double)emptyFloat;
      Masses.push_back(newMass);
    }
    else{
      Masses.push_back(header.mpart_arr[type]);
    }
    Types.push_back(type);
  }

  // Read Fortran buffer

  fread(&gadgetFortranBuffer, 4, 1, file);
  std::cout << "Buffer = "<< gadgetFortranBuffer << std::endl;




  /*
    Get internal energies (empty if no SPH)
  */
  std::cout << "Reading Block 6: Internal Energies" << std::endl;

  fread(&gadgetFortranBuffer, 4, 1, file);

  for (int i = 0; i < header.npart[0]; i++){
    fread(&emptyFloat, sizeof(float), 1, file);
    float newE = emptyFloat;
  }

  fread(&gadgetFortranBuffer, 4, 1, file);
```

```
/*
  Get density (empty if no SPH)
*/


std::cout << "Reading␣Block␣7:␣Densities" << std::endl;
fread(&gadgetFortranBuffer, 4, 1, file);

for (int i = 0; i < header.npart[0]; i++){
  fread(&emptyFloat, sizeof(float), 1, file);
  float newRho = emptyFloat;
}


fread(&gadgetFortranBuffer, 4, 1, file);

/*
  Get smoothing (empty if no SPH)
*/

std::cout << "Reading␣Block␣8:␣Smoothing" << std::endl;
fread(&gadgetFortranBuffer, 4, 1, file);

for (int i = 0; i < header.npart[0]; i++){
  fread(&emptyFloat, sizeof(float), 1, file);
  float newSmooth = emptyFloat;
}
```

```
    fread(&gadgetFortranBuffer, 4, 1, file);

    /*
      Get potentials
    */
    std::cout << "Reading Block 9: Potentials" << std::endl;

    fread(&gadgetFortranBuffer, 4, 1, file);

    for (int i = 0; i < nparts; i++){
      fread(&emptyFloat, sizeof(float), 1, file);
      float newPot = emptyFloat;

#ifdef USE_POTENTIALS
      if (newPot <= 0.){
        Potentials.push_back(newPot);
      }
      else{
        Potentials.push_back(-newPot);
      }
#endif
    }

    fread(&gadgetFortranBuffer, 4, 1, file);

  }

  /*
```

```
    Print snapshot summary
  */

#ifdef GADGET2
  std::cout << "\n" << std::endl;
  PrintGadget2Header();
#endif
}

void Snapshot::PrintGadget2Header(){
  std::cout << "Type 0 (Gas): "\
            << header.npart[0]\
            << " (m="
            << header.mpart_arr[0]
            << ")" << std::endl;

  std::cout << "Type 1 (Halo): "
            << header.npart[1]
            << " (m="
            << header.mpart_arr[1]
            << ")" << std::endl;

  std::cout << "Type 2 (Disk): "
            << header.npart[2]
            << " (m=" << header.mpart_arr[2]
            << ")" << std::endl;

  std::cout << "Type 3 (Bulge): "
            << header.npart[3]
```

```
              << " (m="
              << header.mpart_arr[3]
              << ")" << std::endl;
  std::cout << "Type 4 (Other): "
              << header.npart[4]
              << " (m="
              << header.mpart_arr[4]
              << ")" << std::endl;
  std::cout << "Type 5 (Boundary): "
              << header.npart[5]
              << " (m=" << header.mpart_arr[5]
              << ")" << std::endl;
}


/*
  Write the snapshot
*/

void Snapshot::WriteGadget2(char * FILE_PATH){
  int gadgetFortranBuffer;
  float x,y,z,vx,vy,vz,m;
  // The out stream
  FILE * fp = fopen(FILE_PATH, "wb");

  /*
    Block 1 (header)
  */
```

```
std::cout << "Writing block 1: Header" << std::endl;

// Gadget expects the size of the block
gadgetFortranBuffer = sizeof(header);


fwrite(&gadgetFortranBuffer, 4, 1, fp);
fwrite(&header, sizeof(header), 1, fp);
fwrite(&gadgetFortranBuffer, 4, 1, fp);


/*
  Block 2 (positions)
*/
std::cout << "Writing block 2: Positions" << std::endl;

gadgetFortranBuffer = (3 * 4 * Positions.size());
fwrite(&gadgetFortranBuffer, 4, 1, fp);

for (int i = 0; i < Positions.size(); i++){
  x = (float)Positions[i][0];
  y = (float)Positions[i][1];
  z = (float)Positions[i][2];
  fwrite(&x, 4, 1, fp);
  fwrite(&y, 4, 1, fp);
  fwrite(&z, 4, 1, fp);

}
```

```
fwrite(&gadgetFortranBuffer, 4, 1, fp);


/*
  Block 3 (velocities)
*/

std::cout << "Writing block 3: Velocities" << std::endl;

gadgetFortranBuffer = (3 * 4 * Velocities.size());
fwrite(&gadgetFortranBuffer, 4, 1, fp);

for (int i = 0; i < Velocities.size(); i++){
  vx = (float)Velocities[i][0];
  vy = (float)Velocities[i][1];
  vz = (float)Velocities[i][2];

  fwrite(&vx, 4, 1, fp);
  fwrite(&vy, 4, 1, fp);
  fwrite(&vz, 4, 1, fp);
}


fwrite(&gadgetFortranBuffer, 4, 1, fp);


/*
  Block 4 (IDs)
*/
```

```
std::cout << "Writing block 4: IDs" << std::endl;

gadgetFortranBuffer = (4 * IDs.size());
fwrite(&gadgetFortranBuffer, 4, 1, fp);

for (int i = 0; i < IDs.size(); i++){
  fwrite(&IDs[i], 4, 1, fp);
}

fwrite(&gadgetFortranBuffer, 4, 1, fp);



/*
  Block 5 (masses)
*/

std::cout << "Writing block 5: Masses" << std::endl;

gadgetFortranBuffer =(4 * IDs.size());

fwrite(&gadgetFortranBuffer, 4, 1, fp);

for (int i = 0; i < Masses.size(); i++){
  m = Masses[i];
  fwrite(&m, 4, 1, fp);
}
fwrite(&gadgetFortranBuffer, 4, 1, fp);
```

```
  fclose(fp);
}


/*
  Add disk particles
*/

void Snapshot::AppendDiskParticles(std::vector<double> &disk_x,\
                                   std::vector<double> &disk_y,\
                                   std::vector<double> &disk_z,\
                                   std::vector<double> &disk_vx,\
                                   std::vector<double> &disk_vy,\
                                   std::vector<double> &disk_vz,\
                                   std::vector<double> &disk_m, \
                                   std::vector<int> &disk_ids){
  std::vector<std::vector<double> > newPos;
  std::vector<std::vector<double> > newVel;
  std::vector<double> newM;
  std::vector<int> newIDs;
  std::vector<double >::iterator it;
  std::vector<std::vector<double> >::iterator it2;
  std::vector<int >::iterator it3;
  int npartsBeforeDisk;
  int npartsAfterDisk;

  npartsBeforeDisk = header.npart[0] + header.npart[1];

  for (int i = 0; i < disk_x.size(); i++){
```

```
    std::vector<double> newVector(3,0);
    newVector[0] = disk_x[i];
    newVector[1] = disk_y[i];
    newVector[2] = disk_z[i];
    newPos.push_back(newVector);
  }

  std::cout << "Size of new positions is " << newPos.size() << std::endl;

  for (int i = 0; i < disk_vx.size(); i++){
    std::vector<double> newVector(3,0);
    newVector[0] = disk_vx[i];
    newVector[1] = disk_vy[i];
    newVector[2] = disk_vz[i];

#ifdef GADGET_COSMOLOGY
#endif
    newVel.push_back(newVector);
  }

  std::cout << "Size of new velocities is " << newVel.size() << std::endl;

#ifdef APPEND
  nparts += disk_x.size();
#endif

  for (int i = 0; i < nparts; i++){
    newIDs.push_back(i + 1);
  }
```

```
  for (int i = 0; i < disk_m.size(); i++){
    newM.push_back(disk_m[i]);
  }

#ifdef APPEND
  header.npart[2] += disk_x.size();
  nparts += disk_x.size();
  header.mpart_arr[0] = header.mpart_arr[1] = header.mpart_arr[2] \
    = header.mpart_arr[3] = header.mpart_arr[4] = header.mpart_arr[5] = 0.;

  std::cout << "Arrays constructed. Merging IDs..." << std::endl;

  IDs = newIDs;
#endif

#ifdef REASSIGN
  std::cout << "Merging arrays... " << std::endl;
  int j = 0;



  std::cout << "Reassigning stats to " \
            << header.npart[2] << " particles" << std::endl;
  for (int i = header.npart[1] + header.npart[0];\
       i < header.npart[0] + header.npart[1] +  header.npart[2];\
       i++){
    j = i - header.npart[1] - header.npart[0];

    Masses[i] = newM[j];
```

```
    Positions[i] = newPos[j];
    Velocities[i] = newVel[j];
  }

#endif

#ifdef APPEND
  it = Masses.begin();
  Masses.insert(it+npartsBeforeDisk, newM.begin(), newM.end());
  std::cout << "New mass vector of length " << Masses.size() << std::endl;



  std::cout << "Merging positions... " << std::endl;
  it2 = Positions.begin();
  Positions.insert(it2+npartsBeforeDisk, newPos.begin(), newPos.end());
  std::cout << "New position vector of length " << Positions.size() << std::endl;

  std::cout << "Merging velocities... " << std::endl;
  it2 = Velocities.begin();
  Velocities.insert(it2+npartsBeforeDisk, newVel.begin(), newVel.end());
  std::cout << "New velocity vector of length " << Velocities.size() << std::endl;
#endif

  std::cout << "Arrays reconstructed." << std::endl;
}

/*
  Main loop
*/
```

```
int main(int argc, char ** argv){
  double timeFromRedshift, massUnitConversion;
  std::string x,y,z,vx,vy,vz,m;
  char * haloFile;
  char * diskFile;
  char * outFile;
  int nHaloParts, nDiskParts;
  std::string line;
  std::vector<double> disk_x,disk_y,disk_z;
  std::vector<double> disk_vx,disk_vy,disk_vz;
  std::vector<double> disk_m;
  std::vector<int> disk_ids;
  Snapshot * snap;
  std::fstream inDisk;


  haloFile = argv[1];
  diskFile = argv[2];
  outFile = argv[3];


  try{
    inDisk.open(diskFile);
    if (!inDisk.is_open())
      throw std::exception();
  }
  catch (std::exception &e){
    std::cout << "Could not open disk file. "
              << "Check if it exists. " << std::endl;
```

```
  exit(1);
}




massUnitConversion = 1./4.301;

/*
  The halo file is a Gadget snapshot
*/

snap = new Snapshot(haloFile,1);
timeFromRedshift = 1./(1. + snap->Redshift());

/*
  The disk file will be in GalactICS ASCII
*/

getline(inDisk,line);
std::stringstream iss0(line);
iss0 >> nDiskParts;

std::cout << "\nReading " << nDiskParts <<\
  " disk particles from " << diskFile << std::endl;
int id = 1;
while (id <= nDiskParts){
  getline(inDisk,line);
  std::stringstream iss(line);
```

```
    iss >> m;
    iss >> x;
    iss >> y;
    iss >> z;
    iss >> vx;
    iss >> vy;
    iss >> vz;


    disk_m.push_back(atof(m.c_str())* massUnitConversion);
    disk_x.push_back(atof(x.c_str()));
    disk_y.push_back(atof(y.c_str()));
    disk_z.push_back(atof(z.c_str()));

#ifdef GADGET_COSMOLOGY
    disk_vx.push_back(atof(vx.c_str()) * 100. \
                    / (pow(timeFromRedshift,1.5)));
    disk_vy.push_back(atof(vy.c_str()) * 100. \
                    / (pow(timeFromRedshift,1.5) ));
    disk_vz.push_back(atof(vz.c_str()) * 100. \
                    / (pow(timeFromRedshift,1.5) ));
#else
    disk_vx.push_back(atof(vx.c_str()) * 100.);
    disk_vy.push_back(atof(vy.c_str()) * 100.);
    disk_vz.push_back(atof(vz.c_str()) * 100.);
#endif

    disk_ids.push_back(id);
    id++;
```

```
  }
  std::cout << "Disk file read." << std::endl;

  std::cout << "Appending disk particles..." << std::endl;

  snap->AppendDiskParticles(disk_x, disk_y, disk_z, disk_vx,\
                             disk_vy, disk_vz, disk_m, disk_ids);

  snap->WriteGadget2(outFile);

  delete snap;

  // Test reopen

  std::cout << "Testing by reopening..." << std::endl;
  snap = new Snapshot(outFile, 1);

  delete snap;

  return 0; //success
}
```

]

Appendix F

Referenced Code: timestep.c

```
/*
  Segment of code that handles forcing particles into same timestep bin.

  diskDVars is a differencec array that will be defined later. All other
  variables are explained in allvars.h/c.
*/


#elif defined(RIGID_PARTICLE_DISK)
double rigidDiskAcc;
      rigidDiskAcc = diskDVars[3] * diskDVars[3] + diskDVars[4] *\
        diskDVars[4] +                                            \
        diskDVars[5] * diskDVars[5];
rigidDiskAcc = pow(rigidDiskAcc, 0.5);
if(P[p].Type == 2){
  dt = sqrt(2 * All.ErrTolIntAccuracy *\
            All.cf_atime * All.SofteningTable[P[p].Type] / \
            rigidDiskAcc)/TIMESTEP_REDUCTION;
```

```
  }

  else
    dt = sqrt(2 * All.ErrTolIntAccuracy * All.cf_atime *\
                  All.SofteningTable[P[p].Type] / ac);

#else
```

]

Bibliography

Barnes, J. and Hut, P. (1986). A hierarchical O(N log N) force-calculation algorithm. *Nature*, 324:446–449.

Hernquist, L., Bouchet, F. R., and Suto, Y. (1991). Application of the Ewald method to cosmological N-body simulations. *ApJS*, 75:231–240.

Springel, V. (2005). The cosmological simulation code GADGET-2. *MNRAS*, 364:1105–1134.